MORPHOLOGY ENGINEERING AND PHOTOCATALYTIC ACTIVITY OF ZnO AND CdS NANOSTRUCTURES DERIVED FROM COORDINATION POLYMERS AS PRECURSORS

A thesis submitted for the partial fulfilment of
doctoral degree in Chemical Sciences

By

Smriti Thakur
MP13011

under the supervision of

Professor Sanjay K. Mandal

Department of Chemical Sciences,
Indian Institute of Science Education and Research (IISER) Mohali,
Knowledge city, Sector 81, SAS Nagar, Manauli PO, Mohali 140306, Punjab, India.

March, 2019

DEDICATED to

TO ALL MY RESPECTED TEACHERS,

LOVING FRIENDS and

FAMILY MEMBERS

Declaration

I hereby declare that the matter embodied in this thesis is the result of investigations carried out by me under the supervision of Prof. Sanjay K. Mandal at the Department of Chemical Sciences, Indian Institute of Science Education and Research (IISER) Mohali, SAS Nagar Mohali, India. This work has not been submitted in part or in full for a degree, a diploma, or a fellowship to any other university or institute. Whenever contributions of others are involved, every effort is made to indicate this clearly, with due acknowledgment of collaborative research and discussions. Any omission that might have occurred due to oversight or error in judgment is regretted. This thesis is a bona fide record of original work done by me and a complete bibliography of the books and journals referred to is given at the end of the thesis.

Smriti Thakur

Date:
Place:

In my capacity as the supervisor of the candidate's thesis work, I certify that the above statements by the candidate are true to the best of my knowledge.

Dr. Sanjay K. Mandal

Date:
Place:

Acknowledgments

I would like to express my sincere gratitude to several people who have contributed towards shaping this thesis. The completion of this thesis would have never been possible without their support.

First and foremost, I owe a deep sense of gratitude to my supervisor Prof. Sanjay Mandal for his valuable advice, guidance and consistent encouragement for the past three and half years. His scholarly inputs and comments helped me building concepts to give an overall direction to this research. I thank him for growing me as a research scientist. This accomplishment has been made possible because of his unconditional support and guidance throughout this time.

I am also grateful to my doctoral committee: Dr. Ramesh Ramachandran and Dr. Ananth Venkatesan. Their brilliant comments and suggestions have encouraged me to carry forward this research with in depth investigation and analysis.

I also wish to thank Prof. N. Sathyamurthy and Prof. Debi P. Sarkar, former Directors, IISER Mohali, for providing the infrastructure and central research facilities (FESEM, X-ray, AFM and Library) facilities at IISER Mohali. I want to acknowledge Prof. K. S. Viswanathan and Dr. S. Arulananda Babu, former and current Head of the Department, Chemical Sciences, IISER Mohali, for granting me to use various departmental facilities.

I thank IISER Mohali for providing me a platform to carry out research with very good lab facilities and MHRD for research fellowship.

I would like to deeply acknowledge my current and former lab members, Dr. Sadhika Khullar (for constructing the foundation of this research), Dr. Navnita Kumar, Dr. Sandeep Kashyap (for helping me with the valuable suggestions in the initial days), Biswajit Laha, Vijay Gupta (for his help in the experimental set ups at the start), Datta Markad, Gouri Chakraborty and Prasenjit Das (for their help in fluorescence studies), Shradha Gandhi, Alisha Gogia and Sheeba Khan for their cooperation in creating a good working atmosphere in the lab.

I express my humble gratitude to Mr. Bahadur, Mr. Mangat, Mr. Satwinder, Mr. Prahlad, Mr. Vishal and Mr. Ganesh (lab assistants of chemistry teaching lab) for their time to time help.

I have great pleasure in thanking Mr. Sandeep Badhan (summer project student) for his support in studying the antibacterial properties of nanomaterials.

Words are inadequate to express my hearty thanks to my friends Anita, Nisha, Vivek, Sumit, Manvendra, Pushpendra for their love, care and support throughout this time. The dinners, debates, birthday parties, hang out to different places, general help and friendship all are highly appreciated. I also want to thank my friends – Surbhi, Shivani, Sakshi, Nitika, Ruby and Sarjeet for your well wishes, phone calls, texts, e-mails and your support in the hour of need.

I take this opportunity to thank all my cousins- Yukti, Shrishti, Kriti, Rishabh, Jigyasa, Vaishali, Om, Dhairya for all the fun-filled moments we had together at family gatherings. Thanks for cheering me up throughout this period. I also thank all other relatives – uncles and aunts in the family for their love. Special thanks to my maternal grandmaa who must be happy and showering her blessings from heaven to see her granddaughter accomplish her dream.

I would also like to say a heartful thanks to my parents for always encouraging me to follow my dreams. I am especially grateful to my father, Ram Thakur, for guiding me as a person and supporting me financially and emotionally everytime I need. He has always reminded me life’s true priorities during ups and downs through his spiritual insights. Thankyou mum, Indu Thakur for believing in me and wanting me to do best in life. Her love and patience has always given me strength to overcome the difficult times during this phase. I owe everything to them. I expand my thanks to my lovely sister, Shweta Thakur Gupta and my brother-in-law Ankur Gupta who have been a constant source of motivation for me. They were always beside me during the happy moments. Their emotional support and care in many aspects during these years have helped me in conducting this research well.

Above all, I owe it all to Almighty for granting me wisdom, strength and mercifulness in accomplishing this work.

List of Figures

Chapter I (Introduction)

Chapter III (Results and Discussion)

List of Schemes

Chapter III (Results and Discussion)

List of Tables

Chapter III (Results and Discussion)

Contents

ABSTRACT

The new scientific technologies are the result of human dreams and imagination. The emergence of nanotechnology, a 21st century frontier is the outcome of such dreams. Nanotechnology is any technology at the atomic, molecular or macromolecular levels, whose dimensions are between 1 and 100 nm. It is believed to bring the next industrial revolution for exponential growth. The world of nanotechnology has an enormous impact on human life by providing society with great benefits. Over the past few decades, it has received more attention than ever worldwide for the design and development of nanomaterials and nanodevices used in many sectors like electronics, optics, medicine, plastics, energy, environment and aerospace. Multidisciplinary teams work together on the synthesis and processing of a diverse range of nanomaterials with unique physical and chemical properties of nanomaterials, which bridge between bulk materials and atomic or molecular structures. The control over size, shape and morphology of such materials always remains an ultimate challenge for the researchers. In the literature, two well-known approaches (top-down and bottom-up) have been utilized for the fabrication of desired nanostructures while the second one is preferred, as is the case for this study. Among various nanomaterials, metal oxides and sulphides have the most versatile applications due to their unique properties.

This thesis work mainly focused on the morphology engineering of zinc oxide (ZnO) and cadmium sulphide (CdS) nanostructures using coordination polymers (CPs), having a general formula $\{[M_2(bpxa)_2(adc)_2].yH_2O\}_n$ (where M(II) = Zn(II) or Cd(II); bpxa = N,N'-bis(pyridylmethyl)alkyl amine, alkyl = methyl, ethyl, tert-butyl; adc = acetylene dicarboxylate; y = 0 or 2), as precursors under various fabrication conditions (temperature, pH, time, solvent, post-synthetic annealing, and doping with divalent metal ion). Both hydrothermal and direct calcination fabrication methods utilized for these nanostructures are versatile, reproducible, scalable, efficient, eco-friendly, and surfactant-less. Compared to the traditional use of respective metal salts, such as zinc or cadmium acetate/nitrate, these CPs act as sacrificial templates providing a control over desired morphologies of the nanostructures. Furthermore, the tridentate bis(pyridyl) ligand in the CPs has a profound effect on the formation of these nanostructures. All ZnO and CdS nanostructures were characterized by powder X-ray diffraction (PXRD), field-emission scanning electron microscopy (FESEM), high resolution transmission electron microscopy (HRTEM), atomic force microscopy (AFM), and Raman and UV-VIS spectroscopy. Based on the critical and systematic evaluation (morphology and aspect ratio), and time-dependent study, of six different nanostructures (two of them are rare), their formation and morphology transition (e.g., 3D nanoflowers to 1D nanorods) can be understood. For showcasing their photocatalytic property, relevant examples will be discussed with an emphasis on: (a) the selective and optimum degradation of Congo red among four common dyes by ZnO nanoflowers at pH = 8, and (b) the correlation between morphology and rate of degradation of methylene blue by both ZnO and CdS nanostructures.

CHAPTER I

INTRODUCTION

The new scientific technologies are the result of human dreams and imagination. The emergence of nanotechnology, a 21st century frontier is the outcome of such dreams. The word ‘nano’ is derived from the Greek word which means ‘dwarf’. Thus, nanotechnology is any technology at the atomic, molecular or macromolecular levels, whose dimensions are between 1 and 100 nm. The term ‘nanometer’ was first proposed by Richard Zsigmondy, the 1925 Nobel Prize Laureate in chemistry. He was the first person to characterize the size of particles (gold colloids) using a microscope. Though the human exposure to nanoparticles was not new but it was drastically increased after the industrial revolution. However, the growth of modern nanotechnology began in 1959 when Richard Feynman, a Nobel Prize Laureate in Physics, presented a lecture in the American Physical Society at Caltech. He delivered a speech titled “There’s a plenty of room at the bottom’’. In his speech he introduced the concept of “manipulating and controlling the matter on a small scale’’ and discussed the change in the physical phenomenon that occur on the small scale. Feynman’s hypothesis demonstrated new ways of thinking and paved the way for new technological breakthroughs in the areas of materials, nanoelectronics, biotechnology, information technology, medicine and healthcare.

In 1974, a Japanese scientist, Norio Taniguchi, was the first to use the term ‘nanotechnology’ in a paper on production technology that creates objects which consists of the processing, segregation, blending and deformation of materials on the order of a nanometer.

The year 1980 saw the emergence of golden era of nanotechnology when Kruto, Smalley and Curl discovered fullerenes. In 1986, the American engineer K. Eric Drexler used the term "nanotechnology" in his book titled “Engines of Creation: The Coming Era of Nanotechnology”, which was inspired by Feynman’s ideas “There’s a plenty of room at the bottom’’. In his book he proposed and discussed the idea of a nanoscale "assembler" which would be able to build a copy of itself and of other items of arbitrary complexity with atomic control.

It was back in 1985 when a conflux of events led to an unexpected result with the discovery of new shapes for molecules of carbon, known as the bucky ball which consists of 60 carbon atoms in a shape of soccer ball. In the year 1991, after the discovery of fullerenes, Sumio Iijima of NEC found an extremely thin needle-like material which was proved to have a graphite-like structure was named as ‘carbon nanotubes’ because of a tubular structure made of carbon atom sheets. Whereas the development of quantum dots was observed in the year 1985 when Louis E. Brus discovered the semiconductor nanocrystals in a glass matrix. He called these nanocrystals “quantum dots’’. The properties of these quantum dots are between those of bulk semiconductors and discrete molecules. The central theme of nanotechnology is based on these quantum dots. Since then, the synthesis, processing, designing and fabrication of such materials continued to be the focus of research across the world.

Nanotechnology has been booming worldwide in many areas which include materials science, electronics, optics, medicine, plastics, energy and aerospace. Nanotechnology aims at building nanomaterials which are of great scientific interest because of their unique physical and chemical properties that act as a bridge between bulk materials and atomic or molecular structures. When particles assume nanoscale dimension, the principles of classical mechanics can no longer describe their behavior (movement, energy, etc.). At these dimensions the principles of quantum mechanics apply. Thus, the materials on the nanometer scale may exhibit physical properties entirely different from those of the bulk.[1] This can be attributed to the fact that quantum size effects begin to appear at nanoscale which is a consequence of the strong reduction of allowed states in the small particles resulting in an increase in the band gap. However, the properties of nanomaterials are determined not only by the particle size but also by several other factors: structure, shape and surface status of the particles. In semiconductors, the spatial confinement of electronic motion to a length scale, which is comparable to or smaller than the length of the electron Bohr radius, gives rise to size-dependent optical and electrical properties of nanoparticles. The attenuation of devices in the nanoscale regime has received considerable attention for the realization of better properties of nanomaterials. In this regard, nanotechnology has come as an emerging interdisciplinary technology to meet the increasing energy demands for the realization of new materials with specific functionality and selectivity. Therefore, multidisciplinary teams from various domains of science including physicists, chemists, molecular biologists, material scientists and engineers work together on the synthesis and processing of nanomaterials, design and fabrication of nanodevices with nanomaterials as the building blocks, construction of the novel tools for the characterization of these materials. Nanotechnology is believed to bring the next industrial revolution for exponential growth. The world of nanotechnology has an enormous impact on human life by providing society with great benefits.

1.1 Classification of nanomaterials

1.1.1 *On the basis of origin of nanomaterials*

(i) Natural nanomaterials

Nanomaterials which belong to the natural world and have not been processed or engineered by humans are called natural nanomaterials. Due to the inherent nanostructures, these materials possess remarkable properties. These include:

a) **Natural inorganic nanomaterials.** These materials include a wide spectrum of elements, the most common being:- metal oxides/hydroxides (e.g. manganese oxides and hydroxides, iron oxides/oxyhydroxides), metal alloys, silicates (e.g. allophane, fibrous clay minerals, asbestos), sulphides (FeS_2 and ZnS), sulphates, halides and carbonates. The underlying mechanism for the growth of these materials involves nucleation and growth of various inorganic phases in the atmosphere. The inorganic reactions occuring in the hydrosphere and the lithosphere contributes to the generation of these materials via non-thermal, thermal, photochemical and biological processes (Figure 1.1). For example, volcanic activity give rise to opals. Fires can produce pigments, cement, fused silica etc. Iron-oxidizing bacteria (Leptothrix, Gallionela) of ferrihydrite can produce ferric oxyhydride which can be identified in ground water and soils.

Figure 1.1. (a) Clay nanoparticles (b) Iron Pyrite (FeS_2) (c) Natural processes leading to the formation of inorganic materials in the environment.

b) **Natural organic nanomaterials.** Mother nature has also provided a vast array of organic nanoparticles (Figure 1.2). Nature has given the first carbon nanotube and the first buckyball (carbon fullerene) produced from the combustion of fossil fuels. The volcanic ashes that are released during eruptions contains naturally occurring buckyballs. The petroleum and the natural gas contain organic nanostructures which deposits as nanoscale diamond structures.

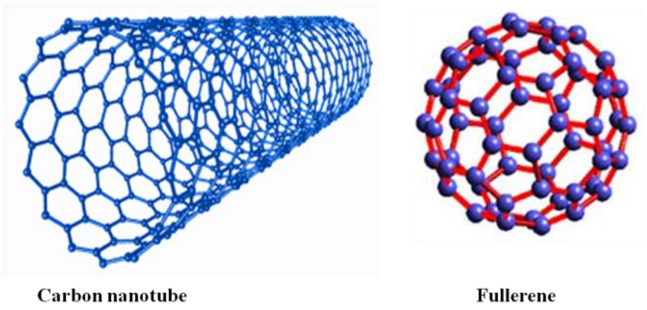

Figure 1.2. Naturally occurring organic nanomaterials.

(ii) Artificial nanomaterials

These are the ones that are fabricated by different experiments. They can be further sub-divided into 4 classes:

a) **Carbon based.** These nanomaterials are composed mostly of carbon, most commonly taking the form of a hollow spheres, ellipsoids, or tubes (Figure 1.3). Spherical and ellipsoidal carbon nanomaterials are referred to as fullerenes, while cylindrical ones are called nanotubes (carbon nanotubes (CNTs)).

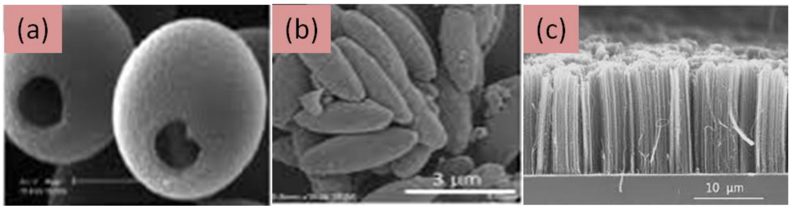

Figure 1.3. (a) Hollow carbon spheres (b) Polydopamine ellipsoids (c) Carbon nanotubes.

b) **Metal-based.** These nanomaterials include quantum dots, nanogold, nanosilver and metal oxides, such as titanium dioxide (Figure 1.4).

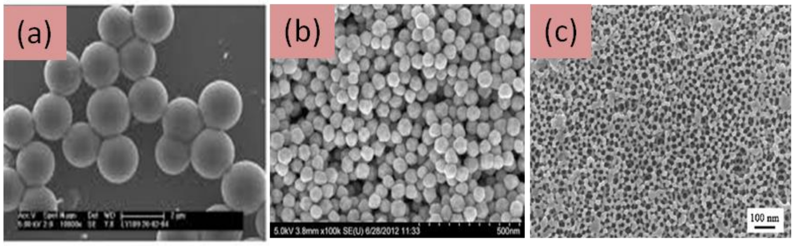

Figure 1.4. (a) CdS quantum dots (b) Gold nanoparticles (c) Thin film of TiO_2 particles.

c) **Dendrimers.** These nanomaterials are nanosized polymers built from branched units. The surface of a dendrimer has numerous chain ends, which can be tailored to perform specific chemical functions. This property could also be useful for catalysis. Also, because three-dimensional dendrimers contain interior cavities into which other molecules could be placed, they may be useful for drug delivery (Figure 1.5).

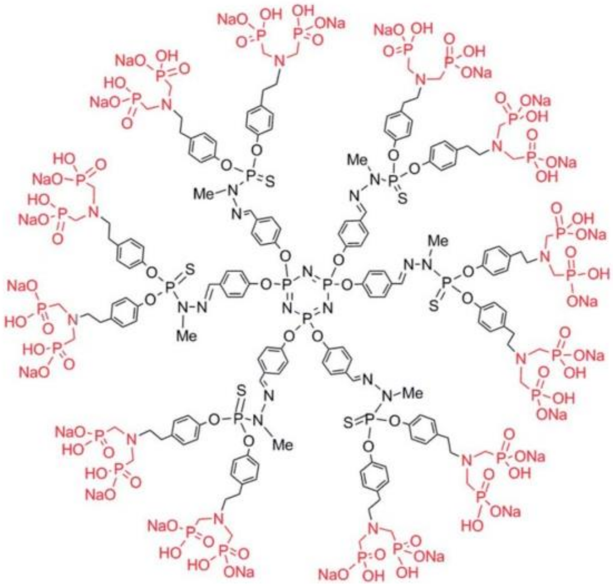

Figure 1.5. Dendrimer ABP (azabisphosphonic end groups on a first generation PPH dendrimer) having immunomodulatory effects on the human immune system. (Adapted from reference 2).

d) **Composites.** Composites combine nanoparticles with other nanoparticles or with larger, bulk-type materials. The composites may be any combination of metal based, carbon based or polymer-based nanomaterials with any form of metal, ceramic, or polymer bulk materials (Figure 1.6).

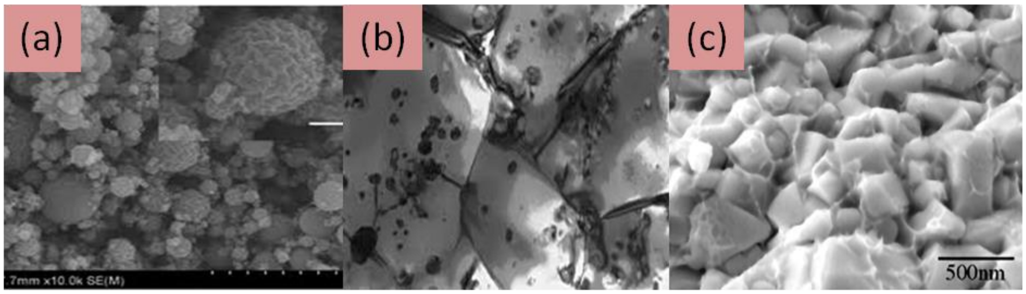

Figure 1.6. (a) Ni-PVP nanocomposite (b) Alumina/SiC nanocomposite (c) Polymer matrix nanocomposite. (Adapted from reference 3 and 4).

1.1.2 *On the basis of dimensions of nanomaterials*

Nanomaterials can also be classified on the basis of dimensions (Figure 1.7)

(i) Zero dimensional (0D) nanomaterials. Materials wherein all the dimensions are measured within the nanoscale (no dimensions larger than 100 nm). For example, uniform particle arrays (quantum dots), heterogeneous particle arrays, core-shell quantum dots, hollow spheres, clusters, cubic, polyhedron-type, metal nanoparticles such as nanogold and nanosilver etc.

(ii) One dimensional (1D) nanomaterials. This class of materials comprises of those materials whose one dimension is outside the nanoscale whereas the other two dimensions are in the nanoscale regime (1-100 nm). For example, nanotubes, nanorods, nanowires etc.

(iii) Two dimensional (2D) nanomaterials. In these materials two dimensions are out of the nanoscale whereas one dimension is in the range of 1-100 nm. For example, nanofilms, nanolayers, nanocoatings, nanoprisms, nanoplates, nanosheets, nanowalls and nanodisks.

(iv) Three dimensional (3D) nanomaterials. The materials wherein all the 3 dimensions are out of nanoscale regime are referred as 3D materials. For example, nanoballs, nanocoils, nanocones, nanopillers and nanoflowers.

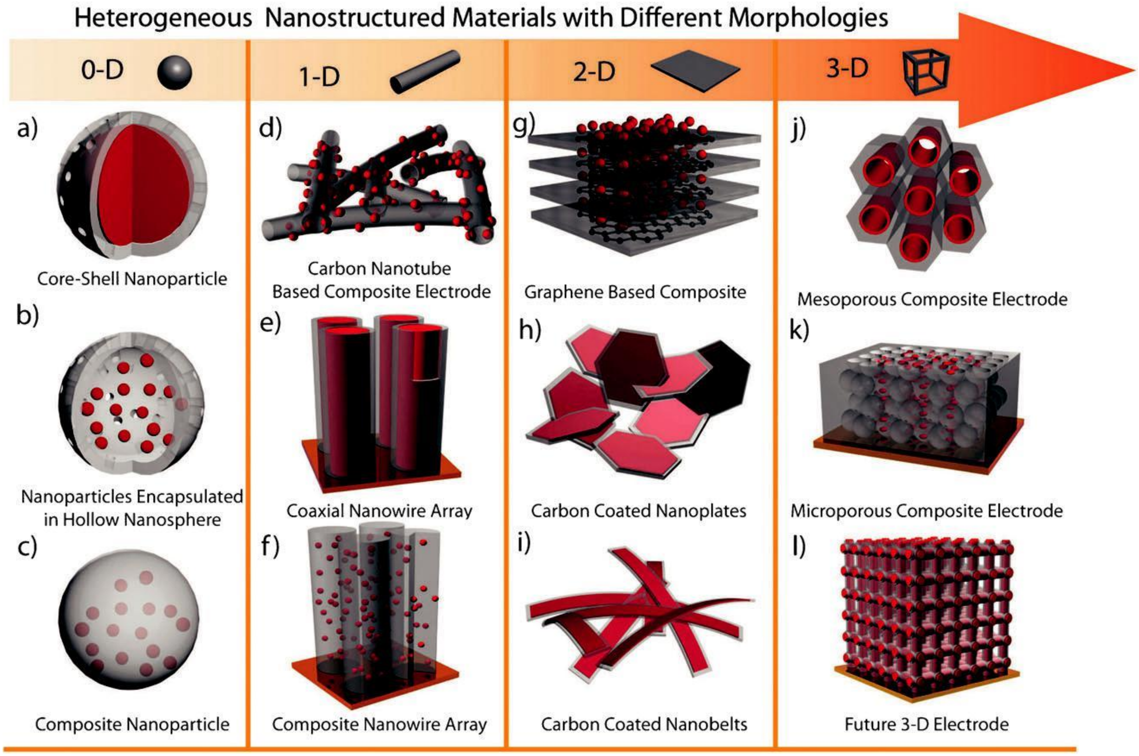

Figure 1.7. Classification of nanomaterials on the basis of dimension (Adapted from reference 5).

1.2 General methods for the synthesis of nanomaterials

There are two general approaches for the synthesis and fabrication of nanomaterials which are as follows:

(i) Bottom-up. This approach involves the miniaturization of material components (up to atomic level) followed by the self assembly process to produce nanoparticles. During the self assembly process, the physical forces operating at nanoscale combine the basic units into larger stable structures. This approach has been proved to be more favourable for the synthesis of nanoparticles. Different techniques have been developed to synthesise the nanomaterials using this approach. Typical examples are the formation of nanoparticles from colloidal dispersions.

(ii) Top-down. This approach involves the formation of nanosized particles by breaking or sculpturing of a large block of material employing physical methods of ball milling, lithography, etching through the mask and application of severe plastic deformation.

The graphical representation of the above two approaches are shown in Figure 1.8.

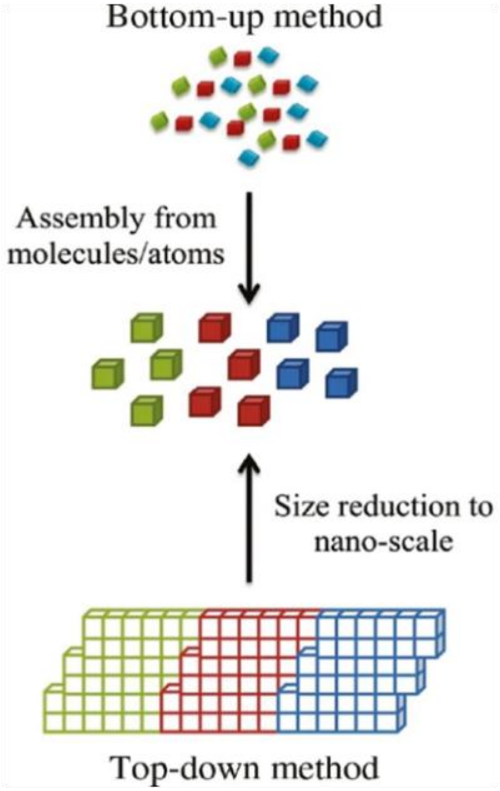

Figure 1.8. Bottom-up and Top-down approaches for the synthesis of nanoparticles. (Adapted from reference 6).

1.3 Synthetic techniques of nanomaterials

Different synthetic techniques can be employed for the synthesis of nanomaterials using the mechnical methods and lithographic techniques under the top-down approach and vapour phase, chemical phase and self assembly techniques under the bottom-up approaches listed below:

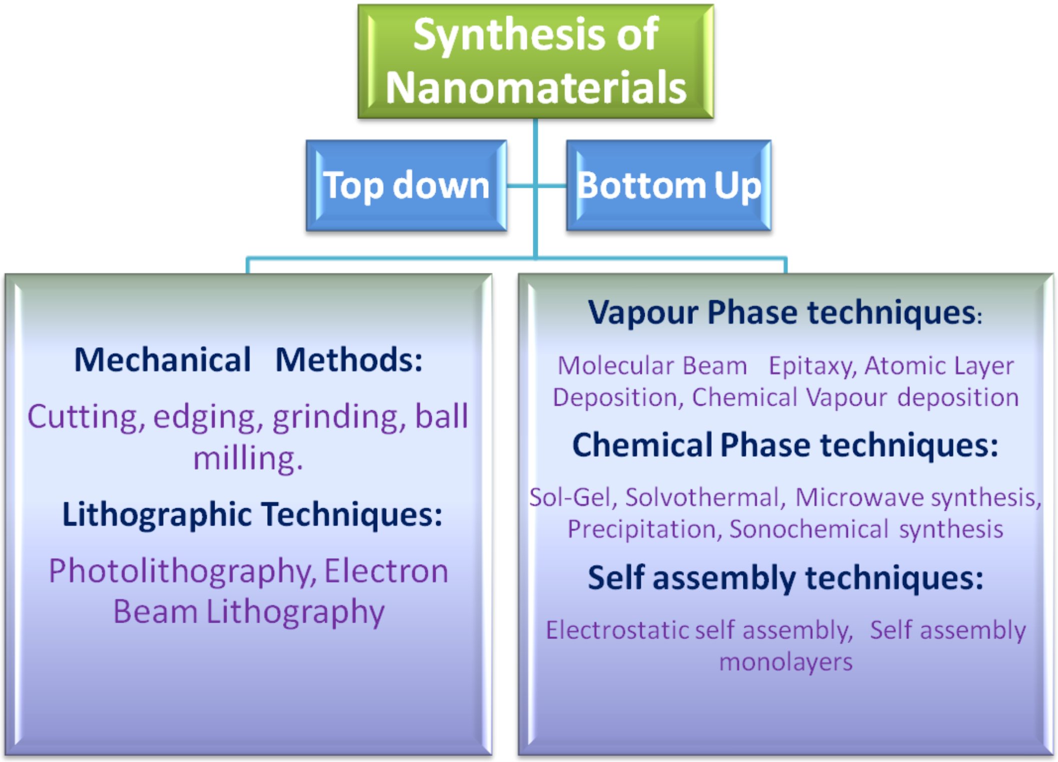

Scheme 1.1. Synthesis of Nanomaterials

(i) Ball milling

This process was first developed in the late 1960s by Benzamin and his co-workers at the Internaional Nickel company. In this process the bulk material (i.e powder mixture) is placed in the ball mill containing balls which rotate with high energy which crush the solid material into nanocrystallites. This method which is termed as mechanical alloying could successfully produce fine, uniform dispersions of oxide particles (Al_2O_3, Y_2O_3, ThO_2) in nickel-based superalloys that couldn't be made by more conventional powder metallurgy methods. The schematic diagram is shown in Figure 1.9.

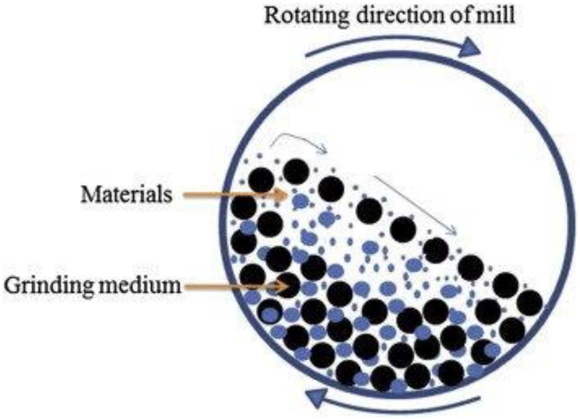

Figure 1.9. Schematic diagram of a ball mill. (Adapted from reference 7).

(ii) Electron beam lithography

The booming of the nanotechnology in the 1980s led to a very powerful technique, electron beam lithography for creating nanostructures or mesoscopic systems by scanning a highly focused beam of electrons to write out a pattern on a surface covered with an electron sensitive film called a resist. The electron beam induces a change in the molecular structure and solubility of the resist film. The resist film can further be immersed in a solvent for the selective removal of either the exposed or the non-exposed regions. This technique offers advantages of high resolution (as good as sub 10 nm), high flexibility that can work with a variety of materials, high reliability in processing and high accuracy in positioning/alignment.[8]

(iii) Hydrothermal/Solvothermal method

This is a solution based approach for synthesizing materials using pressurised vessels called autoclaves that can withstand high temperatures and pressure for a long time. The substances which are practically insoluble under normal conditions:- oxides, silicates and sulphides can be synthesized using this technique.[9] The materials with desired shapes, particle sizes and morphologies can be produced by controlling certain reaction parameters such as temperature, pH, reactant concentration and additives. This method also present many advantages over other growth processes such as the use of simple equipment, low process temperature, catalyst free growth, low cost, high purity, environment friendly and less hazardous. The use of any solvent other than water changes the name from hydrothermal to solvothermal.

Figure 1.10. High pressure stainless steel teflon reaction vessels.

(iv) Chemical vapour deposition

It is one of the most common processes for the production of nanomaterials in the solid state. This method is used for the production of thin films for device applications. The surface of different types of metallic or ceramic compounds, metals and their alloys, intermetallic compounds can be coated using this chemical method. In this method, one or more volatile precursors are transported via the vapor phase to the reaction chamber, where they decompose on a heated substrate. The volatile by products are then removed by gas flow in the reaction chamber.[10] A wide varieties of materials which are volatile in nature have been utilized for this purpose. These materials include metal hydrides (AiH_4, AsH_3), metal halides (WF_6, $TiCl_4$) and metal alkyls ($GaEt_3$, $AliBu_3$) which are industrially important precursors. Example: Preparation of TiB_2, melting point 3325˚C may be deposited by CVD at 1000˚C:

$$TiCl_4 + 2BCl_3 + 5H_2 \rightarrow TiB_2 + 10\ HCl$$

(v) Sol-Gel method

The sol gel process can be described as: "Formation of an oxide network through polycondensation reactions of a molecular precursor in a liquid." This method is used for the fabrication of metal oxides. Sol-gel method consists of few steps which involves hydrolysis, condensation and drying process. Initially, the metal precursor undergoes rapid hydrolysis to produce the metal hydroxide solution, followed by immediate condensation which leads to the formation of three-dimensional gels. The obtained gel is then further subjected to drying process, and the resulting product is readily converted to Xerogel or Aerogel based on the mode of drying as shown in Figure 1.11.

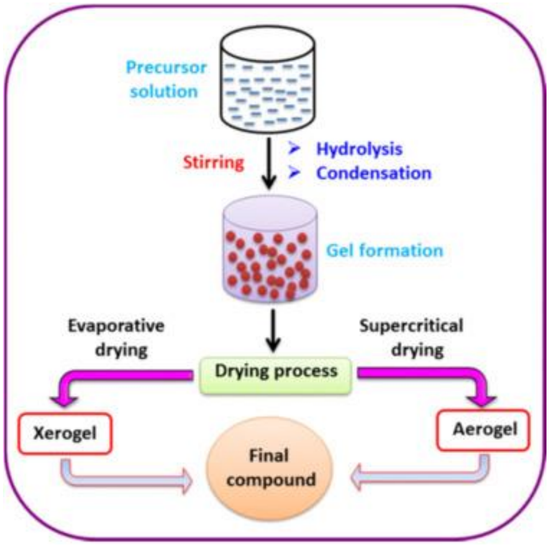

Figure 1.11. The reaction pathway for the production of metal-oxide nanostructures in the sol-gel method. (Adapted from reference 11).

1.4 Properties of nanomaterials

(i) Structural properties

At nanoscale, the decrease in particle size leads to an increase in the surface area and the surface energy due to which the interatomic spacings between the atoms change. It has been observed for semiconductors and metal oxides that interatomic spacings increase with decreasing particle size which is attributed to the compressive strain induced by the internal pressure arising from the small radius of curvature in the nanoparticle.[12] The apparent stability of metastable structures in small nanoparticles and clusters arises due to the loss of all traces of usual bulk atomic arrangement. For example, a particle of size 40 nm will have 5% of its atoms on its surface, while for 20 nm, 30% of atoms will be on its surface, whereas, 5 nm will have 50% of atoms on its surface. Hence, nanomaterials exhibit higher surface area per unit mass compared to their bulk materials. Further, the morphology of the nanomaterials also play an important role on the properties.

(ii) Optical properties

The properties like colour and transparency of a material are considered as optical properties. Due to the reduction in materials dimension, the nanomaterials exhibit unique optical properties. For example, bulk gold appear yellow in colour but at nanoscale, gold appear red in colour. The decrease of particle size leads to an increase in the band gap of the material which can be attributed to “quantum confinement” that appears at nanoscale. Quantum confinement results in the shifting of interband transitions to higher frequencies.[13-14] As a result of quantum confinement, a blue shift in the band gap of nanostructures can be observed which makes the sub bands discrete along the direction of confinement by breaking the continuous density of energy states. The nature of electronic density of states of nanostructures and confinement of the motion of electrons makes these nanostructures makes these nanostructures more efficient for device applications by operating at lower threshold currents than lasers with bulk materials. Since the optical properties of nanostructured materials are highly dependent on the size of the material thus the luminescent properties of these materials can be tuned by varying the size. Owing to their unique optical properties, nanomaterials find diverse applications in electronic devices like computers, cellular phones, LCDs, surface coatings, etc.

(iii) Chemical properties

As the dimensions go into the nanoscale, the percentage of surface atoms in nanomaterials is large compared to their bulk counterparts which imparts them more reactivities than the bulk materials. Hence, these materials find widespread applications in chemical industries owing to their exceptional chemical properties.[15] For example; many new medicines are insoluble in water when in the form of micron sized particles but will dissolve easily when in a nanostructured form. The unique high chemical reactivity makes these materials readily available to catalyze chemical reactions. For example, bulk gold is inert for chemical reactions whereas nano gold particles have been utilized as efficient heterogeneous catalysts for various organic transformations.

(iv) Mechanical properties

The mechanical properties of nanostructured materials tend to modify from those of microparticles and bulk materials in the nanoscale regime. An enhancement of the mechanical properties including the hardness, elastic modulus, fracture, toughness, scratch resistance and fatigue strength can result from the structural imperfections (dislocations, micro twins and impurity precipitates) of materials.[16-17] These imperfections becomes highly energetic and tends to migrate to the surface when annealed at higher temperatures. This makes the surface free of defects leading to an enhancement in the mechanical properties of nanomaterials. These nanomaterials can bring out the effective options to modify the surface of many devices and improving the quality of nanomaterials in cutting tools, wear resistant coatings, ceramics, paints for cars etc.

(v) Magnetic properties

Due to an increase in the surface area to volume ratio, a large proportion of atoms migrate to the surface which changes the magnetic coupling between the neighbouring atoms leading to different magnetic properties. When the particle size reaches nanoregime, ferromagnetic particles becomes paramagnetic. This is because the reduction of particle size to nano-dimension brings the instability in the ferromagnetic particles which can provide the sufficient energy to the domains at the surface to switch polarization directions.[18] Thus small nanoparticles consisting of only one domain exhibit super paramagnetism different from conventional paramagnetism. Due to their interesting magnetic properties, nanomaterials find applications in magnetic resonance imaging (MRI) for disease diagnosis, sensitive analytical instruments, motors in ships, colour imaging, bio processing and refrigeration as well as high storage density magnetic memory media.

(vi) Thermal properties

The small size, the spherical shape, the large interfaces tend to modify the thermal properties of nanomaterials. The size of the nanomaterials becomes comparable to the wavelength and the mean free path of the phonons in the nanoscale regime which brings a significant change in the phonon transport within the materials. This might be due to the phonon confinement which results in showing different thermal behaviour of these materials compared to the macroscopic materials. It has also been observed that the special structure of nanomaterials is an important factor to determine the thermal properties. For example, carbon nanotubes have extremely high conductivity in axial directions because of the tubular structure.[19]

1.5 Current status, trends and future direction of nanotechnology

Nanotechnology is a burgeoning multidisciplinary field having capabilities to design, synthesize and characterize materials and devices in the nanoscale regime (1 to 100 nm). Nanotechnology has been evolving in the area of research and product development owing to the unique properties of nanomaterials. There is a growing trend towards the incorporation of nanomaterials into products such as computers, solid state lighting and solar cells which will be continued for the decades to come. Nanotechnology provides extra ordinary oppportunities to create integrated functional devices leading to the development of nanomachines. Further, these nanomachines get interconnected in a network called ‘nanonetwork’ which can overcome the limitations of individual nanodevices. These nanonetworks give rise to numerous applications in the fields of medicine, industry, environment as well as for the military purpose. The trend towards the miniaturisation, handling and processing for nanomaterials is gaining popularity in the field of nanotechnology. Nanotechnology may be envisioned as to change almost everything in terms of manufacturing and approaching technology. The field of nanotechnology has gained interest after the discovery of ‘carbon nanotubes’ in 1990. This discovery embarks the journey for the study of one dimensional nanostructures which grow in one direction faster than the other growth directions. These nanostructures have one dimension out of nanoscale whereas the other two dimensions are in nanoscale regime. The tailoring and controlling the structure, size and shape of these materials has been the major area of interest for the past few decades. Now a days, the research focuses on discovering novel materials with unique properties which can be further applied to design nanodevices for commercial purpose. For example, the functional ceramics which can withstand high temperature have numerous applications in gas turbines, fuel cells, electronic devices, aircraft engines etc. Though the ceramics possess excellent stability at higher temperatures but they lack the required fracture toughness which can be achieved through the synthesis of hierarchical structures in the nanoscale order. When the dimensions go into the nanoscale, a strong correlation can be observed between the dimensionality of the material and its physical or chemical properties. For example, luminescence of the quantum dots can be shifted from the red end of the visible light spectrum to the blue end by inducing a small change in their size. Thus it becomes necessary to control the dimensionality of these materials within a few nanometers or less to make them use for different applications.

Nanotechnology thus can be seen as today’s most advanced manufacturing technology and considered to be the technology of future for it can reach the dimensions which lie in the nanoscale (i.e. of the order of few nanometers). It possess the potential to provide society the benefits to unleash the breakthroughs in the field of medicine, industry, environment, electronics and optics in the coming decades. Recent advances suggest that nanotechnology will have a profound impact on disease prevention, diagnosis and treatment. The field of nanotechnology has also revolutionised the industries since many industries ensures to adapt such technology in future. Such innovations should be encouraged which are likely to meet the social needs - energy and environmental problems by developing clean energy and resource saving materials.

1.6 Photocatalytic applications of nanomaterials

Nanomaterials have widespread use in numerous fields. Photocatalytic degradation of organic matter present in the waste water is one of the major applications of nanomaterials. Herein, we discuss the photocatalytic degradation of dyes employing nanomaterials.

1.6.1 *Photocatalysis*

Over the years, photocatalysis has emerged as one of the upcoming technologies for providing solutions to environmental remediation and clean energy supply utilizing the energy of natural sunlight. The word "photocatalysis" is derived from the Greek word which consists of two parts: photo and catalysis. The term catalysis can be understood as the process where a substance known to be a catalyst involves in increasing the rate of a reaction by reducing the activation energy. Thus, photocatalysis can be best described as the amalgamation of photochemistry and catalysis. Hence photocatalysis can be defined as "a change in the rate of chemical reactions or their generation under the action of light in the presence of substances called photocatalyst that absorbs light quanta and is involved in the chemical transformations of the reactants". Photocatalysis can be further sub-categorized into two categories:

(a) Homogeneous photocatalytic process. In this process, the transition metal complexes of iron copper, chromium are used as catalysts. These metal ion complexes generate hydroxyl radicals under photon radiation. These hydroxyl radicals oxidize the organic matter in toxic waste leading to the degradation of toxic matter.

(b) Heterogeneous photocatalytic process. In this process, the semiconducting materials (TiO_2, ZnO, SnO_2 and CeO_2) act as heterogeneous catalysts. The favorable electronic structures, light absorption properties, charge transport characteristics and excited state lifetime makes these materials suitable for photocatalytic applications.

It has been observed that heterogeneous photocatalysis has several advantages over homogeneous photocatalysis in terms of complete mineralization of organic pollutants, low cost, mild temperature and pressure conditions and no waste disposal problem.

1.6.2 *Importance of semiconductors as photocatalysts*

Semiconductors (e.g. TiO_2, ZnO, Fe_2O_3, ZrO_2, CdS and ZnS) can act as sensitizers for light stimulated redox process due to their unique band structure suitable for light absorption and charge transport. The theoretical band structure of some of the important semiconductor materials with the band edge potentials of valence band (VB) and conduction band (CB) along with their band gap values is shown in Figure 1.12. When the photons of energy greater than the band gap energy of the semiconductor falls on the surface of photocatalyst, electron-hole pair is generated. The dissipation of stored energy can be observed within a few nanoseconds due to the recombination of electron-hole pairs. This can be prevented if a suitable scavenger is available to trap the electron or hole to allow the redox reactions to occur. The charge carriers (electrons and holes) undergo successive oxidation and reduction leading to the photodegradation of pollutants.

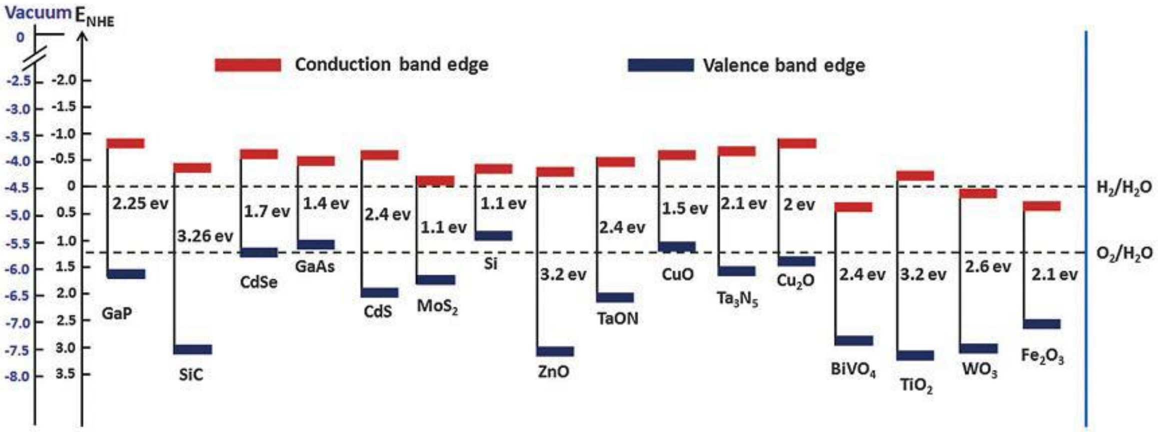

Figure 1.12. Valence and conduction band potentials of various semiconductor materials. (Adapted from reference 20).

Semiconductors can act as suitable photocatalysts because both oxidative and reductive pathways are possible in particle suspensions of semiconductors. Over the years, the use of organic pollutants has increased. The semiconductor photocatalysts possess interesting features to act as a photochemical diode for a metal loaded semiconductor particle. The ease of fabrication, large surface area and wide band gap of semiconductors makes them promising materials for photocatalytic applications. The large band gap semiconductors prove to be better photocatalysts than low band gap energy materials. The literature studies show that TiO_2/ZnO (E_g = 3.2 eV) have been extensively studied for the photocatalytic destruction of organic pollutants. ZnO is more preferred over TiO_2 for the photocatalytic degradation of pollutants owing to its low cost, absorption of a large fraction of solar spectrum and greater quantum efficiency. Unfortunately, both TiO_2 and ZnO are inactive under visible light due to their wide band gaps. Worldwide efforts are in progress to achieve higher degradation efficiency with these materials under visible light.

1.6.3 *Operating and affecting parameters of photocatalysis*

The rate of degradation of various organic pollutants can be affected by variation in the following parameters:

(a) Intensity of light. The intensity of light plays a key role in affecting the rate of degradation. The quantum Yield (the ratio of rate of reaction to the rate of absorption of radiation) depends entirely on the quanta of light absorbed by the photocatalyst. The quantum Yield varies under different wavelengths of light radiation. Thus, the rate of degradation varies for different intensities of light. The rate of reaction for photodegradation depends on the square root of the light intensity (half order) above the certain value (~25 mW/cm^2) of intermediate light intensity. Whereas, the excessive light intensity favors more electron hole recombination leading to a decrease in the reaction rate.

(b) Lifetime of charge carriers. The formation of electron hole pairs in semiconductor materials on absorption of light is prevented by the recombination of these charge carriers. The recombination of charge carriers takes place in the presence of defects or grain boundaries. Therefore, synthesizing highly crystalline photocatalytic materials is highly desirable to minimize the surface defect sites to overcome the electron hole recombination.

(c) Band gap. The photocatalyst should have optimum band gap to absorb a wide range of spectrum (i.e. solar light).

(d) Crystal structure. The structure of photocatalyst plays a major role in determining the photocatalytic activity. For example, TiO_2 consisting of three phases - anatase, rutile and brookite show different photocatalytic activities. The anatase phase of TiO_2 exhibit maximum photocatalytic activity due to its high adsorption power, stability, position of conduction band and higher degree of hydroxylation.

(e) Shape. The shape and morphology also play a key role in affecting the efficiency of degradation. Sarvana et al. reported that spherical shaped ZnO samples show higher efficiency compared with spindle and rod shaped ZnO samples.

(f) Size and surface area. The size and surface area of semiconductor materials act as potential factors in influencing the degradation efficiency. The small size and large surface area of the photocatalyst enhances the number of active sites and interfacial charge carrier transfer rates leading to higher catalytic activities.

1.6.4 *Photocatalysis for the degradation of organic pollutants*

The environment has been polluted and contaminated by waste naturally as well as artificially (man-made) for over a long period of time. However, the environment itself can control the contamination produced by natural waste but the pollution caused by synthetic materials in trace amounts goes on accumulating leading to disastrous effects on human health, environment and ecology. The industrial discharge of heavy metals, pesticide residues, agricultural activities and pesticide manufacturing plants have become a major problem affecting the water bodies in the ecosystem. In the modern era, the depletion of underground water resources due to poor sanitation and inadequate hygiene has affected the quality of water which is creating adverse health effects in humans and other ecological systems. Thus, there is a vital need to adopt ecologically clean chemical technology, materials and processes to eradicate this issue. The main source of water pollution are the synthetic dyes which have widespread use in textile industry, paper industry, leather industry, food industry, medical etc. where these dyes are produced in large scale. The effluents from these industries are released into the environment and cause serious health hazards. Thus, it becomes important to develop such methods to remove the dyes before getting released into the environment. The traditional physical techniques such as adsorption on activated carbon, ultrafiltration, reverse osmosis, ion exchange on synthetic adsorbent resins etc. have been used for the waste water treatment to remove the dye pollutants. The above-mentioned methods create secondary pollution by transferring organic compounds from water to another phase which requires further treatment making the process costlier. Conventional biological water treatment processes are also incapable because of the calcitrant nature of synthetic dyes and high salinity of waste water containing dyes. In this regard, photocatalysis has the potential to provide simple and low-cost solution for degrading the pollutants. Advanced oxidation process (AOP) appears to be the most promising method for the complete oxidation of organic pollutants to CO_2 and H_2O. These methods are of two types:

(a) Non-photochemical AOPs. Non-photochemical AOPs include cavitation, Fenton and Fenton-like processes, ozonation, ozone/hydrogen peroxide, wet air oxidation.[21]

(b) Photochemical AOPs. Photochemical AOPs and photochemical oxidation processes include homogeneous (UV/hydrogen peroxide, UV/ozone, UV/ozone/hydrogen peroxide, photo-Fenton, homogeneous and heterogeneous photocatalytic processes.[22-24] AOPs produces hydroxyl free radicals ($\cdot OH$) which acts as a strong oxidant to oxidize the organic compounds which can’t be oxidized by the conventional oxidants.

Mechanism of photocatalysis

Photocatalytic process mainly depends on the wavelength of the photon energy and the nature of the catalyst. Semiconducting materials act as sensitizers for the light activated redox process due to their electronic structure characterized by a filled valence band and empty conduction band. The energy difference between the valence band and the conduction band is called the band gap. The various steps involved in the photocatalytic degradation is discussed below:

The semiconductor photocatalyst absorbs the light energy in the form of photons and if the incident energy is equal to or higher than the band gap (threshold energy) of the photocatalyst, the semiconductor atom can elevate the electrons in the valence band to move to the conduction band of the semiconductor. This process creates positive holes in the valence band and excited electrons in the conduction band. These charge carriers further take different routes to undergo redox processes. The electrons in the conduction band get trapped either in shallow traps or in deep traps followed by the recombination with the positive holes in the valence band radiatively or non-radiatively dissipating the energy as heat. The holes in the valence band oxidize electron donor molecules and react with water molecules on the surface of the photocatalyst to generate hydroxyl radicals which have strong oxidizing power to degrade the organic pollutants. The electron on the other hand reduces the dissolved oxygen species to generate superoxide ions.

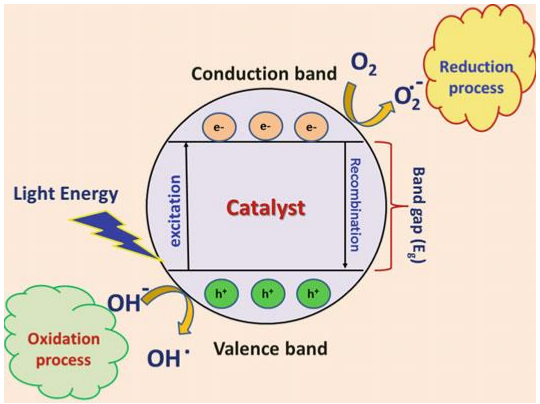

Figure 1.13. Schematic representation of semiconductor photocatalytic mechanism. (Adapted from reference 25).

The electrons and holes involve in the oxidation and reduction of the adsorbed species on the surface of semiconductor which ultimately leads to degradation of pollutants.

The schematic representation indicating the various steps involved in the photocatalytic degradation of organic pollutants by semiconductor photocatalysts is shown in Figure 1.13.

1.7 Scope and significance of present work

The present work is based on the synthesis of nanometal oxides and sulphides using metal organic coordination polymers as the precursors. Metal organic coordination polymers (MOCPs) have been widely researched owing to their specific structures, tailorable properties and potential applications in separation, storage devices, catalysis, sensors and synthesis of nanomaterials. These MOCPs can act as sacrificial templates to obtain the nanomaterials with desired morphologies. The usual approach for the preparation of nano metal oxides consists of the thermal decomposition of these MOCPs at higher temperatures. At such high temperatures, the metal species acquire sufficient mobility whereas the organic linker in MOCPs gets burnt away leading to the rupture of the framework. Once the framework is decomposed, C and N present in these MOCPs get oxidized into gases. The carbon formed during the thermolysis also acts as the reducing agent for the reduction of metal oxides by a simple carbothermic reaction. Thus, MOCPs may be envisioned as the suitable precursors for the formation of highly stable nanomaterials bearing catalytic properties. The main advantage of using MOCPs for the synthesis of nanomaterials lies in the control over structure/morphology of the derived nano metal oxides resulting in outstanding photocatalytic activity.

In the present work, ZnO has been chosen for studying its photocatalytic behavior on cationic and anionic dye based on the different morphologies obtained by optimizing the fabrication parameters. Neutral and water soluble Zn(II) MOCPs with a general formula $\{[M_2(bpxa)_2(adc)_2]{\cdot}xH_2O\}_n$ (where M(II) = Zn(II); bpxa = N,N-bis(pyridylmethyl)alkyl amine; adc = acetylene dicarboxylate; x = 0 or 2) have been utilized for the synthesis of nanometal oxides. Calcination in air at a temperature above the decomposition temperature of the polymers collapses the whole framework and yield ZnO. The metal ions with a standard reduction potential of 0.27 V or higher such as Co, Ni and Cu present in MOCPs form pure metal nanoparticles during calcination whereas metal ions with a reduction potential lower than 0.27 V such as Mg, Al, Mn, Zn or Cr tend to combine with the oxygen of the organic linker present in the polymer and form corresponding metal oxides. Since the reduction potential of Zn^{2+} is lower than 0.27 V and thus calcining at a high temperature in the tube furnace zinc ions are unable to reduce to a zero-oxidation state. The three different ligands present in these MOCPs have a profound effect on the morphology of the obtained nanometal ZnO and their photocatalytic activities. The hydrothermal synthesis route has also been carried out for the formation of 1D, 2D and 3D structures of ZnO by varying the reaction parameters (temperature, pH, time, solvent).

Similarly, nanostructures of CdS (E_g = 2.4 eV), have been synthesized using a novel facile template-free and surfactant-less solvothermal method under mild conditions using 1D coordination polymers of Cd(II) $\{[Cd_2(bpxa)_2(adc)_2]{\cdot}2H_2O\}_n$ (where bpxa = N,N'-bis(pyridylmethyl) alkyl amine and adc = acetylene dicaboxylate) as the source of Cd^{2+} ions and thiourea as the source of sulphide ions. There are various synthetic methods which have been used to synthesize CdS nanoparticles including soft chemical reaction, solid state reaction, sol-gel process, hydrothermal synthesis, sonochemical preparation, microwave heating, reverse micelle. Among all the methods, the hydrothermal technique is a promising one to control the properties of nanocrystallites of CdS, such as crystal phase, size, morphology and luminescence. This method also presents many advantages over other growth processes, such as the use of simple equipment, low process temperature, catalyst free growth, low cost, high purity, environment friendly and less hazardous. High optical and fluorescence properties as well as quantum size effects make CdS a suitable catalyst for the degradation of dyes. Therefore, CdS has been fabricated by controlling the growth parameters (time, temperature, concentration) to utilize them as photocatalyst against methylene blue dye. Due to the tunable electronic band gap of CdS, one may also find its applications in the future optoelectronic devices such as photodetectors, solar cells, photovoltaic devices, photoluminescence sensors and light emitting diodes. It also finds its applications in chemo sensing, biosensing and bioimaging.[26-30]

The structures of the neutral ligands (bpma, bpea and bpta) and anionic linker (adc) used for the synthesis of Zn(II) and Cd(II) MOCP precursors[31] are shown in Figure 1.14.

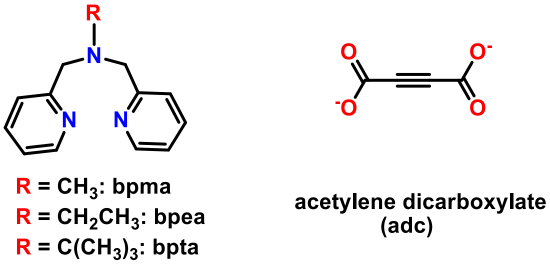

Figure 1.14. Chemical structure of neutral polypyridyl and anionic carboxylate ligands.

The present work is based on the fabrication of two important semiconductors - ZnO and CdS, using hydrothermal (solution based) and direct calcination approaches. The fabrication parameters (time, temperature, pH, solvent, concentration, ancillary ligand) were controlled and optimized to produce desired morphologies of the nanostructures for utilizing them in photocatalysis and analyzing their optical properties. A flow diagram of the present work is shown in Figure 1.15.

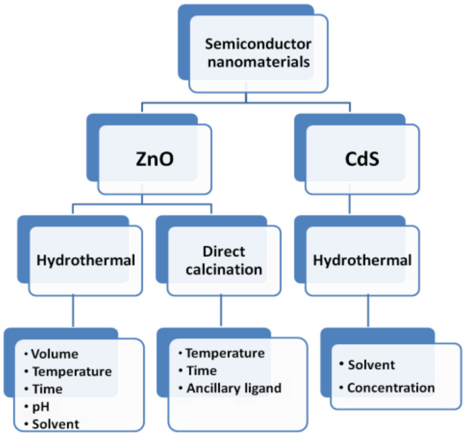

Figure 1.15. Flow diagram of the present work.

CHAPTER II

EXPERIMENTAL SECTION

2.1 Materials and methods

In this research work, all chemicals and solvents used for synthesis were obtained from commercial sources and were used as received, without further purification. All reactions were carried out under aerobic conditions.

2.2 Physical measurements

Raman spectra were recorded on a Renishaw InVia Raman microscope equipped with a 785 nm high-power near-infrared laser working at 300 mW power and a Renishaw CCD detector. Analysis of the Raman spectra were performed in reflection mode on powder samples placed on the sample stage and aligned in optical path by using a camera, with 0.1-0.5% laser power and by using 50X optics in the range of 400-2000 cm^{-1}.

Solid state reflectance Solid state reflectance of solid samples was recorded in Cary 5000 UV-Vis spectrophotometer using the KBr medium.

Fluorescence emission spectra were obtained using a Horiba Scientific Fluorolog 3 spectrofluorometer instrument with a cuvette of 10 mm path length. To obtain the spectra a slurry of compound was prepared in a particular solvent and the spectra was recorded with the stirring mode.

Powder X-ray data were recorded on a Rigaku Ultima IV diffractometer equipped with a 3 KW sealed tube Cu Kα X-ray radiation (generator power settings: 40 kV and 40 mA) and a DTex Ultra detector using parallel beam geometry (2.5° primary and secondary solar slits, 0.5° divergence slit with 10 mm height limit slit). Each sample grounded into a fine powder using a mortar and a pestle was placed on a glass sample holder that was placed on the sample rotation stage (120 rpm) attachment. The data were collected over an angle range 10° to 80° with a scanning speed of 1° per minute with 0.02° step with XRF reduction for the metals.

Field Emission Scanning Electron Microscopy (FESEM) was performed on a JEOL instrument; samples were well dispersed in EtOH and drop casted on a silicon wafer, dried and sputtered with gold for a time period of 20 minutes for increasing the conductivity of the sample and a working distance of 4.5 to 15 mm was used with a voltage of 10 to 15 kV and probe current of 6. For, solvent dependent SEM study, the sample has been prepared with respected solvents.

High resolution transmission electron microscopy (HRTEM) was performed on FEI Technai G2 F20 equipped with a field emission gun operated at 200 Kv with 1 mg sample well dispersed in MeOH (10 mL) using a sonicator for 20 minutes and then put on the copper grid, which was allowed to dry using a lamp for 30 minutes.

Atomic force microscopy (AFM) experiments were conducted with an Asylum Research-Oxford Instrument with 0.5 mg of sample in MeOH, ultra-sonicated, drop casted on mica surface and allowed to dry; the topography was performed in contact mode in air at 25 ^{o}C.

2.3 Synthesis of precursors

General method. All six polymers reported here are synthesized following the reported procedure.[31] Upon addition of 0.125 mmol of the dicarboxylic acid to a clear methanolic (3 mL) solution of 0.125 mmol of $M(OAc)_2$ (M = Zn or Cd) and 0.125mmol of the tridentate ligand, a white precipitate appeared immediately. The reaction mixture was stirred for another 3 to 4 hours at room temperature (RT). The resulting slurry was evaporated to dryness, treated with 2mL of acetonitrile-toluene mixture (50:50 v/v) to completely remove the acetic acid affording a pure solid.

$[Zn_2(bpma)_2(adc)_2]_n$. It was prepared using 42 mg (0.375 mmol) of acetylene dicarboxylic acid, 82.5 mg (0.375 mmol) of $Zn(OAc)_2{\cdot}2H_2O$ in 9 mL methanol and 79.5 mg (0.375 mmol) of bpma. A colorless solid was obtained. Yield: 86.8 mg (49%). Selected FTIR peaks (KBr, cm^{-1}): 3429, 1634, 1606, 1482, 1445, 1323, 1022, 775, 732, 684, 643.

$[Zn_2(bpea)_2(adc)_2]_n$. It was prepared using 42 mg (0.375 mmol) of acetylene dicarboxylic acid, 82.5 mg (0.375 mmol) of $Zn(OAc)_2{\cdot}2H_2O$ in 9 mL methanol and 84 mg (0.375 mmol) of bpea. A colorless solid was obtained. Yield: 77.3 mg (52%). Selected FTIR peaks (KBr, cm^{-1}): 3392, 1637, 1606, 1376, 1314, 1024, 783, 761, 694, 675.

$\{[Zn_2(bpta)_2(adc)_2]{\cdot}2H_2O\}_n$. It was prepared using 42 mg (0.375 mmol) of acetylene dicarboxylic acid, 82.5 mg (0.375 mmol) of $Zn(OAc)_2{\cdot}2H_2O$ in 9 mL methanol and 96 mg

(0.375 mmol) of bpta. A colorless solid was obtained. Yield: 152 mg (89%). Selected FTIR peaks (KBr, cm^{-1}): 3467, 2975, 1621, 1609, 1599, 1370, 1339, 1027, 783, 766, 686.

$\{[Cd_2(bpma)_2(adc)_2]\cdot 2H_2O\}_n$. It was prepared using 42 mg (0.375 mmol) of acetylene dicarboxylic acid, 100.5 mg (0.375 mmol) of $Cd(OAc)_2\cdot 2H_2O$ in 9 mL methanol and 79.5 mg (0.375 mmol) of bpma. A colorless solid was obtained. Yield: 147 mg (90%). Selected FTIR peaks (KBr, cm^{-1}): 3429, 1615, 1587, 1481, 1345, 776.

$[Cd_2(bpea)_2(adc)_2]_n$. It was prepared using 42 mg (0.375 mmol) of acetylene dicarboxylic acid, 100.5 mg (0.375 mmol) of $Cd(OAc)_2\cdot 2H_2O$ in 9 mL methanol and 84 mg (0.375 mmol) of bpea. A colorless solid was obtained. Yield: 132.4 mg (79%). Selected FTIR peaks (KBr, cm^{-1}): 3415, 1603, 1583, 1347, 1018, 766, 690, 642.

$\{[Cd_2(bpta)_2(adc)_2]\cdot 2H_2O\}_n$. It was prepared using 42 mg (0.375 mmol) of acetylene dicarboxylic acid, 100.5 mg (0.375 mmol) of $Cd(OAc)_2\cdot 2H_2O$ in 9 mL methanol and 96 mg (0.375 mmol) of bpta. A colorless solid was obtained. Yield: 171.2 mg (91%). Selected FTIR peaks (KBr, cm^{-1}): 3426, 1618, 1604, 1569, 1376, 1331, 1096, 778, 770, 695.

2.4 Synthesis of ZnO nanostructures

Method 1. For a general reaction, 0.05 mmol (39 mg) of $[Zn_2(bpma)_2(adc)_2]_n$ is added in a 3 mL of Teflon reactor containing certain amount of water. The hydrothermal reaction was carried out at 180 ^{o}C for 24 hours. The as-synthesized mixture was centrifuged at 4000 rpm for 15 minutes to separate the solid from the solvent followed by washing the solid several times with ethanol. A solid collected at the bottom of centrifuge tube was dried in air at 60 ^{o}C for 3-4 hours to obtain the powdered ZnO nanoparticles of fine size.

ZnO-1. It was prepared following method 1 in which 0.5 mL of water was used in the reaction mixture. A white colored product was isolated (Yield: 78%).

ZnO-2. It was prepared following method 1 where 1 mL of water was used in the reaction mixture. A white colored product was isolated (Yield: 81%).

ZnO-3. It was prepared following method 1 where 2 mL of water was used in the reaction mixture. A white colored product was isolated (Yield: 80%).

Method 2. For a general reaction, 0.05 mmol (40.5 mg) of $[Zn_2(bpea)_2(adc)_2]_n$ is added in a 3 mL of Teflon reactor containing certain amount of water. The hydrothermal reaction was carried out at 180 °C for 24 hours. The as-synthesized mixture was centrifuged at 4000 rpm for 15 minutes to separate the solid from the solvent followed by washing the solid several times with ethanol. A solid collected at the bottom of centrifuge tube was dried in air at 60 °C for 3-4 hours to obtain the powdered ZnO nanoparticles of fine size.

ZnO-4. It was prepared following method 2 in which 0.5 mL of water was used in the reaction mixture. A white colored product was isolated (Yield: 84%).

ZnO-5. It was prepared following method 2 where 1 mL of water was used in the reaction mixture. A white colored product was isolated (Yield: 79%).

ZnO-6. It was prepared following method 2 where 2 mL of water was used in the reaction mixture. A white colored product was isolated (Yield: 82%).

Method 3. For a general reaction, 0.05 mmol (45 mg) of $\{[Zn_2(bpta)_2(adc)_2]\cdot 2H_2O\}_n$ is added in a 3 mL of Teflon reactor containing certain amount of water. The hydrothermal reaction was carried out at 180 °C for 24 hours. The as-synthesized mixture was centrifuged at 4000 rpm for 15 minutes to separate the solid from the solvent followed by washing the solid several times with ethanol. A solid collected at the bottom of centrifuge tube was dried in air at 60 °C for 3-4 hours to obtain the powdered ZnO nanoparticles of fine size.

ZnO-7. It was prepared following method 3 where 0.5 mL of water was used in the reaction mixture. A white colored product was isolated (Yield: 72%).

ZnO-8. It was prepared following method 3 where 1 mL of water was used in the reaction mixture. A white colored product was isolated (Yield: 78%).

ZnO-9. It was prepared following method 3 where 2 mL of water was used in the reaction mixture. A white colored product was isolated (Yield: 81%).

Method 4. For a general reaction, 0.05 mmol (39 mg) of $[Zn_2(bpma)_2(adc)_2]_n$ and certain amount of water containing KOH at a pH>13 was added in a 3 mL Teflon reactor. The hydrothermal reaction was carried out at 180 °C for 24 hours. The as-synthesized mixture was centrifuged at 4000 rpm for 15 minutes to separate the solid from the solvent followed by washing the solid several times with ethanol. A solid collected at the bottom of centrifuge tube was dried in air at 60 °C for 3-4 hours to obtain the powdered ZnO nanoparticles of fine size.

ZnO-10. It was prepared following method 4 where 1 mL of water was used in the reaction mixture. A white colored product was isolated (Yield: 98%).

ZnO-11. It was prepared following method 4 where 2 mL of water was used in the reaction mixture. A white colored product was isolated (Yield: 95%).

ZnO-12. It was prepared following method 4 where 3 mL of water was used in the reaction mixture. A white colored product was isolated (Yield: 97%).

ZnO-13. It was prepared following method 4 where 4 mL of water was used in the reaction mixture. A white colored product was isolated (Yield: 45%).

ZnO-14. It was prepared following method 4 where 5 mL of water was used in the reaction mixture. A white colored product was isolated (Yield: 73%).

Method 5. For a general reaction, 0.05 mmol (39 mg) of $[Zn_2(bpma)_2(adc)_2]_n$ and 3 mL of basic aqueous solution containing KOH at a pH=13 was added in a 3 mL Teflon reactor. The hydrothermal reaction was carried out at 120 ^{o}C for different time intervals (6, 12, 18 and 24 hours). The as-synthesized mixture was centrifuged at 4000 rpm for 15 minutes to separate the solid from the solvent followed by washing the solid several times with ethanol. A solid collected at the bottom of centrifuge tube was dried in air at 60 ^{o}C for 3-4 hours to obtain the powdered ZnO nanoparticles of fine size.

ZnO-15. It was prepared following method 5 and the reaction was carried out for 6 hours. A white colored product was isolated (Yield: 81%).

ZnO-16. It was prepared following method 5 and the reaction was carried out for 12 hours. A white colored product was isolated (Yield: 74%).

ZnO-17. It was prepared following method 5 and the reaction was carried out for 18 hours. A white colored product was isolated (Yield: 65%).

ZnO-18. It was prepared following method 5 and the reaction was carried out for 24 hours. A white colored product was isolated (Yield: 86%).

Method 6. For a general reaction, 0.05 mmol (39 mg) of $[Zn_2(bpma)_2(adc)_2]_n$ and 3 mL of basic aqueous solution containing KOH at a pH=13 was added in a 3 mL Teflon reactor. The hydrothermal reaction was carried out at 150 ^{o}C for different time intervals (6, 12, 18 and 24 hours). The as-synthesized mixture was centrifuged at 4000 rpm for 15 minutes to separate the solid from the solvent followed by washing the solid several times with ethanol. A solid collected at the bottom of centrifuge tube was dried in air at 60 ^{o}C for 3-4 hours to obtain the powdered ZnO nanoparticles of fine size.

ZnO-19. It was prepared following method 6 and the reaction was carried out for 6 hours. A white colored product was isolated (Yield: 83%).

ZnO-20. It was prepared following method 6 and the reaction was carried out for 12 hours. A white colored product was isolated (Yield: 85%).

ZnO-21. It was prepared following method 6 and the reaction was carried out for 18 hours. A white colored product was isolated (Yield: 78%).

ZnO-22. It was prepared following method 6 and the reaction was carried out for 24 hours. A white colored product was isolated (Yield: 81%).

Method 7. For a general reaction, 0.05 mmol (39 mg) of $[Zn_2(bpma)_2(adc)_2]_n$ and 3 mL of basic aqueous solution containing KOH at a pH=13 was added in a 3 mL Teflon reactor. The hydrothermal reaction was carried out at 180 ^{o}C for different time intervals (6, 12, 18 and 24 hours). The as-synthesized mixture was centrifuged at 4000 rpm for 15 minutes to separate the solid from the solvent followed by washing the solid several times with ethanol. A solid collected at the bottom of centrifuge tube was dried in air at 60 ^{o}C for 3-4 hours to obtain the powdered ZnO nanoparticles of fine size.

ZnO-23. It was prepared following method 7 and the reaction was carried out for 6 hours. A white colored product was isolated (Yield: 84%).

ZnO-24. It was prepared following method 7 and the reaction was carried out for 12 hours. A white colored product was isolated (Yield: 87%).

ZnO-25. It was prepared following method 7 and the reaction was carried out for 18 hours. A white colored product was isolated (Yield: 75%).

ZnO-26. It was prepared following method 7 and the reaction was carried out for 24 hours. A white colored product was isolated (Yield: 77%).

ZnO-27. It was prepared using **ZnO-23**, by further calcination at 500 ^oC for 6 hours to yield ZnO with high crystallinity. A white colored powdered product was obtained (Yield: 72%).

ZnO-28. It was prepared using **ZnO-24,** by further calcination at 500 ^oC for 6 hours to yield ZnO with high crystallinity. A white colored powdered product was obtained (Yield: 75%).

ZnO-29. It was prepared using **ZnO-25,** by further calcination at 500 ^oC for 6 hours to yield ZnO with high crystallinity. A white colored powdered product was obtained (Yield: 68%).

ZnO-30. It was prepared using **ZnO-26,** by further calcination at 500 ^oC for 6 hours to yield ZnO with high crystallinity. A white colored powdered product was obtained (Yield: 73%).

Method 8. For a general reaction, 0.05 mmol (39 mg) of $[Zn_2(bpma)_2(adc)_2]_n$ and 3 mL of water containing KOH at a certain pH was added in a 5 mL Teflon reactor. The hydrothermal reaction was carried out at 180 ^oC for 12 hours. The as-synthesized mixture was centrifuged at 4000 rpm for 15 minutes to separate the solid from the solvent followed by washing the solid several times with ethanol. A solid collected at the bottom of centrifuge tube was dried in air at 60 ^oC for 3-4 hours to obtain the powdered ZnO nanoparticles.

ZnO-31. It was prepared following method 8 where the reaction mixture was kept at a pH=9 by adjusting the amount of KOH in the water medium. A white colored product was isolated (Yield: 85%).

ZnO-32. It was prepared following method 8 where the reaction mixture was kept at a pH=10 by adjusting the amount of KOH in the water medium. A white colored product was isolated (Yield: 87%).

ZnO-33. It was prepared following method 8 where the reaction mixture was kept at a pH=11 by adjusting the amount of KOH in the water medium. A white colored product was isolated (Yield: 81%).

ZnO-34. It was prepared following method 8 where the reaction mixture was kept at a pH=12 by adjusting the amount of KOH in the water medium. A white colored product was isolated (Yield: 87%).

Method 9. The synthesis was carried out using 0.05 mmol (39 mg) of $[Zn_2(bpma)_2(adc)_2]_n$ and 2 mL of solvent (methanol, ethanol, THF, toluene, hexane) at 180 ^oC for 24 hours. The as-synthesized mixture was centrifuged at 4000 rpm for 15-20 minutes to separate the solid from the solvent followed by washing the solid several times with the solvents employed for synthesis. A solid collected at the bottom of centrifuge tube was dried in air at 60 °C for 3-4 hours to obtain the powdered ZnO particles.

ZnO-35. It was prepared following method 9 where methanol was used as the solvent. A white colored product was isolated (Yield: 68%).

ZnO-36. It was prepared following method 9 where ethanol was used as the solvent. A white colored product was isolated (Yield: 65%).

ZnO-37. It was prepared following method 9 where THF was used as the solvent. A white colored product was isolated (Yield: 67%).

ZnO-38. It was prepared following method 9 where toluene was used as the solvent. A white colored product was isolated (Yield: 62%).

ZnO-39. It was prepared following method 9 where hexane was used as the solvent. A white colored product was isolated (Yield: 65%).

Method 10. The synthesis is carried out in a conventional horizontal tube furnace composed of an alumina tube, a rotary pump system, a gas supply and control system. About 0.05 mmol of $\{[Zn_2(bpxa)_2(adc)_2]\cdot xH_2O\}_n$ (where bpxa = bpma, bpea, bpta) was taken in a silica crucible and loaded on an alumina boat and positioned at the center of the tube to get the maximum temperature. The temperature of the source material was set at 700 °C and the heating was maintained at the rate of 3 °C/min. After attaining this temperature, it was maintained for different retention times (6, 12, 18, 24 hours). The furnace was then allowed to cool at the same rate.

ZnO-40. It was synthesized following method 10 where $[Zn_2(bpma)_2(adc)_2]_n$ was taken in a silica crucible and the temperature was maintained for 6 hours. A white powder was obtained (Yield: 87%).

ZnO-41. It was synthesized following method 10 where $[Zn_2(bpma)_2(adc)_2]_n$ was taken in a silica crucible and the temperature was maintained for 12 hours. A white powder was obtained (Yield: 84%).

ZnO-42. It was synthesized following method 10 where $[Zn_2(bpma)_2(adc)_2]_n$ was taken in a silica crucible and the temperature was maintained for 18 hours. A white powder was obtained (Yield: 88%).

ZnO-43. It was synthesized following method 10 where $[Zn_2(bpma)_2(adc)_2]_n$ was taken in a silica crucible and the temperature was maintained for 24 hours. A white powder was obtained (Yield: 81%).

ZnO-44. It was synthesized following method 10 where $[Zn_2(bpea)_2(adc)_2]_n$ was taken in a silica crucible and the temperature was maintained for 6 hours. A white powder was obtained (Yield: 77%).

ZnO-45. It was synthesized following method 10 where $[Zn_2(bpea)_2(adc)_2]_n$ was taken in a silica crucible and the temperature was maintained for 12 hours. A white powder was obtained (Yield: 83%).

ZnO-46. It was synthesized following method 10 where $[Zn_2(bpea)_2(adc)_2]_n$ was taken in a silica crucible and the temperature was maintained for 18 hours. A white powder was obtained (Yield: 86%).

ZnO-47. It was synthesized following method 10 where $[Zn_2(bpea)_2(adc)_2]_n$ was taken in a silica crucible and the temperature was maintained for 24 hours. A white powder was obtained (Yield: 82%).

ZnO-48. It was synthesized following method 10 where $\{[Zn_2(bpta)_2(adc)_2]\cdot 2H_2O\}_n$ was taken in a silica crucible and the temperature was maintained for 6 hours. A white powder was obtained (Yield: 86%).

ZnO-49. It was synthesized following method 10 where $\{[Zn_2(bpta)_2(adc)_2]\cdot 2H_2O\}_n$ was taken in a silica crucible and the temperature was maintained for 12 hours. A white powder was obtained (Yield: 81%).

ZnO-50. It was synthesized following method 10 where $\{[Zn_2(bpta)_2(adc)_2]\cdot 2H_2O\}_n$ was taken in a silica crucible and the temperature was maintained for 18 hours. A white powder was obtained (Yield: 84%).

ZnO-51. It was synthesized following method 10 where $\{[Zn_2(bpta)_2(adc)_2]^{\cdot}2H_2O\}_n$ was taken in a silica crucible and a temperature of 700 ^oC was maintained for 24 hours. A white powder was obtained (Yield: 77%).

2.5 Synthesis of CdS nanostructures

Method 1. For a general reaction, 0.034 mmol (30 mg) of $\{[Cd_2(bpma)_2(adc)_2]^{\cdot}2H_2O\}_n$ and 0.34 mmol (26 mg) thiourea ($NH_2C(S)NH_2$) (in the ratio 1:10) were added in a 5 mL Teflon reactor containing 3 mL of solvent. The hydrothermal reaction was carried out at 120 ^oC for 6 hours. The as-synthesized mixture was centrifuged at 4000 rpm for 15 minutes to separate the solid from the solvent followed by washing the solid several times with the methanol. A solid collected via filtration was dried in air at 60 ^oC for 3 hours to obtain the powdered CdS nanoparticles of fine size.

CdS-1. It was synthesized following the method 1 using methanol as the solvent (Yield: 41%).

CdS-2. It was synthesized following the method 1 using ethanol as the solvent (Yield: 42%).

CdS-3. It was synthesized following the method 1 using tert-butanol as the solvent (Yield: 40%).

CdS-4. It was synthesized following the method 1 using water as the solvent (Yield: 43%).

CdS-5. It was synthesized following the method 1 except $Cd(OAc)_2.2H_2O$ was utilized as precursor instead of Cd(II) coordination polymer using methanol as the solvent (Yield: 39%).

Method 2. For a general reaction, 0.034 mmol (30 mg) of $\{[Cd_2(bpma)_2(adc)_2].2H_2O\}_n$ was used as a cadmium source and thiourea was used as a sulphur source. The precursors were mixed in different ratios (1:3, 1:5, 1:7, 1:10) and water was used as a solvent. The hydrothermal reaction was carried out at a temperature of 180 ^oC for 24 hours in a Teflon autoclave. The precipitates were collected and centrifuged at 4000 rpm for 15 minutes, washed three times with methanol and dried in air at 60 ^oC for 3 hours to obtain the powdered CdS nanoparticles of fine size.

CdS-6. It was synthesized following the method 2 where Cd^{2+} and S^{2-} source was taken in 1:3 ratio with 0.034 mmol (30 mg) of Cd (II) coordination polymer and 0.102 mmol (7.76 mg) of thiourea (Yield: 64%).

CdS-7. It was synthesized following the method 2 where Cd^{2+} and S^{2-} source was taken in 1:5 ratio with 0.034 mmol (30 mg) of Cd(II) coordination polymer and 0.17 mmol (12.94 mg) of thiourea (Yield: 62%).

CdS-8. It was synthesized following the method 2 where Cd^{2+} and S^{2-} source was taken in 1:7 ratio with 0.034 mmol (30 mg) of Cd(II) coordination polymer and 0.238 mmol (18.11 mg) of thiourea (Yield: 66%).

CdS-9. It was synthesized following the method 2 where Cd^{2+} and S^{2-} source was taken in 1:10 ratio with 0.034 mmol (30 mg) of Cd(II) coordination polymer and 0.34 mmol (25.88 mg) of thiourea (Yield: 63%).

CHAPTER III

RESULTS AND DISCUSSION

This chapter comprises of two major sections: (a) ZnO nanostructures and (b) CdS nanostructures. These sections are further divided into subsections depending on the different processing parameters (volume, pH, solvent, time, temperature, ancillary ligand) altered in the reaction system. In the first section, ZnO nanostructures have been synthesized hydrothermally by making variation in the volume of water in the neutral conditions. Further calcination of the as-synthesized ZnO nanostructures grown hydrothermally in neutral conditions results in varying the dimensionality of the original nanostructure. In the basic conditions under the hydrothermal approach, ZnO nanorods were obtained. Temperature dependent synthesis was carried out at two different temperatures (120 and 150 ^{o}C). The increase of temperature resulted in an increase in the aspect ratios of the rods. Also, annealing 1D ZnO nanostructures (synthesized at 180 ^{o}C) grown in the basic conditions induces a change in the aspect ratios of the structures. The high aspect ratio nanorods have shown to be efficient in the photocatalytic degradation of Congo Red dye. The change in the pH of the reaction mixture results in the formation of 2D nanoplatelets and their self- assembly results in generation of 3D micro flowers with the progress of time. The effect of different solvents based on the difference in their boiling points, saturated vapor pressures and polarities bring about the change in the overall size and shape of the nanostructures. Further, the direct calcination of coordination polymers also yields ZnO with diverse morphologies resulting from the variation in the ligand in precursor and the retention time. All the synthesized ZnOs have shown to be efficient in the photocatalysis of dyes and thereby are favorable for the removal of organic pollutants from the waste water. Also, antibacterial activity against *E.coli* was observed with the flower like morphology of ZnO made of nanorods. In the second section, rare morphologies of CdS nanostructures have been obtained in different solvents. Furthermore, the effect of changing the concentration of sulphur source on the particle sizes was also observed. The structure and composition of these nanostructures were characterized by X-ray diffraction (XRD), scanning electron microscopy (SEM), energy dispersive X-ray spectroscopy (EDS), UV-vis diffusive reflectance spectroscopy, high resolution transmission electron microscope (HRTEM) and fluorescence spectroscopy.

3.1 ZnO NANOSTRUCTURES

3.1.1 Fabrication of ZnO nanostructures in neutral conditions

(i) Using $[Zn_2(bpma)_2(adc)_2]_n$. ZnO nanostructures have been fabricated hydrothermally utilizing coordination polymer $[Zn_2(bpma)_2(adc)_2]_n$ as the Zn^{2+} source in different volumes of water (0.5, 1 and 2 mL) at 180 °C for 24 hours to yield ZnO (Scheme 3.1). This is the first example where the coordination polymer has been utilized in water to achieve diversity in the morphology of nanostructures. Further, the as-synthesized ZnO nanostructures have been employed for annealing at 800 °C for bringing different dimensionalities in these structures. The 3D nanostructures were converted to more stable 0D and 1D structures by post synthetic annealing process (Scheme 3.2).

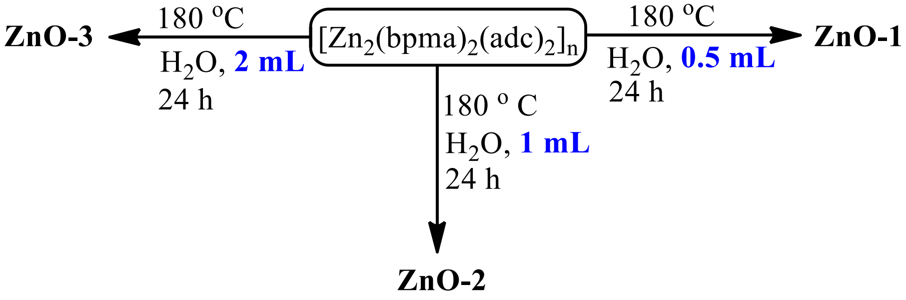

Scheme 3.1. Synthesis of **ZnO-1** to **ZnO-3** in neutral conditions.

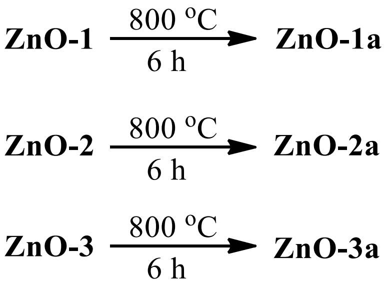

Scheme 3.2. Synthesis of **ZnO-1a** to **ZnO-3a** by post annealing process.

Powder X-ray diffraction studies. The X-ray diffraction patterns of **ZnO-1** to **ZnO-3** synthesized with different volumes of water (0.5, 1 and 2 mL) using hydrothermal method are shown in Figure 3.1. The peaks from the patterns could be clearly indexed to hexagonal wurtzite phase of ZnO which is in good agreement to those of bulk ZnO (JCPDS 06-2151). The strong and intense peaks in the patterns show highly crystalline nature of ZnO nanostructures. The lattice parameters of these nanostructures were calculated using the equation 1,[32] and the values obtained are listed in Table 3.1.

$$\frac{1}{d^2} = \frac{4}{3(h^2+hk+\frac{k^2}{a^2})} + \frac{l^2}{c^2} \qquad (1)$$

Table 3.1. Lattice parameters for ZnO samples (**ZnO-1** to **ZnO-3**)

Sample	h k l	2θ values (degrees)	Lattice constants a, b, c (Å)	Volume of unit cell (Å^3)	Atomic packing fraction	d spacing (Å)	FWHM
ZnO-1	(100)	31.74	a = b = 3.26,	48.08	0.755	2.82	0.313
	(002)	34.42	c = 5.22			2.61	
	(101)	36.25				2.48	
ZnO-2	(100)	31.70	a = b = 3.26,	48.22	0.755	2.82	0.379
	(002)	34.40	c = 5.22			2.61	
	(101)	36.20				2.48	
ZnO-3	(100)	31.85	a = b = 3.25,	47.63	0.754	2.81	0.525
	(002)	34.51	c = 5.20			2.60	
	(101)	36.34				2.47	

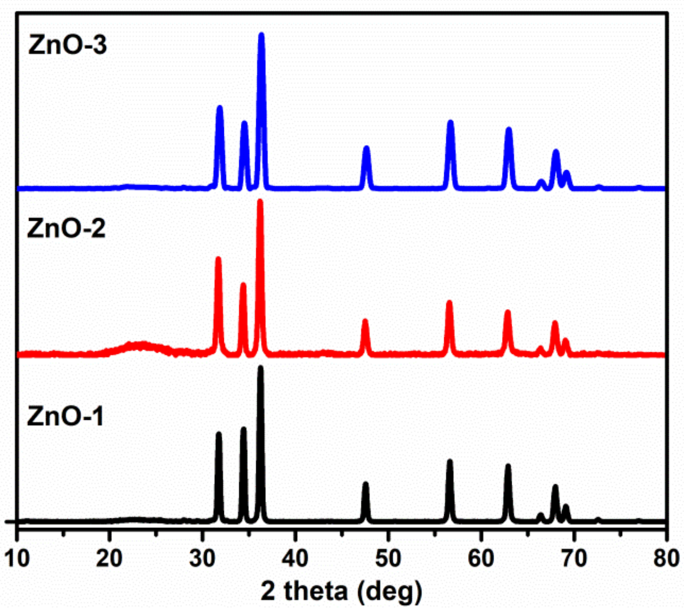

Figure 3.1. PXRD patterns of **ZnO-1** to **ZnO-3**.

Surface analysis. The evolution of varied morphologies with the change in the amount of water added was systematically studied by FESEM. It has been observed that when 0.5 mL of water was used, 3D micro flowers were obtained with average size of 1.5 μm. When the volume of water was further increased to 1 mL, there was no significant change in the morphology of ZnO. However, when the volume of water was further increased to 2 mL, 3D micro flowers assembled by 2D nanosheets were obtained. The above results indicate that growth of 2D nanostructures takes place in the initial stages of the reaction and it continues until the growth conditions are consistent (Figure 3.2). The presence of small amount of H_2O causes the reaction to proceed much more slowly, and hence the initial nucleus had sufficient time to grow in the lateral directions along (0001) and (0110) plane resulting in the formation of 2D nanosheets. The surface energy of the individual nanosheet is quite high with (2110) and (1210) exposed planes. Thus, these 2D nanostructures tend to interact with each other and aggregate via self-assembly process to form 3D nanostructures by minimizing their overall surface energy (Figure 3.3).[32]

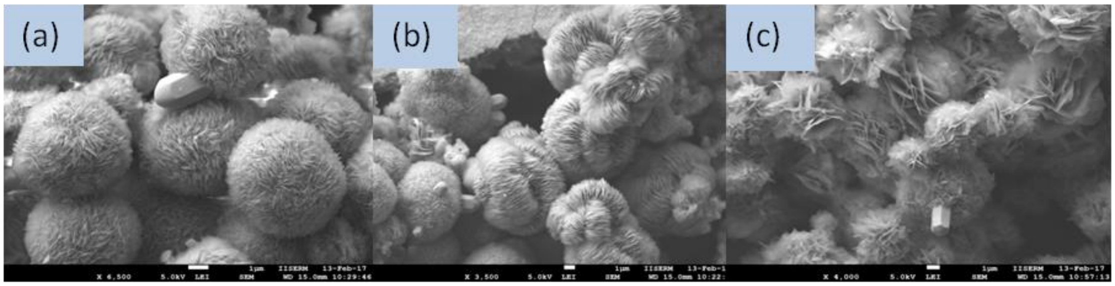

Figure 3.2. ZnO-1 to **ZnO-3** obtained with different volumes of water (a) 0.5 mL, (b) 1 mL and (c) 2 mL.

In the second step, annealing of the as-synthesized ZnO nanostructures (**ZnO-1** to **ZnO-3**) resulted in qualitative shape change from 3D microspheres **ZnO-1** and **ZnO-2** to 0D spheres (**ZnO-1a** and **ZnO-2a**) (Figure 3.4a and b). Whereas, 3D micro flowers assembled by 2D nanosheets (**ZnO-3**) yielded 1D nanorods (**ZnO-3a**, with length 2 μm, diameter 470 nm) (Figure 3.4c). The transformation to 1D nanorods is resulted from the excess oxygen molecules present on the surface trapped in the vacant sites between the interconnected nanosheets. During the annealing at a temperature of 800 ^{o}C, the excess oxygen molecules interacts with the surface resulting in enhancing the oxygen pressure and temperature in these areas and create active sites for the formation of ZnO nanorods. The constant heat treatment for 6 hours resulted in the uniform growth of these rods. Annealing at a high temperature for a period of 6 hours favors the longitudinal growth which continued to form ZnO nanorod arrays.

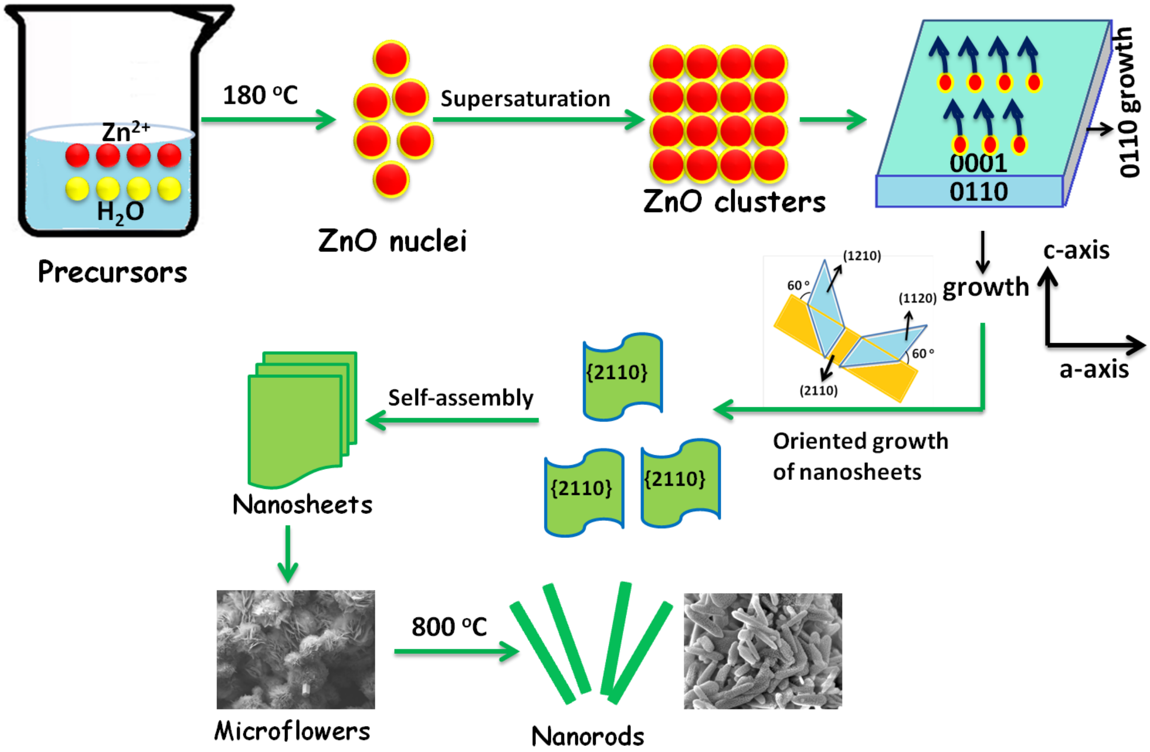

Figure 3.3. Mechanism of transformation of self-assembled nanosheets into nanorods.

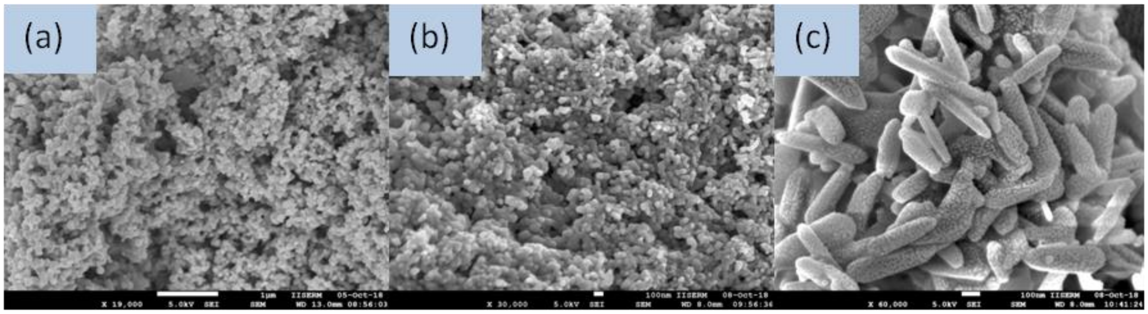

Figure 3.4. ZnO nanostructures obtained after annealing hydrothermal synthesized ZnO nanostructures (a) **ZnO-1a**, (b) **ZnO-2a** and (c) **ZnO-3a**.

Optical properties. Solid state UV-vis diffuse reflectance is done in order to investigate the light scattering ability of nanostructures. The spectra were recorded in the wavelength range of 200-800 nm using KBr as the reference sample. Figure 3.5 shows the spectra of **ZnO-1** to **ZnO-3** in which the highest excitonic absorption is located at 368 nm for ZnO. The experimental results are closely in agreement with the results obtained in the literature which showed the excitonic absorption at a wavelength of 378 nm.[33-34] The obtained results indicate a strong exciton binding energy in the samples. For direct band gap semiconductor like ZnO, the characterization of the energy band gap (E_g) using Tauc relation:

$$\alpha(h\nu)^{1/n} = B\left(h\nu - E_{gap}\right) \tag{2}$$

where α is the absorption coefficient, hν is the photon energy, B is the band form parameter, E_{gap} is the optical band gap of the nanoparticles, and n=1/2 for direct band gap and 2 for indirect band gap. Since ZnO is a direct band gap semiconductor thus n=1/2 is used for the calculations. Thus, energy band gaps can be determined from the Tauc plot between $\alpha h\nu^2$ vs hν(eV) shown in Figure 3.5. The intersection of the x-axis and the extrapolated line gives the energy band gap values. The band gap values were found to be 3.18, 3.24 and 3.20 for **ZnO-1**, **ZnO-2** and **ZnO-3**, which is lower than that of bulk ZnO (3.37 eV) due to optical confinement.

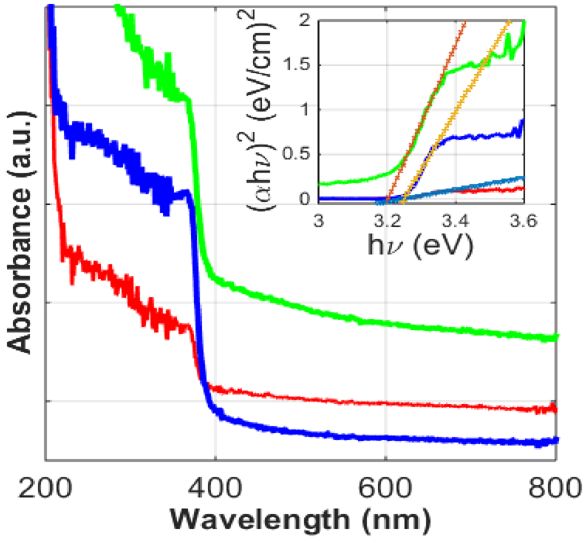

Figure 3.5. Solid state absorption spectra of **ZnO-1** and **ZnO-3** where red is for **ZnO-1**, green colour is for **ZnO-2** and blue colour represents **ZnO-3** and (inset) plot is between $(\alpha h\nu)^2$ versus (hν).

Photoluminescence properties. Figure 3.6 shows the photoluminescence spectra of the as-synthesized ZnO nanostructures (**ZnO-1** to **ZnO-3**) at different volumes. The xenon lamp was used as the excitation source. At an excitation wavelength of 350 nm, all the samples displayed similar spectra with a slight shift in their emission wavelengths. A broad emission band has been observed for **ZnO-1** in the range of 460-490 nm. Similarly, **ZnO-2** showed emission band within a range of 430-460 nm. Whereas in case of **ZnO-3**, the maximum absorption was observed between 435-450 nm. The photoluminescence in the visible region of the spectrum originates from the defect states of zinc interstitials, zinc vacancies and oxygen vacancies.[35-37] Also, a diminishing effect on the emission intensities were observed as a result of increase in the volume from 0.5 mL to 2 mL.

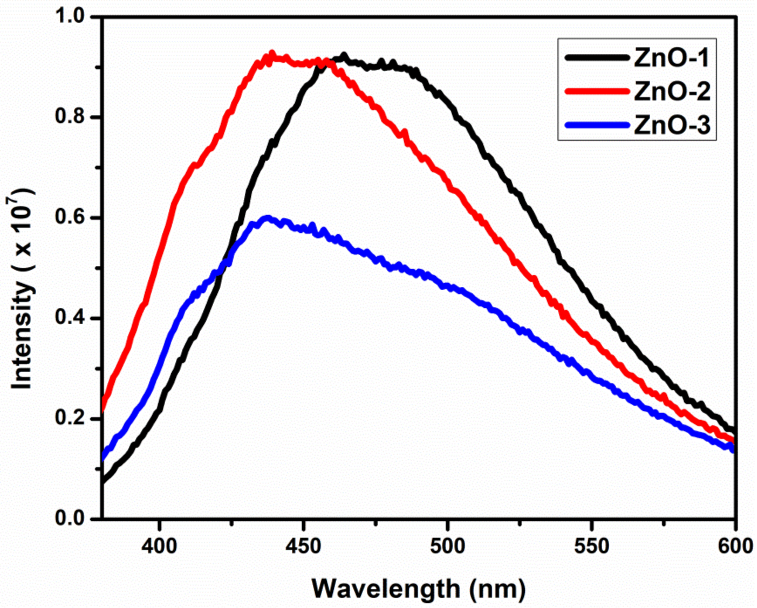

Figure 3.6. Photoluminescence spectra of **ZnO-1** to **ZnO-3**.

(ii) Using [$Zn_2(bpea)_2(adc)_2]_n$. In another study, $[Zn_2(bpea)_2(adc)_2]_n$ had been employed for the fabrication of ZnO nanostructures. The hydrothermal reaction was carried out utilizing this polymer in different volumes of water (0.5 mL, 1 mL and 2 mL) at 180 °C for 24 hours (Scheme 3.3). The annealing of the hydrothermal synthesized nanostructures resulted in the change in the dimensionalities of the obtained nanostructures shown in Scheme 3.4. Annealing favours the growth along (0001) direction.

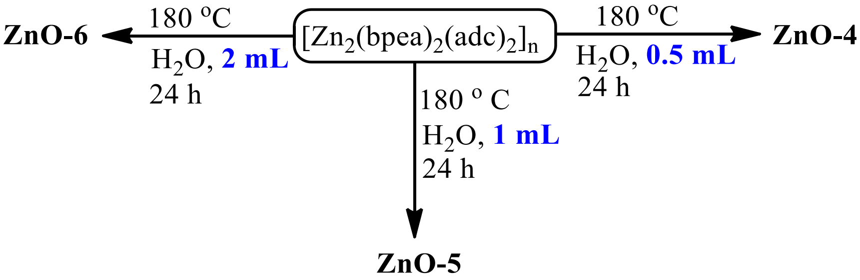

Scheme 3.3. Synthesis of **ZnO-4** to **ZnO-6** in neutral conditions.

$$\textbf{ZnO-4} \xrightarrow[\text{6 h}]{\text{800 }^{o}\text{C}} \textbf{ZnO-4a}$$

$$\textbf{ZnO-5} \xrightarrow[\text{6 h}]{\text{800 }^{o}\text{C}} \textbf{ZnO-5a}$$

$$\textbf{ZnO-6} \xrightarrow[\text{6 h}]{\text{800 }^{o}\text{C}} \textbf{ZnO-6a}$$

Scheme 3.4. Synthesis of **ZnO-4a** to **ZnO-6a** by post annealing process.

Powder X-ray diffraction studies. The crystallinity of the as-synthesized nanostructures was characterized by XRD analysis as shown in Figure 3.7. The XRD patterns of the hydrothermal synthesized ZnO nanostructures in different volumes of water (0.5 mL, 1 mL and 2 mL) were perfectly indexed to the hexagonal phase of wurtzite ZnO with the lattice constants: a = 3.26 Å = b and c = 5.22 Å and agrees well with the literature ((JCPDS 06-2151). The lattice parameters were calculated using equation 1 and the values obtained are given in Table 3.2. All the samples are crystalline in nature and no impurity peaks were observed indicating high purity of the obtained nanostructures.

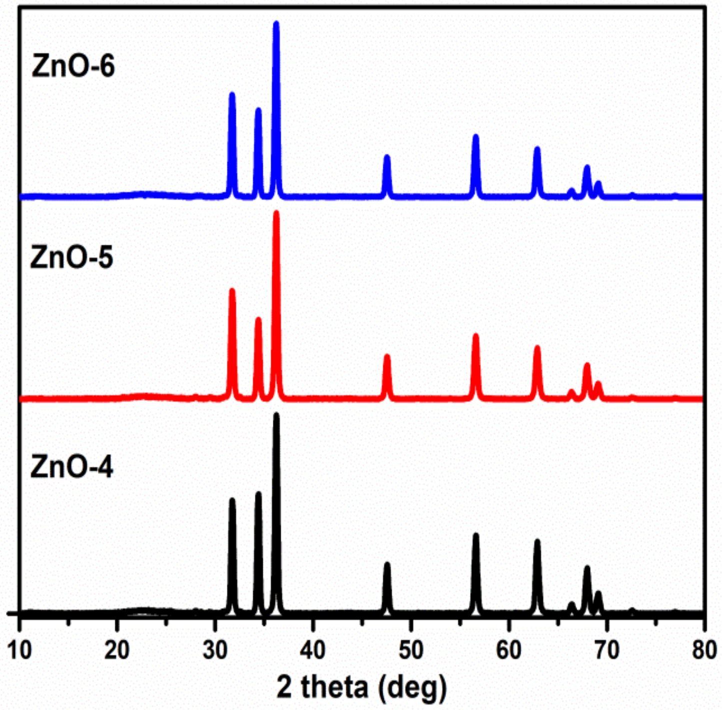

Figure 3.7. PXRD patterns of **ZnO-4** to **ZnO-6**.

Table 3.2. Lattice parameters for ZnO samples (**ZnO-4** to **ZnO-6**)

Sample	h k l	2θ values (degrees)	Lattice constants a, b, c (Å)	Volume of unit cell (Å^3)	Atomic packing fraction	d spacing (Å)	FWHM
ZnO-4	(100)	31.75	a = b = 3.26,	48.05	0.754	2.82	0.314
	(002)	34.42	c = 5.22			2.61	
	(101)	36.26				2.48	
ZnO-5	(100)	31.74	a = b = 3.26,	48.08	0.755	2.82	0.335
	(002)	34.42	c = 5.22			2.61	
	(101)	36.24				2.48	
ZnO-6	(100)	31.73	a = b = 3.26,	48.11	0.755	2.82	0.318
	(002)	34.42	c = 5.22			2.61	
	(101)	36.23				2.48	

Surface analysis. Figure 3.8 shows the FESEM images of the obtained ZnO nanostructures from $[Zn_2(bpea)_2(adc)_2]_n$ at different volumes of water (0.5 mL, 1 mL and 2 mL). In this case, 0.5 mL of water yielded beautiful lilies assembled by 2D nanosheets. The increase in volume to 1 mL produced 3D micro flowers clustered together by sheaves of nanosheets. Whereas further increase in volume to 2 mL generated 1D nanotubes. Over the past two decades, the nanostructured ZnO have received enormous attention. Among all these nanostructures, a number of inorganic tubular microstructures have attracted more interest owing to their large surface area than rest of the crystal shapes. These nanotubes show potential applications in solar cells, photocatalysis, field emission studies, chemical sensors etc.[38-41] In comparison to other synthetic techniques, hydrothermal synthesis have been proved to more favorable for the production of monocrystalline micro and nanotubes of ZnO at large scale offering high quality and low cost. Vaysseirs et. al have well explained the formation of microtubes through etching process.[42] Wang et. al explained a different mechanism for the formation of tubular structures of ZnO.[43] In the present work, the formation of 1D nanotubes by exploiting coordination polymer without the addition of any template/surfactant is reported for the first time.

Further annealing of the obtained nanostructures (**ZnO-4** to **ZnO-6**) resulted in the mixture of microrods and polyhedrons (**ZnO-4a**) and 1D nanorods (**ZnO-5a** with A.R.~7 and **ZnO-6a** with A.R.~4.62) illustrated in Figure 3.9. Thus, it can be concluded that annealing resulted in altering the dimensionalities in ZnO nanostructures.

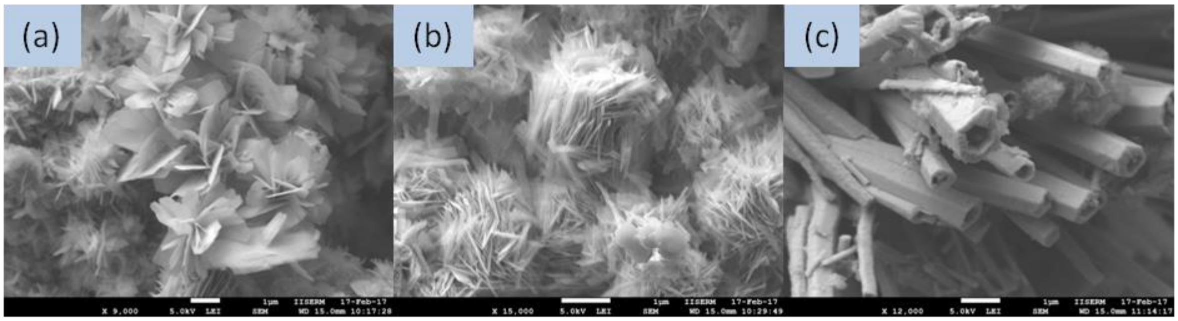

Figure 3.8. ZnO-4 to **ZnO-6** obtained with different volumes of water (a) 0.5 mL, (b) 1 mL and (c) 2 mL.

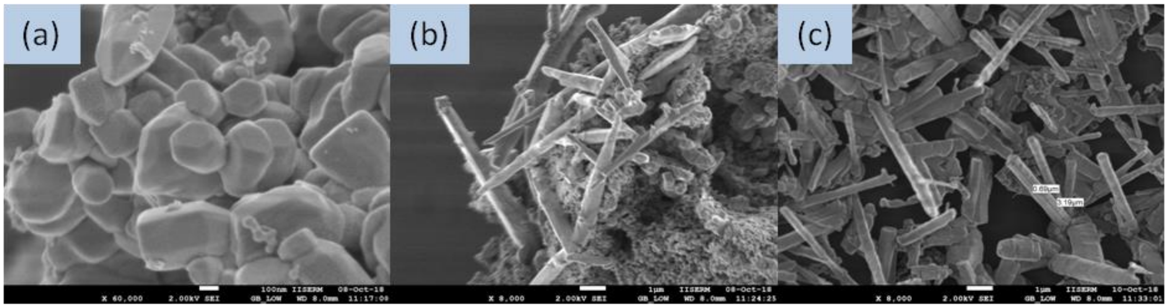

Figure 3.9. ZnO nanostructures obtained after annealing hydrothermal synthesized ZnO nanostructures (a) **ZnO-4a**, (b) **ZnO-5a** and (c) **ZnO-6a**.

The mechanism of formation of tubular rods can be explained by the lattice structure of wurtzite ZnO which consists of several planes: a polar oxygen plane (0001) at the base, polar Zinc (0001) face at the top and non-polar {1010} planes parallel to the c-axis. During the reaction, Zn^{2+} ions from the solution reacts with H_2O molecules to give $Zn(OH)_2$. ZnO nanostructures grow along (0001) direction with a concave growing head because of low saturation of coordination atoms at the edges of (0001) planes. Also, the precursor species can easily diffuse to the edges than to the center creating the growth front for their deposition by accommodating more incoming species owing to its large surface area. Thus, the rate of consumption of Zn^{2+} becomes more and more leading to the removal of polar plane (0001) faster by dissolution in comparison to non-polar plane {1010} owing to less stability of

(0001) plane. As a result, small craterlets started appearing on the top of the rods due to removal of atoms from (0001) planes which continued after attaining a stable hexagonal shape as shown in Figure 3.10.

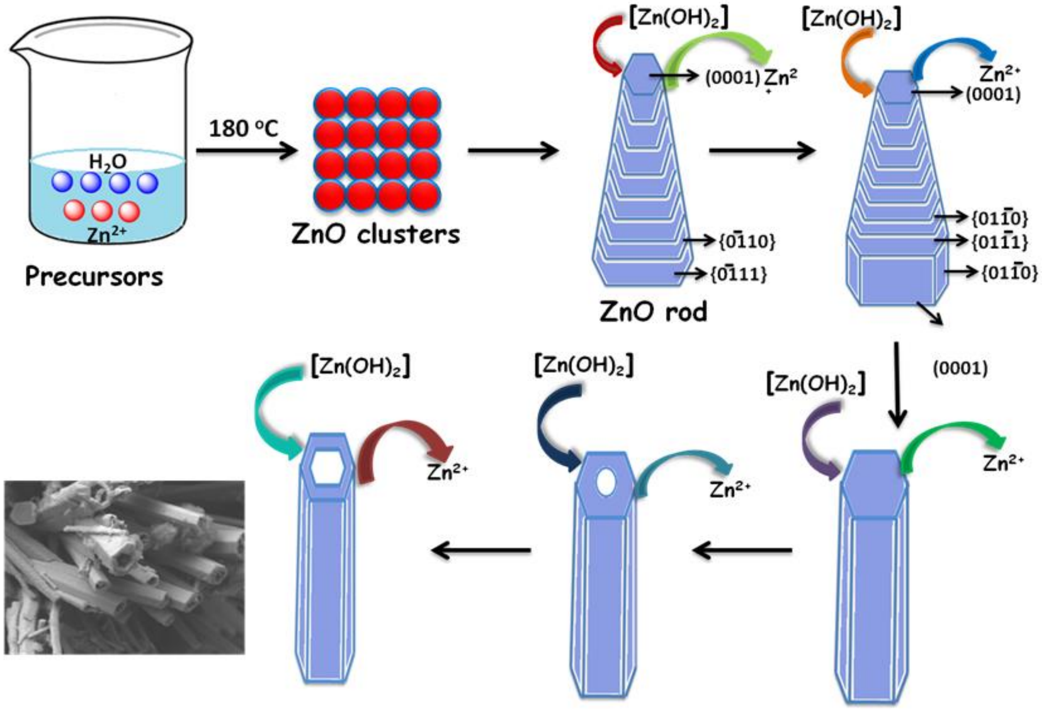

Figure 3.10. Mechanism of formation of nanotubes.

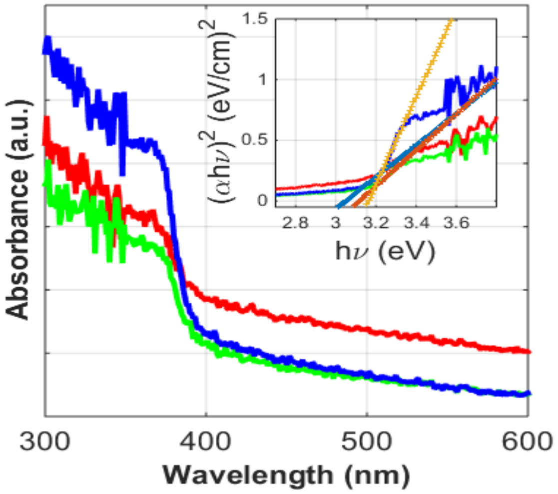

Figure 3.11. Solid state absorption spectra of **ZnO-4** to **ZnO-6** where red is for **ZnO-4**, green colour is for **ZnO-5** and blue colour represents **ZnO-6** and (inset) plot is between $(\alpha h\nu)^2$ versus $(h\nu)$.

Optical properties. The optical properties of the obtained nanostructures were analyzed by using UV-visible spectroscopy shown in Figure 3.11. **ZnO-4** to **ZnO-6** exhibited well defined absorption peaks between 360 and 380 nm in the UV region.[44-45] The presence of UV emission peak in the absorption spectra is attributed to the exciton recombination. The intrinsic band gap of nanostructures is dependent on the absorption peaks in the spectra due to charge transfer from valence band to conduction band in the nanostructures. The band gap energies of **ZnO-4** to **ZnO-6** calculated using equation 2 are given in Table 3.3.

Table 3.3. The band gap energies of **ZnO-4** to **ZnO-6**

Sample	Band Gap (E_g)
ZnO-4	3.12
ZnO-5	3.23
ZnO-6	3.18

Photoluminescence properties. The photoluminescence experiments were performed on **ZnO-4** to **ZnO-6** using xenon lamp as the excitation source. The experiments were conducted at an excitation wavelength of 350 nm. All the spectra showed identical characteristics with three emission bands. The first emission band at 410 nm in the spectra originated from the recombination of excitons (Figure 3.12).

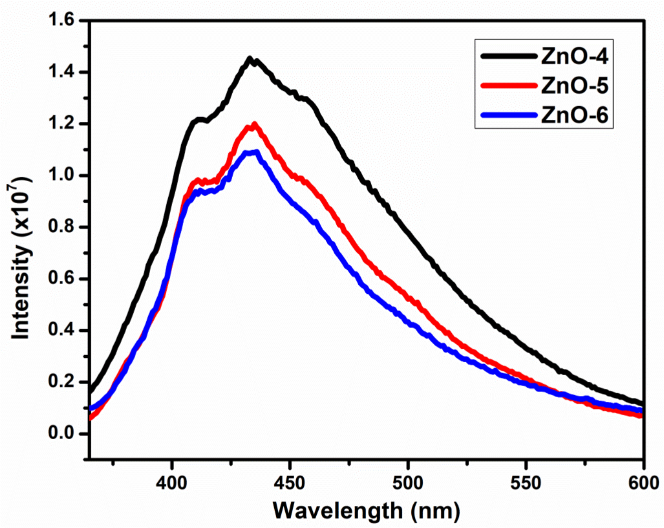

Figure 3.12. Photoluminescence spectra of **ZnO-4** to **ZnO-6**.

The other bands at 434 and 456 nm in the visible range are due to the presence of deep level defects such as singly ionized oxygen vacancies[46-48], Zn interstitials or their complexes. In this case also it has been observed that dilution of the samples played an important role in controlling the emission intensities of the ZnO nanostructures. The **ZnO-4** grown with 0.5 mL of water showed higher emission intensity than the **ZnO-5** and **ZnO-6** synthesized with 1 and 2 mL of water. Thus, it can be concluded that a high concentration of Zn(II) ion in the reaction mixture is responsible for a high emission intensity.

(iii) Using $\{[Zn_2(bpta)_2(adc)_2]\cdot 2H_2O\}_n$. In this case, $\{[Zn_2(bpta)_2(adc)_2]\cdot 2H_2O\}_n$ had been employed for the formation of ZnO nanostructures. Following the same procedure, the hydrothermal reaction was carried out using this polymer in different volumes of water (0.5 mL, 1 mL and 2 mL) at 180 °C for 24 hours (Scheme 3.5). The post annealing of the obtained nanostructures resulted in changing the dimensionalities of ZnO from 2D nanosheets to 1D nanorods in all the cases (Scheme 3.6).

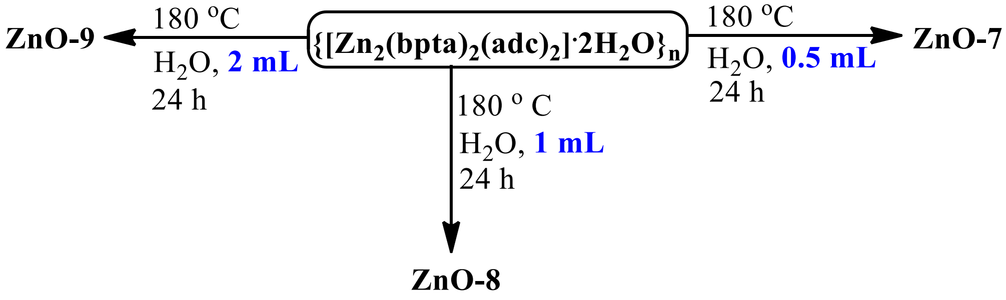

Scheme 3.5. Synthesis of **ZnO-7** to **ZnO-9** in neutral conditions.

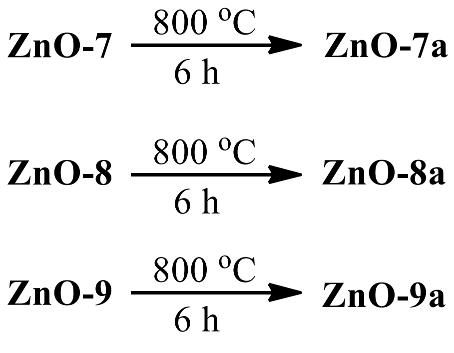

Scheme 3.6. Synthesis of **ZnO-7a** to **ZnO-9a** by post annealing process.

Powder X-ray diffraction studies. The crystal phase and purity of the obtained nanostructures was confirmed by X-ray diffraction analysis. All the samples exhibit hexagonal wurtzite structure of ZnO. The peaks match well with the reported values of ZnO and the lattice parameters, a = 3.26 Å, c = 5.22 Å, are in accordance with the JCPDS 06-2151 (Figure 3.13).

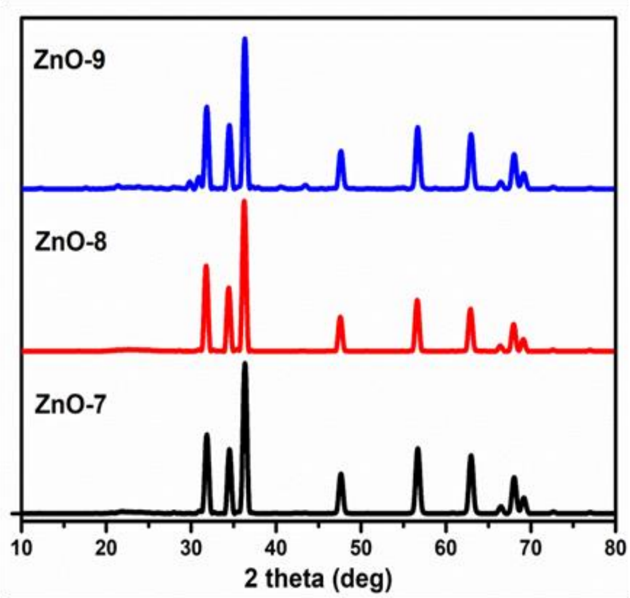

Figure 3.13. PXRD patterns of **ZnO-7** to **ZnO-9**.

The lattice parameters shown in Table 3.4 were determined using equation 1. No other characteristic peaks for impurities were detected indicating the pure crystalline phase of ZnO.

Surface analysis. Figure 3.14 shows FESEM images of the samples (**ZnO-7** to **ZnO-9**) obtained after adding different volumes of water (0.5, 1 and 2 mL). When 0.5 mL of water was added into the precursor, 2D hexagonal sheets were formed with an average thickness of ~10-20 nm. The change in volume to 1 mL also produced nanosheets with an average thickness of 20-25 nm. Furthermore, the nanosheets obtained with 2 mL of water showed an average thickness between 10-20 nm. However, few nanoparticles were also obtained along with nanosheets in this case. These sheets are stacked together and even distorted. The annealing of these 2D nanosheets at 800 ^{o}C resulted in the transformation to 1D nanorods constructed individually with clear edges and with very less aggregation (Figure 3.15). The aspect ratios of the rods obtained after annealing are given in Table 3.5.

Table 3.4. Lattice parameters for ZnO samples (**ZnO-7** to **ZnO-9**)

Sample	**h k l**	**2θ values (degrees)**	**Lattice constants a, b, c (Å)**	**Volume of unit cell (Å ^{3})**	**Atomic packing fraction**	**d spacing (Å)**	**FWHM**
ZnO-7	(100)	31.74	a = b = 3.26,	48.08	0.754	2.82	0.316
	(002)	34.42	c = 5.22			2.61	
	(101)	36.26				2.48	
ZnO-8	(100)	31.70	a = b = 3.26,	48.22	0.755	2.82	0.381
	(002)	34.40	c = 5.22			2.61	
	(101)	36.20				2.48	
ZnO-9	(100)	31.83	a = b = 3.25,	47.69	0.754	2.82	0.517
	(002)	34.51	c = 5.20			2.60	
	(101)	36.32				2.47	

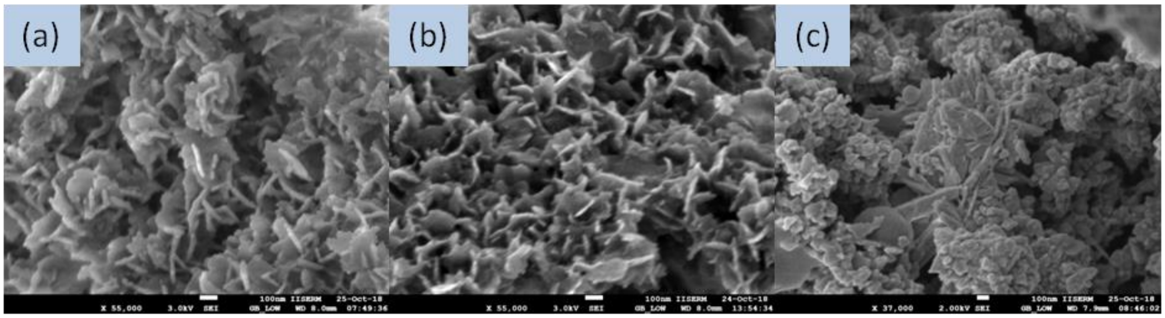

Figure 3.14. ZnO-7 to **ZnO-9** obtained with different volumes of water (a) 0.5 mL, (b) 1 mL and (c) 2 mL.

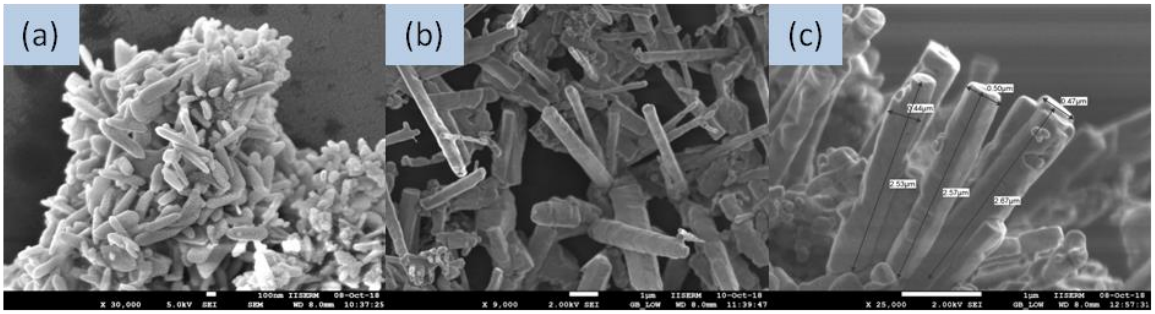

Figure 3.15. ZnO nanostructures obtained after annealing hydrothermal synthesized ZnO nanostructures (a) **ZnO-7a**, (b) **ZnO-8a** and (c) **ZnO-9a**.

Table 3.5. Aspect ratios of the ZnO nanorods (**ZnO-7a** to **ZnO-9a**)

Sample	Length	Diameter	Aspect ratio
ZnO-7a	626 nm	128 nm	4.89
ZnO-8a	3.23 μm	590 nm	5.47
ZnO-9a	2.57 μm	500 nm	5.14

Optical properties. The UV-visible absorption spectra of **ZnO-7** to **ZnO-9** at different volumes of water are shown in Figure 3.16. A typical exciton absorption in the range of 360-380 nm has been observed. The absorption in the UV region is due to the recombination of free excitons.[44-45] Since the absorption coefficient (α) is strongly dependent on the photon energy at the onset of UV absorption, the band gap values (E_g) were calculated using equation 2. The values obtained are given in Table 3.6.

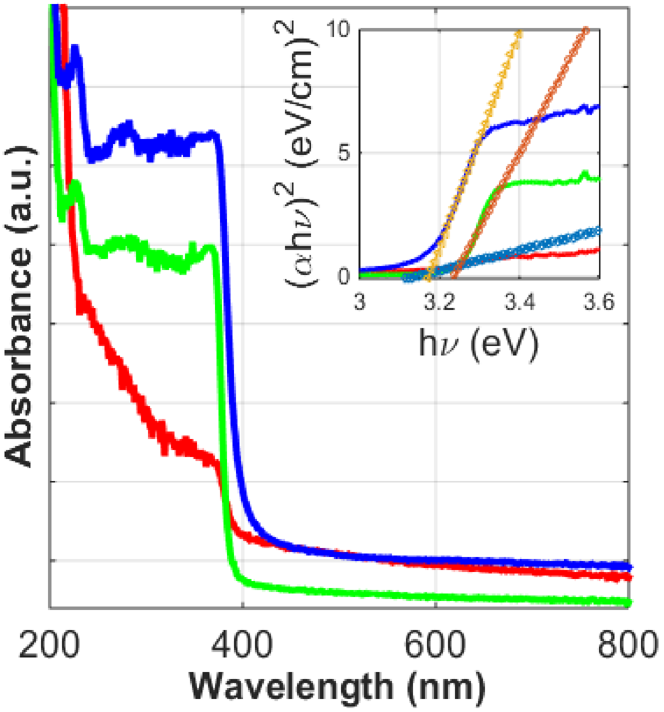

Figure 3.16. Solid state absorption spectra of **ZnO-7** and **ZnO-9** where red is for **ZnO-7**, green colour is for **ZnO-8** and blue colour represents **ZnO-9** and (inset) plot is between $(\alpha h\nu)^2$ versus (hν).

Table 3.6. Bandgap values of **ZnO-7** to **ZnO-9**

Sample	Band Gap (E_g)
ZnO-7	3.01
ZnO-8	3.15
ZnO-9	3.09

Photoluminescence properties. The photoluminescence measurements were carried out at room temperature using xenon lamp as the source at an excitation wavelength of 350 nm. The visible emissions were observed in all the cases (Figure 3.17). **ZnO-7** displays emission in the range of 435-460 nm. Whereas **ZnO-8** exhibits three emission bands at 437, 456 and 492 nm in the visible range of spectrum. Furthermore, **ZnO-9** showed a broad emission between 450-490 nm. It is well known that the visible emissions are related to several intrinsic defects in ZnO which include Zn vacancies (V_{Zn}), O vacancies (V_o), interstitial Zn (Zn_i), interstitial O (O_i) and substitution of oxygen at zinc position (O_{Zn}). The blue emission in all the cases resulted from the donor level of Zn_i to acceptor level of V_{Zn}.

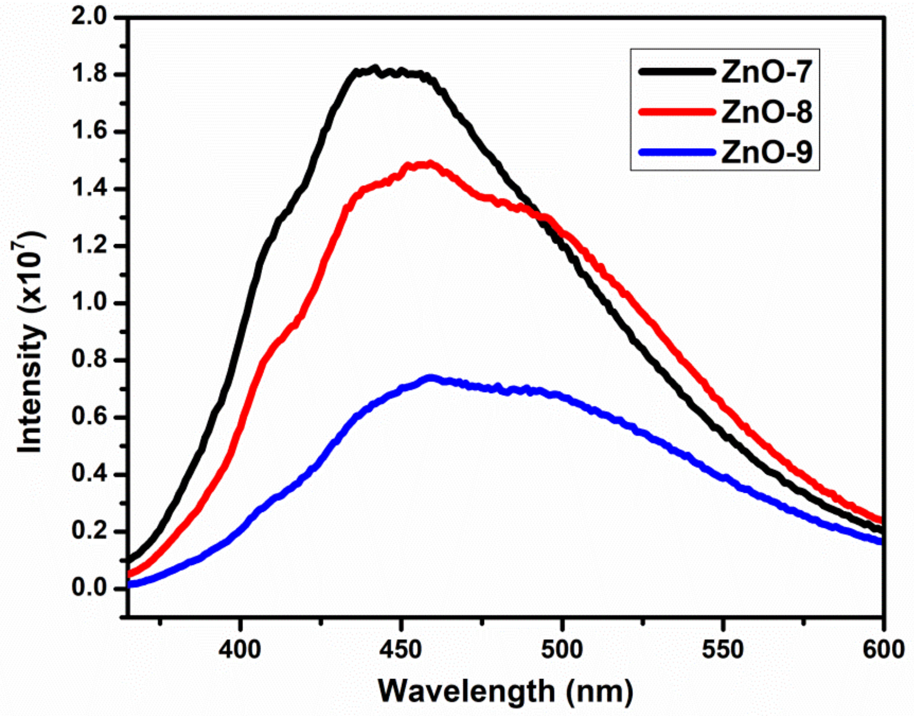

Figure 3.17. Photoluminescence spectra of **ZnO-7** to **ZnO-9**.

3.1.2 Fabrication of ZnO nanostructures in basic conditions

3.1.2.1 Effect of volume

(i) **Using $[Zn_2(bpma)_2(adc)_2]_n$.** The coordination polymer $[Zn_2(bpma)_2(adc)_2]_n$ has been utilized to fabricate ZnO nanostructures hydrothermally in basic conditions where KOH has been used as OH^- ion source in different volumes of water (1, 2, 3, 4 and 5 mL) at 180 °C for 6 hours (Scheme 3.7). 1D nanorods was successfully obtained with a slight variation in their aspect ratios.

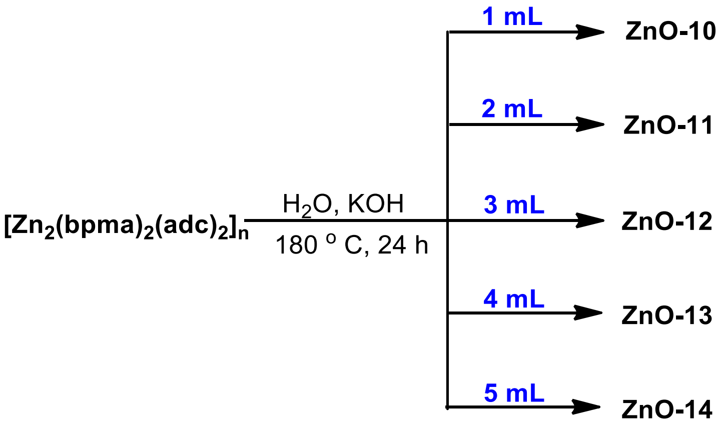

Scheme 3.7. Synthesis of ZnO nanostructures (**ZnO-10** to **ZnO-14**) in basic conditions at 180 °C.

Powder X-ray diffraction studies. The crystallinity and purity of the obtained nanostructures was characterized by X-ray diffraction analysis. All the samples synthesized with different volumes of water (1 to 5 mL) exhibited hexagonal wurtzite structure of ZnO (Figure 3.18).

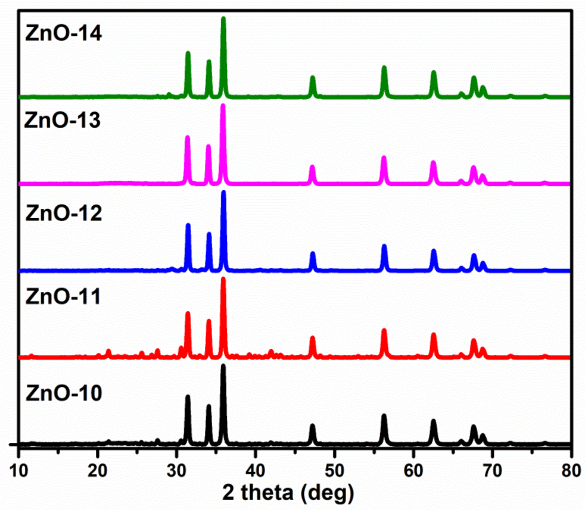

Figure 3.18. PXRD patterns of **ZnO-10** to **ZnO-14**.

The peaks are in accordance with the JCPDS 06-2151. Since no other characteristic peaks for any impurity was detected which confirmed the pure crystalline phase of ZnO. The lattice parameters of ZnO samples were calculated using equation 1 and the data obtained are given in Table 3.7.

Table 3.7. Lattice parameters for ZnO samples (**ZnO-10** to **ZnO-14**)

Sample	hkl	2θ values (degrees)	Lattice constants a, b, c (Å)	Volume of unit cell (Å^3)	APF	d spacing (Å)
ZnO-10	(100)	31.51	a = b = 3.28, c = 5.26	49.12	0.755	2.84
	(002)	34.14				2.63
	(101)	35.98				2.50
ZnO-11	(100)	31.52	a = b = 3.28, c = 5.25	49.10	0.755	2.84
	(002)	34.17				2.62
	(101)	36.01				2.49
ZnO-12	(100)	31.48	a = b = 3.28, c = 5.26	49.22	0.755	2.84
	(002)	34.13				2.63
	(101)	35.97				2.50
ZnO-13	(100)	31.49	a = b = 3.28, c = 5.25	49.18	0.755	2.84
	(002)	34.15				2.63
	(101)	35.97				2.50
ZnO-14	(100)	31.48	a = b = 3.28, c = 5.25	49.19	0.755	2.84
	(002)	34.13				2.62
	(101)	35.92				2.51

Surface analysis. Figure 3.19 shows FESEM images of the samples (**ZnO-10** to **ZnO-14**) obtained in basic conditions at pH>13 with addition of different volumes of water (1, 2, 3, 4 and 5 mL). It has been observed that with an increase in the volume of water i.e. with more dilution of the reaction mixture the aspect ratios of nanorods were decreasing achieving the maximum value at 3 mL. The aspect ratios of the nanorods obtained at different volumes are given in Table 3.8.

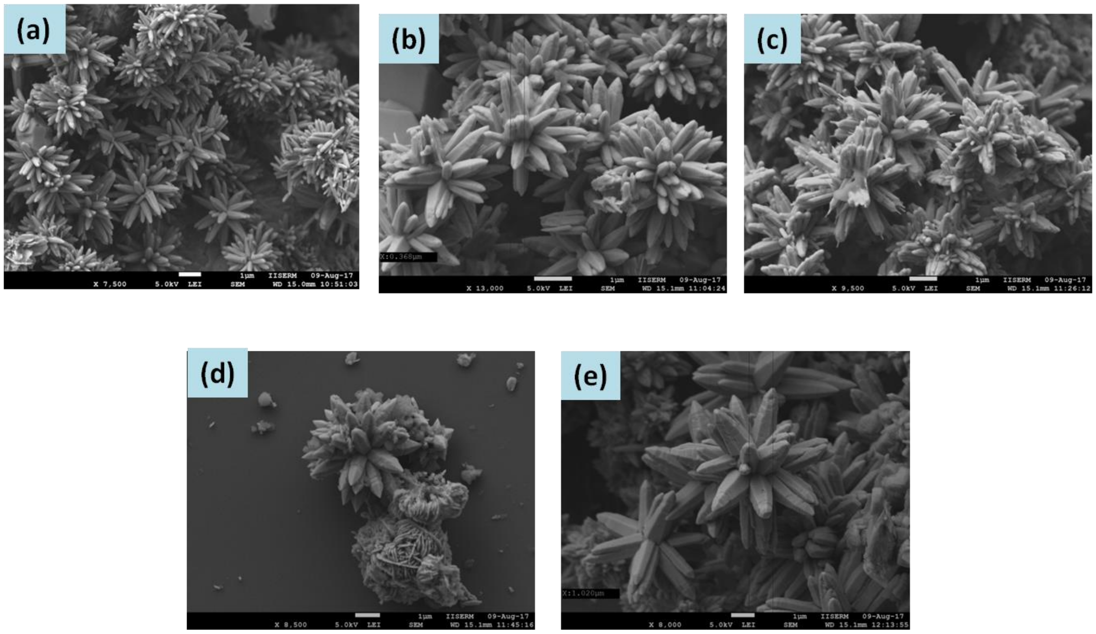

Figure 3.19. ZnO-10 to **ZnO-14** obtained in basic conditions after adding (a) 1 mL, (b) 2 mL, (c) 3 mL, (d) 4 mL and (e) 5 mL of water.

Table 3.8. Aspect ratios of **ZnO-10** to **ZnO-14**

Sample	**Aspect ratio**
ZnO-10	2.68
ZnO-11	2.19
ZnO-12	2.77
ZnO-13	1.55
ZnO-14	1.33

Photoluminescence properties. The photoluminescence spectra were recorded to investigate the luminescent properties of the as obtained ZnO nanorods. The xenon lamp was used as the excitation source and the excitation wavelength was set at 350 nm. The spectra were recorded in a range of 365-600 nm. All the samples showed a broad blue emission band with a slight shift in their emission spectra. The blue emission resulted from the intrinsic defects in ZnO (zinc vacancies and oxygen vacancies).[49] It has been observed that an increase in the volume of water resulted in increase in the intensity of absorption as illustrated in Figure 3.20.

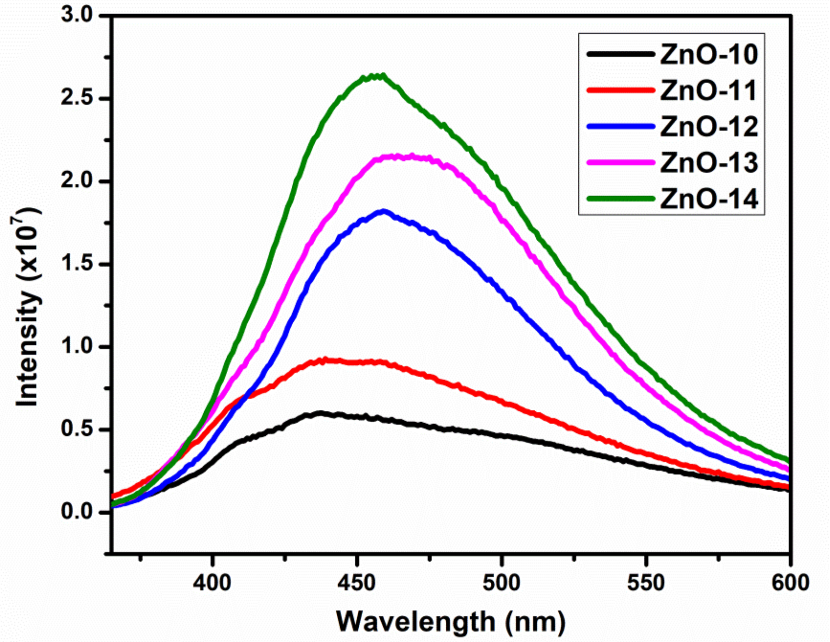

Figure 3.20. Photoluminescence spectra of **ZnO-10** to **ZnO-14**.

3.1.2.2 Effect of temperature

(i) Using [Zn$_2$(bpma)$_2$(adc)$_2$]$_n$. ZnO nanostructures were fabricated at different temperatures 120 and 150 °C. The fabrication was carried out hydrothermally for different times (6 hours, 12 hours, 18 hours and 24 hours) in basic conditions at pH>13. Interesting results were obtained with respect to their aspect ratios when ZnO nanorods were synthesized at different temperatures for different time intervals (Scheme 3.8 to 3.9). Thus, the processing parameters – temperature, time and pH help in controlling and altering the aspect ratios of nanorods.[50-54] These parameters play a crucial role in manipulating the length and diameter of the rods. The rods were grown at different temperatures for different growth times in order to optimize the condition for obtaining a high aspect ratio of the rods.

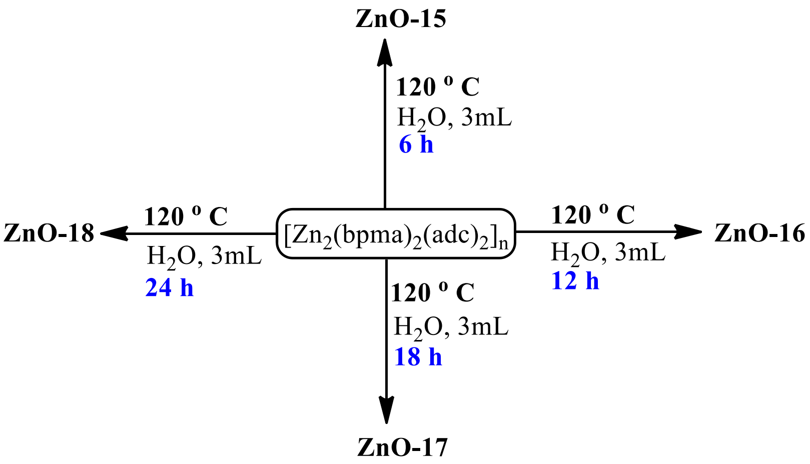

Scheme 3.8. Synthesis of ZnO nanostructures (**ZnO-15** to **ZnO-18**) in basic conditions at 120 °C.

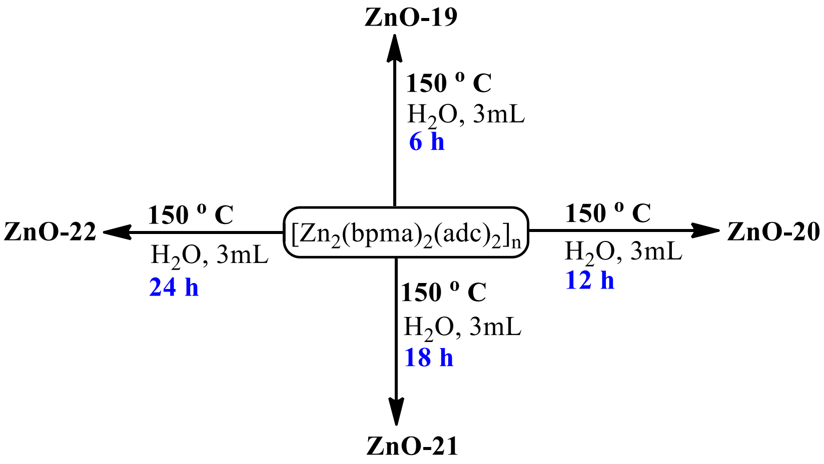

Scheme 3.9. Synthesis of ZnO nanostructures (**ZnO-19** to **ZnO-22**) in basic conditions at 150 °C.

Powder X-ray diffraction studies. The diffraction patterns of ZnO nanorods grown with different aging times (6 h, 12 h, 18 h, 24 h) at different temperatures 120 °C and 150 °C (**ZnO-15** to **ZnO-26**) were taken to determine the crystalline phase of the nanorods. The 2θ values of diffraction peaks obtained are in good agreement with the standard JCPDS data for ZnO (JCPDS No. 89-1397) (Figure 3.21). The ZnO nanorods contain only hexagonal wurtzite structure as the crystalline phase. The formation of nanorods with wurtzite structure could be attributed to the anisotropic growth along (001) plane owing to a faster growth velocity in this direction under hydrothermal conditions. The higher intensity of the (101) diffraction peak in all the patterns further provides the evidence of the preferential growth direction along the c-axis.[55] No other traces of impurity were observed in the reflection peaks indicating high purity of the obtained nanorods. The strong and narrow peaks further revealed good crystallinity of the rods. The lattice parameters of the ZnO hexagonal wurtzite structure can be determined from the equation:

$$\frac{1}{d^2} = \frac{4}{3(h^2 + hk + \frac{k^2}{a^2})} + \frac{l^2}{c^2}$$

where a, b and c are the lattice parameters and d is the spacing between the planes in the atomic lattice which can be calculated from Bragg’s law: $2d \sin \theta = n\lambda$. The volume of the hexagonal unit cell was calculated using the relation: $V = 0.866\ a^2c$ and the atomic packing fraction of the obtained nanorods were determined using the following relation:

$$\text{Atomic packing fraction (A.P.F)} = \frac{2\pi a}{3\sqrt{3}c}$$

The calculated values obtained using the above relations are given in Table 3.9.

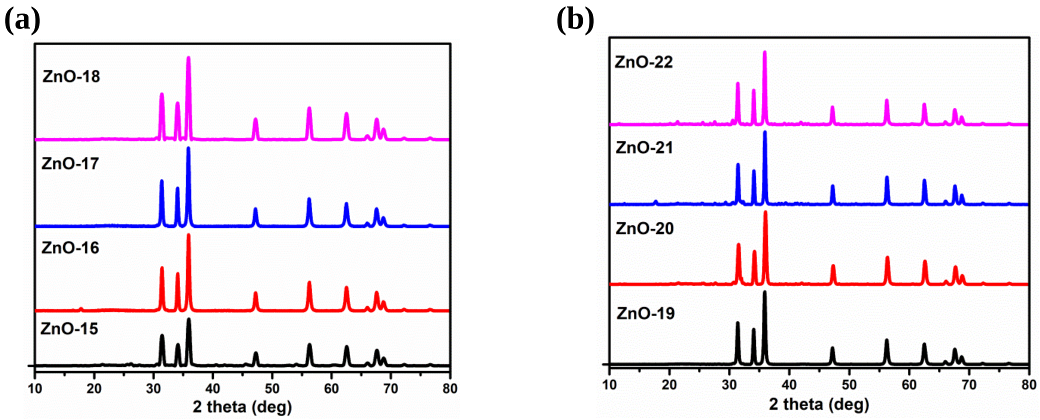

Figure 3.21. PXRD patterns of (a) **ZnO-15** to **ZnO-18** obtained at 120 °C, (b) **ZnO-19** to **ZnO-22** obtained at 150 °C.

Surface analysis. A series of experiments were carried out at 120 and 150 °C for different duration from 6 hours to 24 hours to synthesize the nanorods with different aspect ratios. Figure 3.21 shows the typical FESEM images of the as-grown ZnO nanorods at 120 and 150 °C. The multipod structures composed of more than 10 nanorods were observed at all the temperatures. The nanorods in **ZnO-15** fabricated at 120 °C have a typical length of 1.04 μm and diameter of 300 nm (Figure 3.21). As the hydrothermal time was increased to 12 hours, the rods get broader and longer (A.R ~ 3.53). The lengthening of the rods continued for 18 hours as shown in Table 3.10. However, at the end of 24 hours a decrease in the length as well as diameter was observed which might be due to dissolution of Zn^{2+} ions in the system

Table 3.9. Lattice parameters for ZnO samples (**ZnO-15** to **ZnO-22)**

Sample	h k l	2θ values (degrees)	Lattice constants a, b, c (Å)	Volume of unit cell (Å ^{3})	Atomic packing fraction	d spacing (Å)	FWHM
ZnO-15	(100)	31.44	a = b = 3.29,	49.41	0.755	2.85	0.492
	(002)	34.11	c = 5.26			2.63	
	(101)	35.94				2.50	
ZnO-16	(100)	31.42	a = b = 3.29,	49.52	0.755	2.85	0.491
	(002)	34.07	c = 5.27			2.63	
	(101)	35.91				2.50	
ZnO-17	(100)	31.40	a = b = 3.29,	49.61	0.755	2.85	0.338
	(002)	34.05	c = 5.27			2.63	
	(101)	35.87				2.51	
ZnO-18	(100)	31.40	a = b = 3.29,	49.60	0.755	2.85	0.334
	(002)	34.06	c = 5.27			2.63	
	(101)	35.89				2.51	
ZnO-19	(100)	31.41	a = b = 3.29,	49.58	0.755	2.85	0.311
	(002)	34.06	c = 5.27			2.63	
	(101)	35.89				2.50	
ZnO-20	(100)	31.54	a = b = 3.28,	48.97	0.755	2.85	0.358
	(002)	34.19	c = 5.25			2.63	
	(101)	36.02				2.50	
ZnO-21	(100)	31.44	a = b = 3.29,	49.40	0.755	2.85	0.265
	(002)	34.10	c = 5.26			2.63	
	(101)	35.93				2.50	
ZnO-22	(100)	31.41	a = b = 3.29,	49.53	0.755	2.85	0.258
	(002)	34.07	c = 5.27			2.63	
	(101)	35.90				2.50	

from the ends. At 150 °C, a high aspect ratio of the nanorods has been achieved. The solubility of the crystallites increased as the temperature increased leading to a higher growth rate at 150 °C compared to 120 °C. Furthermore, the length and the diameter of the rods increased on extending the growth time from 6 hours to 12 hours (Figure 3.22). The length and diameter of the rods continued to increase up to 18 hours (Table 3.10) as observed in the previous case. The average length and diameter of the rods produced at 150 °C is more than that at 120 °C (Figure 3.23). The trend for the increase in the aspect ratios with the extension of growth time is also similar in this case. The experimental results suggest that temperature and growth time control the aspect ratio of nanorods.

In this work, the effect of temperature (with different growth times) on the aspect ratio of the nanorods has been investigated in detail. In order to control and design the rods with tailored aspect ratios it is imperative to understand the growth mechanism of these rods. The internal structure as well as the external conditions such as temperature, growth time etc. are the important parameters in influencing the growth of a crystal. The chemical reactions involved in the hydrothermal conditions are as follows:

$$Zn^{2+} + 2OH^{-} \rightleftharpoons Zn(OH)_2$$

$$Zn(OH)_2 + 2OH^{-} \rightleftharpoons [Zn(OH)_4]^{2-}$$

$$[Zn(OH)_4]^{2-} \rightleftharpoons ZnO + H_2O + 2OH^{-}$$

$[Zn(OH)_4]^{2-}$ acts as the growth unit for the formation of ZnO nanorods where a number of dissolution-nucleation cycles evolves the nanorods.[56-58] The different growth rate of planes are: $V_{0001} > V_{\bar{1}0\bar{1}\bar{1}} > V_{\bar{1}010} > V_{\bar{1}011} > V_{000\bar{1}}$. The higher growth rate along (0001) direction results in rapid disappearance of this plane leading to a pointed shape at the end of the c-axis which explains the formation of rods with pointed tips at the ends. After a certain time, these rods unite with other neighboring rods to evolve into flower-like structures by reducing their surface energy. It has been observed that temperature plays a significant role in tuning the dimensions and aspect ratios of these rods. A higher temperature (150 °C) and an optimized growth time of 18 hours resulted in giving the rods with high aspect ratios. Thus, the temperature as well as the growth time helped in manipulating and tailoring the length and diameter of these rods.

Table 3.10. Aspect ratios of ZnO nanorods (**ZnO-15** to **ZnO-22**)

Sample	Length (μm)	Diameter (μm)	Aspect Ratio
ZnO-15	1.04	0.30	3.46
ZnO-16	1.38	0.39	3.53
ZnO-17	1.81	0.44	4.11
ZnO-18	1.03	0.41	2.56
ZnO-19	2.18	0.45	4.84
ZnO-20	2.41	0.49	4.91
ZnO-21	3.19	0.55	5.80
ZnO-22	1.02	0.22	4.63

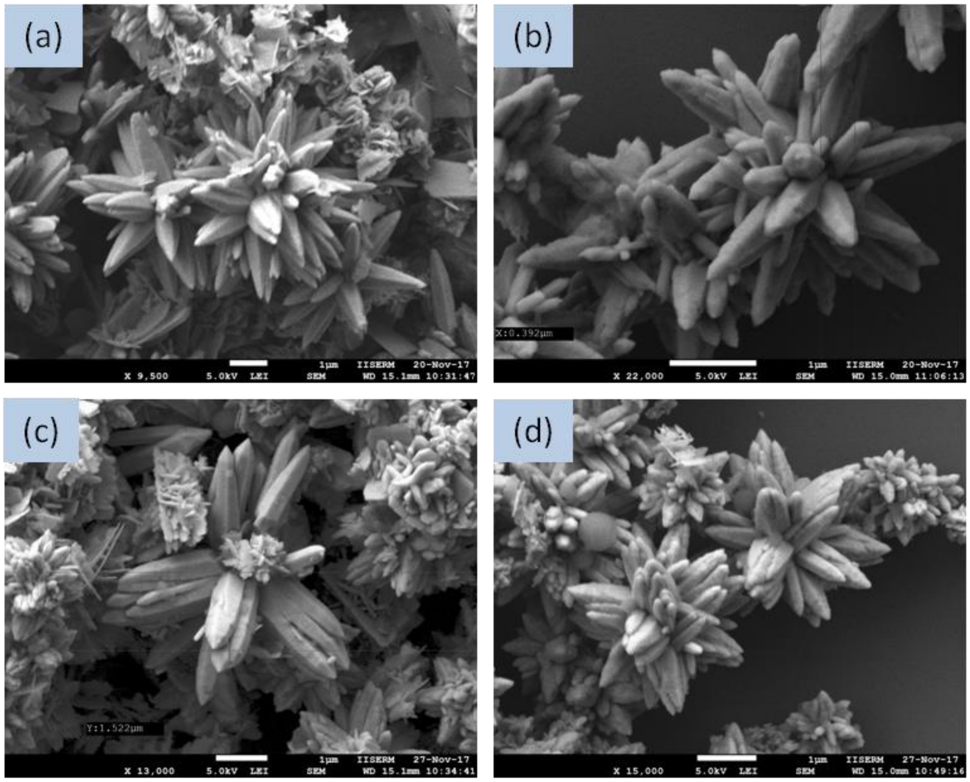

Figure 3.22. Nanorods fabricated at 120 °C for (a) 6 hours, (b) 12 hours, (c) 18 hours, (d) 24 hours.

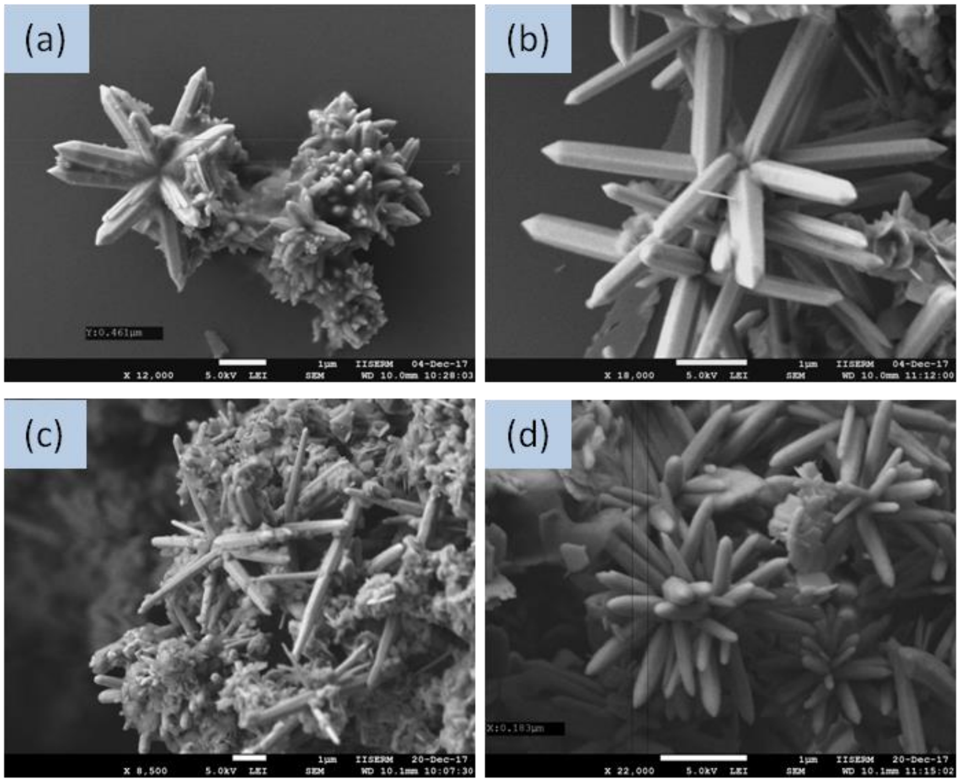

Figure 3.23. Nanorods fabricated at 150 ^{o}C for (a) 6 hours, (b) 12 hours, (c) 18 hours, (d) 24 hours.

Optical properties. UV-vis absorption spectra of the as grown ZnO nanorods at different temperatures in the wavelength range of 300-600 nm are shown in Figure 3.24. The spectra at different temperatures observed for different growth duration showed the absorption edge between 363-368 nm followed by a sharp decrease. The blue shift in the absorption spectra with respect to the bulk absorption edge at 376 nm is attributed to the effect of nanocrystalline size of the synthesized nanorods. A slight shift in the absorption edges has been observed for ZnO nanorods with different growth duration. There is a blue shift in the absorption spectra for the nanorods with lower diameters. Since rods with lower diameters were observed with longer growth time. Thus, the blue shift in the absorption edge increases slightly with increasing growth time. Furthermore, the rods with increasing growth time from 6 hours to 18 hours also showed an increase in the intensities of their absorption except the case of rods obtained with 24 hours. Since the rods with minimum aspect ratios has been obtained at the end of 24 hours; a minimum intensity has been observed in this case and the highest peak of excitonic absorption were observed for the nanorods with a growth time of 18 hours. The higher defect density of the nanorods on their surfaces resulted in different binding energies which explain the reason of the spectral shift in the nanorods. The band gap energies of the ZnO nanorods (**ZnO-15** to **ZnO-26**) were calculated using the following equation:

$$\alpha(h\nu)^{1/n} = B\left(h\nu - E_{gap}\right)$$

where α is the absorption coefficient, $h\nu$ is the photon energy, B is the band form parameter, E_{gap} is the optical band gap of the nanoparticles and n is an index whose value depends on the type of transition in the process of absorption. For direct transition in the semiconductor like ZnO, n = 1/2. The graphs were plotted between $\alpha h\nu^2$ vs $h\nu$ and the line was extrapolated to x-axis to obtain the values of band gap. The band gap energies obtained for **ZnO-15** to **ZnO-26** are given in Table 3.11.

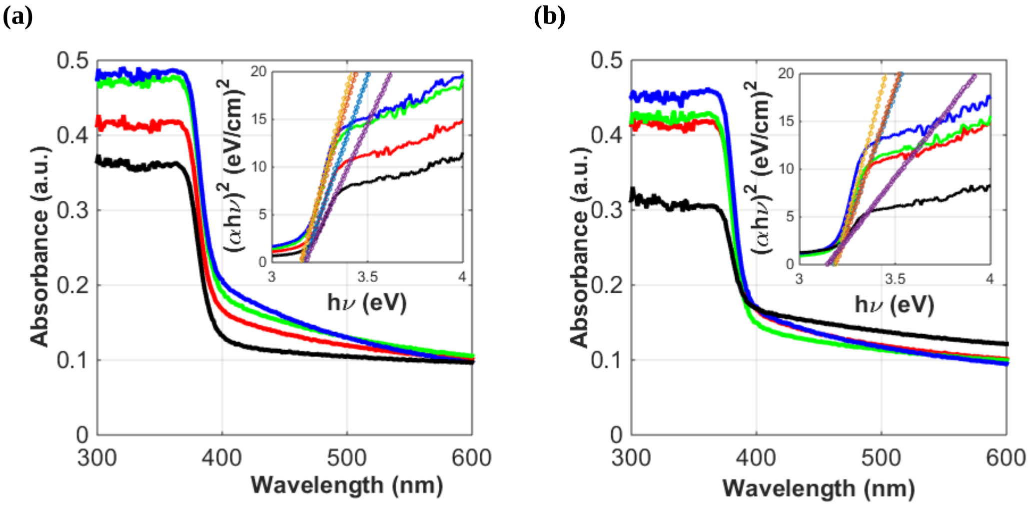

Figure 3.24. Solid state absorption spectra of (a**) ZnO-15 to ZnO-18** where red is for **ZnO-15**, green colour is for **ZnO-16,** blue colour represents **ZnO-17** and black colour represents **ZnO-18**, (b) **ZnO-19 to ZnO-22** where red is for **ZnO-19**, green colour is for **ZnO-20**, blue colour represents **ZnO-21** and black colour represents **ZnO-22** where (inset) plot is between $(\alpha h\nu)^2$ versus $(h\nu)$.

Table 3.11. Band gap values of as-grown ZnO nanorods

Sample	Band Gap (E_g) (eV)
ZnO-15	3.14
ZnO-16	3.15
ZnO-17	3.16
ZnO-18	3.17
ZnO-19	3.10
ZnO-20	3.15
ZnO-21	3.16
ZnO-22	3.17

Photoluminescence properties. The room temperature photoluminescence of the grown ZnO nanorods at different temperatures (120 ^{o}C and 150 ^{o}C) were carried out using xenon lamp as the source at an excitation wavelength of 350 nm. The spectra were recorded in the wavelength range of 380 to 600 nm. A broad emission band in the visible range of the spectra could be clearly observed for the as grown ZnO nanorods (Figure 3.25). The strong blue emission band within a range of 410-430 nm for the ZnO nanorods is mainly caused due to the defects resulted from the zinc interstitials, zinc vacancies and oxygen vacancies.[35-37,49] The electronic transition from either the Zn_i to valence band or from the bottom of conduction band to O_i level resulted in blue emission of these nanorods. With the increase of aspect ratios from 6 hours to 18 hours, a significant increase in the intensity of emission has also been observed in all the cases (**ZnO-15** to **ZnO-17**) at 120 ^{o}C. However, a decrease in the emission intensity has been observed for **ZnO-18** obtained with a growth time of 24 hours. A similar trend has been observed at 150 ^{o}C for different growth times. Thus, the nanorods with higher aspect ratios can show intense emission in the visible range ensuring the exploitation of these rods in the light emitting devices.

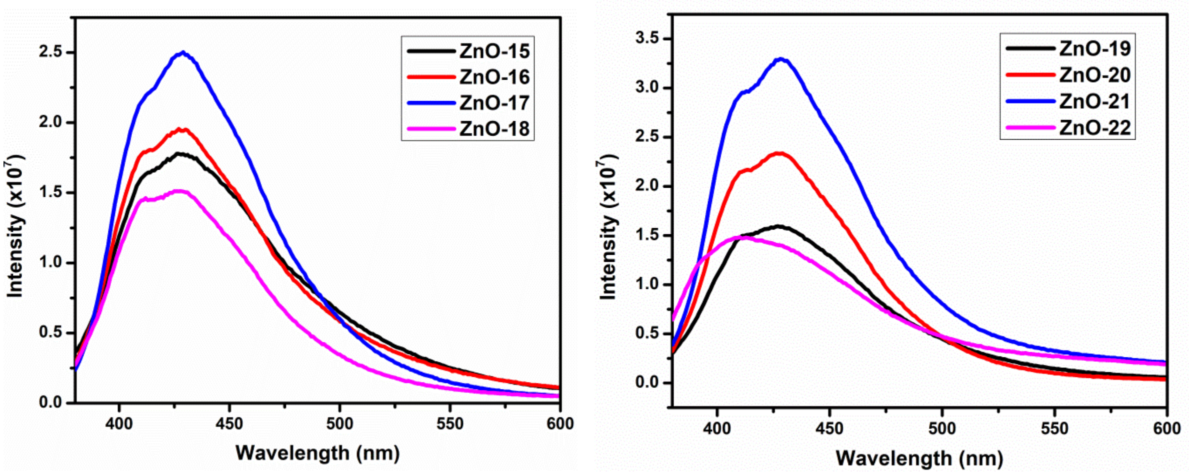

(a) (b)

Figure 3.25. Photoluminescence spectra of (a) **ZnO-15** to **ZnO-18**, (b) **ZnO-19** to **ZnO-22**.

3.1.2.3 Effect of time

ZnO nanostructures were prepared hydrothermally by utilizing Zn(II) coordination polymer $[Zn_2(bpma)_2(adc)_2]_n$ as the Zn^{2+} source and KOH as OH^- source (Scheme 3.10). The pH of the reaction mixture was maintained above 13 at 180 ^{o}C for different aging times (6 h, 12 h, 18 h, 24 h). The resulting morphology was nanorods in each case which were getting self-assembled via the oriented attachment to produce 3D flower-like nanostructures. The growth time have a profound influence on the aspect ratio of nanorods.[59-60] These nanorods were further annealed to produce nanorod arrays with low aspect ratios (Scheme 3.11).

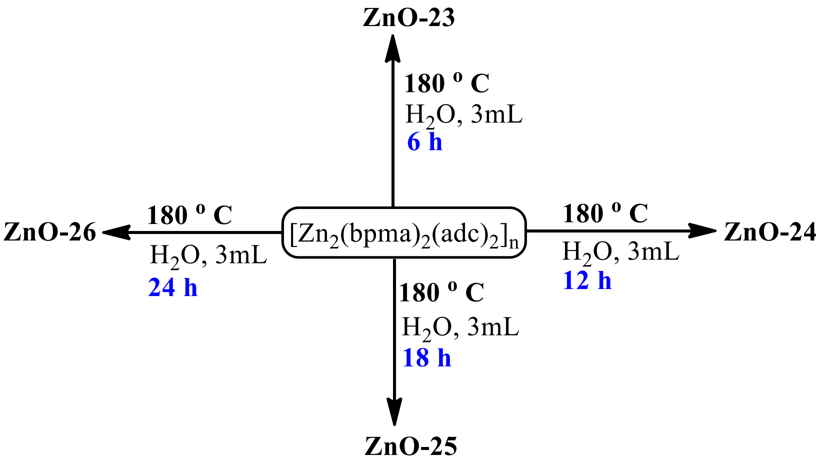

Scheme 3.10. Synthesis of **ZnO-23** to **ZnO-26** at 180 °C for different growth times.

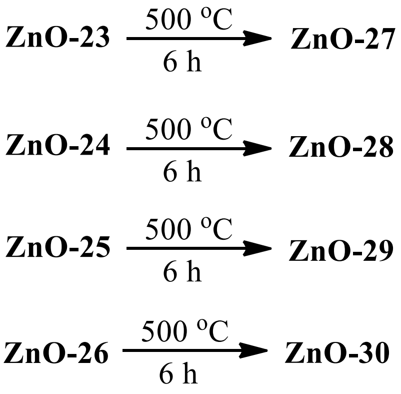

Scheme 3.11. Synthesis of **ZnO-27** to **ZnO-30** by post synthetic annealing of hydrothermally obtained ZnO nanorods.

The X-ray diffraction (XRD) data confirmed that the as-synthesized ZnO nanorods exhibited hexagonal wurtzite structure (JCPDS 06-2151). The narrow and highly intense peaks in the pattern confirm the high crystallinity of the nanorods. Figure 3.26 (a) shows the XRD patterns of the as-synthesized nanorods obtained at different times (6 h, 12 h, 18 h, 24 h) labelled as **ZnO-23**, **ZnO-24**, **ZnO-25** and **ZnO-26**. The XRD patterns of the nanorods obtained by post synthetic annealing (**ZnO-27** to **ZnO-30**) is shown in Figure 3.26 (b). These nanorod arrays were assembled to form 3D flower-like ZnO nanostructures. The lattice parameters for hexagonal ZnO nanoparticles were estimated from the equation:

$$\frac{1}{d^2} = \frac{4}{3(h^2 + hk + \frac{k^2}{a^2})} + \frac{l^2}{c^2}$$

where a and c are the lattice parameters and h, k and l are the Miller indices and $d_{h\ k\ l}$ is the interplanar spacing for the plane (h k l). This interplanar spacing for the plane (h k l) can be calculated from Bragg's law: 2d sin θ = nλ. The crystallite size was calculated using Debye's Scherrer Equation:

$$d\ (nm) = \frac{0.9\ \lambda}{\beta\ \cos\theta}$$

where d (nm) is the crystallite size, λ is the X-ray wavelength (Cu-kα = 0.154 nm), β is FWHM (full width at half maximum) and θ is in radians. All the data obtained is given in Table 3.12.

The compositional characterization of ZnO nanorods were performed by Energy dispersive X-ray analysis (EDX) to investigate the chemical stoichiometry of Zn and O in the nanorods. The strong Zn and O peaks in the EDX patterns could be clearly observed (Figure 3.27 to 3.42). No other characteristic peak for any impurity was found which verified the purity of the as-synthesized ZnO nanorods. Whereas, the peak at 0.2 keV is of carbon (C) which is due to the carbon tape used for the sample preparation and a peak at 3.2 keV is of gold (Au) observed due to the gold coating of the samples. The average atomic ratio for the as-synthesized ZnO nanorods at different times (6 h, 12 h, 18 h, 24 h) was found to be ~ 1:1.

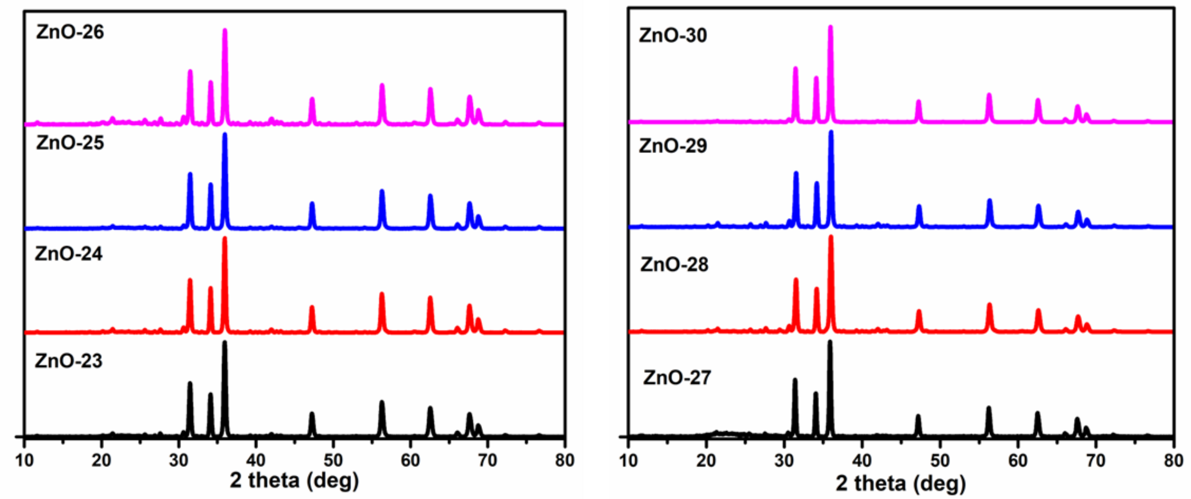

(a) (b)

Figure 3.26. PXRD patterns of (a) **ZnO-23** to **ZnO-26**, (b) **ZnO-27** to **ZnO-30**.

Table 3.12. Lattice parameters for ZnO samples (**ZnO-23** to **ZnO-30**)

Sample	**h k l**	**2θ values (degrees)**	**Lattice constants a, b, c (Å)**	**Volume of unit cell (Å ^{3})**	**Atomic packing fraction**	**d spacing (Å)**	**FWHM**
ZnO-23	(100)	31.4586	a = 3.28 = b,	49.34	0.755	2.84	0.306
	(002)	34.1174	c = 5.26			2.63	
	(101)	35.9500				2.50	
ZnO-24	(100)	31.4674	a = 3.28 = b,	49.31	0.755	2.84	0.294
	(002)	34.1204	c = 5.26			2.63	
	(101)	35.9504				2.50	
ZnO-25	(100)	31.4726	a = 3.28 = b,	49.26	0.755	2.84	0.306
	(002)	34.1403	c = 5.26			2.63	
	(101)	35.9714				2.50	
ZnO-26	(100)	31.4844	a = 3.28 = b,	49.22	0.755	2.84	0.321
	(002)	34.1479	c = 5.26			2.63	
	(101)	35.9682				2.50	
ZnO-27	(100)	31.4559	a = 3.28 = b,	49.35	0.755	2.84	0.300
	(002)	34.1170	c = 5.26			2.63	
	(101)	35.9535				2.50	
ZnO-28	(100)	31.4662	a = 3.28 = b,	49.30	0.755	2.84	0.286
	(002)	34.1267	c = 5.26			2.63	
	(101)	35.9514				2.50	
ZnO-29	(100)	31.4737	a = 3.28 = b,	49.26	0.755	2.84	0.299
	(002)	34.1399	c = 5.26			2.63	
	(101)	35.9644				2.50	
ZnO-30	(100)	31.4881	a = 3.28 = b,	49.21	0.755	2.84	0.312
	(002)	34.1459	c = 5.26			2.63	
	(101)	35.9778				2.50	

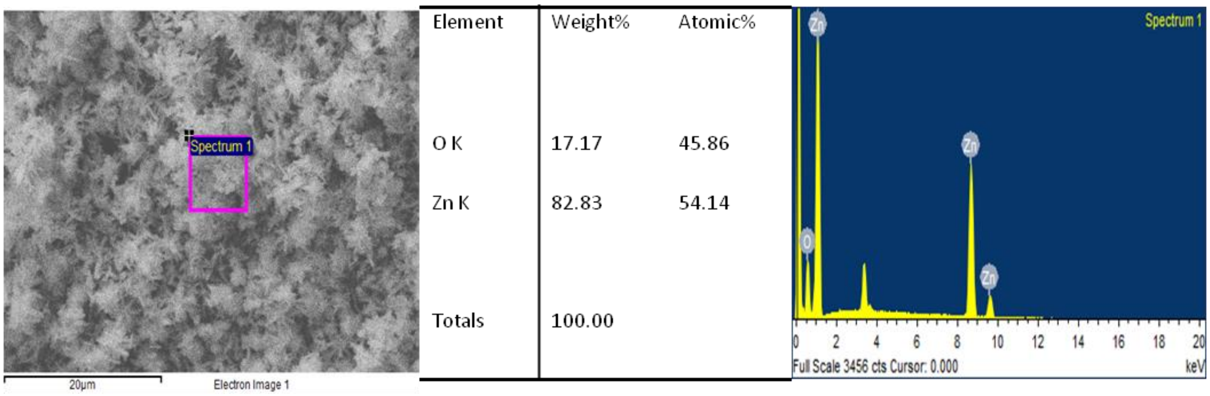

Element	Weight%	Atomic%
O K	17.17	45.86
Zn K	82.83	54.14
Totals	100.00	

Figure 3.27. EDX spectrum of **ZnO-23**.

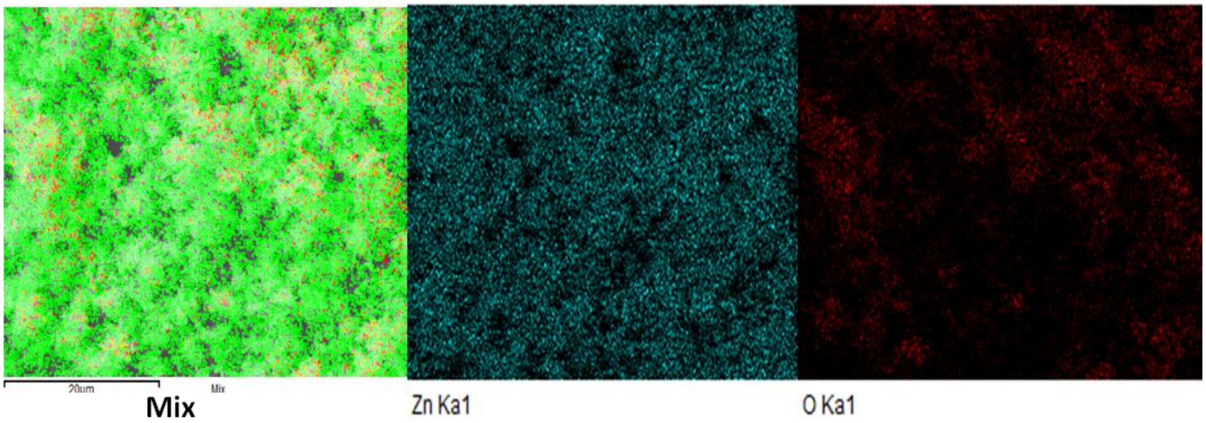

Figure 3.28. Elemental mapping of **ZnO-23**.

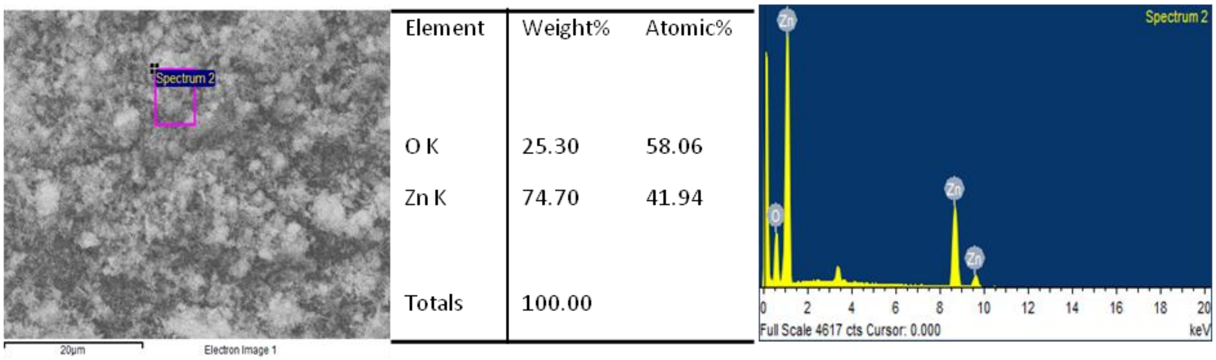

Element	Weight%	Atomic%
O K	25.30	58.06
Zn K	74.70	41.94
Totals	100.00	

Figure 3.29. EDX spectrum of **ZnO-24**.

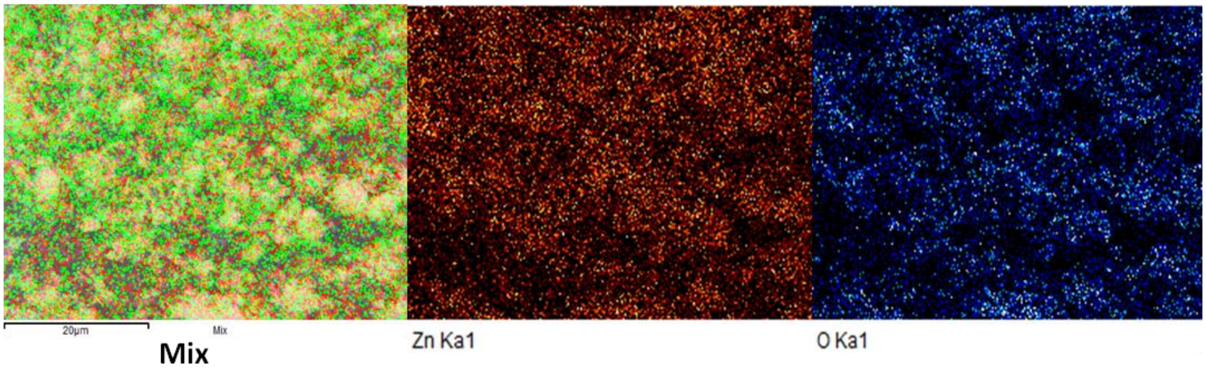

Figure 3.30. Elemental mapping of **ZnO-24**.

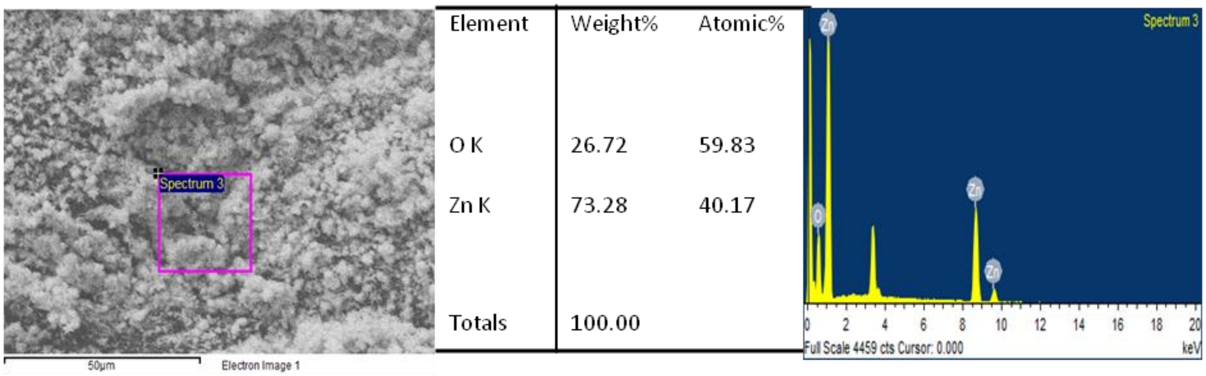

Element	Weight%	Atomic%
O K	26.72	59.83
Zn K	73.28	40.17
Totals	100.00	

Figure 3.31. EDX spectrum of **ZnO-25**.

Figure 3.32. Elemental mapping of **ZnO-25**.

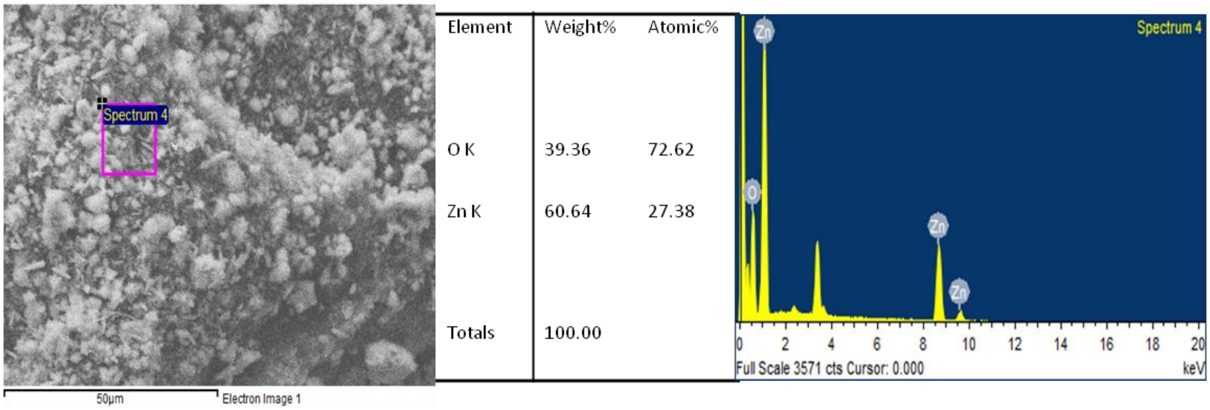

Element	Weight%	Atomic%
O K	39.36	72.62
Zn K	60.64	27.38
Totals	100.00	

Figure 3.33. EDX spectrum of **ZnO-26**.

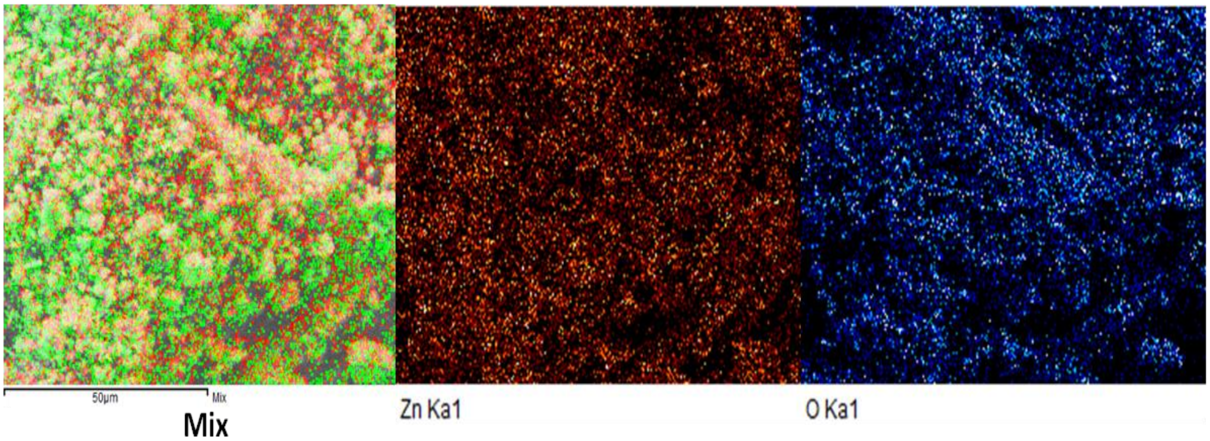

Figure 3.34. Elemental mapping of **ZnO-26**.

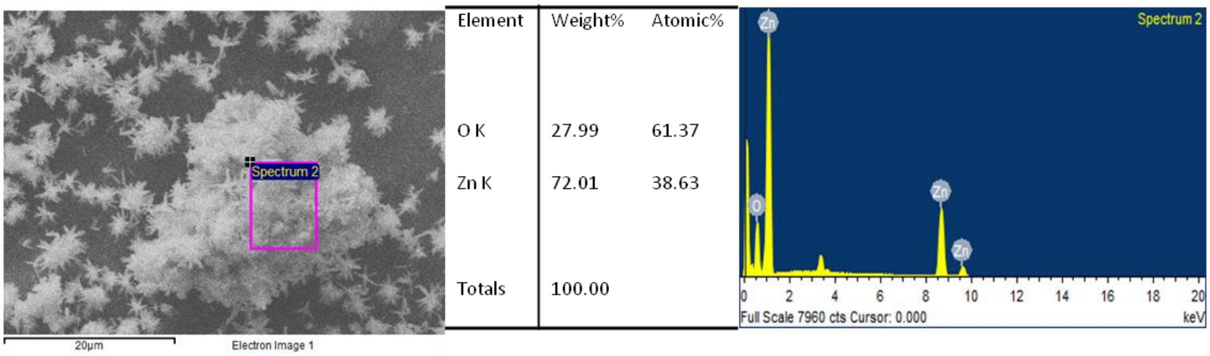

Element	Weight%	Atomic%
O K	27.99	61.37
Zn K	72.01	38.63
Totals	100.00	

Figure 3.35. EDX spectrum of **ZnO-27**.

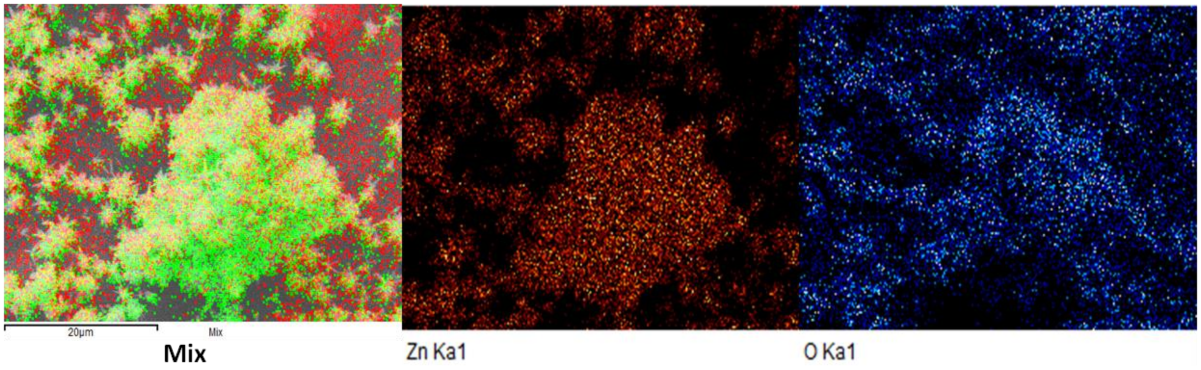

Figure 3.36. Elemental mapping of **ZnO-27**.

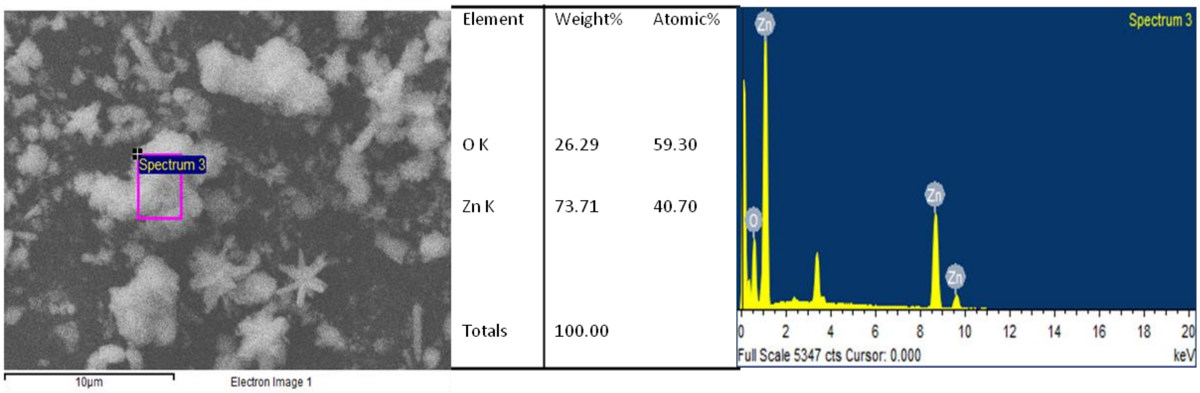

Element	Weight%	Atomic%
O K	26.29	59.30
Zn K	73.71	40.70
Totals	100.00	

Figure 3.37. EDX spectrum of **ZnO-28**.

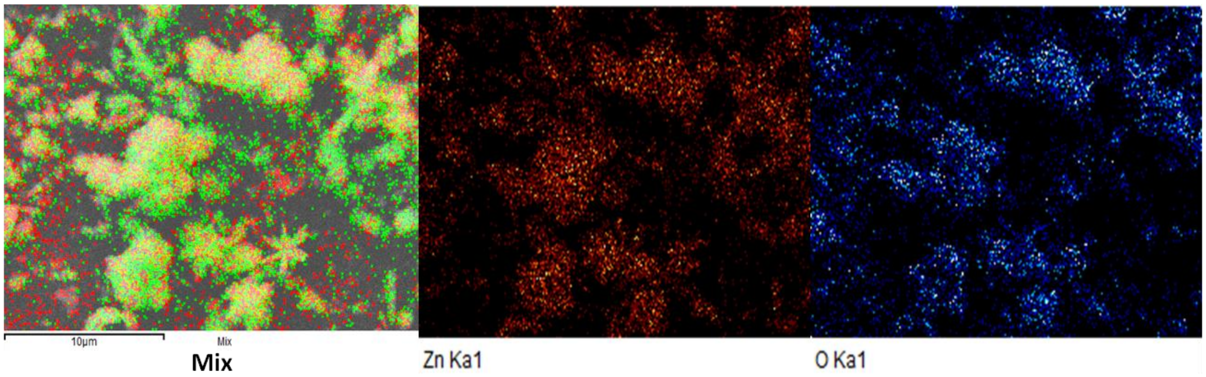

Figure 3.38. Elemental mapping of **ZnO-28**.

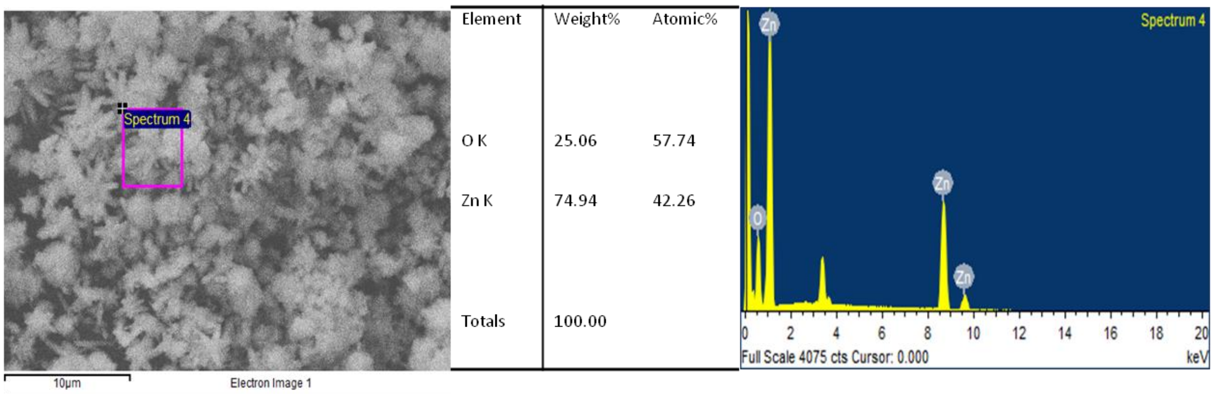

Element	Weight%	Atomic%
O K	25.06	57.74
Zn K	74.94	42.26
Totals	100.00	

Figure 3.39. EDX spectrum of **ZnO-29**.

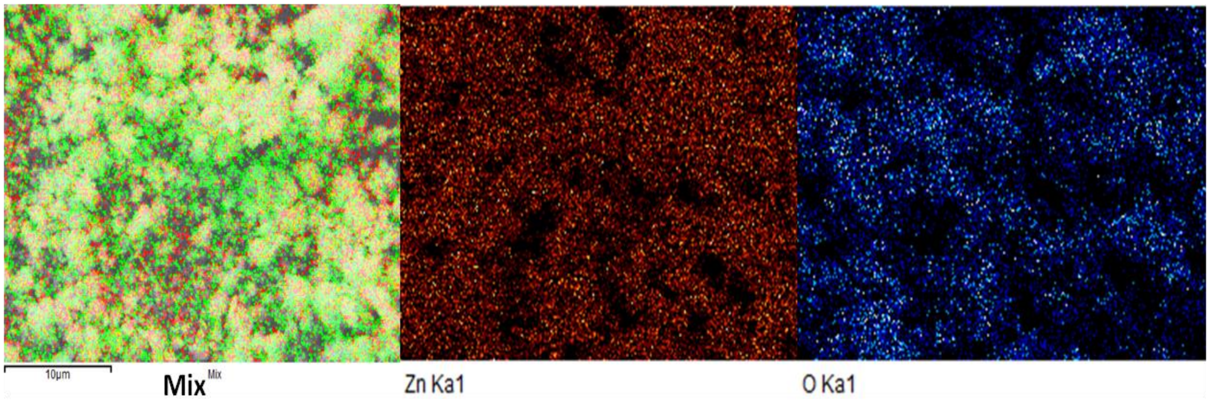

Figure 3.40. Elemental mapping of **ZnO-29**.

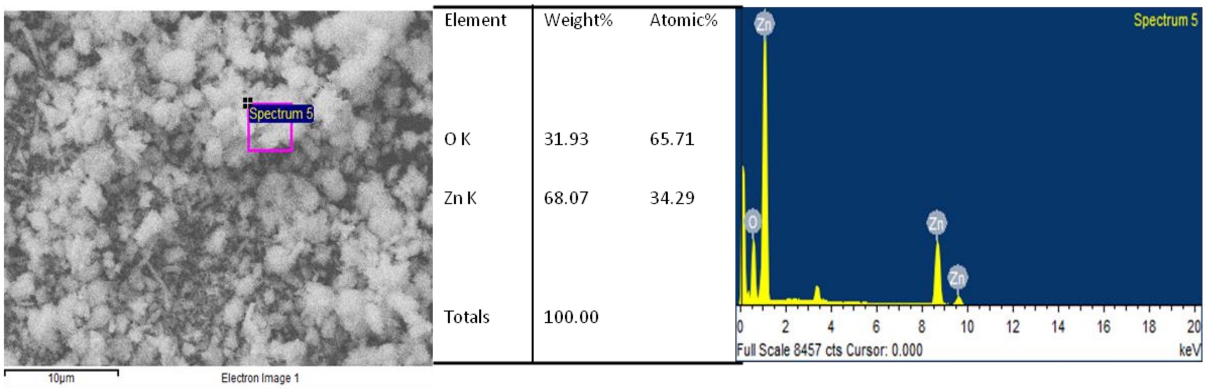

Element	Weight%	Atomic%
O K	31.93	65.71
Zn K	68.07	34.29
Totals	100.00	

Figure 3.41. EDX spectrum of **ZnO-30**.

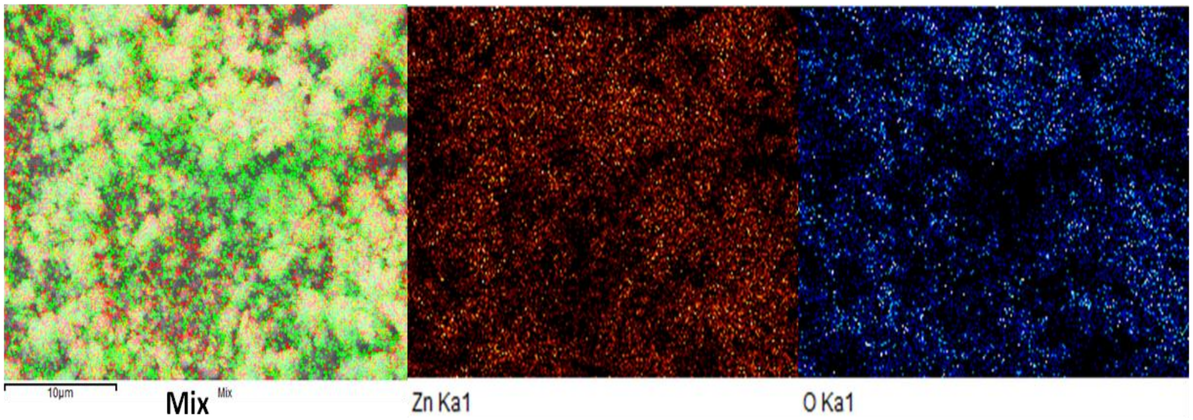

Figure 3.42. Elemental mapping of **ZnO-30**.

Figure 3.43 shows the FESEM images of the ZnO nanorods obtained at different aging times (6 h, 12 h, 18 h, 24 h). It had been observed that with the progress of time the morphology was more or less similar but an increase in the aspect ratios (length/width of rods) was observed (Table 3.13). The average aspect ratio of **ZnO-23** was found to be 4.27 with a length of 1.41 μm and a diameter of 0.33 μm. As the synthesis time was increased to 12 hours (**ZnO-24**), a very little increase in the aspect ratio A.R ~ 4.41 was achieved. Whereas after 18 hours of aging (**ZnO-25**) an aspect ratio of 4.76 for nanorods was observed (length ~ 1.81 μm and diameter ~ 0.38 nm). Furthermore, the nanorods synthesized after 24 hours of retention time (**ZnO-26**) are thinner with an aspect ratio of 4.94 (length ~ 1.93 μm and diameter ~ 0.39 μm). The nanorod arrays share common crystallographic faces which get interweaved together to form 3D flowers in order to reduce the overall surface area by minimizing the surface energy for achieving thermodynamic stability.[61] An increase in the length of the nanorods with the increased growth duration can be attributed to the crystal growth habits of wurtzite ZnO which grows rapidly along the [0001] plane. The length of the nanorods can be controlled by the growth time. A longer growth duration results in a longer rod. The adjacent rods unite together to form nanorods with larger diameters. The duration of the initial nucleation process for the nanorod growth is quite long followed by the crystal growth at a faster rate which continues to grow until it reaches the maximum rod length. No further increase in the growth rate is observed once the Zn^{2+} ions in the reaction mixture get consumed. This results in no change in diameter with the further growth time resulting in the attachment of the neighboring single rods to increase the density and overall diameter of the as obtained nanorod arrays. Now, when the as-synthesized ZnO nanostructures were further annealed at 500 ^{o}C for 6 hours, a decrease in the length along with a growth in the diameter was observed for nanorods (**ZnO-26** to **ZnO-30**)

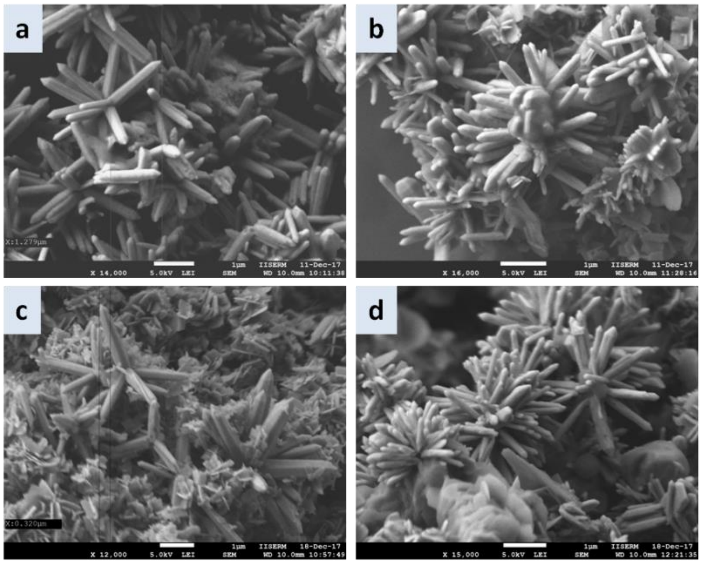

Figure 3.43. ZnO nanorods obtained at different aging times (a) 6 hours (**ZnO-23**) (b) 12 hours (**ZnO-24**) (c) 18 hours (**ZnO-25**) (d) 24 hours (**ZnO-26**).

leading to an overall decrease in the aspect ratios (Figure 3.44). From Table 3.13 it can be clearly observed that the post synthetic annealing results in an increase in the average diameter of the rods. At higher temperature of 500 ^{o}C, the lattice atoms become mobile and start vibrating in order to reduce the strain energy by exchanging the energy with the neighboring atoms. At this stage, the atoms have sufficient energy to diffuse to produce small seeds (i.e. the rods with shorter length) with lowest strain energy.

Table 3.13. Aspect ratios of ZnO nanorods (**ZnO-23** to **ZnO-30**)

Sample	Length (μm)	Diameter (μm)	Aspect Ratio
ZnO-23	1.41	0.33	4.27
ZnO-24	1.50	0.34	4.41
ZnO-25	1.81	0.38	4.76
ZnO-26	1.93	0.39	4.94
ZnO-27	1.35	0.34	3.97
ZnO-28	1.06	0.29	3.65
ZnO-29	1.75	0.46	3.80
ZnO-30	1.80	0.40	4.50

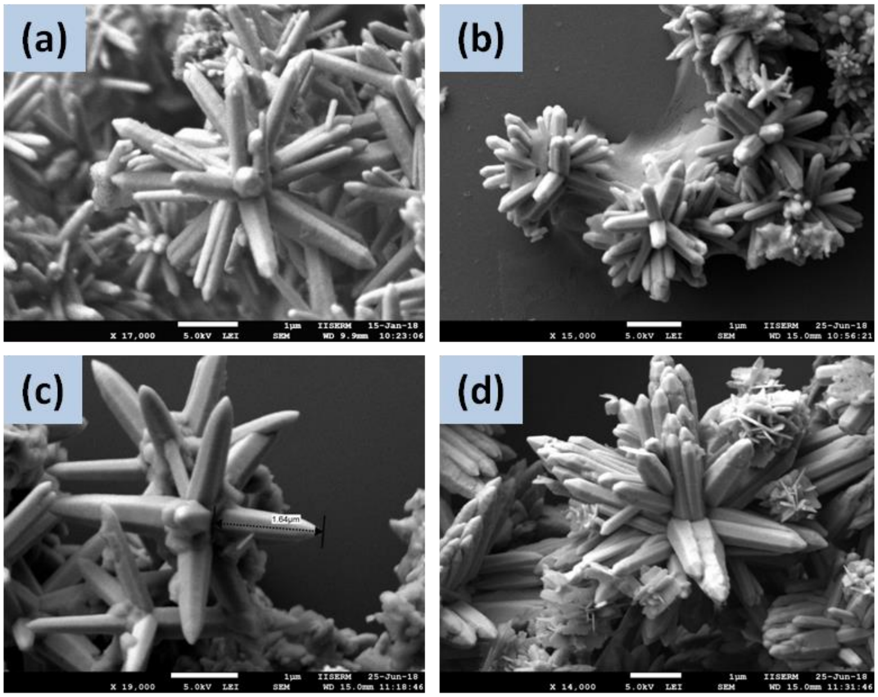

Figure 3.44. ZnO nanorods obtained after post synthetic annealing at 500 ^{o}C (a) **ZnO-27** (b) **ZnO-28** (c) **ZnO-29** (d) **ZnO-30**.

Growth mechanism for the formation of ZnO nanoflowers

The mechanism of formation of 3D flower like structures can be understood as the result of anisotropic growth under the effects of basic conditions in hydrothermal process (Figure 3.45). During the hydrothermal approach, the Zinc ion precursor first get decomposed to generate Zn^{2+} ions followed by the reaction with OH- ions to form $Zn(OH)_2$ (equation 1). This $Zn(OH)_2$ further reacts with OH- to give $[Zn(OH)_4]^{2-}$ according to equation 2. The $[Zn(OH)_4]^{2-}$ acts as the tetrahedral growth unit (where Zn^{2+} is bonded with four OH^- ions) which serves as the new growth precursor for the production of wurtzite ZnO crystal.[56-58] On the other hand, ZnO nuclei obtained from the equation 3 serves as the seed for the anisotropic growth of ZnO. ZnO crystals grow anisotropically at the active site of ZnO seed (Scheme 3.11). Owing to high concentrations in highly basic conditions at pH=13, OH^- ions gets attracted by the positively charged Zn-terminated surface. This promotes the Zn-bond in the atomic structure due to the formation of strong Zn-O bond facilitating the growth direction along [0001] direction due to lower surface energy.[62] Also, when the concentration of OH^- ions is more than Zn^{2+} ions, the OH^- ions acts as a caping agent leading to the formation of ZnO nanorods with tapered ends which get interweaved together under the self-assembly process generating the flower like structures (Figure 3.45). These nanoflowers were attracted against the sides of grooves due to the polarity of the surfaces of the ZnO nanorods.

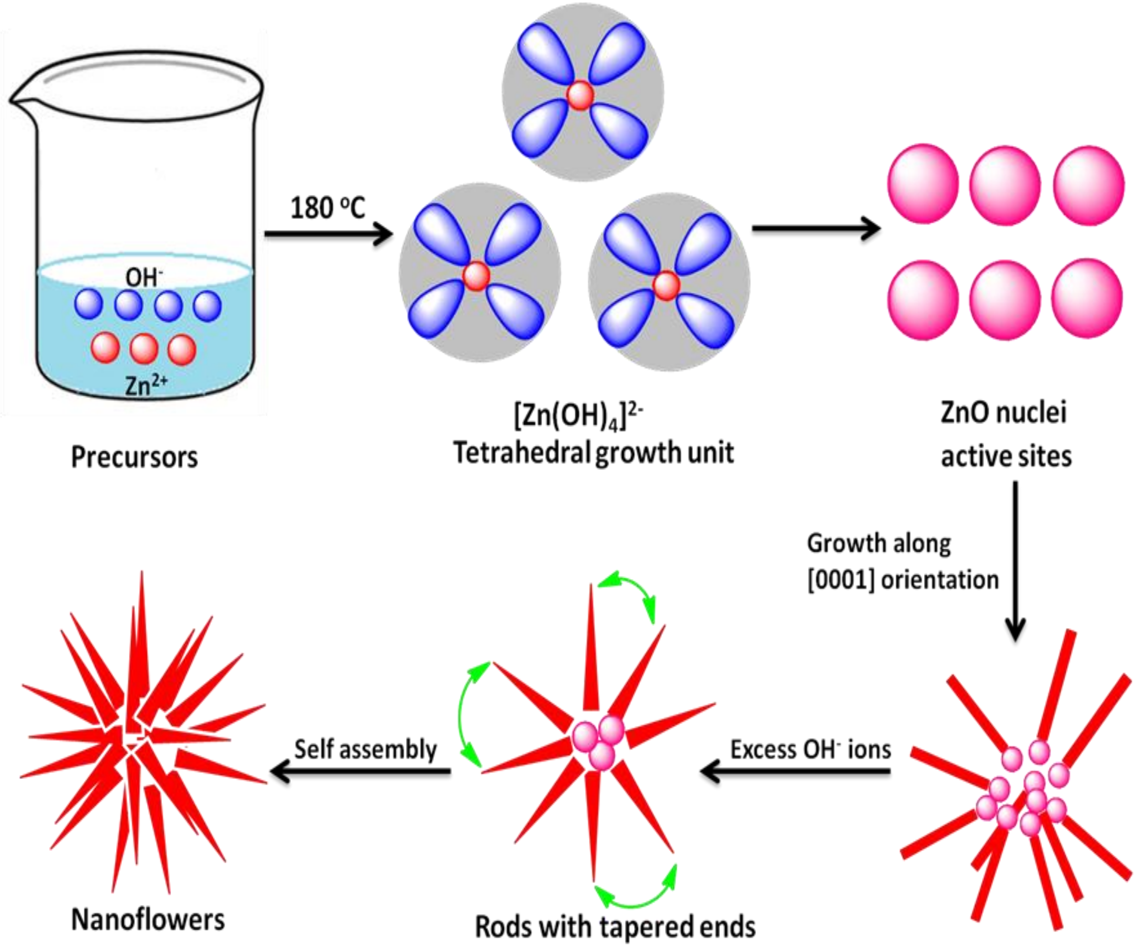

Figure 3.45. Mechanism of evolution of nanoflowers assembled by nanorod arrays.

With the increase in heating time from 6 hours to 24 hours, ZnO nanorods will be decomposed into Zinc ions in solution which starts transferring directly to the polar Zn-terminated [0001] planes resulting in an increase in the length and aspect ratio. The increase of the growth time not only boosts the length of the nanorods but also results in the joining of adjacent rods to form nanorods with larger diameters and thereby increasing the density of nanorods.[63-65]

$$Zn^{2+} + 2OH^- \longrightarrow Zn(OH)_2 \quad (1)$$

$$Zn(OH)_2 + 2OH^- \longrightarrow Zn(OH)_4^{2-} \quad (2)$$

$$Zn(OH)_4^{2-} \longrightarrow ZnO + H_2O + 2OH^- \quad (3)$$

UV-vis absorption and optical energy band gap

UV-vis absorption spectroscopy was performed on the as-synthesized ZnO nanostructures to investigate the optical properties by measuring the band-edge absorption of these samples. Figure 3.46 indicates that all ZnO nanostructures with a variation in the growth time (i.e. 6, 12, 18 and 24 hours) showed the maximum absorption at around 370 nm wavelength which is in close agreement to that of bulk ZnO. These results confirm high optical activity and strong exciton binding energy of the ZnO nanostructures. For direct band gap semiconductor, the energy band gap was calculated using Kulbenka Munk equation[66] which can be determined from Tauc plot (Figure 3.46) by plotting $(\alpha h\nu)^2$ vs hν(eV), where α is the absorption coefficient, ν is the frequency, and h is Planck's constant. The intersection of the line extrapolation and the x-axis gives the energy band gap values. The values obtained are given in Table 3.14.

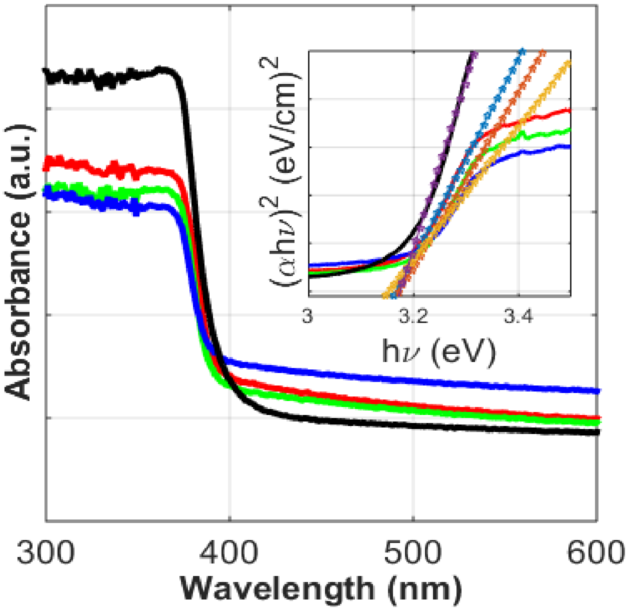

Figure 3.46. Solid state absorption spectra of **ZnO-23** and **ZnO-26** where red is for **ZnO-23**, green colour is for **ZnO-24**, blue colour represents **ZnO-25** and black colour represents **ZnO-26** where (inset) plot is between $(\alpha h\nu)^2$ versus (hν).

Table 3.14. Band gap values of as-grown ZnO nanostructures (**ZnO-23** to **ZnO-26**)

Sample	**Band Gap (E_g) (eV)**
ZnO-23	3.19
ZnO-24	3.18
ZnO-25	3.20
ZnO-26	3.19

Photocatalytic Activity

The photocatalytic degradation efficiency of the cationic and anionic dye (Methylene Blue and Congo Red) was tested by **ZnO-23** under UV light illumination for different time intervals (30, 60, 90, 120 and 180 minutes). Figure 3.47 shows the comparison of photodegradation efficiencies and rate constants for the **ZnO-23** among the two dyes indicating that the anionic dye Congo Red (CR) dye shows the maximum degradation efficiency which is 86% in the first 30 minutes whereas the cationic dye Methylene Blue (MB) showed an efficiency of only 36% after an interval of 30 minutes. CR showed an efficiency of 98% and MB showed an efficiency of 67% after 180 minutes of irradiation. Since **ZnO-23** showed better catalytic activity for anionic dye CR, different pH solutions were prepared ranging from 6 to 12 and the degradation efficiency of **ZnO-23** on the CR dye was studied. The degradation was avoided for the pH solutions less than 6 in order to avoid the aggregation of dye in highly acidic medium. The results of the experiments indicated that pH of the reaction mixture have a profound influence on the efficiency of the dye. The CR exhibits the maximum absorption band at 497 nm which is the characteristic feature of anionic monomer whereas the absorption at 347 nm is attributed to the naphthalene rings. A slight shift in the maxima absorption band from 495 nm to 498 nm was observed for pH range 6 to 12. The intensity of strong absorption decreases gradually with time during the process of photodegradation resulting in the breaking of the conjugated π–structure through oxidative decomposition. As the pH value increases from 6 to 7, a gradual decrease in the rate of degradation was observed from 3.107×10^{-2} min^{-1} to 3.034×10^{-2} min^{-1} followed by an abrupt increase at pH = 8 (9.028×10^{-2} min^{-1}). A sharp decrease in the degradation was further observed at pH = 9 (3.095×10^{-2} min^{-1}) which continued to decrease at pH = 10 (2.677×10^{-2} min^{-1}) and pH = 11 (0.811×10^{-2} min^{-1}) till pH = 12 (0.385×10^{-2} min^{-1}).

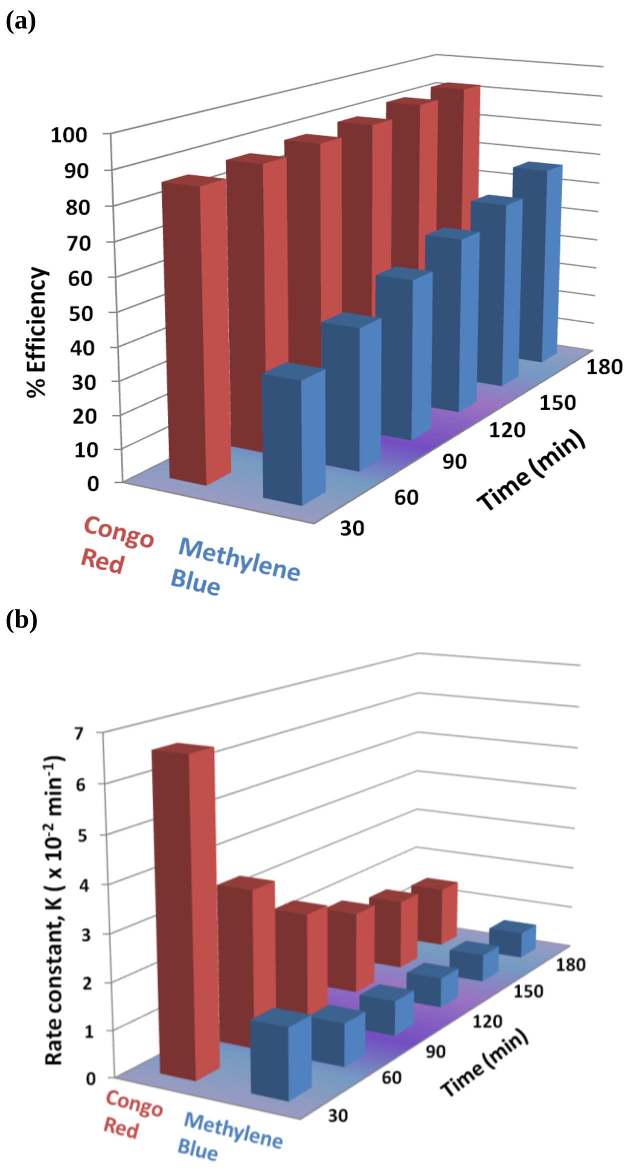

Figure 3.47. (a) Comparison of percentage efficiencies of cationic dye Methylene Blue and anionic dye Congo Red on **ZnO-23** (b) Comparison of rate constants of cationic dye Methylene Blue and anionic dye Congo Red on **ZnO-23**.

All the rates of degradation were recorded after an interval of 30 minutes (Figure 3.48).

In general, the activity of ions (e.g. H^+ or pH) determines the potential of the surface charge on the photocatalyst. The surface of photocatalyst has the tendency to become either positively charged or negatively charged as a function of pH. At a certain pH, the surface acquires zero net charge (pH_{zpc}), a critical value to determine the sign and magnitude of the net charge carried by the photocatalyst during the course of photodegradation. The zero-point charge pH_{zpc} for ZnO has found to be 9. So, the surface becomes positively charged for the pH values lower than pH_{zpc} of ZnO according to the equation **4**. Whereas, for the pH values higher than pH_{zpc}, the ZnO surface becomes negatively charged according to equation **5**.[67-68]

$$pH < pH_{zpc} \qquad \text{Zn-OH} + H^+ \longrightarrow ZnOH_2^+ \qquad \textbf{(4)}$$

$$pH > pH_{zpc} \qquad \text{Zn-OH} + OH^- \longrightarrow ZnO^- + H_2O \qquad \textbf{(5)}$$

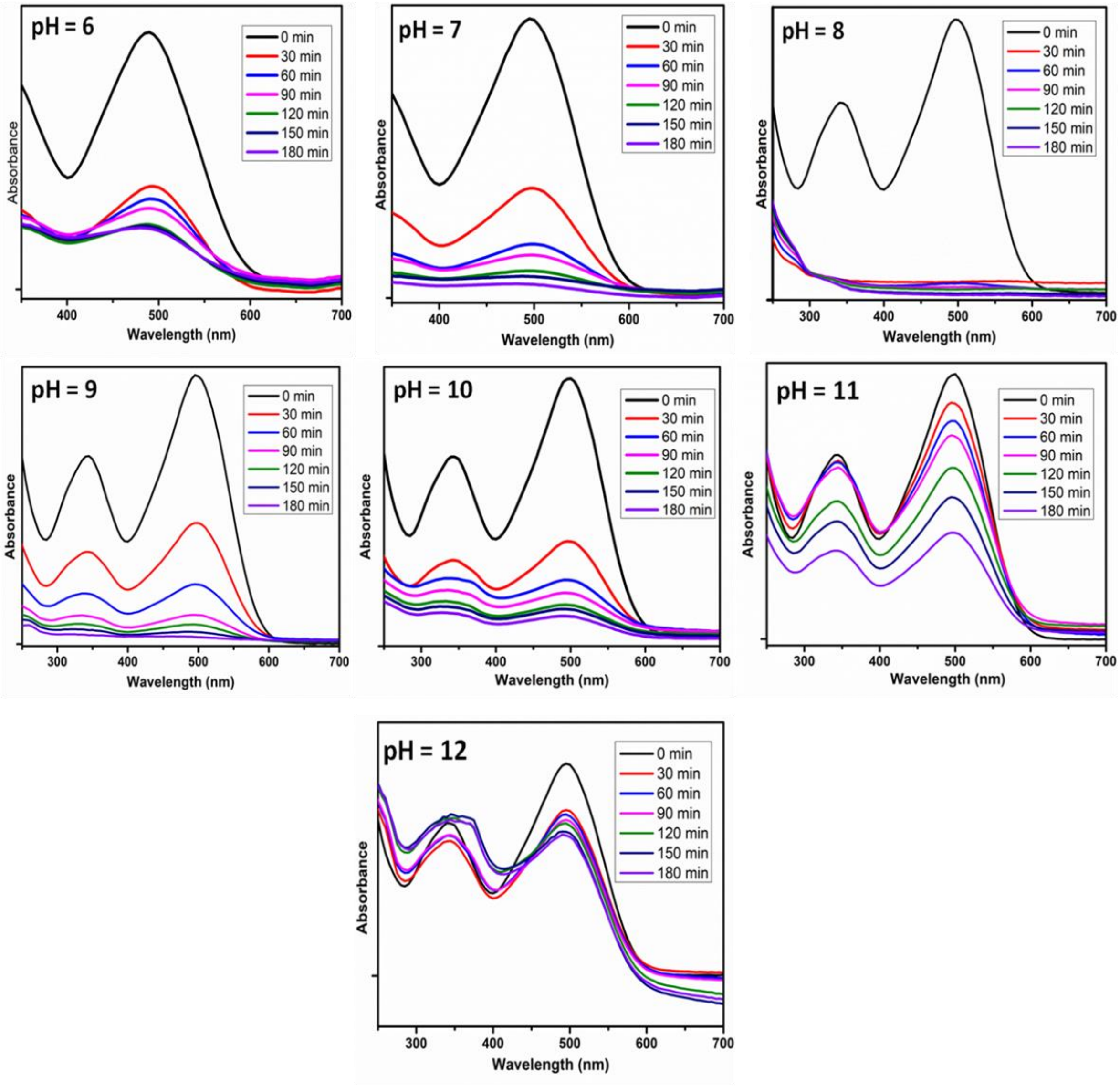

Figure 3.48. Comparison of photodegradation of Congo Red by **ZnO-23** at different pH conditions.

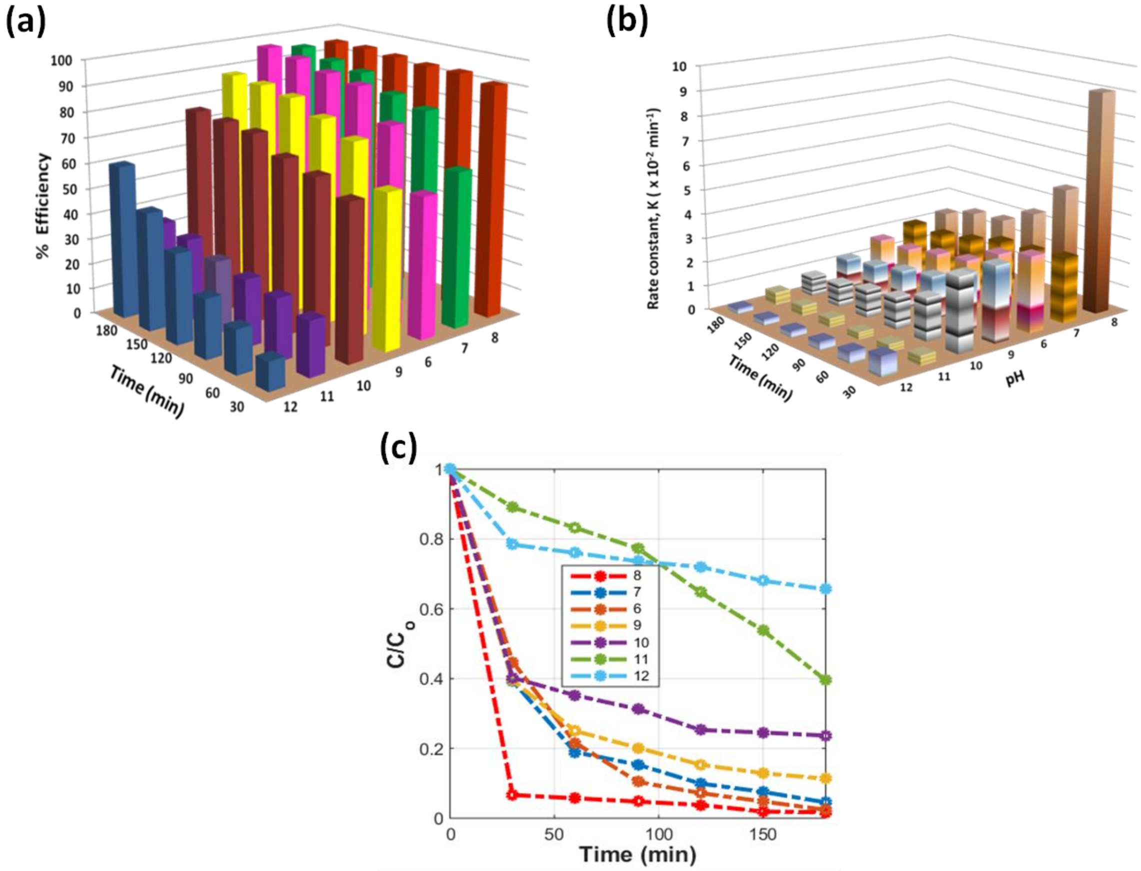

Figure 3.49. (a) Comparison of photodegradation efficiencies of Congo Red by **ZnO-23** at different pH, (b) comparison of rate constants of Congo Red by **ZnO-23** at different pH and (c) Kinetics of photodegradation of Congo Red by **ZnO-23** at different pH.

Because of the anionic nature of the CR dye, the adsorption on its surface occurs via the electrostatic interactions between the positive ZnO surface and CR anions at pH less than pH_{zpc} leading to a maximum extent at pH = 6 followed by a decrease at pH = 7 (Figure 3.49). This decrease in trend can be attributed to decrease in the active centers on the photocatalyst surface leading to a decrease in the absorption of light quanta by the catalyst resulting in the reduction of rate of degradation. Ease of availability of oxidative species i.e. hydroxyl radicals and holes during the photodegradation process is one of the major factors influencing the activity of ZnO along with the stability of ZnO surface in the selected pH range. The adsorption of CR anions on ZnO surface is maximum at pH = 6 thus the interaction with the light quanta is minimal thereby the generation of hydroxyl radicals is less resulting in the decrease of rate of degradation. Though the efficient trapping of the photogenerated holes by the hydroxyl groups facilitates the production of hydroxyl radicals in highly basic conditions (equation 6) but due to self-induced corrosion (equation 7), there occurs a loss of Zn^{2+} ions consequently leading to a decrease in its photocatalytic activity. The above results explain the reason of hindering of the rate of degradation in highly basic conditions. Thus, photocatalytic degradation process is not only determined by the concentration of hydroxyl radicals but also by the stability and surface charge on ZnO at different pH conditions.

$$OH^- + h^+ \longrightarrow OH^{\cdot} \qquad \textbf{(6)}$$

$$ZnO + 2h^+ \longrightarrow Zn^{2+} + 1/2\ O_2 \qquad \textbf{(7)}$$

Large surface area and high photocatalytic activity of (0001) surface results in greater photodegradation of CR dye by ZnO nanorods. The nanorods with high aspect ratios showed better photocatalytic activity compared with the rods of low aspect ratios. Further, the crystalline phase and the exposed facets of ZnO nanostructures remained unchanged with post-synthetic annealing of the above nanostructures but a decrease in the aspect ratios had been achieved.

When the annealed samples were tested for CR degradation, a sharp decrease in their activities were observed at pH = 8 (Figure 3.50). This could be attributed to be arising from the drop in the aspect ratios and surface defects on annealing. In general, the photocatalytic ability primarily depends on the separation of e^-/h^+ pairs and the separation of these charge carriers is highly dependent on the intrinsic electronic structure of facets, crystalline phase, aspect ratio and defects. The aspect ratio, defects and exposed facets in the semiconductors are believed to improve the separation of photogenerated charge carriers. Thus, the high aspect ratio nanorods with relatively more surface defects decrease the recombination of these charge carriers thereby decreasing the number of interparticle junctions expediting the electron delocalization resulting in higher efficiency and greater rate constant (Figure 3.51). Hence, it can be concluded that obtaining nanorods with high aspect ratios becomes essential in order to obtain a better photocatalytic activity against the degradation of dyes.

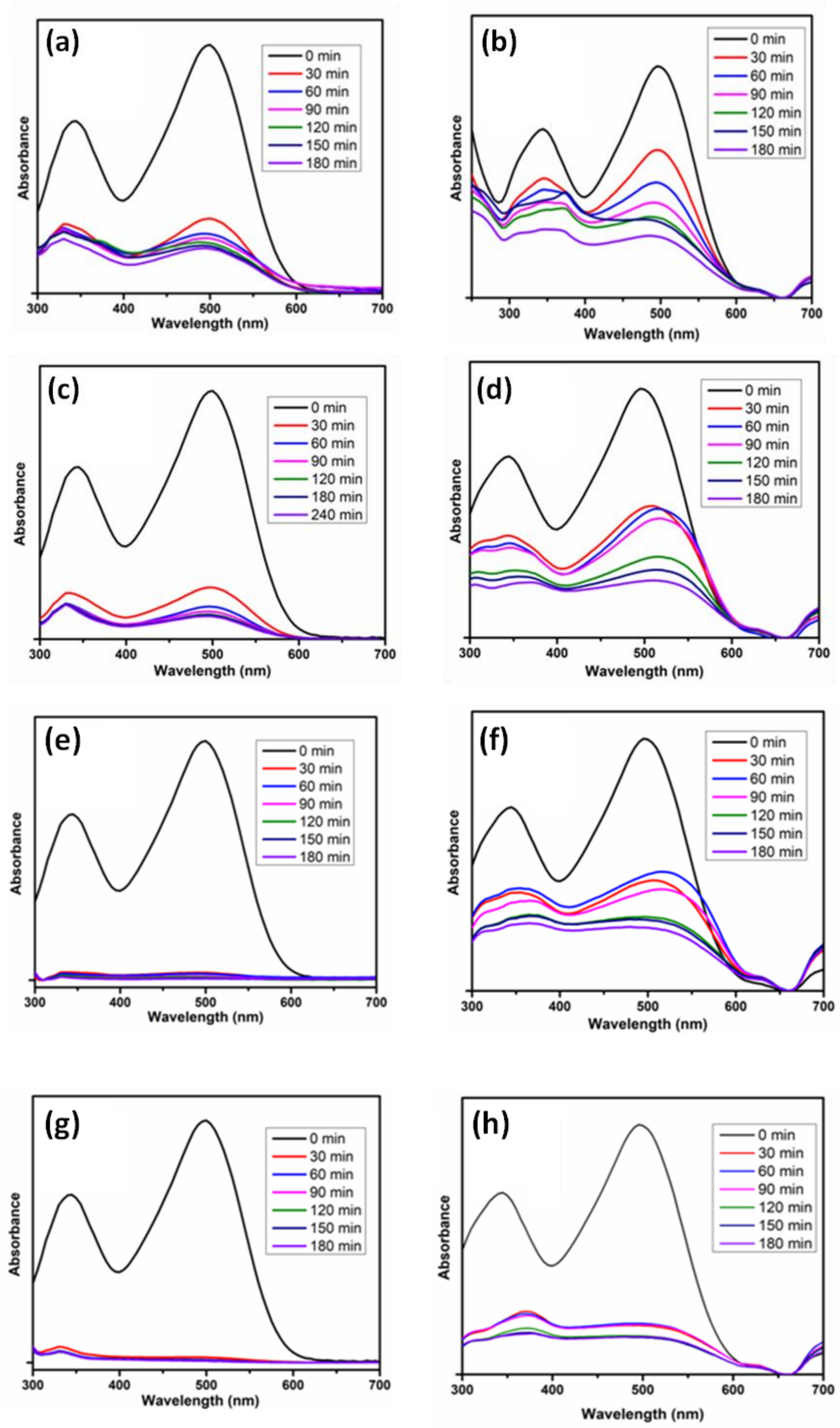

Figure 3.50. Comparison of photodegradation of Congo Red by ZnO nanorod arrays with high aspect ratios and their annealed samples with low aspect ratios (a) **ZnO-23**, (b) **ZnO-27**, (c) **ZnO-24**, (d) **ZnO-28**, (e) **ZnO-25**, (f) **ZnO-29**, (g) **ZnO-26** and (h) **ZnO-30**.

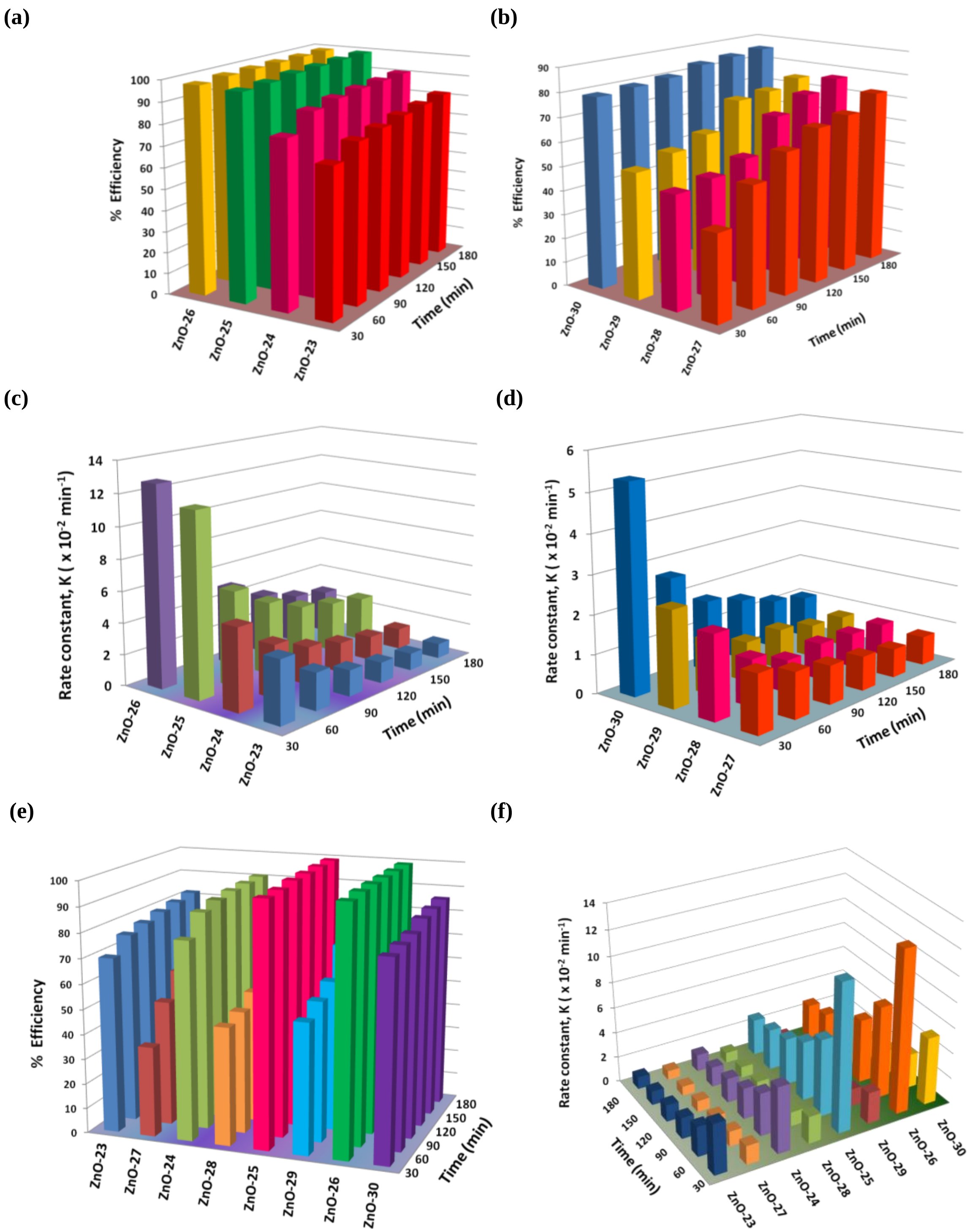

Figure 3.51. (a) Comparison of photodegradation efficiencies of Congo Red by (a) **ZnO-23** to **ZnO-26** and (b) **ZnO-27** to **ZnO-30**, (c) Comparison of rate constants of Congo Red by **ZnO-23** to **ZnO-26** and (d) **ZnO-27** to **ZnO-30**, (e) Comparison between photodegradation efficiencies of Congo Red by high aspect ratios (**ZnO-23** to **ZnO-26**) and low aspect ratios (**ZnO-27** to **ZnO-30**) and (f) Comparison between rate constants of Congo Red by high aspect ratios ZnO nanorod arrays (**ZnO-23** to **ZnO-26**) and low aspect ratios ZnO nanorod arrays (**ZnO-27** to **ZnO-30**).

With UV-light illumination, e^-/h^+ pairs are generated on the ZnO surface which undergoes rapid recombination in the absence of surface defects. Whereas, the high aspect ratio of ZnO nanorods with enough surface defects ensures the trapping of the photogenerated holes alleviating the separation of e^-/h^+ pairs. The trapped holes then react with e^- donor molecules stimulating the process of photodegradation. On the other hand, photogenerated electrons flow along the longitudinal direction (0001) surface of 1D nanorods due to the increased delocalization of electrons further facilitates the decrease in the recombination centers. Hence it can be deduced that the existence of the surface defects and high aspect ratios of nanorods plays a crucial role in enhancing the photocatalytic activity.[69-71]

Antibacterial properties. The antibacterial effectiveness of the ZnO nanorods (**ZnO-23**) was tested against gram negative *E.Coli*. The batch cultures containing varying concentrations of nanorods in 10 mL of sterilized Luria Bertani (LB) medium was sonicated for 2 minutes after addition. The test tubes with different concentration of **ZnO-23** were inoculated with 100 μL of bacterial cultures. The test tubes were then kept in a shaken incubator at 300 rpm and 37 °C for 24 hours. The bacterial growth was monitored by measuring the optical density (O.D.) at a fixed wavelength of 650 nm. Aliquots were taken after every 10 minutes for the measurement of O.D. (Figure 3.52). The optical density was measured without and with different ZnO concentrations. The samples prepared with 100 and 150 mg/L concentration of ZnO were found

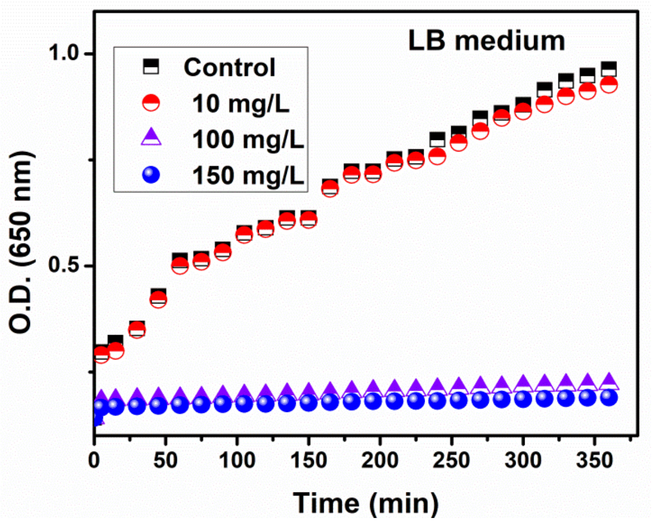

Figure 3.52. Growth curve of *E.Coli* in the presence of ZnO nanorods (**ZnO-23**) at concentrations 10 mg/L, 100 mg/L and 150 mg/L.

effective in inhibiting the growth of general strain *E.Coli* whereas a limited inhibition was observed with 10 mg/L. Also, with 10 mg/L, a high level of turbidity was observed confirming the growth of bacteria. Unlike the previous case, the samples with 100 and 150 mg/L concentration of ZnO didn't result in a high turbidity indicating almost no change over time. The plate count was also used to monitor the bacterial growth. *E.Coli* strains containing different concentrations of ZnO (10, 100 and 150 mg/L) were cultured in LB medium on agar plates and incubated at 37 ºC for a period of 24 hours. The colonies were counted after 24 hours (Figure 3.53). It has been observed that the sample with 10 mg/L concentration of ZnO minimized the growth to a little extent. However, when we increased the concentration to 100 mg/L, the no. of colonies observed was less. The bacterial effectiveness increased more on further increase in concentration of ZnO to 150 mg/L resulting in giving even less no of colonies. The no. of colonies can be calculated using the following formula (Maneerung et. al., 2008).[72]

$$\frac{Viable\ count\ at\ 0\ h - Viable\ count\ at\ 24\ h}{Viable\ count\ at\ 0\ h} \times 100 = X$$

The no. of colonies observed at different concentrations and the percentage of bacterial cell inhibition is given in Table 3.15.

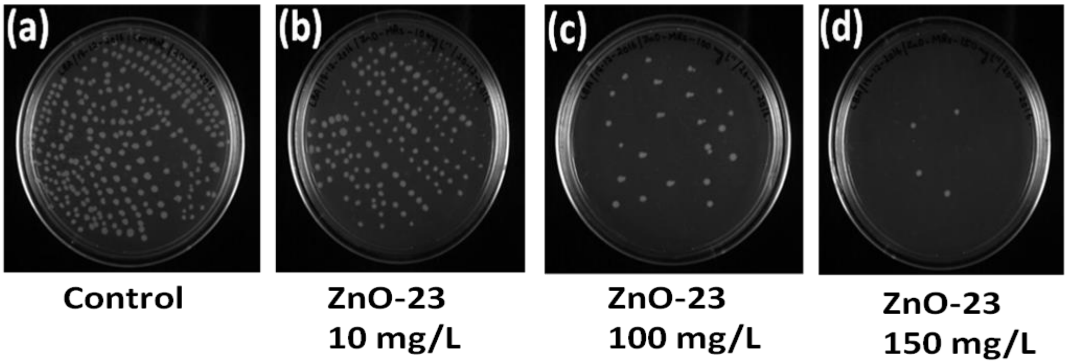

Figure 3.53. *E.coli* culture plates (a) Control, (b) in the presence of **ZnO-23** with a concentration of 10mg/L, (c) in the presence of **ZnO-23** with a concentration of 100 mg/L, (d) in the presence of **ZnO-23** with a concentration of 150 mg/L.

Each morphology accounts for a certain mechanism of action. Though the exact mechanism has not been fully understood as there are some queries within the spectrum of antibacterial activity requiring deep explanations. Distinctive mechanisms have been put forward in the literature: direct contact of ZnO-NPs with cell walls, resulting in destructing bacterial cell integrity, liberation of antimicrobial ions mainly Zn^{2+} ions and reactive oxygen species (ROS) formation. ZnO-NPs are bactericidal and thus disrupt the membrane causing membrane dysfunction, resulting in their internalization into the bacteria. Interestingly, ZnO-NPs contain positive charge in water suspension and the *E.Coli* surface is negatively charged which causes the electrostatic interaction between the nanoparticles and the bacterial cell surface causing the inhibition of growth.[73-74] As a result cell membrane is damaged.

Table 3.15. Bacterial growth inhibition results of **ZnO-23**

Sample	No. of colonies observed	Percentage bacterial inhibition
Control	252	0
ZnO-23 with 10 mg/L	154	38.90
ZnO-23 with 100 mg/L	28	88.89
ZnO-23 with 150 mg/L	4	98.41

3.1.2.4 pH dependent synthesis

(i) Using $[Zn_2(bpma)_2(adc)_2]_n$. ZnO nanostructures have also been fabricated at different pH varying from 9 to 12 employing Zn(II) coordination polymer $[Zn_2(bpma)(adc)_2]_n$. The hydrothermal reaction was carried out at 180 °C in 3 mL of water containing varying amount of KOH to maintain pH ranging from 9 to 12. The reaction was carried out for different aging times from 30 minutes to 12 hours with a gap of 60 minutes to monitor the growth of micro flowers. Initially, 2D nanosheets have been obtained in the reaction mixture followed by self-assembly of nanosheets to produce 3D flowers after a certain amount of time. The growth was observed for 12 hours. After 12 hours, no further change in the morphology was observed.

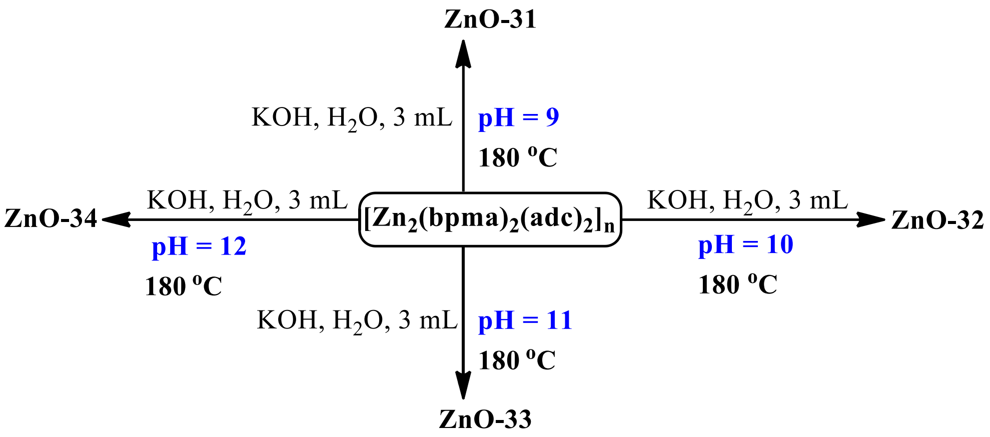

Scheme 3.12. Synthesis of **ZnO-31** to **ZnO-34** at different pH.

Powder X-ray diffraction studies. The as-obtained ZnO micro flowers obtained after 12 hours of aging time were characterized by PXRD technique. The peaks obtained in the spectra could be clearly indexed to hexagonal wurtzite structure of ZnO (JCPDS 06-2151). The sharp and intense peaks confirm the purity of the obtained samples (Figure 3.54). No other impurity peak has been obtained which further confirms the purity of the ZnO nanostructures. The lattice parameters determined using equation 1 are given in Table 3.16.

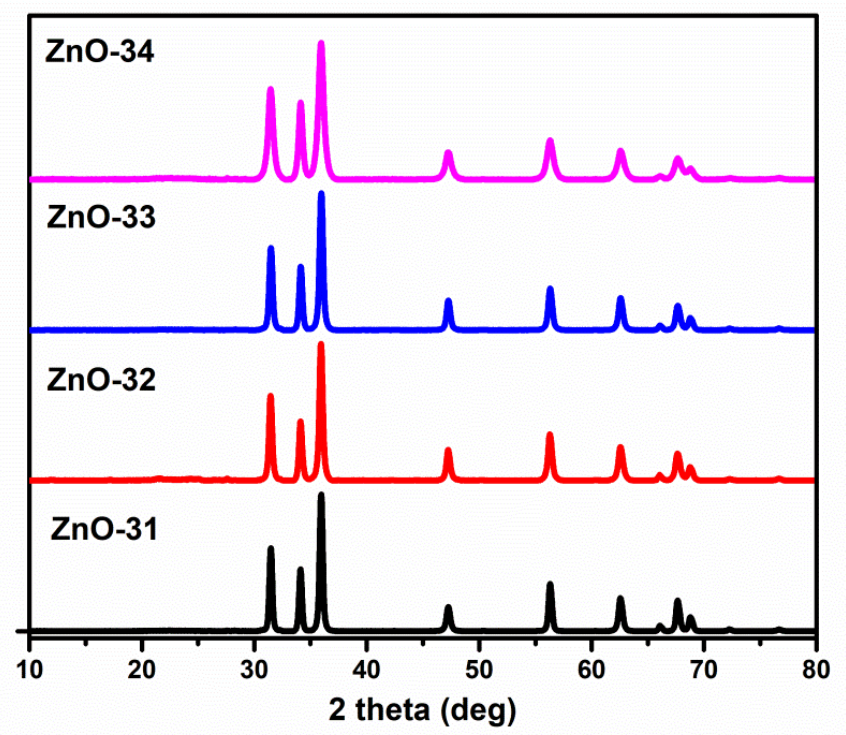

Figure 3.54. PXRD patterns of as-synthesized ZnO nanostructures (**ZnO-31** to **ZnO-34**).

Table 3.16. Lattice parameters for ZnO samples (**ZnO-31** to **ZnO-34**)

Sample	h k l	2θ values (degrees)	Lattice constants a, b, c (Å)	Volume of unit cell (Å ^{3})	Atomic packing fraction	d spacings (Å)
ZnO-31	(100)	31.69	a = b = 3.26,	48.07	0.754	2.82
	(002)	34.45	c = 5.22			2.61
	(101)	36.23				2.48
ZnO-32	(100)	31.74	a = b = 3.26,	48.08	0.755	2.82
	(002)	34.44	c = 5.22			2.61
	(101)	36.22				2.48
ZnO-33	(100)	31.74	a = b = 3.25,	48.14	0.755	2.82
	(002)	34.42	c = 5.20			2.61
	(101)	36.21				2.48
ZnO-34	(100)	31.73	a = b = 3.25,	48.14	0.755	2.82
	(002)	34.42	c = 5.20			2.61
	(101)	36.23				2.48

Surface analysis. The surface analysis of the ZnO nanostructures obtained at different pH conditions was analyzed by FESEM. The nanostructures were fabricated for different aging times to observe the overall evolution of micro flowers (Figure 3.55 to 3.58). Initially, the two-dimensional growth in the reaction mixture was observed for the first 2 hours with the formation of nanosheets. These nanosheets started getting assembled with the neighboring nanosheets to form 3D flowers to lower their surface energy. At the end of 4 hours, the formation of flowers could be clearly observed except in the case of pH=11 and pH=12 where 1D rods were also obtained along with 2D sheets due to the presence of a greater number of OH^- ions compared to the previous two cases. The sheets unite together with neighboring sheets to form 3D flowers by decreasing the overall surface energy. The optimized time for the evolution of full bloom flowers were observed to be 12 hours in each case. After extending the synthesis time, not much change has been observed in the overall morphology of the ZnO micro flowers.

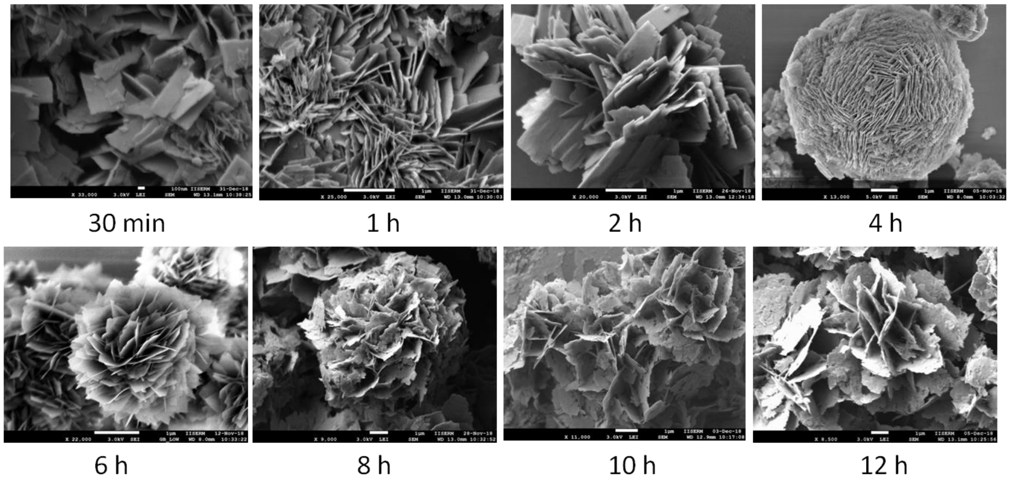

30 min 1 h 2 h 4 h

6 h 8 h 10 h 12 h

Figure 3.55. ZnO nanostructures obtained at pH=9.

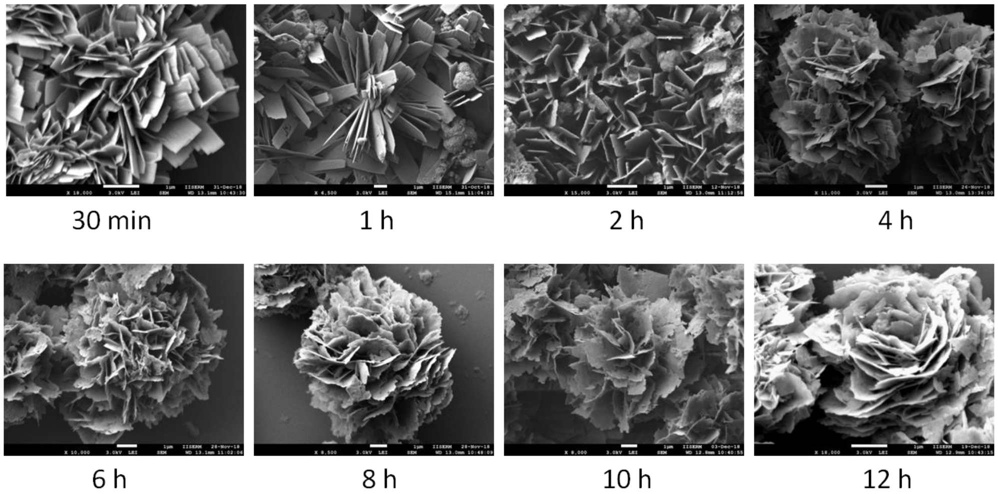

30 min 1 h 2 h 4 h

6 h 8 h 10 h 12 h

Figure 3.56. ZnO nanostructures obtained at pH=10.

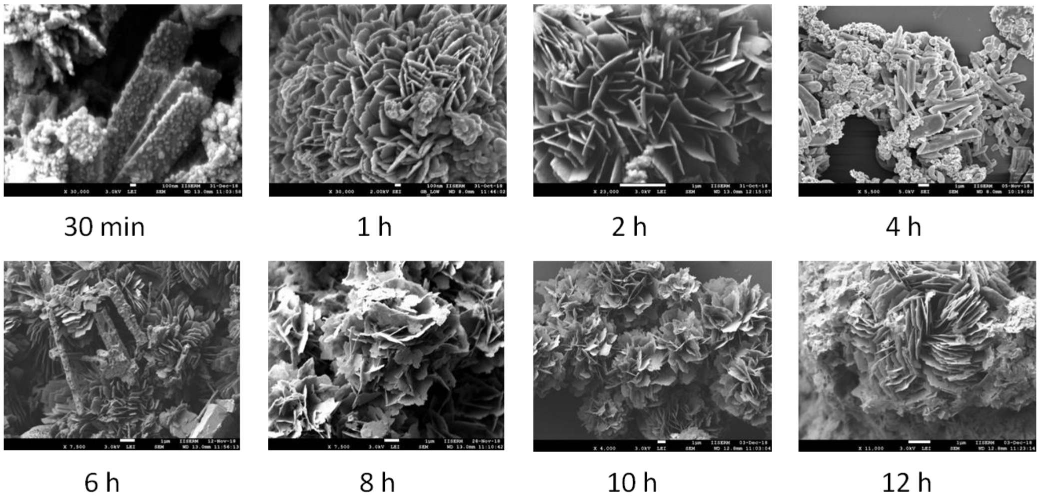

30 min 1 h 2 h 4 h

6 h 8 h 10 h 12 h

Figure 3.57. ZnO nanostructures obtained at pH=11.

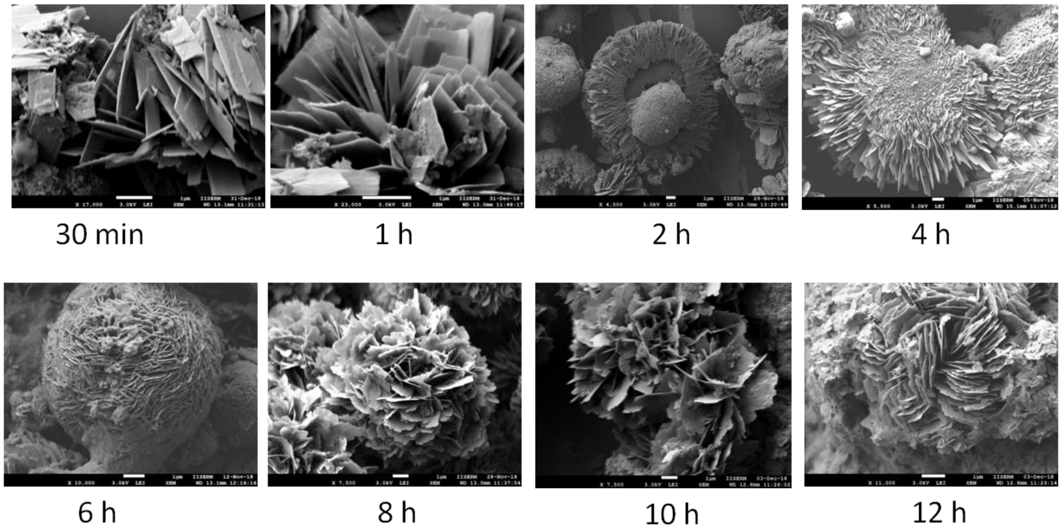

30 min 1 h 2 h 4 h

6 h 8 h 10 h 12 h

Figure 3.58. ZnO nanostructures obtained at pH=12.

Optical properties. UV-Vis diffused reflectance of the obtained ZnO nanostructures was recorded in the wavelength range of 200-800 nm to study the absorption properties of the structures and also to obtain the band gap values. In the spectra, ZnO nanostructures (**ZnO-31** to **ZnO-34**) exhibited highest absorption band around 368 nm which confirms a strong binding in the obtained nanostructures (Figure 3.59). The characterization of the energy band gap (E_g) values for the **ZnO-31** to **ZnO-34** was done using Tauc relation (equation 2). Though the energy band gap values were found to be very close to each other but an increasing trend in the values has been observed with the increase of pH values. The values were found to be 3.13 for **ZnO-31**, 3.14 for **ZnO-32**, 3.17 for **ZnO-33** and 3.21 for **ZnO-34**.

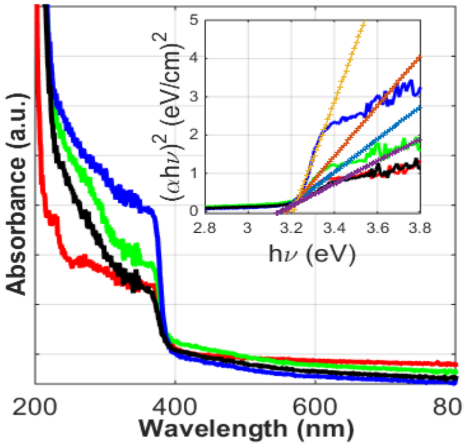

Figure 3.59. Solid state absorption spectra of **ZnO-31** to **ZnO-34** where red is for **ZnO-31**, green colour is for **ZnO-32**, blue colour represents **ZnO-33** and black colour represents **ZnO-34** where (inset) plot is between $(\alpha h\nu)^2$ versus ($h\nu$).

Photoluminescence properties. The photoluminescence measurements were carried out on the as-obtained ZnO nanostructures at an excitation wavelength of 350 nm where xenon lamp was used as the excitation source. The spectra were recorded within a range of 380-600 nm. A broad blue emission band in the range of 400-430 nm could be clearly observed in all the nanostructures. This blue emission is attributed to the intrinsic defects present in ZnO (zinc vacancies and oxygen vacancies) nanostructures. A decrease in the intensities has been observed for the structures synthesized in more basic conditions with a greater value of pH as illustrated in Figure 3.60. The ZnO nanostructures obtained at a pH=9 showed the maximum intensity of absorption whereas a decreasing trend has been observed with increase in pH conditions from 10 to 12.

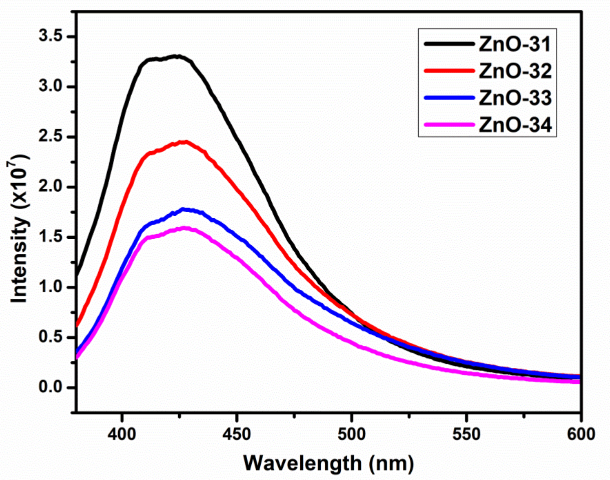

Figure 3.60. Room temperature photoluminescence spectra of **ZnO-31** to **ZnO-34**.

3.1.2.5 Effect of Solvent

(i) Using $[Zn_2(bpma)_2(adc)_2]_n$. A solvent dependent study was carried out in different solvents (MeOH, EtOH, THF, Toluene and Hexane) at 180 °C for 24 hours using $[Zn_2(bpma)_2(adc)_2]_n$ to yield ZnO (Scheme 3.13). Different morphologies were obtained with the variation in the solvent based on the different polarity, saturated vapor pressure and boiling point of the solvents.[75] Nanospheres and nanorods have been obtained based on the different saturated vapour pressure and boiling point of the solvents. The anisotropic growth is favored in high boiling point solvents inducing the growth in (0001) direction. Whereas the homogeneous nucleation is observed in the case of low boiling solvents.

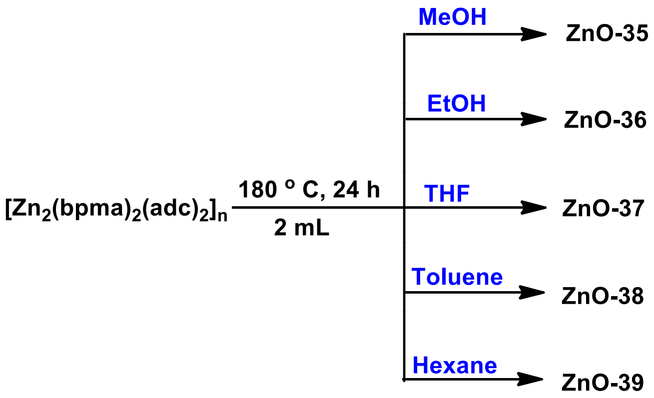

Scheme 3.13. Synthesis of ZnO nanostructures (**ZnO-35** to **ZnO-39**) in different solvents.

Powder X-ray diffraction studies. The ZnO nanostructures obtained with the variation in the solvents were characterized by powder diffraction technique. All the samples exhibited hexagonal wurtzite phase of ZnO (JCPDS 06-2151). The sharpness of the intense peaks obtained confirms the purity of the structures (Figure 3.61). The as-obtained ZnO nanostructures exhibited high crystallinity. The lattice parameters obtained using equation 1 is given in Table 3.17.

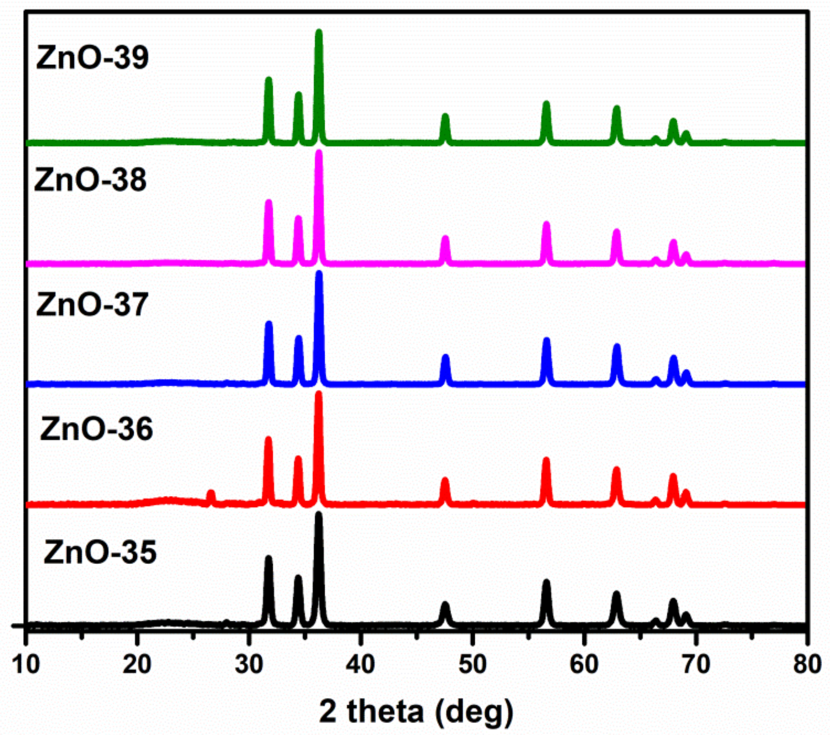

Figure 3.61. PXRD patterns of as-synthesized ZnO nanostructures (**ZnO-35** to **ZnO-39**).

Table 3.17. Lattice parameters for ZnO samples (**ZnO-35** to **ZnO-39**)

Sample	**hkl**	**2θ values (degrees)**	**Lattice constants a, b, c (Å)**	**Volume of unit cell (Å^3)**	**APF**	**d spacings (Å)**
ZnO-35	(100)	31.49	a = b = 3.28, c = 5.26	49.11	0.755	2.84
	(002)	34.13				2.63
	(101)	35.95				2.50
ZnO-36	(100)	31.51	a = b = 3.28, c = 5.25	49.10	0.755	2.84
	(002)	34.14				2.62
	(101)	36.04				2.49
ZnO-37	(100)	31.45	a = b = 3.28, c = 5.26	49.23	0.755	2.84
	(002)	34.11				2.63
	(101)	35.94				2.50
ZnO-38	(100)	31.46	a = b = 3.28, c = 5.25	49.17	0.755	2.84
	(002)	34.16				2.62
	(101)	35.95				2.50
ZnO-39	(100)	31.46	a = b = 3.28, c = 5.25	49.16	0.755	2.84
	(002)	34.14				2.62
	(101)	35.97				2.50

Surface analysis. The surface morphology of the ZnO nanostructures obtained in different solvents was studied by FESEM (Figure 3.62). ZnO nanoparticles of size 7-10 nm were obtained in case where methanol has been used as the solvent. Whereas, nanoparticles of size 4-5 nm were observed in ethanol. However, tetrahydrofuran (THF) with high boiling point yielded rods with aspect ratio 4.72. In case of toluene also, the rods were obtained with aspect ratio of 5. Hexane, on the other hand yielded nanoparticles of size 30-40 nm. Thus, it has been observed that low boiling point solvents (ethanol, methanol and hexane) resulted in producing the spherical structures and high boiling point solvents resulted in giving 1D nanorods.[76-77] In general, the initial nucleation of the crystals and the solubility of the precursor in the solvents play a crucial role in contributing to the overall morphology of the products. Under the hydrothermal conditions, the saturated vapor pressure and boiling points of the solvents are inversely related to each other.[78] The boiling points of toluene, THF, ethanol, hexane and methanol are 110.63, 88, 78.29, 68, 64.78 respectively. Thus, the saturated vapor pressures of these solvents follow the reverse order.

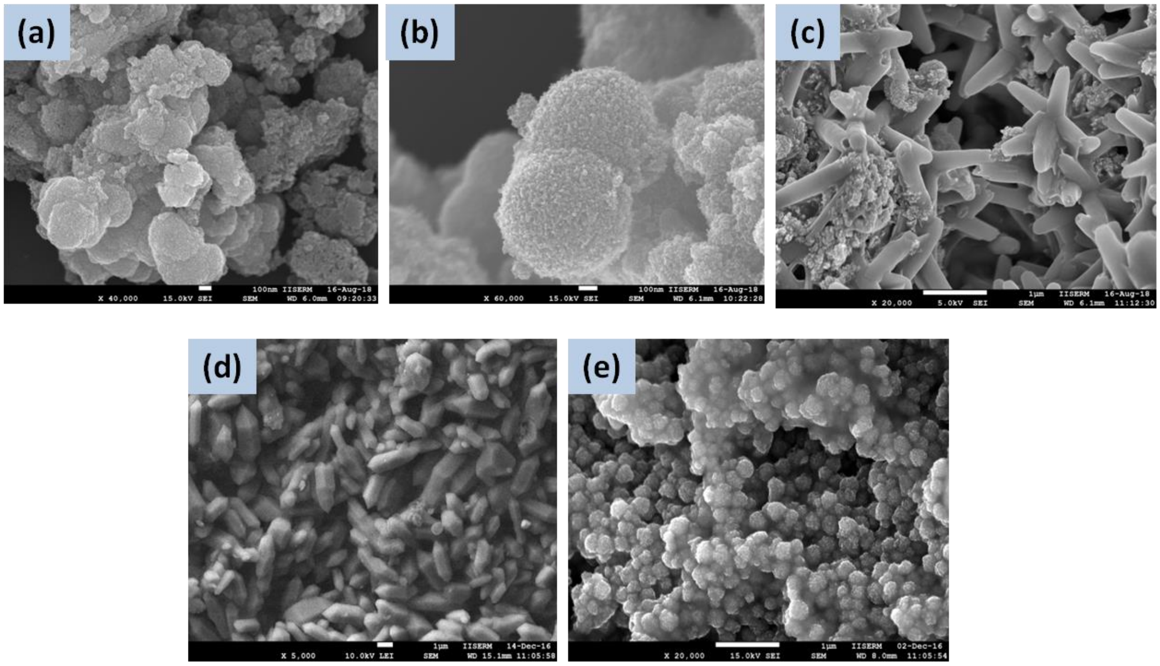

Figure 3.62. ZnO nanostructures (**ZnO-35** to **ZnO-39**) obtained in different solvents: (a) methanol, (b) ethanol, (c) THF, (d) Toluene and (e) Hexane.

A high saturated vapor pressure of the solvents like methanol, ethanol and hexane resulted in a limited growth of ZnO nuclei which gives rise to substantial nucleation of particles. The nanoparticles aggregated by clustering together to reduce the overall surface energy. On the other hand, when the solvents such as toluene and THF were used, which have relatively low saturated vapor pressures, anisotropic growth was favored to yield ZnO nanorods. Hence, the above results clearly indicated the role of saturated vapor pressure of the solvent in producing the ZnO nanostructures with different morphologies.

Photoluminescence properties. In order to understand the luminescent properties of the ZnO nanostructures obtained in different solvents, the experiments were carried out with xenon lamp at an excitation wavelength of 350 nm. **ZnO-35** showed three emission bands in the blue region of the visible spectrum whereas in case of **ZnO-36** and **ZnO-37**, a broad blue emission band in the range of 410-460 nm has been obtained (Figure 3.63). Furthermore, similar result has been obtained for **ZnO-38** except the blue region of the spectrum is wider here. However, **ZnO-39** showed a similar result as obtained in the previous cases. The intrinsic defects present in ZnO in the form vacancies of zinc and oxygen shows blue emission as a result of recombination of charge carriers.

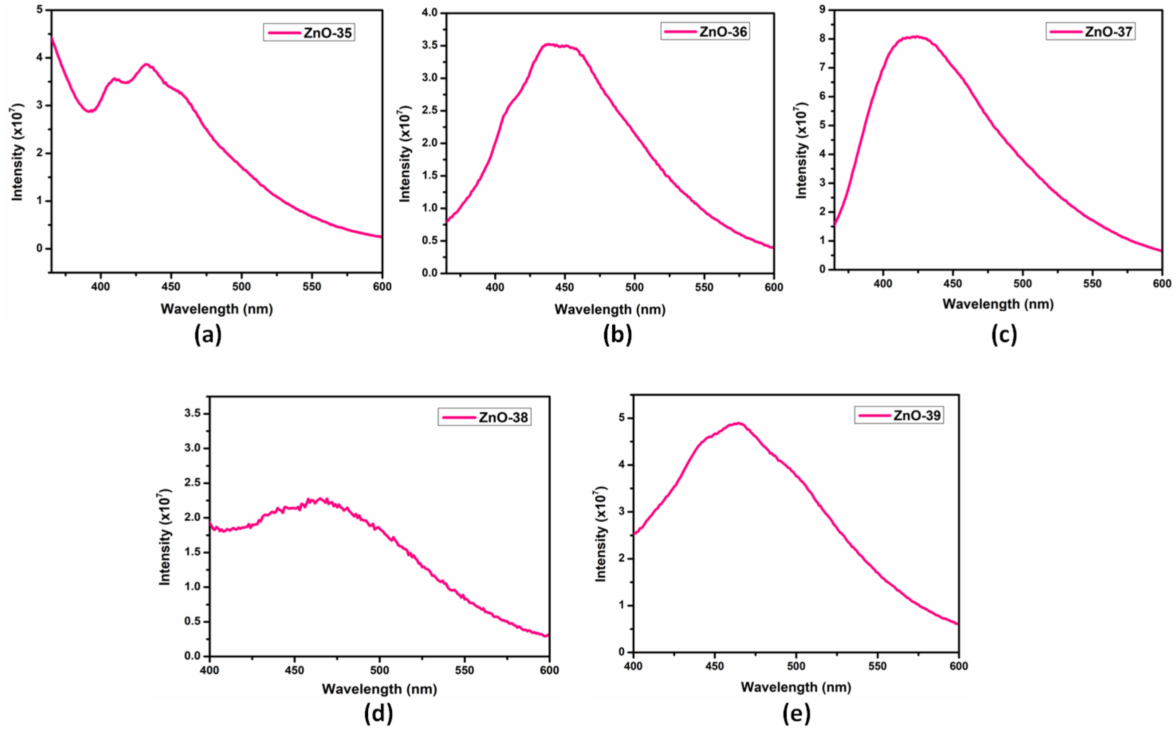

Figure 3.63. Photoluminescence spectra of **ZnO-35** to **ZnO-39**.

3.1.3 Fabrication via direct calcination

ZnO nanostructures were successfully synthesized at high temperature of 700 °C in the tube furnace by direct annealing using Zn(II) coordination polymers $[Zn_2(bpma)_2(adc)_2]_n$, $\{[Zn_2(bpea)_2(adc)_2]_n$ and $\{[Zn_2(bpta)_2(adc)_2]\cdot 2H_2O\}_n$. The effect of different ligands presents in the precursors as well as the variation in the retention time during synthesis resulted in different morphologies of ZnO. Calcination in air at a temperature above the decomposition temperature of the polymers collapse the whole framework and yield ZnO. The metal ions with a standard reduction potential of 0.27 V or higher such as Co, Ni and Cu present in coordination polymers (CPs) form pure metal nanoparticles during calcination whereas metal ions with a reduction potential lower than 0.27 V such as Mg, Al, Mn, Zn or Cr tend to combine with the oxygen of the organic linker present in the polymer and form corresponding metal oxides.[79-81] Since the reduction potential of Zn^{2+} is lower than 0.27 V and thus calcining at a temperature of 700 °C in the tube furnace zinc ions are unable to reduce to a zero oxidation state. The three different ligands present in these CPs have a profound effect on the morphology of the obtained nanometal ZnO and their photocatalytic activities. The synthesis of these ZnO is given in scheme 3.14 to 3.16. These are fully characterized by PXRD, FESEM, Raman spectroscopy and UV-vis spectroscopy. ZnO were obtained bearing good photocatalytic properties.

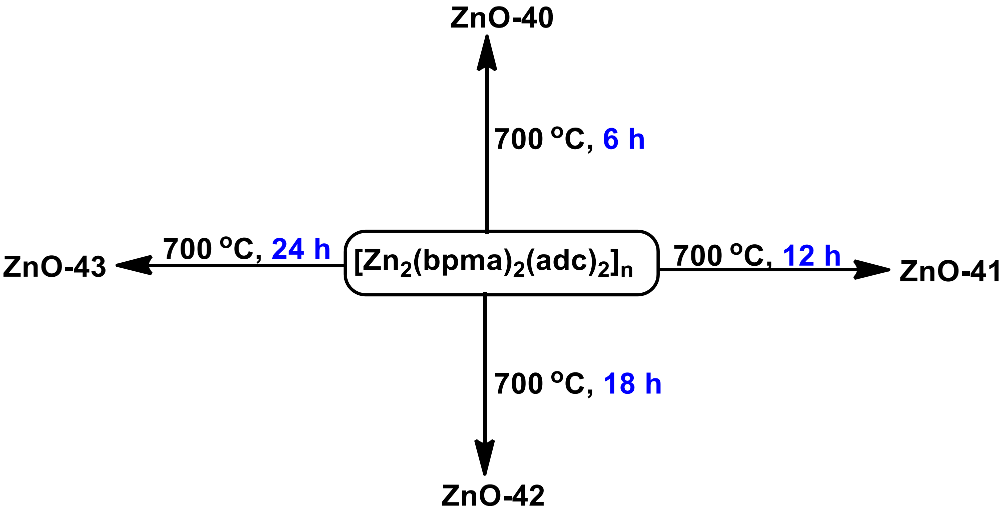

Scheme 3.14. Synthesis of **ZnO-40** to **ZnO-43**.

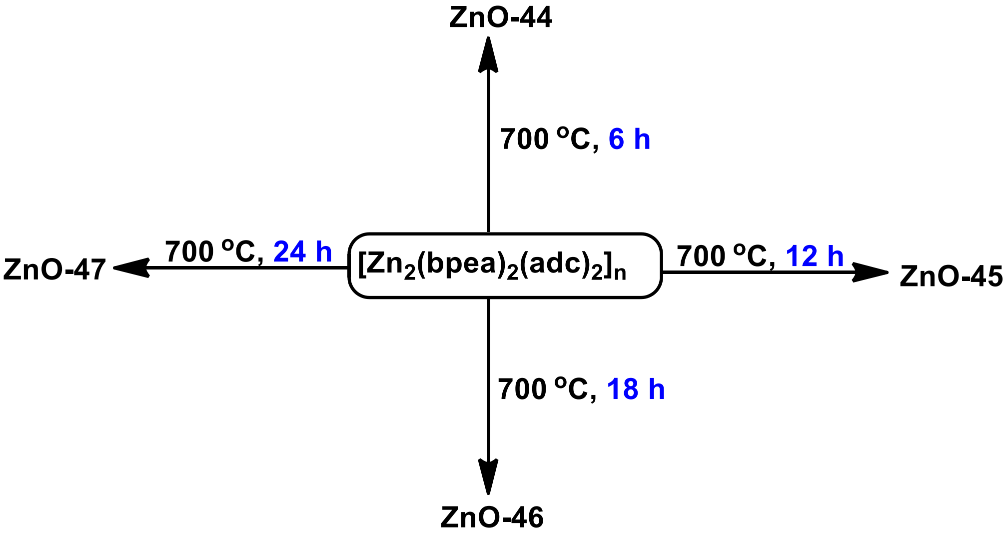

Scheme 3.15. Synthesis of **ZnO-44** to **ZnO-47**.

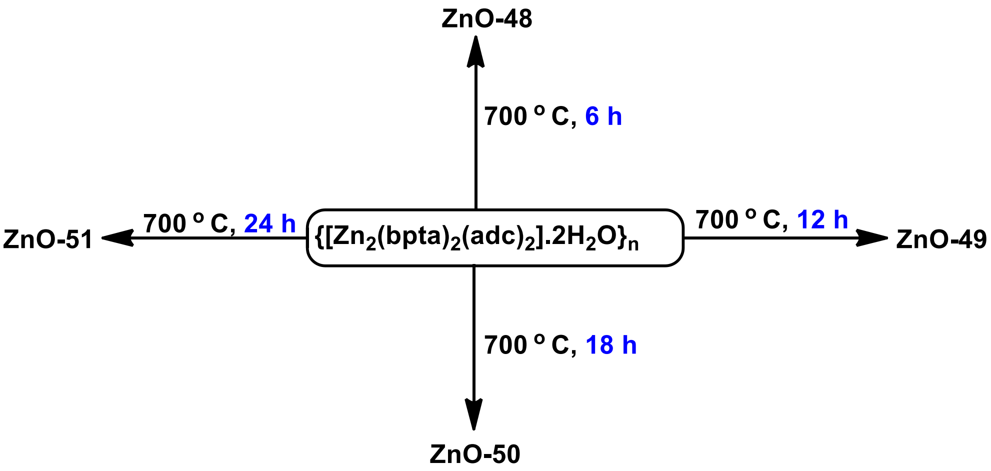

Scheme 3.16. Synthesis of **ZnO-48** to **ZnO-51**.

Powder X-ray diffraction studies. Figure 3.64 shows XRD patterns of all the powder samples from 6 h to 24 h. All the peaks could be clearly indexed to the hexagonal wurtzite phase of ZnO which matches well with the JCPDS card no of 36-1451. The observed peaks could be indexed to scattering from the (100), (002) and (101) planes and no other characteristic peak for any impurity was observed. This indicates high crystallinity and purity of the as-prepared ZnO samples.

The lattice parameters (Table 3.18) for hexagonal ZnO nanoparticles were estimated from the following equation:

$$\frac{1}{d^2} = \frac{4}{3(h^2 + hk + \frac{k^2}{a^2})} + \frac{l^2}{c^2}$$

where a and c are the lattice parameters and h, k and l are the Miller indices and $d_{h\,k\,l}$ is the interplanar spacing for the plane (h k l). This interplanar spacing for the plane (h k l) can be calculated from Bragg's law: $2d \sin\theta = n\lambda$

The volume (V) of the unit cell for hexagonal system can be calculated from the following equation:

$$V = 0.866 \times a^2 \times c$$

The atomic packing fraction can be calculated using the following equation:

Atomic packing fraction (APF) = $\frac{2\pi a}{3\sqrt{3}\,c}$

The data obtained accordingly are given in Table 3.18.

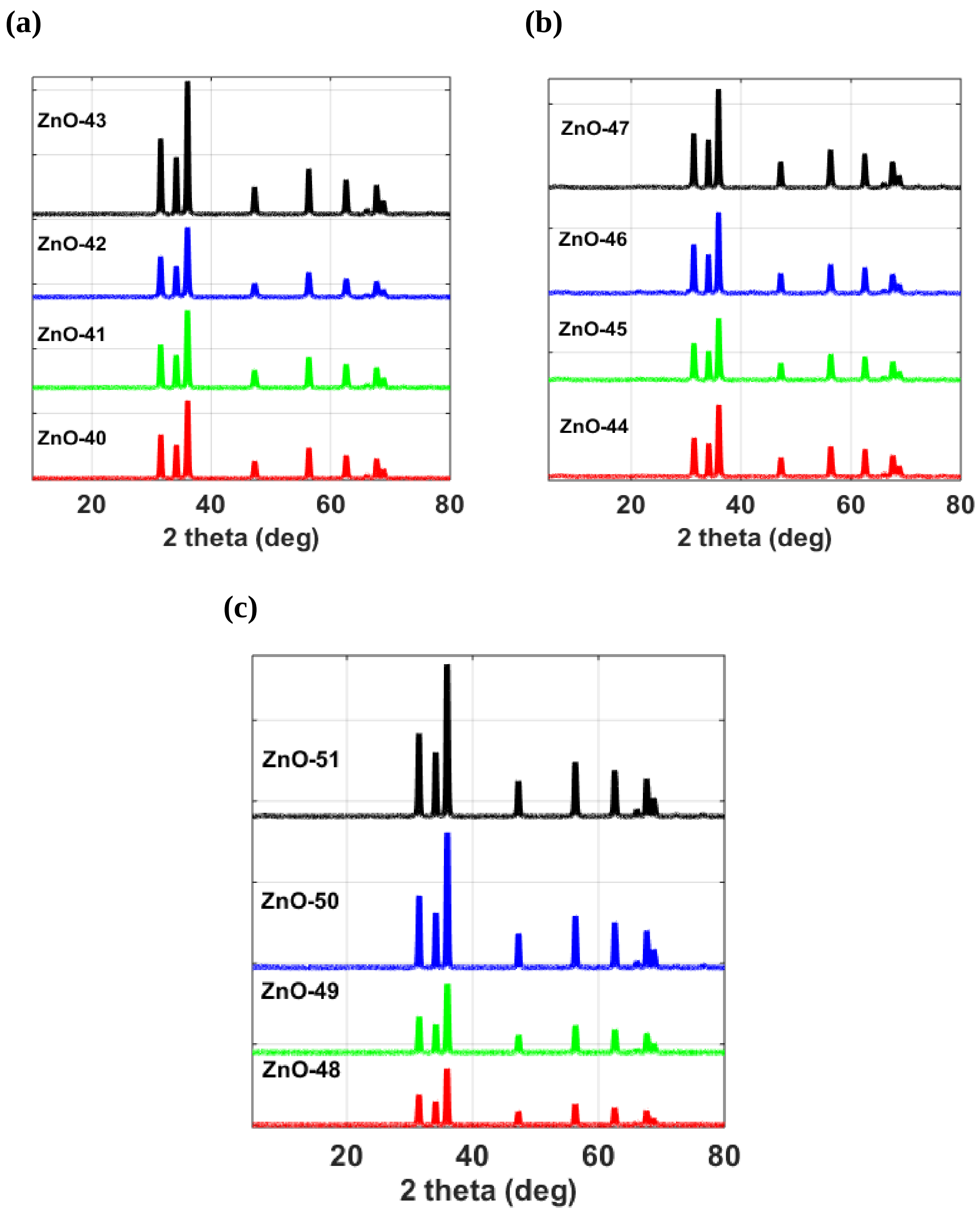

Figure 3.64. PXRD patterns of as-synthesized ZnO nanostructures (a) **ZnO-40** to **ZnO-43**, (b) **ZnO-44** to **ZnO-47** and (c) **ZnO-48** to **ZnO-51**.

Table 3.18. Lattice parameters for **ZnO-40** to **ZnO-51**

Sample	hkl	2θ values (degrees)	Lattice constants a, b, c (Å)	Volume of unit cell (Å^3)	APF	d spacing (Å)
ZnO-40	(100)	31.50	a = b = 3.28, c = 5.26	49.15	0.755	2.84
	(002)	34.15				2.63
	(101)	35.98				2.50
ZnO-41	(100)	31.52	a = b = 3.28, c = 5.25	49.05	0.755	2.84
	(002)	34.17				2.62
	(101)	36.01				2.49
ZnO-42	(100)	31.49	a = b = 3.28, c = 5.26	49.23	0.755	2.84
	(002)	34.14				2.63
	(101)	35.97				2.50
ZnO-43	(100)	31.49	a = b = 3.28, c = 5.25	49.18	0.755	2.84
	(002)	34.15				2.62
	(101)	35.98				2.50
ZnO-44	(100)	31.43	a = b = 3.29, c = 5.27	49.45	0.755	2.85
	(002)	34.09				2.63
	(101)	35.91				2.50
ZnO-45	(100)	31.50	a = b = 3.29, c = 5.26	49.34	0.755	2.85
	(002)	34.16				2.63
	(101)	35.98				2.50
ZnO-46	(100)	31.45	a = b = 3.29, c = 5.26	49.76	0.755	2.85
	(002)	34.13				2.63
	(101)	35.96				2.50

ZnO-47	(100)	31.44	a = b = 3.29, c = 5.26	49.44	0.755	2.85
	(002)	34.11				2.63
	(101)	35.92				2.50
ZnO-48	(100)	31.49	a = b = 3.29, c = 5.26	49.20	0.755	2.84
	(002)	34.12				2.63
	(101)	35.94				2.51
ZnO-49	(100)	31.46	a = b = 3.29, c = 5.26	49.33	0.755	2.84
	(002)	34.12				2.63
	(101)	35.94				2.50
ZnO-50	(100)	31.50	a = b = 3.28, c = 5.26	49.16	0.755	2.84
	(002)	34.16				2.63
	(101)	35.98				2.50
ZnO-51	(100)	31.45	a = b = 3.29, c = 5.26	49.36	0.755	2.85
	(002)	34.10				2.63
	(101)	35.94				2.50

Surface analysis. Figure 3.65 shows the SEM images of nanoparticles emerged after the heat treatment of $[Zn_2(bpma)_2(adc)_2]_n$ to 700 ^oC after 6 hours of retention time. As a result of spheroidization process, the necks and grain boundaries started emerging between these particles. These particles continued to grow with a little variation in size up to 18 hours of retention time and eventually get assembled to produce nanorods (80 nm) after 24 hours of retention time. Whereas, ZnO microrods were obtained with the change in ligand from bpma to bpea following the same procedure. After 6 hours retention, the etching started from the top end of the microrods to overall erode downwards towards the c-axis as shown in Figure 3.66a. As a result of fast etching from the corners the tips started emerging from the top ends of the microrods. With the increase in the retention time from 6 hours to 12 hours, the length of the tip increased. When the retention time was further extended to 18 hours, a decrease in the length of the microrods was observed; however, the diameters from the top and bottom ends of the rods changed very little. Finally, after 24 hours of retention, the tips started disappearing to produce rods with hexagonal ends. Thus, it can be concluded that the shortening of microrods was observed as a result of retention which happens to be the dominant process instead of growth. When $\{[Zn_2(bpta)_2(adc)_2]^{\cdot}2H_2O\}_n$ was calcined to 6 hours, ZnO nanoparticles grew up to 50-70 nm and assembled into nanoscale polyhedrons shown in Figure 3.67a. With the elongation in time from 12 hours to 24 hours these nanoparticles continued to grow to produce nanoscale polyhedrons with a little variation in their sizes. Figure 3.68, 3.69 and 3.70 shows HRTEM images of nanospheres, microrods and polyhedrons of ZnO after 12 hours of retention time. The distance of 0.22-0.26 nm between the lattice fringes of ZnO nanostructures coincides with the distance between crystallographic planes of hexagonal wurtzite ZnO. The selected area electron diffraction (SAED) patterns shown in Figure 3.68c, 3.69c and 3.70c confirm the results of XRD patterns.

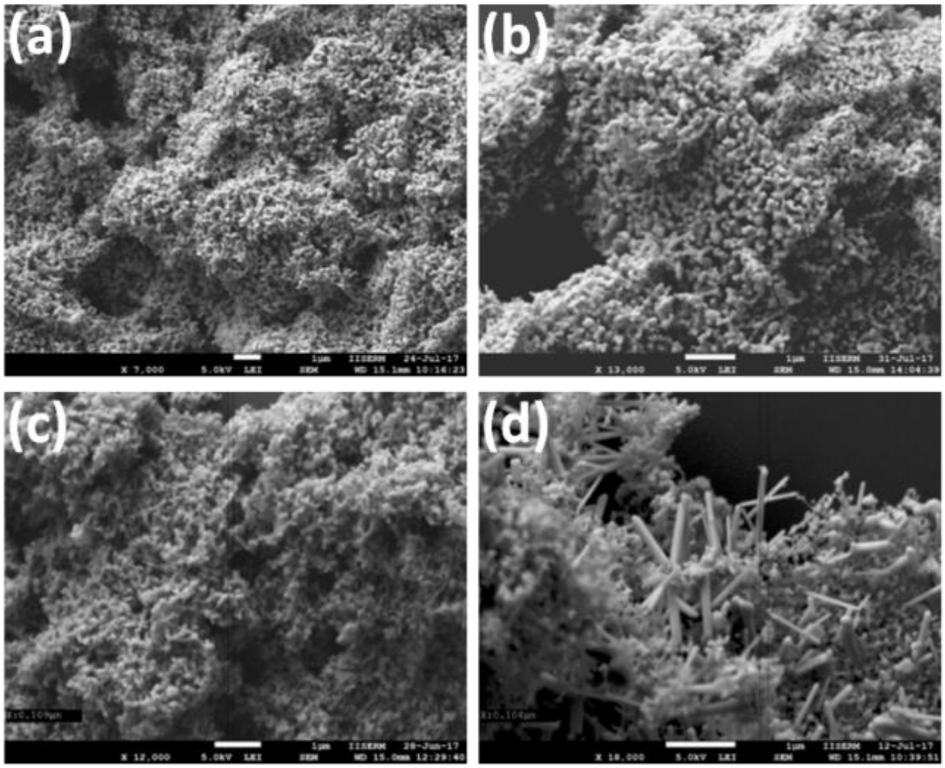

Figure 3.65. FESEM images of (a) **ZnO-40**, (b) **ZnO-41**, (c) **ZnO-42** and (d) **ZnO-43**.

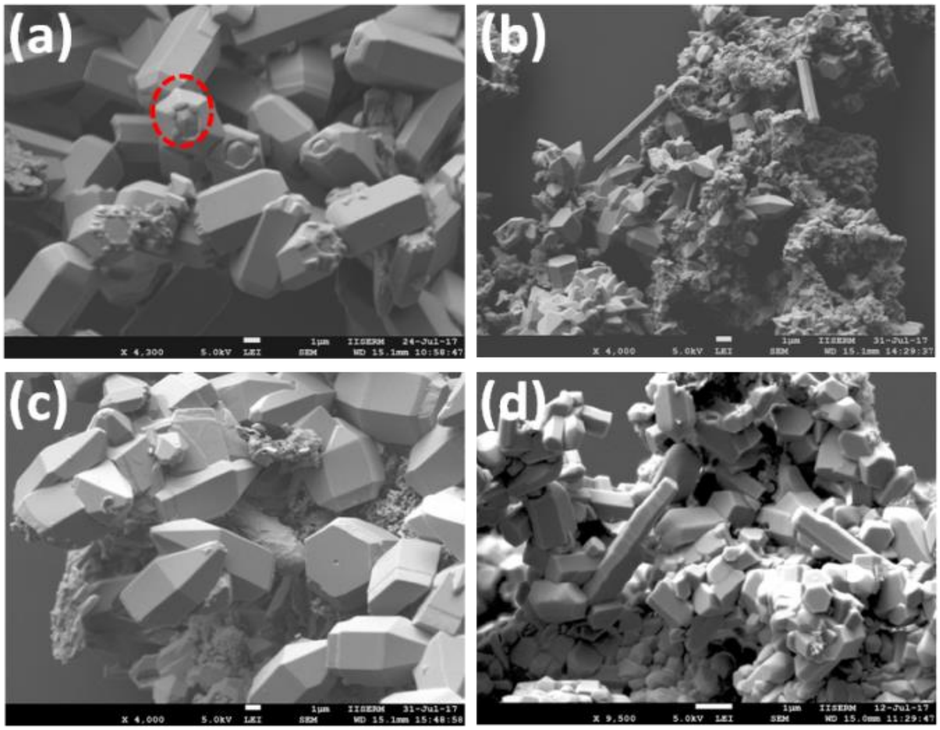

Figure 3.66. FESEM images of (a) **ZnO-44**, (b) **ZnO-45**, (c) **ZnO-46** and (d) **ZnO-47**.

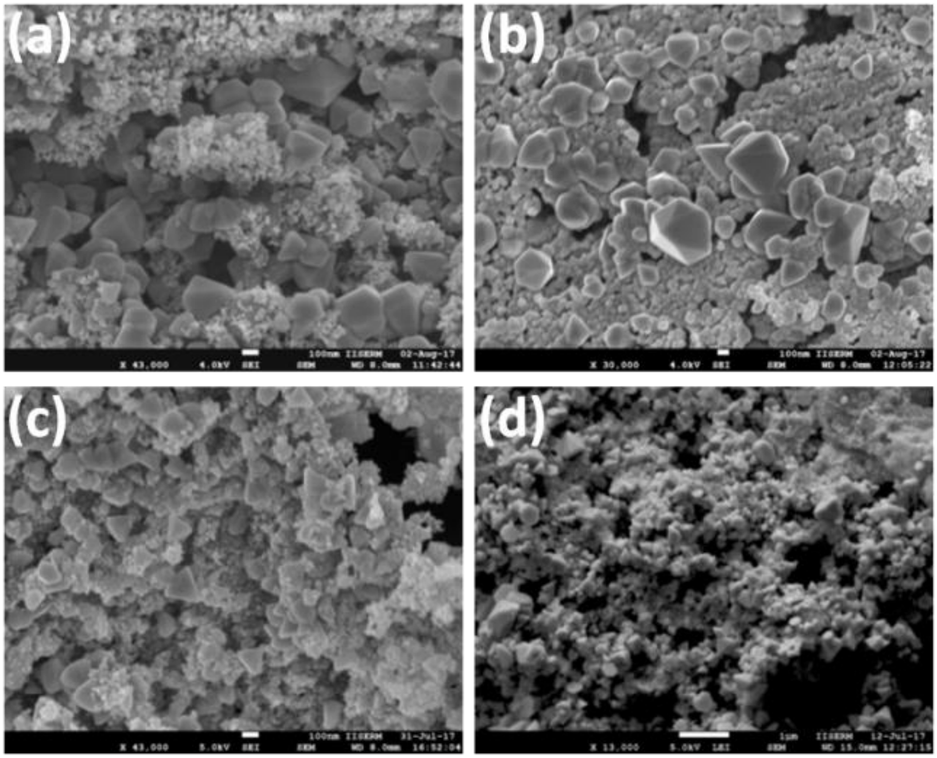

Figure 3.67. FESEM images of (a) **ZnO-48**, (b) **ZnO-49**, (c) **ZnO-50** and (d) **ZnO-51**.

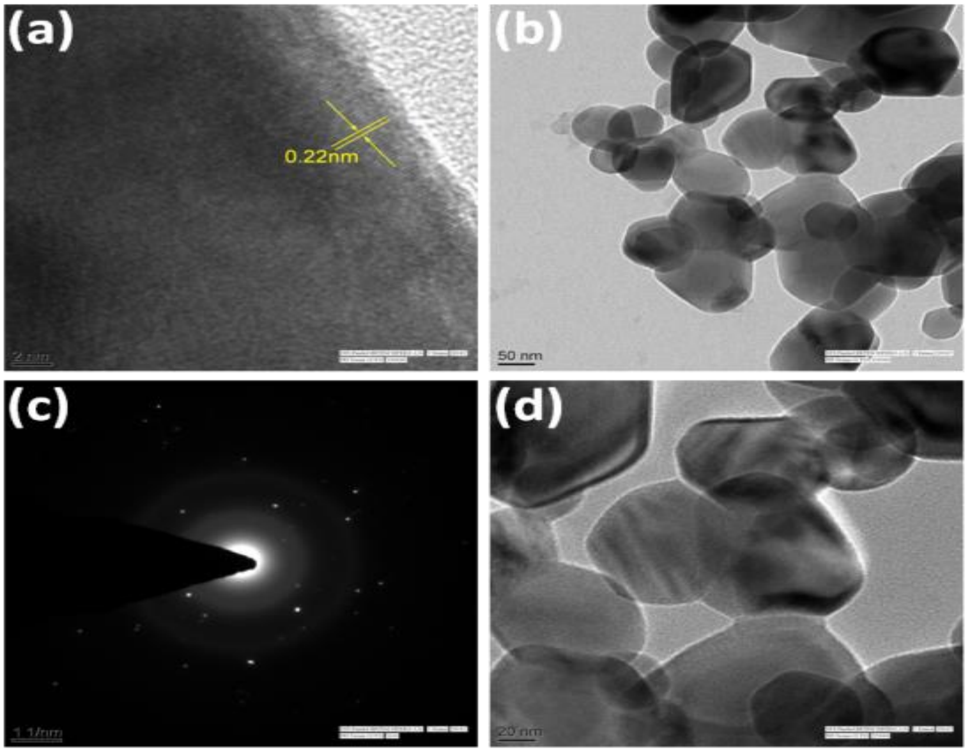

Figure 3.68. (a) Lattice fringe, (b), (c) HRTEM images and (d) SAED pattern of **ZnO-41**.

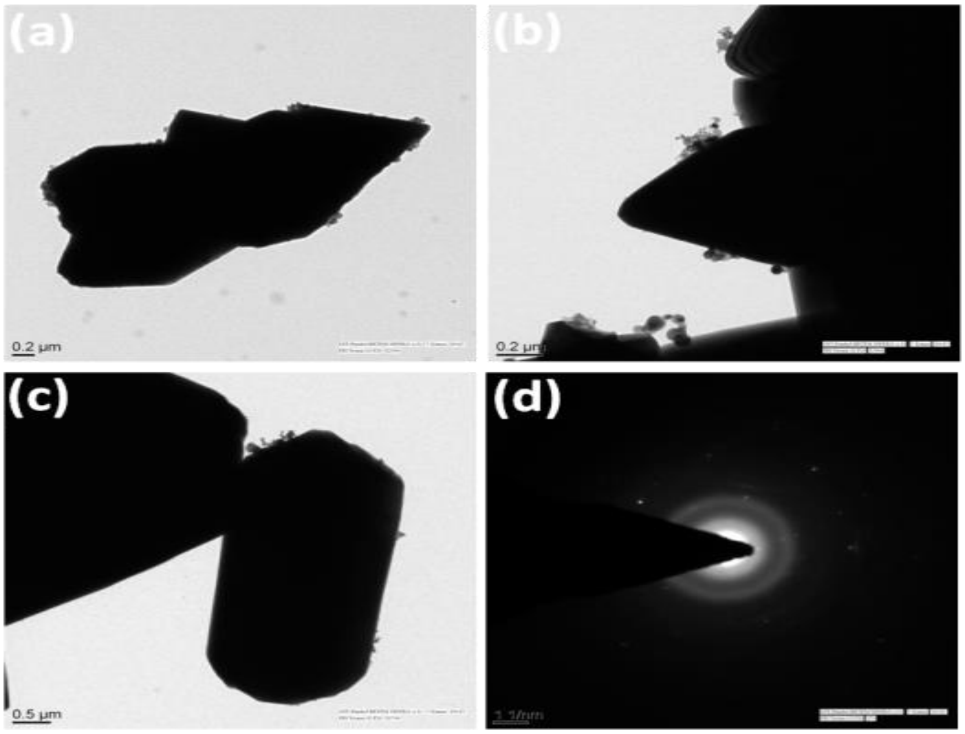

Figure 3.69. (a) Lattice fringe, (b), (c) HRTEM images and (d) SAED pattern of **ZnO-45**.

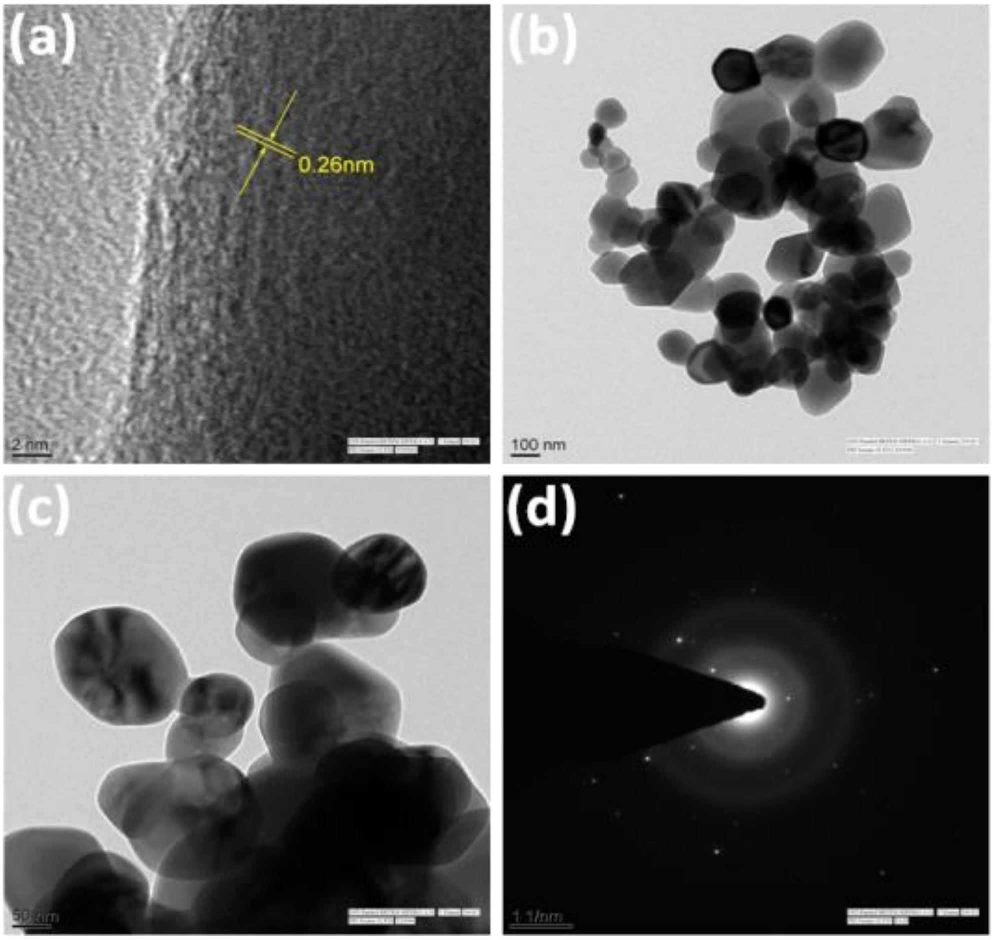

Figure 3.70. (a) Lattice fringe, (b), (c) HRTEM image and (d) SAED pattern of **ZnO-49**.

Raman studies. Raman spectroscopy is a nondestructive characterization technique to investigate the vibrational properties of nanomaterials. The vibrational spectra of the nanomaterials are greatly influenced by surface and size of the nanomaterials. The Raman scattering spectra of as prepared ZnO nanostructures are shown in Figure 3.71 with 785 nm laser light as an excitation source. For wurtzite phase ZnO which belongs to the space group $P6_3mc$ group theory predicts the existence of the following optic modes: $\Gamma_{opt} = A_1 + E_1 + 2E_2 + 2B_1$. A_1 and E_1 are polar modes whereas E_2 modes are non-polar modes. All are Raman active modes except two B_1 modes which are characterized as silent modes. The main dominant intense and sharp peak at around 436 cm^{-1} is assigned to E_2 high mode of wurtzite ZnO and the peak at 325 cm^{-1} is associated with the second-order Raman spectrum originating from the Zone-boundary phonons.[82] Since no peak at around 584 cm^{-1} was observed which clearly indicates the absence of defects in the as-prepared samples.

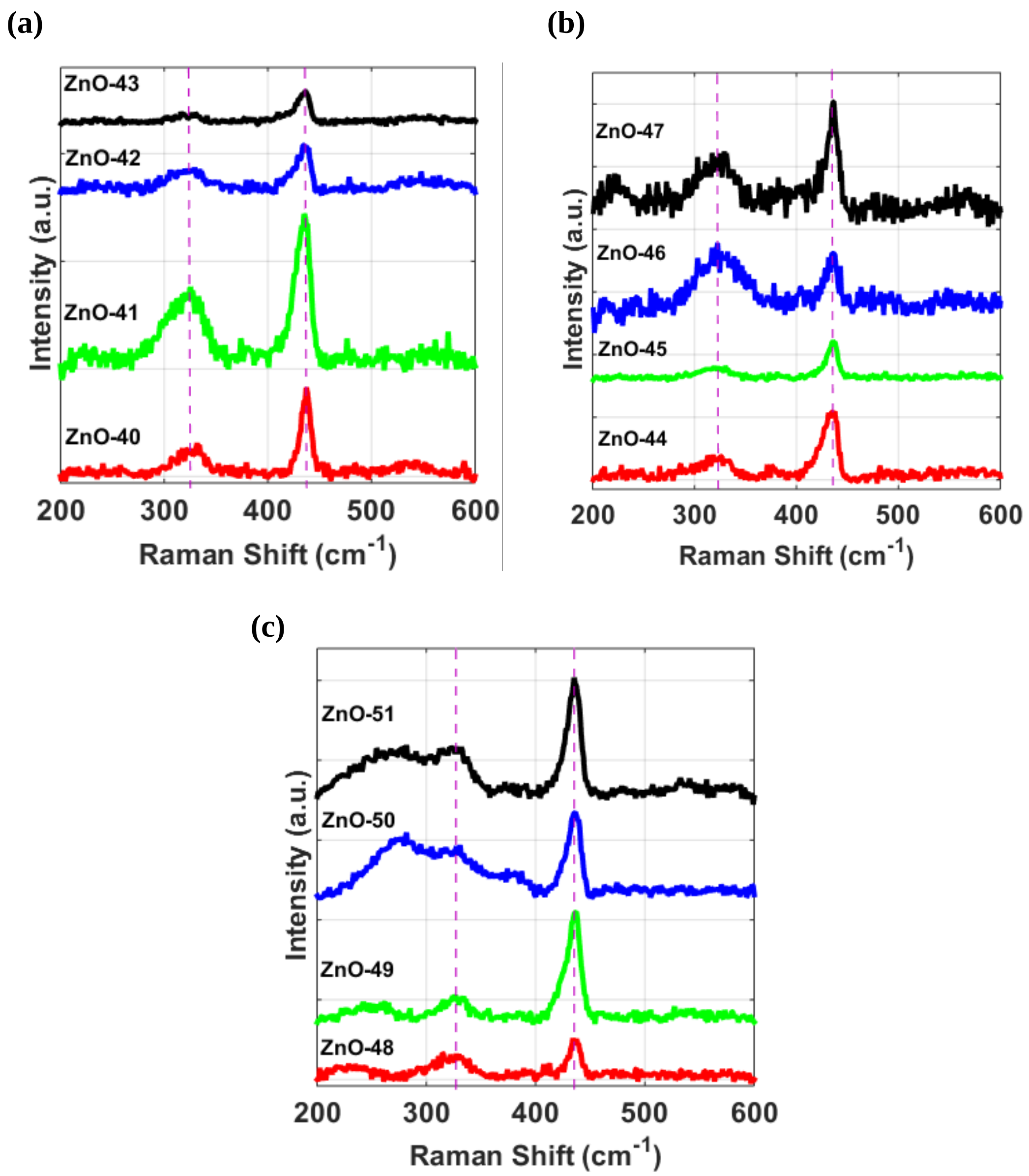

Figure 3.71. Raman spectra of as-grown ZnO nanostructures (a) **ZnO-40** to **ZnO-43**, (b) **ZnO-44** to **ZnO-47** and (c) **ZnO-48** to **ZnO-51**.

Optical properties. UV-visible absorption spectroscopy is widely being used technique to study the optical properties of the semiconductor nanoparticles. The size of the nanoparticles has a major role in changing the optical properties of the materials. Figure 3.72 represents the room temperature UV-visible absorption spectrum of the as-prepared ZnO samples. At a particular wavelength, a sharp decrease in the reflectance represents the uniform distribution of the particles in the sample.

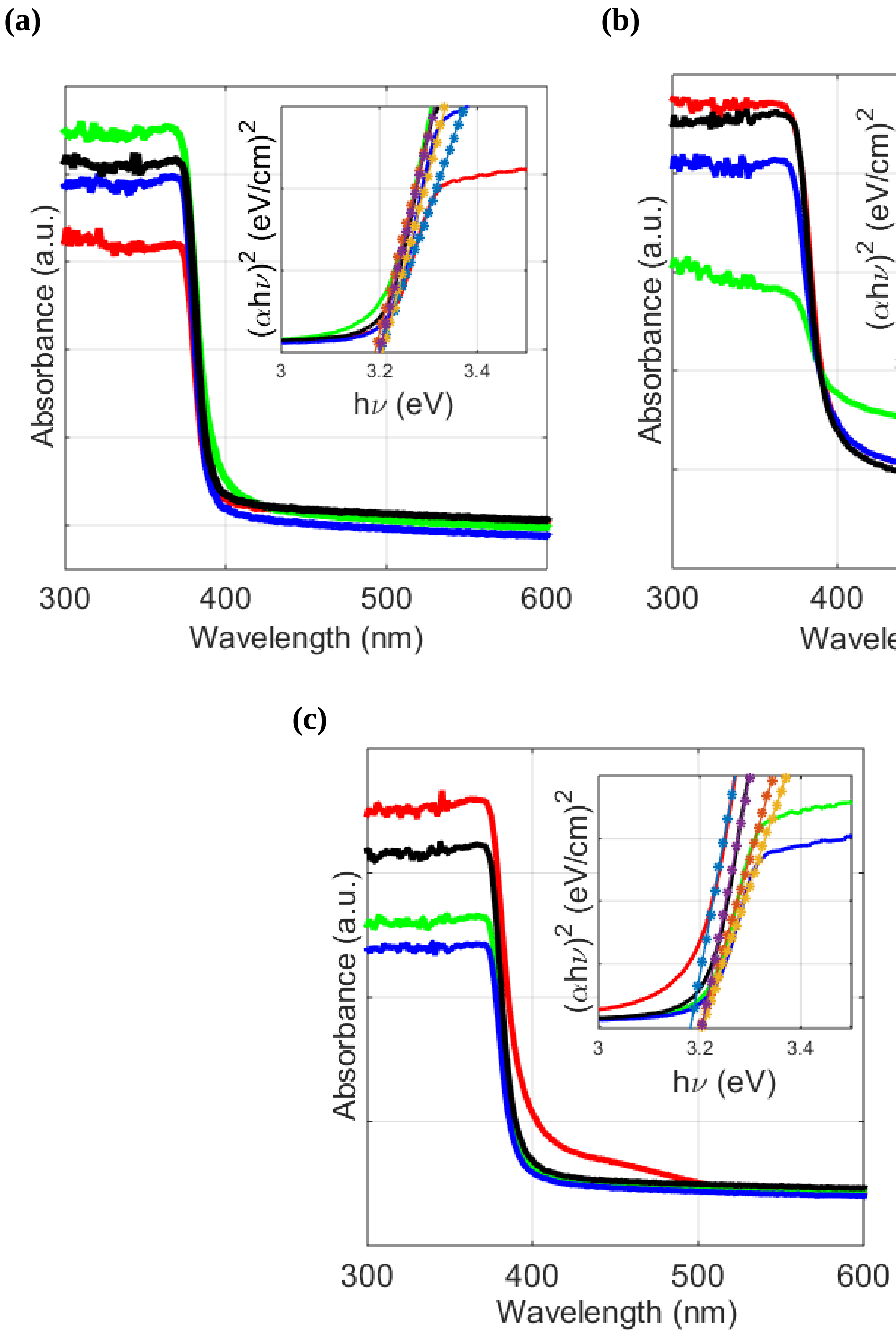

Figure 3.72. Solid state absorption spectra of (a) **ZnO-40 to ZnO-43** where red is for **ZnO-40**, green colour is for **ZnO-41,** blue colour represents **ZnO-42** and black colour represents **ZnO-43**, (b) **ZnO-44 to ZnO-47** where red is for **ZnO-44**, green colour is for **ZnO-45**, blue colour represents **ZnO-46** and black colour represents **ZnO-47**, (c) **ZnO-48 to ZnO-51** where red is for **ZnO-48**, green colour is for **ZnO-49**, blue colour represents **ZnO-50** and black colour represents **ZnO-51** where (inset) plot is between $(\alpha h\nu)^2$ versus $(h\nu)$.

The direct band gap energy (E_g) for the ZnO samples is determined from the graph of hν vs $(\alpha h\nu)^2$ for the absorption coefficient α which is related to the band gap E_g as $(\alpha h\nu)^2 = E_d (h\nu -$

$E_g)$[83], where hν is the photon energy and E_d is a constant. The extrapolation of the linear portion of the curve to absorption equal to zero gives the value of band gap energy E_g. The inset in the Figure 3.72 shows the band gap energies of the ZnO nanostructures. The band gap values of these nanostructures are given in Table 3.19. The average particle sizes of the ZnO samples can be calculated from the absorption spectra by using the method proposed by Meulenkamp:[84]

$$\frac{1240}{\lambda_{1/2}} = a + \frac{b}{D^2} - \frac{c}{D}$$

where a = 3.301, b = 294.0 and c = -1.09, $\lambda_{1/2}$ (nm) is the wavelength at which absorption becomes half of that of the shoulder, D (Å) is the diameter of the particle. Table 3.20 shows the particle sizes of the as-prepared ZnO samples.

Table 3.19. Band gap values of **ZnO-40** to **ZnO-51**

Sample	**Band Gap (E_g) (eV)**
ZnO-40	3.19
ZnO-41	3.18
ZnO-42	3.20
ZnO-43	3.19
ZnO-44	3.15
ZnO-45	3.03
ZnO-46	3.15
ZnO-47	3.17
ZnO-48	3.18
ZnO-49	3.19
ZnO-50	3.19
ZnO-51	3.20

Table 3.20. Calculated particle sizes of **ZnO-40** to **ZnO-51** from Meulenkamp's equation

Sample	Particle Size (nm)
ZnO-40	67
ZnO-41	67
ZnO-42	73
ZnO-43	171
ZnO-44	56
ZnO-45	55
ZnO-46	56
ZnO-47	62
ZnO-48	60
ZnO-49	68
ZnO-50	70
ZnO-51	74

Photoluminescence properties. At nanoscale, the physical properties of the semiconducting materials undergo drastic changes due to “quantum size effects”. As a result of quantum confinement, the band gap energy of the materials increases which can be clearly observed from the photoluminescence spectra for such materials. Further, the photocatalytic performance of as-prepared ZnO samples is closely associated with the surface defects. The surface defects or the surface conditions can be effectively studied by measuring their optical properties. Figure 3.73 shows the photoluminescence spectrum of ZnO samples with an excitation wavelength of 320 nm at room temperature. All the samples showed a strong and broad emission band at around 395 nm which corresponds to a near band gap excitonic emission originating from the radiative recombination of excitons whereas the emission band at around 508 nm in some of the samples originates from deep level transition in the surface defects[85]. This emission is caused by the radiative recombination of charge carriers due to the oxygen vacancies and the interstitials of O and Zn atoms. High crystal quality can be observed in some of the samples where only the UV emission is centered around 398 nm. Energy level diagrams for ZnO nanostructures are shown in Figure 3.74.

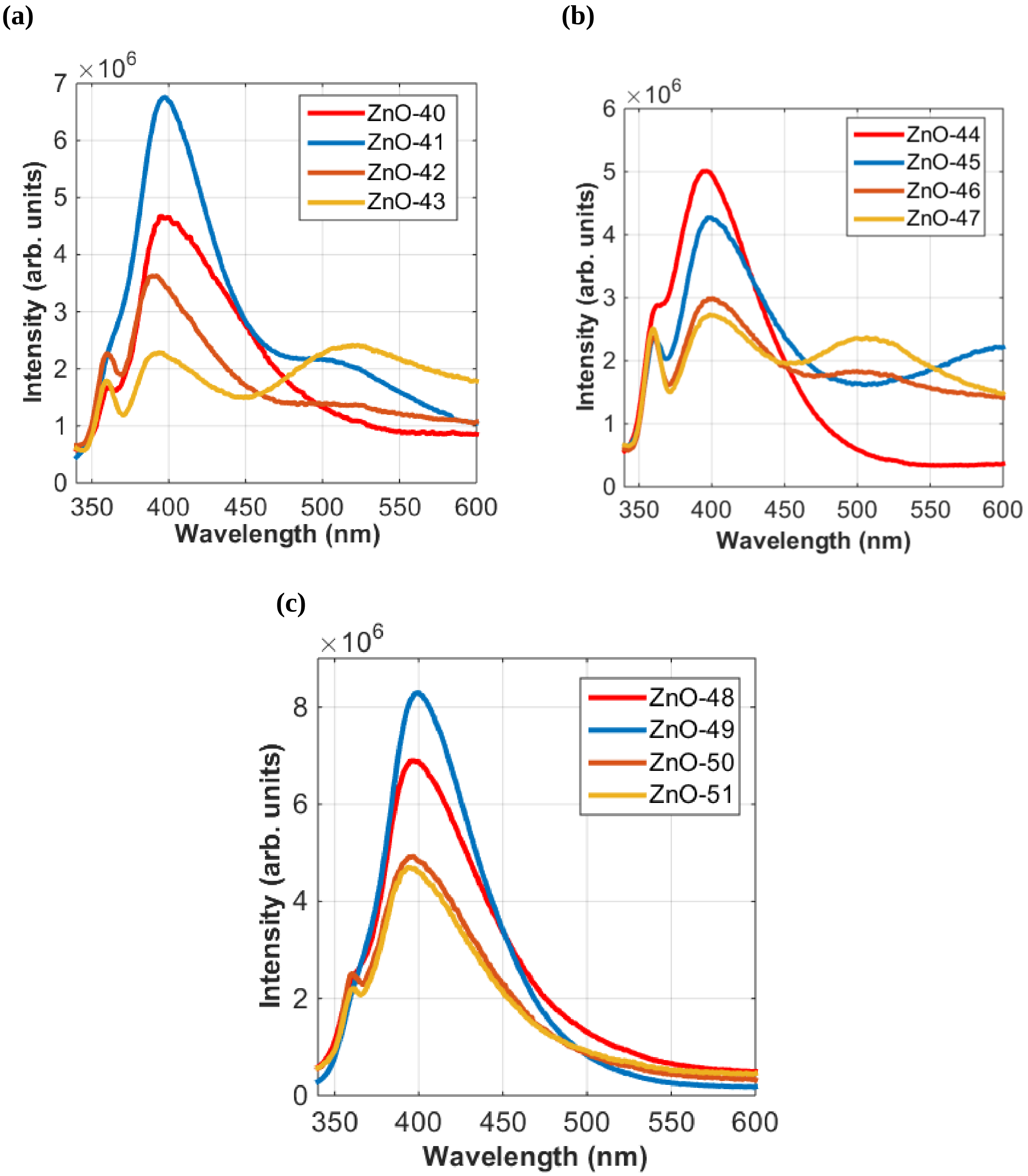

Figure 3.73. Room temperature photoluminescence spectra of (a) **ZnO-40** to **ZnO-43**, (b) **ZnO-44** to **ZnO-47**, (c) **ZnO-48** to **ZnO-51**.

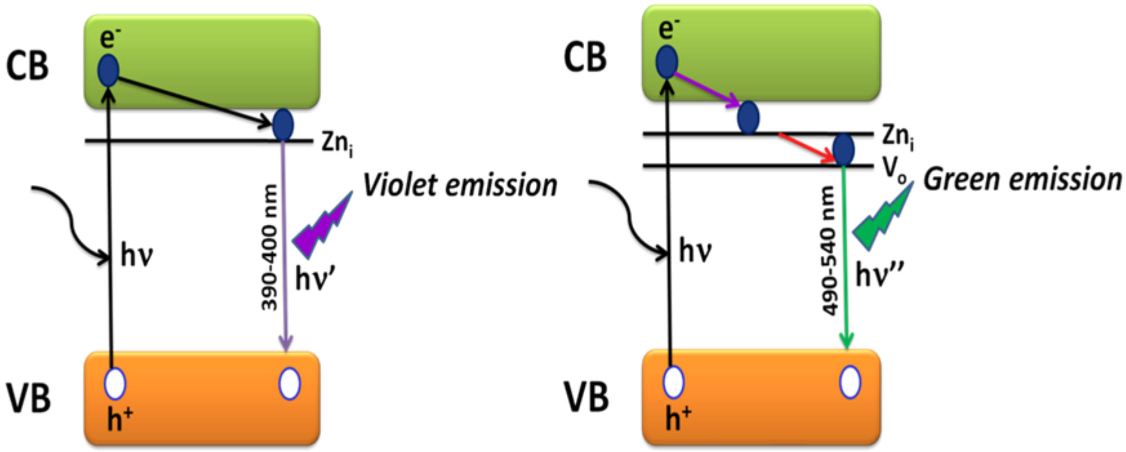

Figure 3.74. Energy level diagrams for **ZnO-40** to **ZnO-51**.

Photocatalytic Activity. The cationic dye, methylene blue (MB) was used as a contaminant to study the photocatalytic activity of the as-prepared ZnO samples. Owing to the absorption in the visible region MB has been extensively used as an indicator to verify the photocatalytic activities of the samples. The characteristic absorption peak at 663 nm for methylene blue dye is used to monitor the photocatalytic activities of the samples. A 100 mL of reaction mixture containing aqueous solution of methylene blue (9.37×10^{-2} M) and catalytic amount (0.2 g/L) of ZnO samples are taken in 15 mL glass vials and the mixtures were magnetically stirred in the dark for 30 mins to achieve absorption-desorption equilibrium and after that the samples were irradiated under UV light. With time evolution, the decolorization of MB was observed in terms of change in intensity of λ_{max} shown in Figure 3.75, 3.76 and 3.77. The percentage of decolorization was calculated as follows: [86]

$$\% \text{ decolorization} = \left[\frac{A_0 - A_t}{A_0}\right] \times 100$$

where A_o is the initial absorbance and A_t is the absorbance after irradiation at various time intervals. The photodegradation of methylene blue can be considered as a Langmuir-Hinshelwood first order kinetics reaction which can be expressed as: $\ln(C_0/C) = Kt$, where K is the reaction rate constant. A comparison of the adsorption behaviors of methylene blue dye on the surface of ZnO samples is shown in Figure 3.78. The degradation ability and the rate constants of the **ZnO-40** to **ZnO-51** are given in Table 3.21, 3.22 and 3.23. It was observed that the ZnO samples calcined for 12 hours showed better photocatalytic performance than rest of the samples. From the photocatalytic studies of MB, it can be concluded that the rate of degradation was found to be faster for ZnO synthesized from bpta ligand with the retention time of 12 hours. The percent degradation of MB using as-grown ZnO catalysts follows the order: **ZnO-49** > **ZnO-41** > **ZnO-45**.

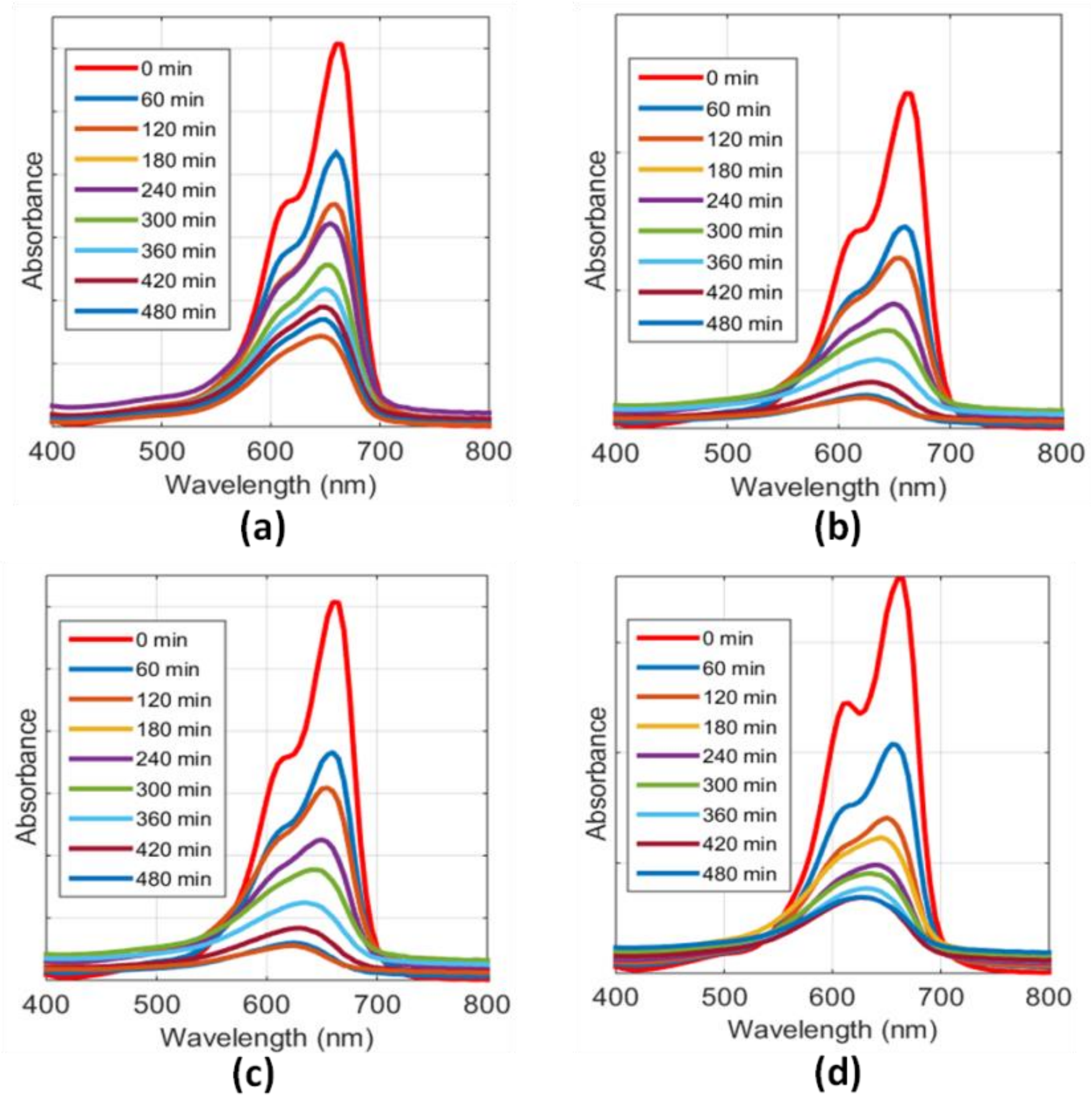

Figure 3.75. Absorption spectra of MB using as-grown **ZnO-40** to **ZnO-43** (a-d) catalysts for 8 hours under UV light.

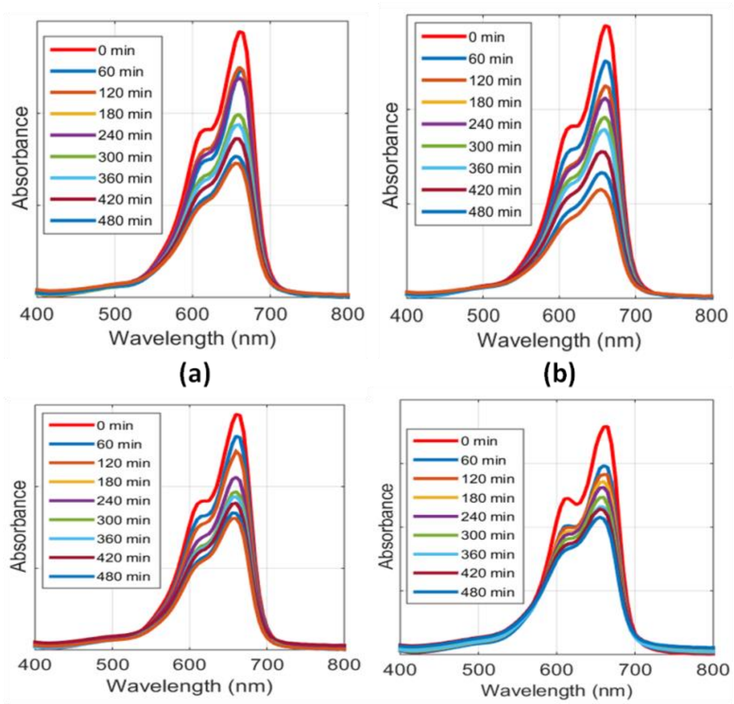

(c) (d)

Figure 3.76. Absorption spectra of MB using as-grown **ZnO-44** to **ZnO-47** (a-d) catalyst**s** for 8 hours under UV light.

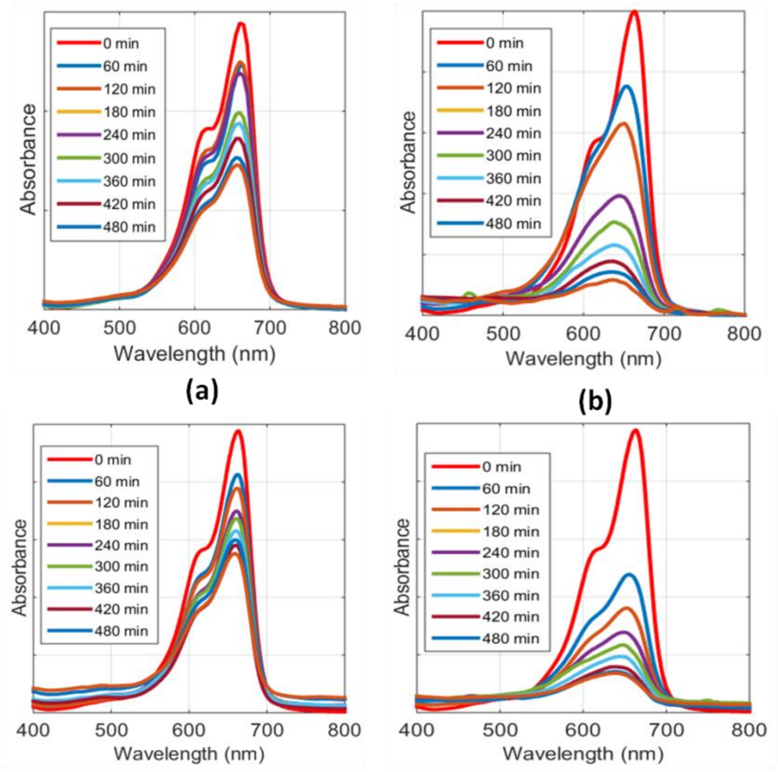

(c) (d)

Figure 3.77. Absorption spectra of MB using as-grown **ZnO-48** to **ZnO-51** (a-d) for 8 hours under UV light.

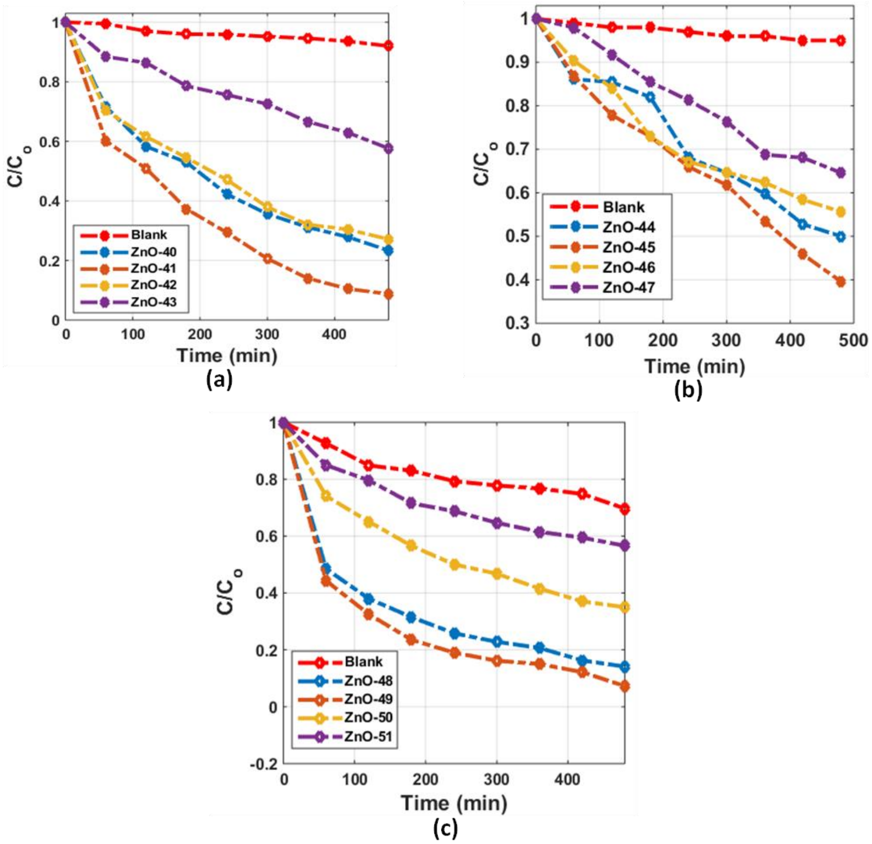

Figure 3.78. Comparison of photocatocatalytic degradation of MB over as-grown ZnO catalysts.

Table 3.21. Percentage decolorization of **ZnO-40** to **ZnO-43** and their rate constants at different time intervals

Time (min)	% Decoloriz -ation **ZnO-40**	Rate Constant (min^{-1})	% Decoloriz -ation **ZnO-41**	Rate Constant (min^{-1})	% Decoloriz -ation **ZnO-42**	Rate Constant (min^{-1})	% Decoloriz -ation **ZnO-43**	Rate Constant (min^{-1})
0	0	0	0	0	0	0	0	0
60	29	0.00565	40	0.00852	30	0.00586	42	0.00902
120	42	0.00452	49	0.00562	38	0.00402	60	0.00775
180	47	0.00351	63	0.00554	45	0.00335	65	0.00592
240	58	0.00361	71	0.00514	52	0.00312	72	0.00538
300	64	0.00342	79	0.00529	62	0.00324	75	0.00461
360	69	0.00322	86	0.00548	69	0.00323	78	0.00427
420	72	0.00303	90	0.00553	70	0.00286	81	0.00393
480	76	0.00301	91	0.00502	73	0.00271	81	0.00343

Table 3.22. Percentage decolorization of **ZnO-44** to **ZnO-47** and their rate constants at different time intervals

Time (min)	% Decolori-zation **ZnO-44**	Rate Constant (min^{-1})	% Decolori-zation **ZnO-45**	Rate Constant (min^{-1})	% Decolori-zation **ZnO-46**	Rate Constant (min^{-1})	% Decolori-zation **ZnO-47**	Rate Constant (min^{-1})
0	0	0	0	0	0	0	0	0
60	13	0.00236	13	0.00236	9	0.00163	2	0.00391
120	14	0.00131	22	0.00211	16	0.00146	8	0.00251
180	18	0.00108	27	0.00173	27	0.00176	14	0.00207
240	31	0.00154	34	0.00172	33	0.00167	19	0.00177
300	35	0.00143	38	0.00160	35	0.00144	23	0.00160
360	40	0.00143	46	0.00172	38	0.00132	31	0.00161
420	47	0.00151	54	0.00185	42	0.00129	32	0.00142
480	49	0.00143	60	0.00191	44	0.00121	35	0.00135

Table 3.23. Percentage decolorization of **ZnO-48** to **ZnO-51** and their rate constants at different time intervals

Time (min)	% Decolori-zation **ZnO-48**	Rate Constant (min^{-1})	% Decolori-zation **ZnO-49**	Rate Constant (min^{-1})	% Decolori-zation **ZnO-50**	Rate Constant (min^{-1})	% Decolori-zation **ZnO-51**	Rate Constant (min^{-1})
0	0	0	0	0	0	0	0	0
60	15	0.00272	55	0.01353	26	0.00503	51	0.02212
120	20	0.00190	67	0.00933	34	0.00353	63	0.01337
180	28	0.00186	76	0.00800	44	0.00318	72	0.01037
240	31	0.00154	81	0.00688	49	0.00285	76	0.00850
300	35	0.00146	84	0.00613	53	0.00254	80	0.00743
360	38	0.00134	85	0.00533	59	0.00245	84	0.00677
420	40	0.00122	87	0.00500	63	0.00237	85	0.00599
480	43	0.00119	93	0.00543	65	0.00220	86	0.00536

Adsorption Dynamics

To identify the type of adsorption mechanism in order to determine the effectiveness of sorption of ZnO samples onto the MB dye, three different models were studied to predict the adsorption kinetics[87] of ZnO samples on methylene blue dye (MB). These kinetic models included Elovich's, Intra-particle diffusion and Pseudo-second order.

Elovich's equation:

Elovich's equation is used to describe the second-order kinetics which involves the chemisorption process but no specific mechanism for adsorbate-adsorbent can be proposed from the application of this equation. This model indicates how strong the adsorbates are held on the surface of adsorbents.[88-89] The linear form of the equation is proposed by Chien and Clayton[90] which can be expressed as follows:

$$q_t = \frac{lna_e\, b_e}{b_e} + \frac{\ln t}{b_e}$$

where a_e is the initial adsorption rate (mg/g min), and the parameter b_e is related to the extent of surface coverage and activation energy for chemisorptions (g/mg). These constants can be obtained from the slope and intercept of the plot of q_t vs ln(t). The plots of the samples fitted by this equation are shown in (Figure 3.79 to 3.81). The coefficient of regression values clearly indicates that the data is fitting well into this model.

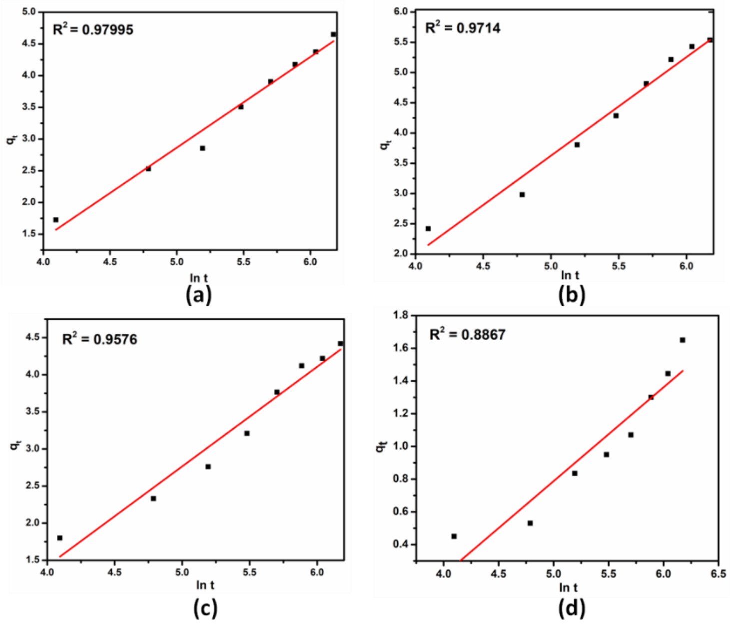

Figure 3.79. Elovich's kinetic model of **ZnO-40** to **ZnO-43** (a-d) for the removal of MB dye.

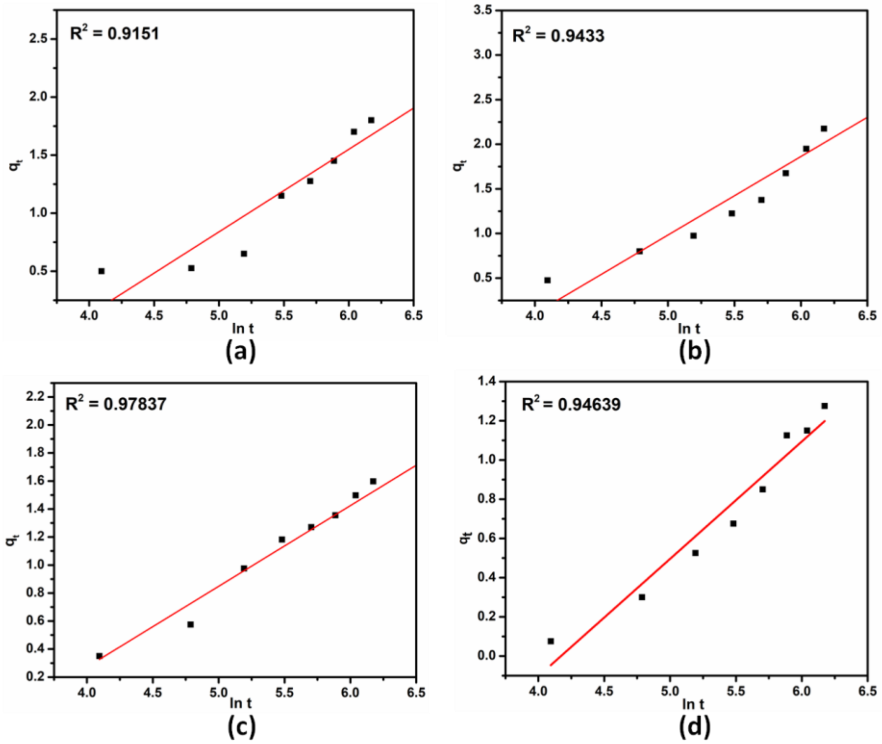

Figure 3.80. Elovich's kinetic model of **ZnO-44** to **ZnO-47** (a-d) for the removal of MB dye.

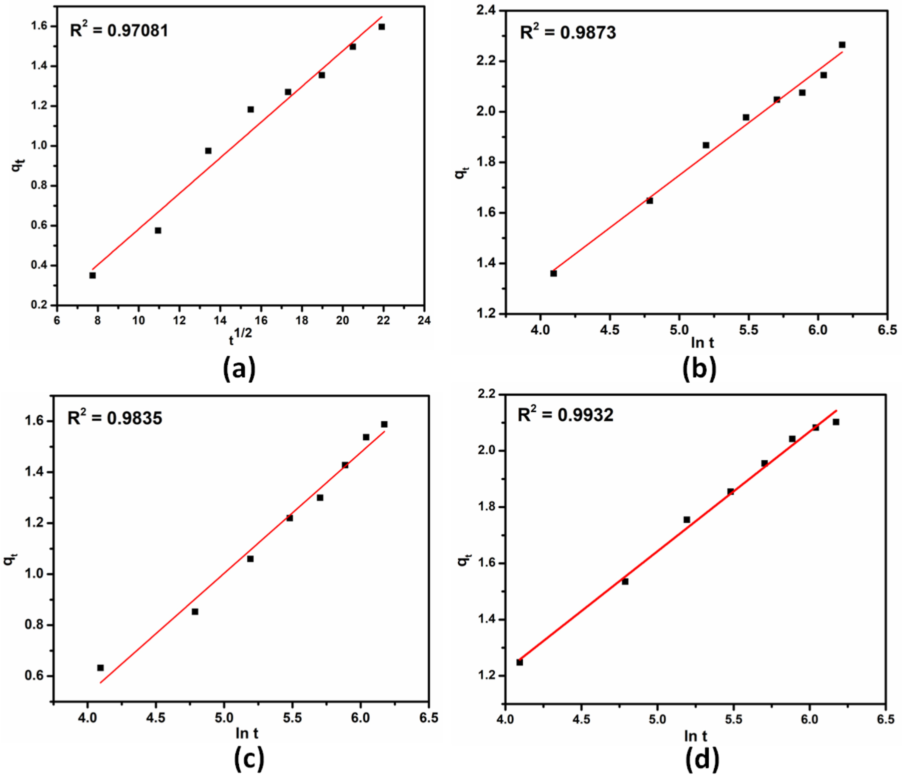

Figure 3.81. Elovich's kinetic model of **ZnO-48** to **ZnO-51** (a-d) for the removal of MB dye.

Table 3.24. Fitted elovich's kinetic model parameters for the removal of MB dye

Sample	Initial adsorption rate, a_e (mg/g min)	Activation energy, b_e (g/mg)	R^2
ZnO-40	0.0174	0.6993	0.9799
ZnO-41	0.1016	0.6137	0.9714
ZnO-42	0.0709	0.7451	0.9576
ZnO-43	0.0152	1.7436	0.8867
ZnO-44	0.0155	1.4066	0.9151
ZnO-45	0.0181	1.1362	0.9433
ZnO-46	0.0169	1.7355	0.9783
ZnO-47	0.0092	1.6708	0.9463
ZnO-48	0.0144	2.9282	0.9708
ZnO-49	0.1886	2.4084	0.9873
ZnO-50	0.0265	2.1105	0.9835
ZnO-51	0.1362	2.3502	0.9932

Intraparticle diffusion model:

This model describes that the rate of adsorption process is controlled by the speed of diffusion of adsorbate into the adsorbent.[91-92] The initial rate of intra-particle diffusion is given by Webber and Morris[93] and can be expressed as:

$$q_t = k_i t^{1/2}$$

If the plot of q_t vs $t^{1/2}$ is linear and passes through the origin then the rate of adsorption is controlled by this model. It is observed that other kinetic models may be operating when the plots don't pass through the origin. The plots of the samples fitted according to this model are shown in (Figure 3.82 to 3.84).

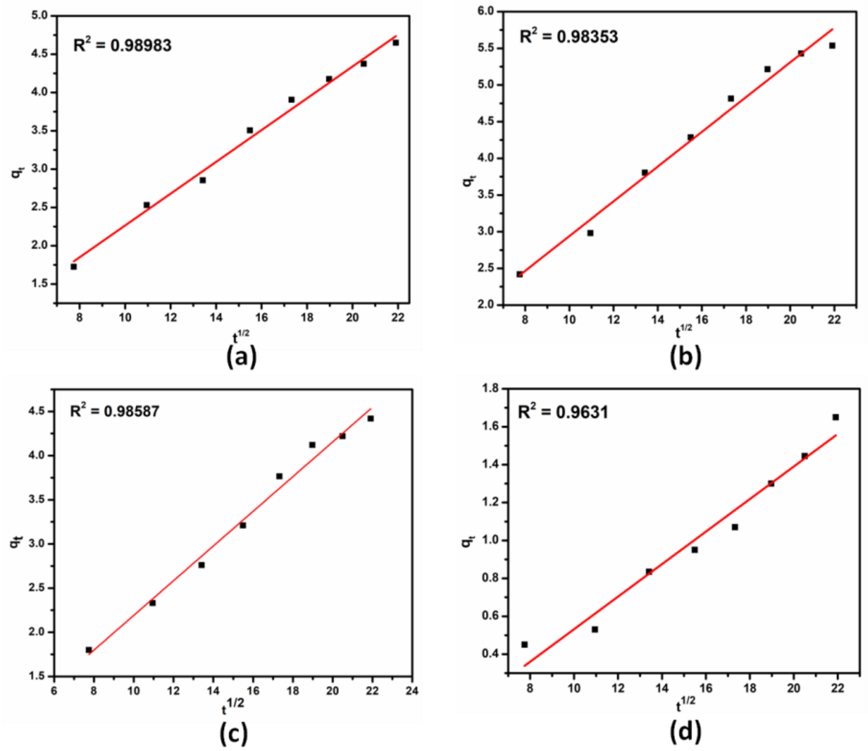

Figure 3.82. Intraparticle diffusion kinetic model of **ZnO-40** to **ZnO-43** (a-d) for the removal of MB dye.

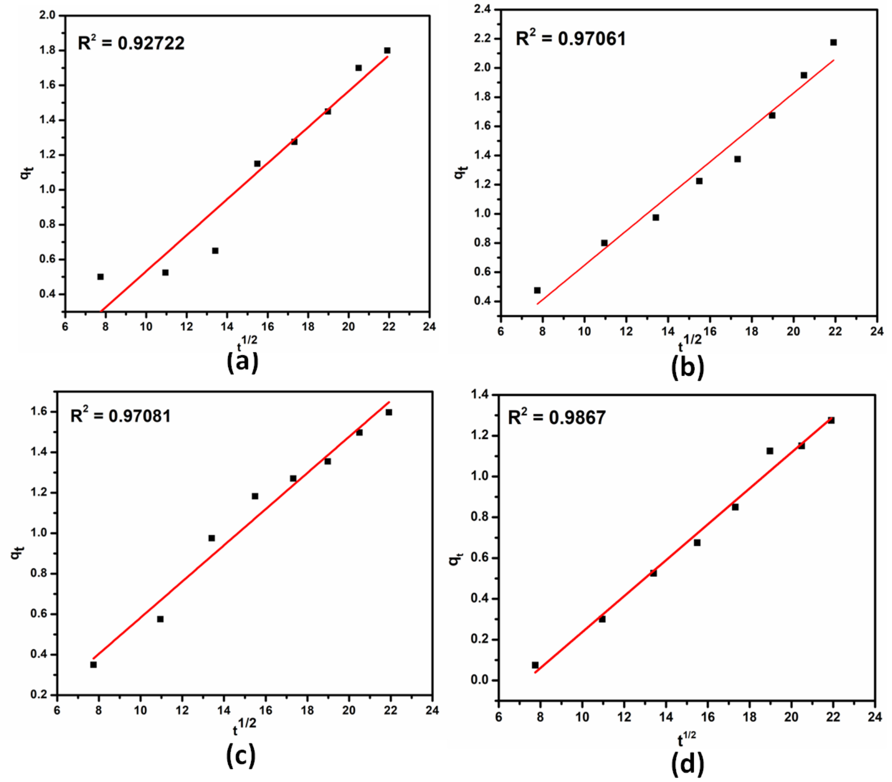

Figure 3.83. Intraparticle diffusion kinetic model of **ZnO-44** to **ZnO-47** (a-d) for the removal of MB dye.

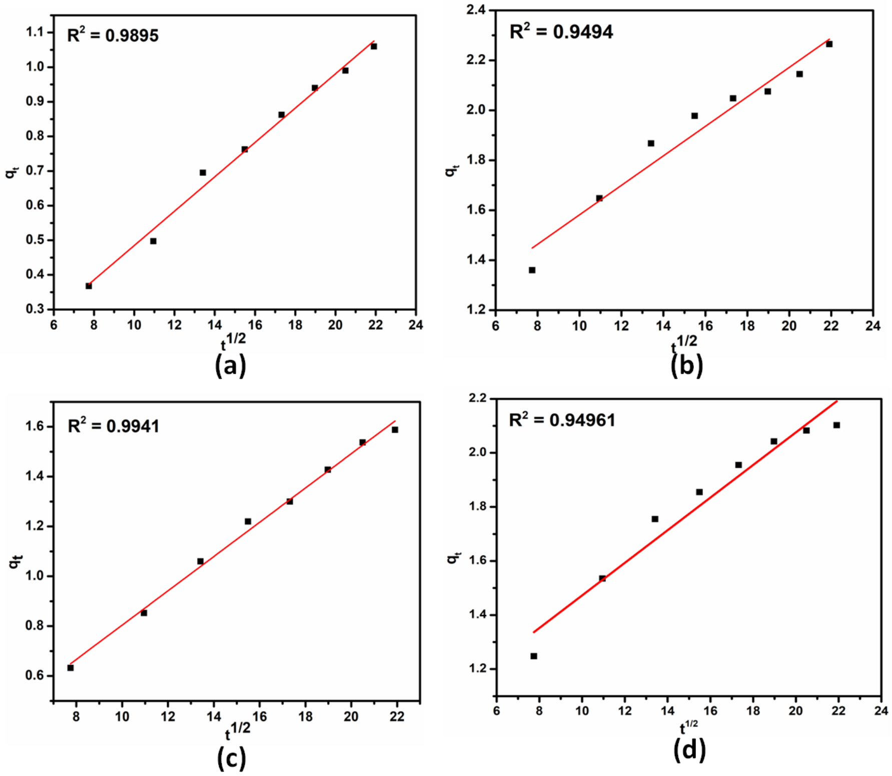

Figure 3.84. Intraparticle diffusion kinetic model of **ZnO-48** to **ZnO-51** (a-d) for the removal of MB dye.

Table 3.25. Fitted intraparticle diffusion kinetic model parameters for the removal of MB dye

Sample	**Rate constant, K$_i$ (mg/g min$^{1/2}$)**	**Intercept, C**	**R^2**
ZnO-40	0.2075	0.1886	0.98983
ZnO-41	0.2367	0.5735	0.98353
ZnO-42	0.1963	0.2278	0.98587
ZnO-43	0.0740	-0.1240	0.96310
ZnO-44	0.1033	-0.5011	0.92722
ZnO-45	0.1179	-0.5315	0.97061
ZnO-46	0.0894	-03113	0.97081
ZnO-47	0.0880	-0.6432	0.98671
ZnO-48	0.0496	-0.0113	0.98950
ZnO-49	0.0590	0.9914	0.94946
ZnO-50	0.0687	0.1162	0.99412
ZnO-51	0.0603	0.8694	0.94961

Pseudo-second-order model:

When the rate of sorption follows the second order mechanism, the pseudo-second order rate equation is represented by its linear form as shown below:

$$\frac{t}{q_t} = \frac{1}{k_2 q_e^2} + \frac{t}{q_e}$$

where k_2 is the rate constant of pseudo-second-order adsorption (g/mg min) and q_t (mg/g) is the amount of adsorbate retained at time (t).
The initial adsorption rate, h, (mg/g min) is expressed as:

$$h = k_2\ q_e^2$$

If the plot of t/qt versus t gives a linear relationship the constants k_2 and h can be determined from the intercept and slope of the line obtained from the plot. The surface adsorption involving chemisorption is the rate limiting step for this process.[94-96] The removal of the dye from the aqueous solution is due to the physicochemical interactions between the phases. (Figure 3.85, 3.86 and 3.87) shows the plots fitted using this model. From the correlation coefficients it can be concluded that this model has the best agreement with the experimental data.

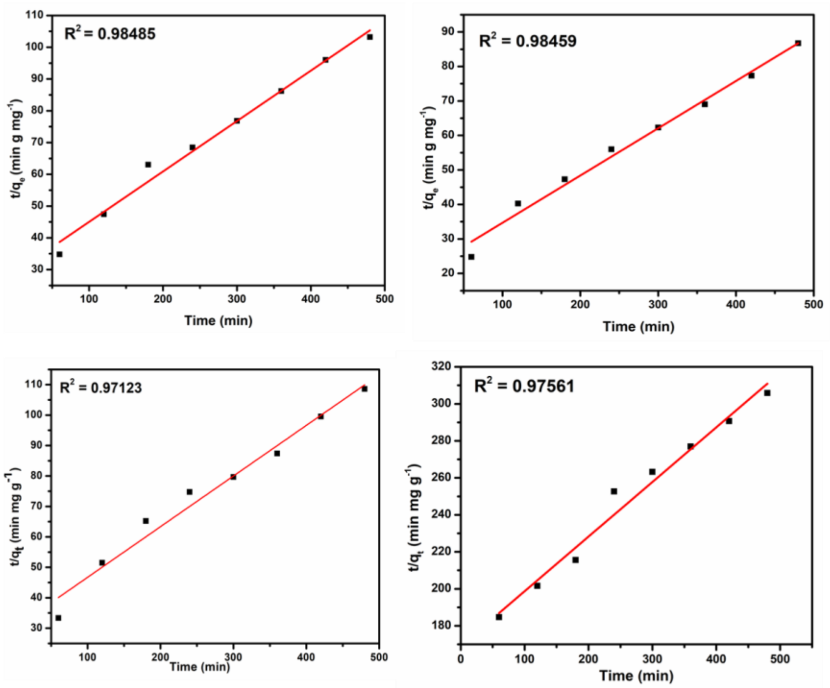

Figure 3.85. Pseudo second order kinetic model of **ZnO-40** to **ZnO-43** (**a-d**) for the removal of MB dye.

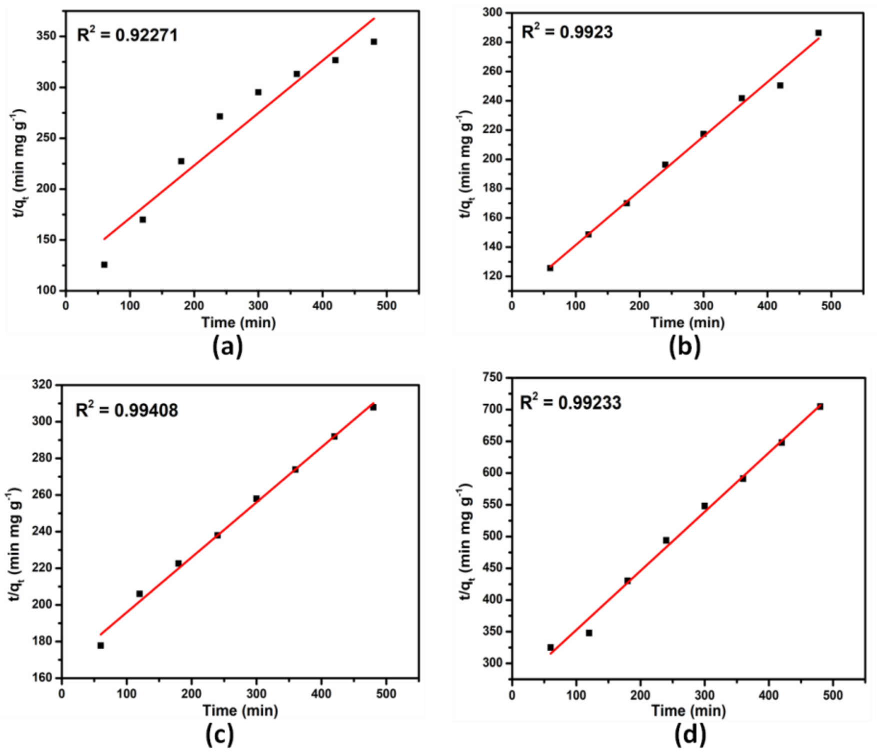

Figure 3.86. Pseudo second order kinetic model of **ZnO-44** to **ZnO-47** (**a-d**) for the removal of MB dye.

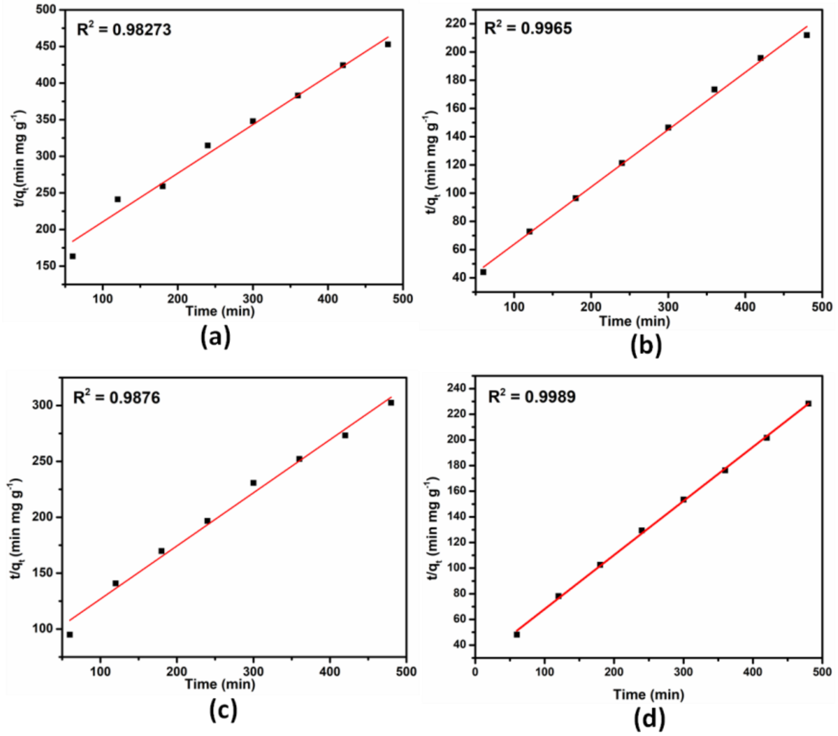

Figure 3.87. Pseudo second order kinetic model of **ZnO-48** to **ZnO-51** (**a-d**) for the removal of MB dye.

Table 3.26. Fitted pseudo-second-order kinetic model parameters for the removal of MB dye

Sample	Initial adsorption rate, h (mg/g min)	Rate constant, K_2 (g/mg)	R^2
ZnO-40	0.0343	0.000864	0.9848
ZnO-41	0.0476	0.000893	0.9845
ZnO-42	0.0332	0.000919	0.9712
ZnO-43	0.0059	0.000516	0.9756
ZnO-44	0.0083	0.002217	0.9227
ZnO-45	0.00958	0.00132	0.9923
ZnO-46	0.00603	0.000544	0.9940
ZnO-47	0.00385	0.003342	0.9923
ZnO-48	0.0069	0.003064	0.9827
ZnO-49	0.0431	0.007101	0.9965
ZnO-50	0.0126	0.002851	0.9876
ZnO-51	0.0385	0.006844	0.9989

3.2 CdS NANOSTRUCTURES

Chalcogenides, such as CdS, is one of the most important semiconductors with a direct band gap of 2.43 eV at room temperature and find its applications in the future optoelectronic devices such as photodetectors, solar cells, photovoltaic devices, photoluminescence sensors and light emitting diodes[97-114] due to the tunable electronic band gap depending on the size and shape of nanocrystals. It also finds its applications in chemo sensing, biosensing and bioimaging. Various synthetic methods have been used to synthesise CdS nanoparticles including soft chemical reaction, solid state reaction, sol-gel process, hydrothermal synthesis, sonochemical preparation, microwave heating and reverse micelle.[115-120] Among all the methods, the hydrothermal technique is a promising one to control the properties of nanocrystallites of CdS, such as crystal phase, size, morphology and luminescence. This method also presents many advantages over other growth processes, such as the use of simple equipment, low process temperature, catalyst free growth, low cost, high purity, environment friendly and less hazardous.[121-123]

3.2.1 Effect of solvent

In this study, we have designed a novel facile template-free and surfactant-less solvothermal method under mild conditions (120 °C for 6 h) for the synthesis of pure CdS nanostructures (**CdS-1** to **CdS-5**) with different morphologies using a 1D coordination polymer of Cd(II) $\{[Cd_2(bpma)_2(adc)_2]\cdot 2H_2O\}_n$ (where bpma = N,N'-bis(pyridylmethyl) amine and adc = acetylene dicaboxylate) as the source of Cd^{2+} ions and thiourea as the source of sulphide ions in different solvents (methanol, ethanol, t-butanol and water). For comparison, the use of $Cd(OAc)_2.2H_2O$ as the precursor in methanol under the same conditions provides aggregated microspheres of CdS. Two such morphologies which are rare for any other nanomaterials, namely walnut-shaped multi-hollow hierarchical microspheres and honeycomb like porous nanostructures, are discovered for CdS for the first time in methanol and t-butanol. There is a tremendous effect on the mean size with the diversity of these nanostructures.

Synthesis of CdS nanostructures. CdS nanoparticles were synthesised using $\{[Cd_2(bpma)_2(adc)_2]\cdot 2H_2O\}_n$ as the Cd(II) source and thiourea as the sulphur source in four different solvents (methanol, ethanol, t-butanol or water). For a typical synthesis, 0.034 mmol of $\{[Cd_2(bpma)_2(adc)_2]\cdot 2H_2O\}_n$ and 0.34 mmol thiourea (in the ratio 1:10) were added in a 7 mL Teflon reactor containing 3 mL of solvent. The hydrothermal reaction was carried out at 120 °C for 6 h. The as-synthesised mixture was centrifuged at

4000 rpm for 15 minutes to separate the solid from the solvent followed by washing the solid several times with the same solvent used in the synthesis. A solid collected via filtration was dried in air at 60 °C for 3 hours to obtain the powdered CdS nanoparticles of fine size (Scheme 3.17 and 3.18).

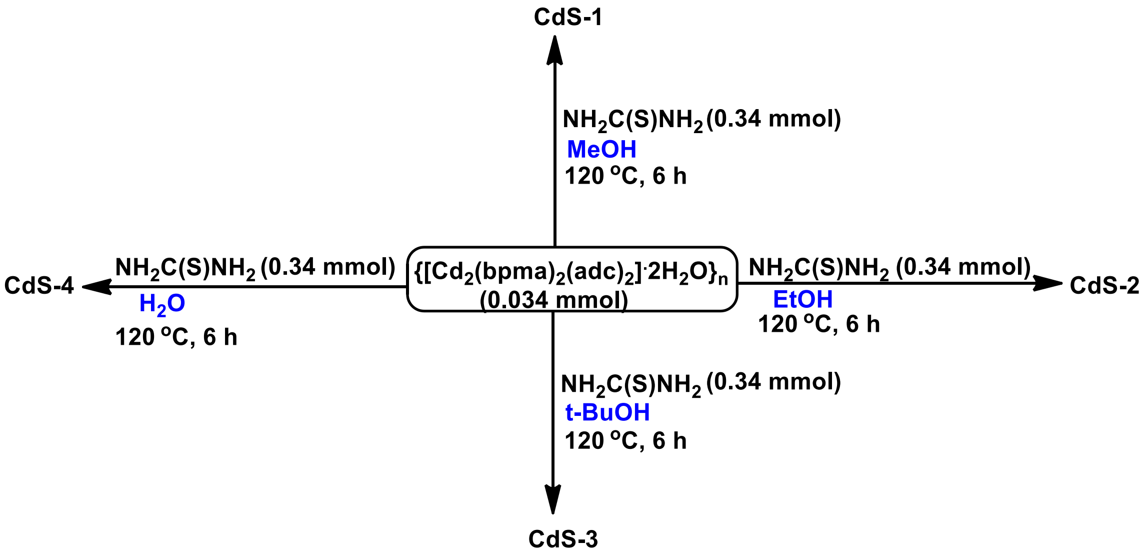

Scheme 3.17. Synthesis of **CdS-1** to **CdS-4**.

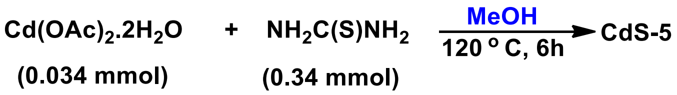

$$\underset{(0.034\ \mathrm{mmol})}{\mathrm{Cd(OAc)_2.2H_2O}} + \underset{(0.34\ \mathrm{mmol})}{\mathrm{NH_2C(S)NH_2}} \xrightarrow[120\ ^{\circ}\mathrm{C,\ 6h}]{\mathrm{MeOH}} \mathrm{CdS\text{-}5}$$

Scheme 3.18. Synthesis of **CdS-5**.

Powder X-ray diffraction studies. The purity and crystalline phase of hydrothermally synthesised CdS nanostructures were analysed by PXRD. The PXRD patterns of CdS samples synthesised in different solvents is shown in Figure 3.88. All the peaks could be clearly indexed to cubic phase CdS (JCPDS 75-1546). The strong and sharp diffraction peaks from the (111), (220) and (311) facets suggests that the as-prepared samples are well crystallised.[124] It can be clearly observed that there is no formation of (311) plane in the alcoholic solvents (Figure 3.88a) whereas its formation can be seen in aqueous solution and methanol (Figure 3.88b).

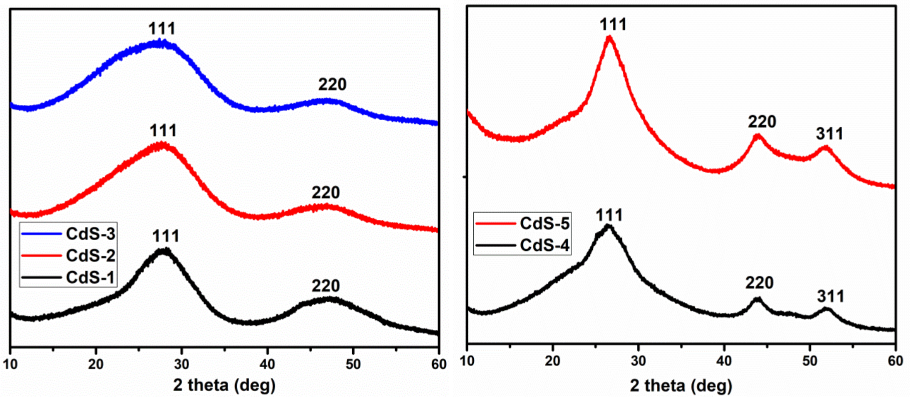

(a) **(b)**

Figure 3.88. (a) PXRD patterns of **CdS-1** to **CdS-3**, (b) PXRD patterns of **CdS-4** and **CdS-5**.

Surface analysis. The surface analysis of the as prepared samples was done by FESEM, HRTEM and AFM. The overall growth of CdS nanostructures were observed after 6 hours shown in Figure 3.89a-e. The rare morphology of walnut like multi-hollow hierarchical structures in **CdS-1** could be clearly observed. The elemental mapping and EDX spectrum are shown in Figure 3.89f. The hierarchical structure is composed of dense and short nanofibers with 172 nm diameter.

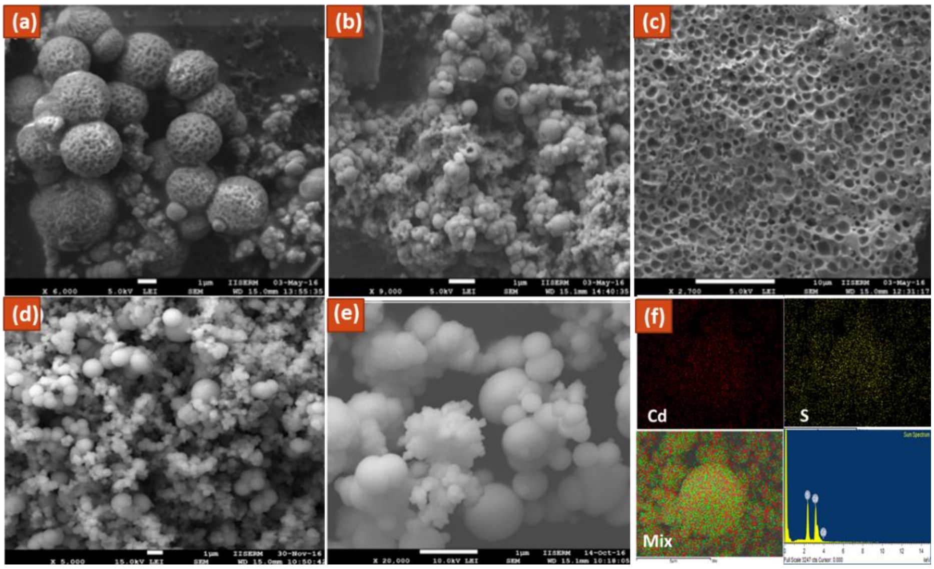

Figure 3.89. FESEM images of (a) walnut like multi-hollow hierarchical structures (**CdS-1**), (b) hollow nanospheres (**CdS-2**), (c) honeycomb like porous nanostructures (**CdS-3**), (d) aggregated nanospheres (**CdS-4**) (e) aggregated microspheres (**CdS-5**), (f) Elemental mapping and EDX spectrum of walnut like multi-hollow hierarchical structures (**CdS-1**).

These nanofibers are connected to one another to form a sophisticated non-woven mesh. The surface of the material becomes more accessible with such network structure and is favourable for the applications as catalytic and sensing materials. Similarly, aggregated hollow nanospheres were observed in **CdS-2** whereas **CdS-3** yielded porous honeycomb like CdS nanostructures. Aggregated nanospheres were obtained in **CdS-4** and aggregated microspheres were seen in **CdS-5**. The SEM image gives the size of aggregated CdS nanoparticles and not the mean crystallite size. For further investigation of the morphology and crystallographic features, HRTEM measurements of **CdS-1** and **CdS-3** were performed. The low and high resolution TEM images show that the as-synthesised CdS samples are grown in high densities (Figure 3.90). The lattice spacing of 0.31 nm and 0.20 nm corresponds to d-spacing between the adjacent crystallographic faces of walnut like hierarchical structures. Whereas the lattice spacing of 0.33 nm is observed for honey-comb structure (Figure 3.90 (b)). The diffraction planes obtained from SAED pattern matches well with the XRD patterns in both the cases. The EDX spectra of **CdS-1** to **CdS-5** is shown in Figure 3.91 to 3.95.

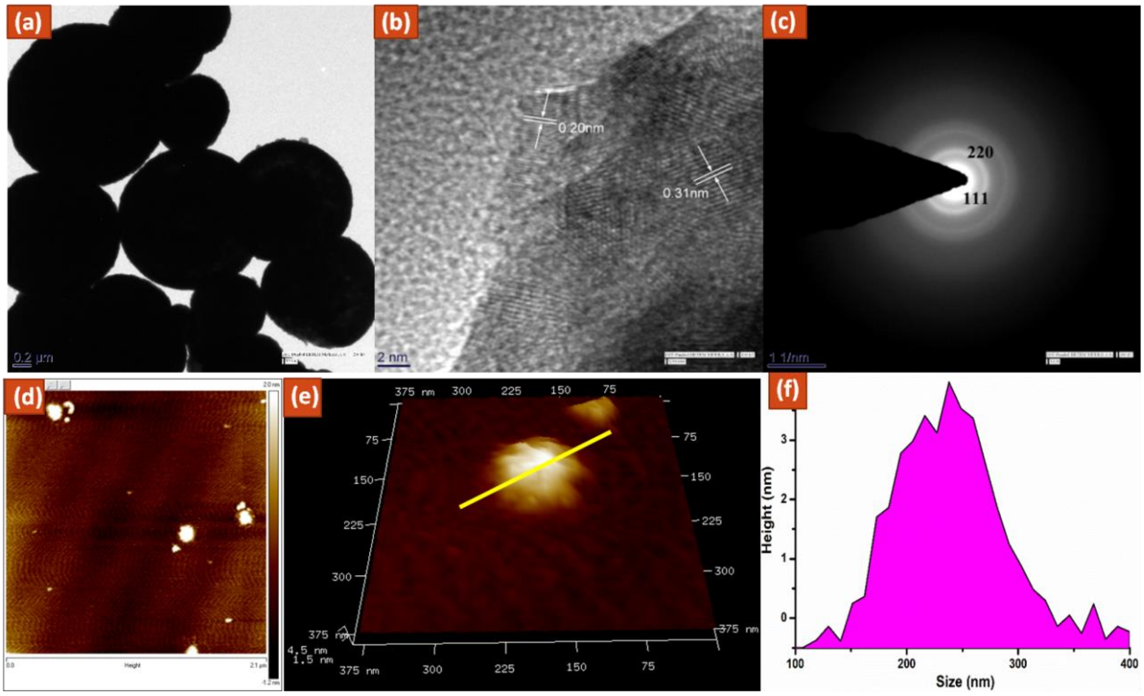

Figure 3.90. (a) HRTEM image, (b) the lattice fringe, (c) SAED pattern, (d) 2D AFM image, (e) 3D AFM image and (f) height profile of walnut like multi-hollow hierarchical structures of **CdS-1**.

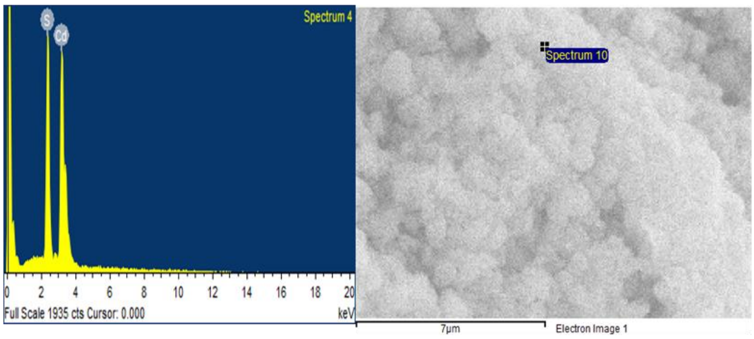

Element	Weight%	Atomic%
S K	25.10	54.02
Cd L	74.90	45.98
Totals	100.00	

Figure 3.91. EDX spectrum of **CdS-1**.

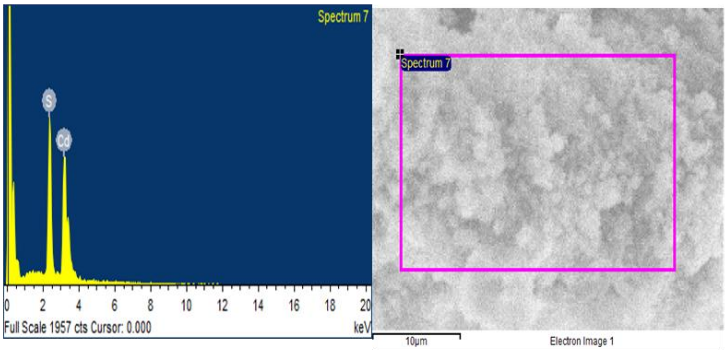

Element	Weight%	Atomic%
S K	28.55	58.35
Cd L	71.45	41.65
Totals	100.00	

Figure 3.92. EDX spectrum of **CdS-2**.

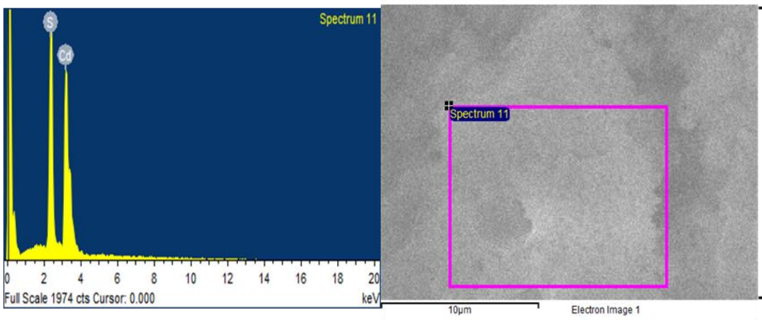

Element	Weight%	Atomic%
S K	28.00	57.69
Cd L	72.00	42.31
Totals	100.00	

Figure 3.93. EDX spectrum of **CdS-3**.

\

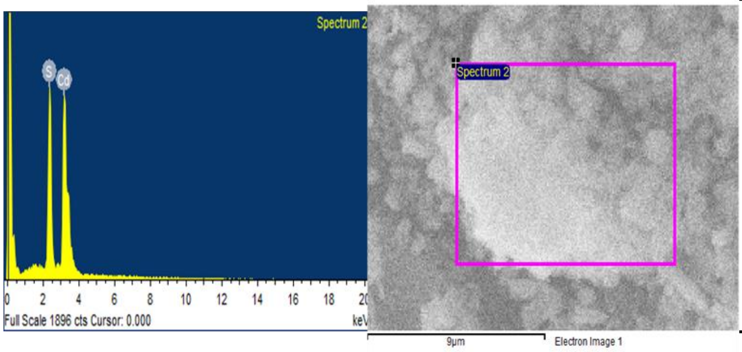

Element	Weight%	Atomic%
S K	24.34	52.99
Cd L	75.66	47.01
Totals	100.00	

Figure 3.94. EDX spectrum of **CdS-4**.

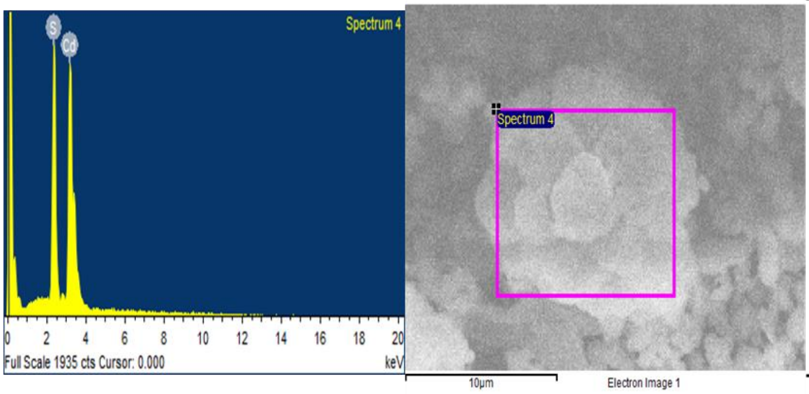

Element	Weight%	Atomic%
S K	25.10	54.02
Cd L	74.90	45.98
Totals	100.00	

Figure 3.95. EDX spectrum of **CdS-5**.

Furthermore, spherical walnut on the mica were observed for 1 by AFM where the section analysis profiles of the ring shaped assemblies of **CdS-1** showed height of 4-4.5 nm and average diameter of 150-200 nm (Figure 3.90 (f)) and spherical honeycomb on the mica were observed for **CdS-3** by AFM where the section analysis profiles of the ring shaped assemblies of **CdS-3** showed height of 20-22 nm and average diameter of 80-100 nm (Figure 3.96e).

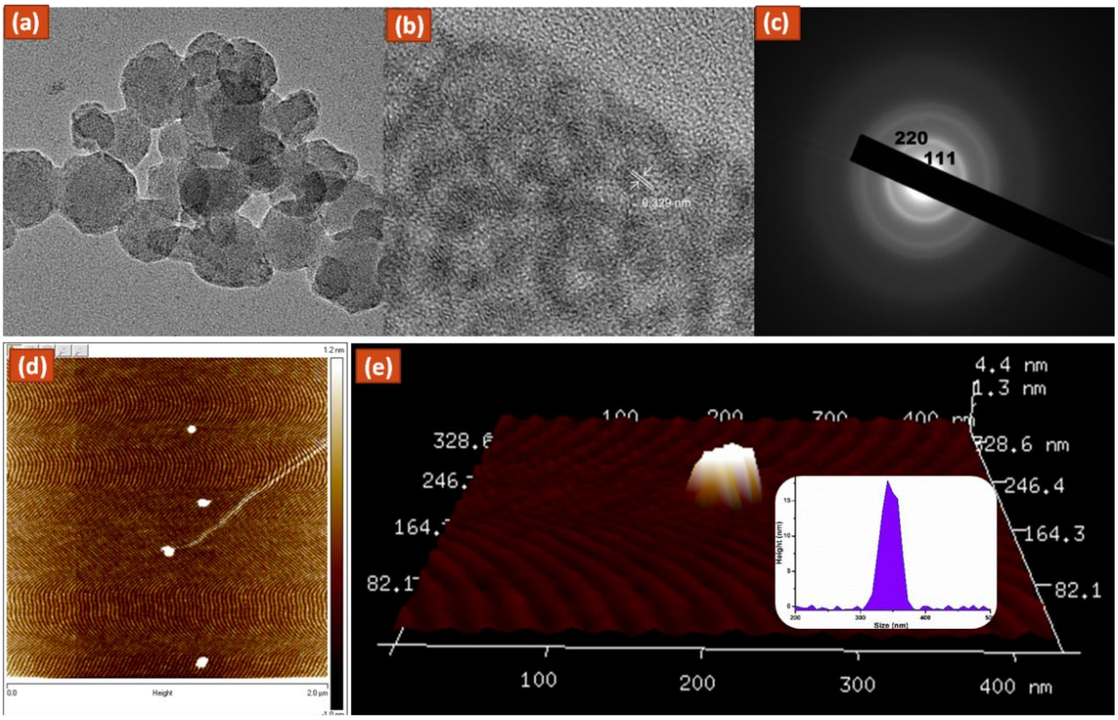

Figure 3.96. (a) HRTEM image, (b) the lattice fringe, (c) SAED pattern, (d) 2D AFM image and (e) 3D AFM image; (inset) height profile of honeycomb like porous nanostructures of **CdS-3**.

Formation mechanism of different CdS nanostructures. The formation of walnut like hierarchical structures for **CdS-1** can be explained by Ostwald Ripening Mechanism. Ostwald Ripening is an observed phenomenon in the colloidal dispersions and suspensions with polydisperse particle size distribution which describes the formation of larger particles at the expense of smaller particles. Initially, the nucleation starts in the reaction mixture followed by aggregation of the nanocrystals. Since larger particles are more energetically stable than the smaller particles, there is a gradual disappearance of smaller particles and eventually the large particles further grow in size with the progress of time. The formation of nanofibers was also observed in the reaction mixture at this stage. These nanofibers form a network outside the microspheres which explains the formation of walnut like hierarchical structures (Figure 3.97). Whereas, in case of **CdS-2** the aggregation of CdS particles give rise to the formation of solid sphere. Being highly soluble the small CdS particles slowly dissolve and diffuse into the surrounding solution at this stage. This leads to increase in the concentration of $Cd^{2+}$and S^{2-} ions in ethanol medium. With increased concentration levels, new CdS particles gets formed and attached to the pre-existing CdS particles on its exterior layer which explains the internal CdS dissolution and the growth of exterior shell forming a hollow CdS microsphere (Figure 3.97). The growth mechanism of honeycomb structures of **CdS-3** in t-BuOH can be well explained as follows: Initially, the nucleation occurs in the supersaturated solution which leads to the formation of CdS nuclei. The concentration of these CdS nuclei gets reduced and the formation of hexagonal nanoparticles takes place by Ostwald Ripening mechanism. These hexagonal nanoparticles grow anisotropically in t-BuOH to form a 2D thin-layered CdS nanosheet by oriented attachment. As the reaction proceeds further, a 2D growth of these nanoparticles leads to the formation of even bigger sheets and the self-organisation of these nanosheets form honeycomb structures with cavities. So far, this rare morphology has not been reported for CdS. Similarly, **CdS-4** and **CdS-5** follows the Ostwald Ripening mechanism where the formation of aggregated nanospheres and microspheres can be clearly observed. The above-mentioned methods for the formation of these CdS nanostructures using different solvents are cheap, environment friendly and can be obtained in very less time.

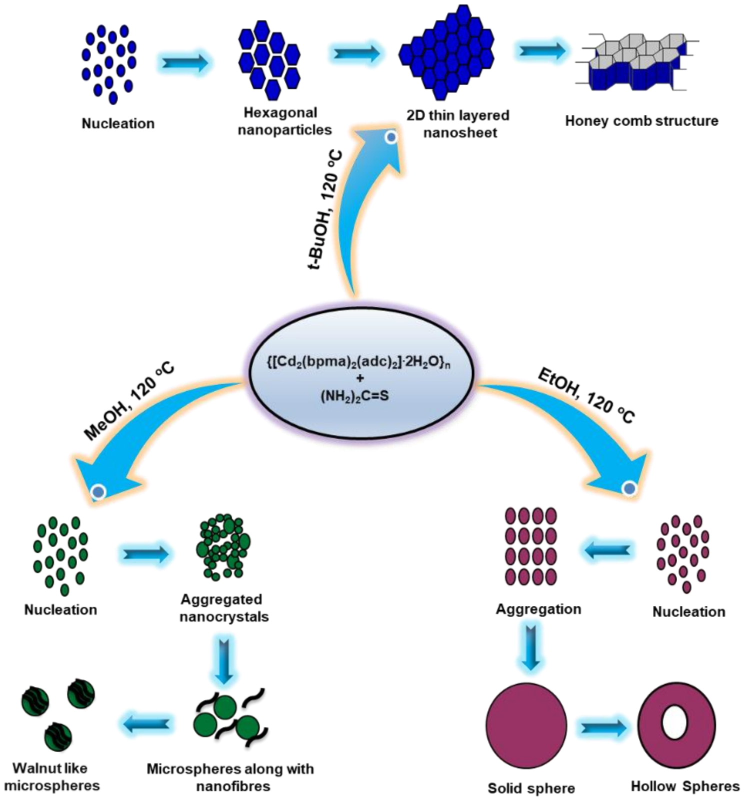

Figure 3.97. Mechanism of formation of hollow spheres, microspheres and honeycomb like nanostructures.

Optical properties. Absorption spectra in the UV-VIS of CdS nanostructures (**CdS-1** to **CdS-3**) prepared in different solvents are displayed in Figure 3.98. The blue shift in the absorption of the samples in comparison with that of bulk CdS (515 nm) can be attributed to quantum confinement effect. A similar observation of blue shift in the absorption edge has been reported for CdS microspheres (walnut like hierarchical structures), which clearly suggests that the absorption is mainly size dependent and the hierarchical CdS microspheres exhibit the activity of their nanoscale building blocks. In crystalline semiconductors, the direct optical band gap energies can be obtained from absorption coefficients data as a function of wavelength using the ''Tauc relation''[125-126] as shown in equation 1:

$$\alpha(hv) = B\left(hv - E_{gap}\right) \qquad (1)$$

where E_{gap}, B, and $h\nu$ are the optical gap, constant, and incident photon energy, respectively; where α is the absorption coefficient, hν is the photon energy, B is the band form parameter, E_{gap} is the optical band gap of the nanoparticles, and n=1/2 for direct band gap and 2 for indirect band gap. It this case, n=1/2 as CdS is a direct band gap semiconductor. Therefore, the direct band gap values were obtained from the plots of $(\alpha h\nu)^2$ versus (hν) and extrapolating the straight portion of the graph to (hν) axis.

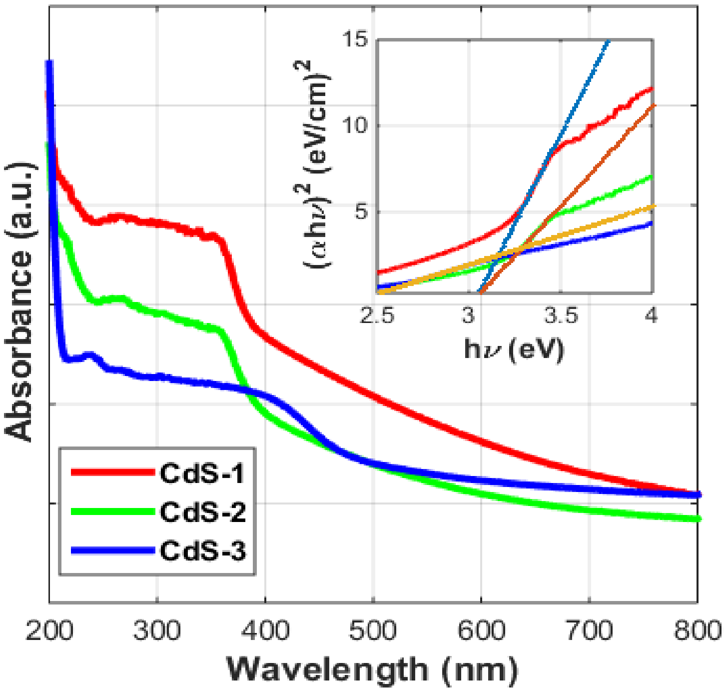

Figure 3.98. Solid state absorbance of **CdS-1 to CdS-3** where (inset) plot of $(\alpha h\nu)^2$ versus (hν)**.**

Using the above band gap calculations, the band gap values of **CdS-1** to **CdS-3** synthesised in different solvents were determined as 3.04 eV, 3.04 eV and 2.43 eV as shown in Figure 3.98. Thus, it can be concluded that the band gap energies of CdS nanostructures remains same in both methanol and ethanol whereas it decreases in t-BuOH. Further, the band gap energies were found to be almost same for **CdS-3** and **CdS-4** (2.45 eV) but for **CdS-5** (2.55 eV) (Figure 3.99), the value was found to be close to **CdS-1** and **CdS-2**.

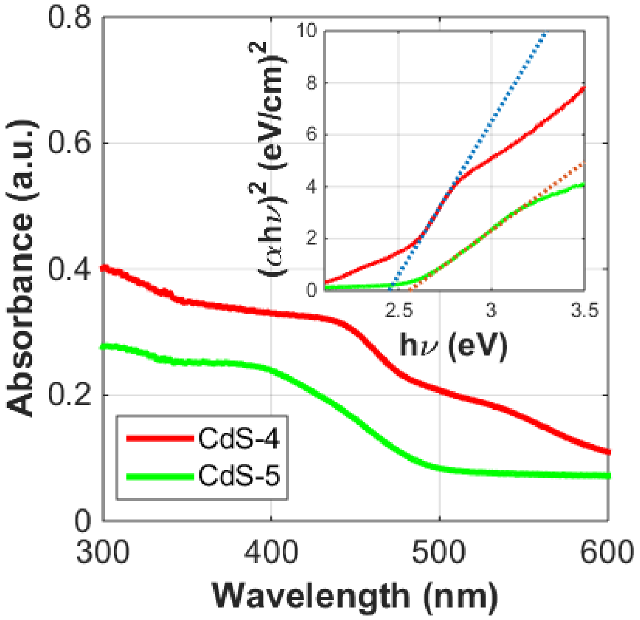

Figure 3.99. Solid state absorption spectra of **CdS-4** to **CdS-5** where (inset) plot of $(\alpha h\nu)^2$ versus ($h\nu$).

Photoluminescence properties. The emissions from the nanoparticles prepared in different solvents **CdS-1** to **CdS-3** revealed blue emission bands at 427, 421 and 431 nm with a blue shift as shown in Figure 6 compared to bulk CdS which show emission band at 560 nm.[127] This shift can be attributed due to quantum size effect. The dominant blue emission from the CdS samples can be assigned to the recombination of free charge carriers at the surface defect sites of the CdS nanocrystals. Both shallow trap luminescence and exciton luminescence contribute to the broad luminescence in **CdS-1** to **CdS-3** (Figure 3.100a). The strong intensity of photoluminescence indicates that the surface states remain very shallow, as it is reported that the quantum yields of band edge will decrease exponentially with increasing depth of surface state energy levels.[128] The peaks at 410 nm in **CdS-4** (Figure 3.100b) corresponds to band edge luminescence which is due to the recombination of excitons in the mostly delocalised states in nanoparticles and it determines the crystalline nature of nanoparticles. For **CdS-5**, emission bands at 435, 461 and 585 nm are observed (Figure 3.100c). The emission in the range 550-650 nm shows the well-known green emission band in the CdS nanoparticles.[129] The photoluminescence spectrum in **CdS-5** consists of many emission peaks indicating broad particle size distribution in it.

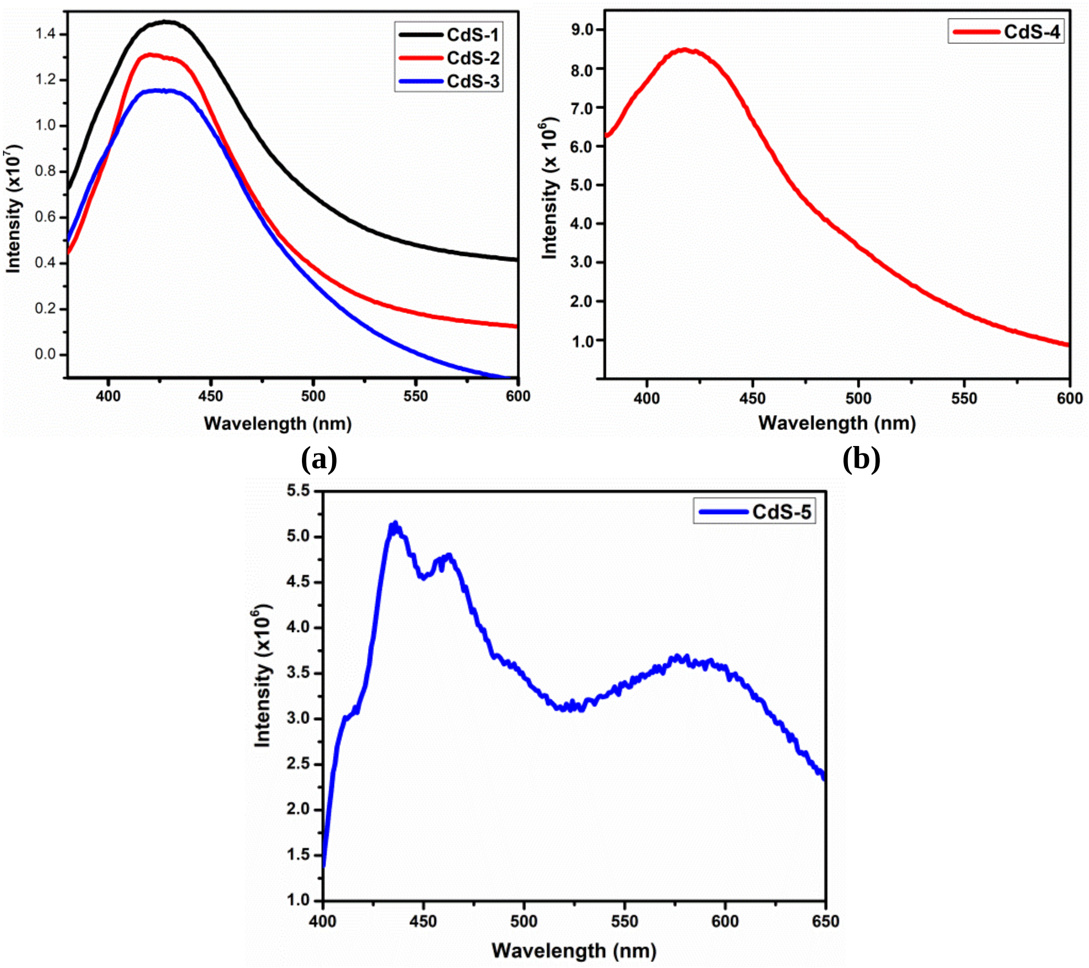

(a) (b)

(c)

Figure 3.100. Photoluminescence spectra of **CdS-1** to **CdS-5**.

Photocatalytic activity of CdS nanostructures. In light of the results obtained from UV-VIS absorption and Photoluminescence measurements, the CdS nanostructures synthesized in different solvents showed enhanced photocatalytic performance in UV light illumination. The photocatalytic activity of samples was estimated by monitoring the decomposition of MB aqueous solution. The intensity of the characteristic absorption peak at 663 nm decreased as the irradiation proceeded with a change in the color. Figure 3.101(a-e) shows the plot of degradation ability of the samples by monitoring the concentration of methylene blue solution at 663 nm in which C/C_o stands for the concentration ratio after and before a certain length of reaction time. The approximate linear relationship of ln (C_o/C) versus irradiation time t for different samples indicates the photodegradation process of methylene blue which can be considered as a Langmuir-

Hinshelwood first order kinetics reaction due to low concentration of the substrate.[130] Its kinetics can be expressed as follows: ln (C_o/C) = Kt, where K is the degradation reaction rate constant. The kinetics of the degradation is shown in Figure 3.101f. The apparent reaction rate constants for 2.307 mmol of catalyst (**CdS-1** to **CdS-5**) are determined as 1.17 x 10^{-2}, 1.07 x 10^{-2}, 0.63 x 10^{-2} min^{-1}, 0.80 x 10^{-2} min^{-1} and 0.20 x 10^{-2} min^{-1}, respectively. Whereas it is 0.01 x 10^{-2} min^{-1} without the catalyst. The percent degradation efficiency of 88% was observed in 3 hours in UV conditions for **CdS-1** whereas it was 83%, 68%, 76% and 33% for **CdS-2**, **CdS-3, CdS-4** and **CdS-5** respectively. Only 1% degradation was observed in 3 hours for the blank sample without the catalyst under the same conditions. A comparison with the literature values reveals that the rate constant value for walnut like hierarchical structures was found to be greater than PVP-capped nanoparticles, hollow microspheres, nanospheres but less in comparison to agglomerated nanoparticles and nanospheres[131-135] (Table 3.27).

Table 3.27. Comparison of rate constant values of as-synthesised **CdS-1** to **CdS-5** with literature values

Morphology	**Rate constant (min^{-1})**	**Time**	**Reference**
Agglomerated Nanoparticles	1.57 x 10^{-2}	120 min	135
PVP Capped Nanoparticles	0.29 x 10^{-2}	360 min	131
Hollow microspheres	1.09 x 10^{-2}	210 min	132
Nanospheres	1.03 x 10^{-2}	90 min	133
Nanospheres	1.78 x 10^{-2}	180 min	134
Walnut shaped hierarchical microspheres (Rare morphology) **(CdS-1)**	**1.17 x 10^{-2}**	**180 min**	**This work**
Hollow nanospheres **(CdS-2)**	**1.07 x 10^{-2}**	**180 min**	**This work**
Honeycomb nanostructures (Rare morphology) **(CdS-3)**	**0.63 x 10^{-2}**	**180 min**	**This work**
Aggregated nanospheres **(CdS-4)**	**0.80 x 10^{-2}**	**180 min**	**This work**
Aggregated microspheres **(CdS-5)**	**0.20 x 10^{-2}**	**180 min**	**This work**

Further, the rate constant values for the hollow nanospheres are almost similar to those of hollow microspheres reported in literature. Whereas, the rate constant values for honeycomb nanostructures, aggregated nanospheres and aggregated microspheres were found to be less than the reported literature values. In general, the enhanced specific area and improved charge separation results in high photocatalytic activity. Also, the adsorption and desorption on the surface play significant role in enhancing the activity of catalysts. For an improved photocatalytic activity, the catalyst should have high crystallinity with lesser defects for these defects become the cause of recombination of electrons and holes which may result in lowering the system's photocatalytic activity. It has been observed that CdS nanostructures possess high crystallinity which results in the high photocatalytic activity of these nanostructures.

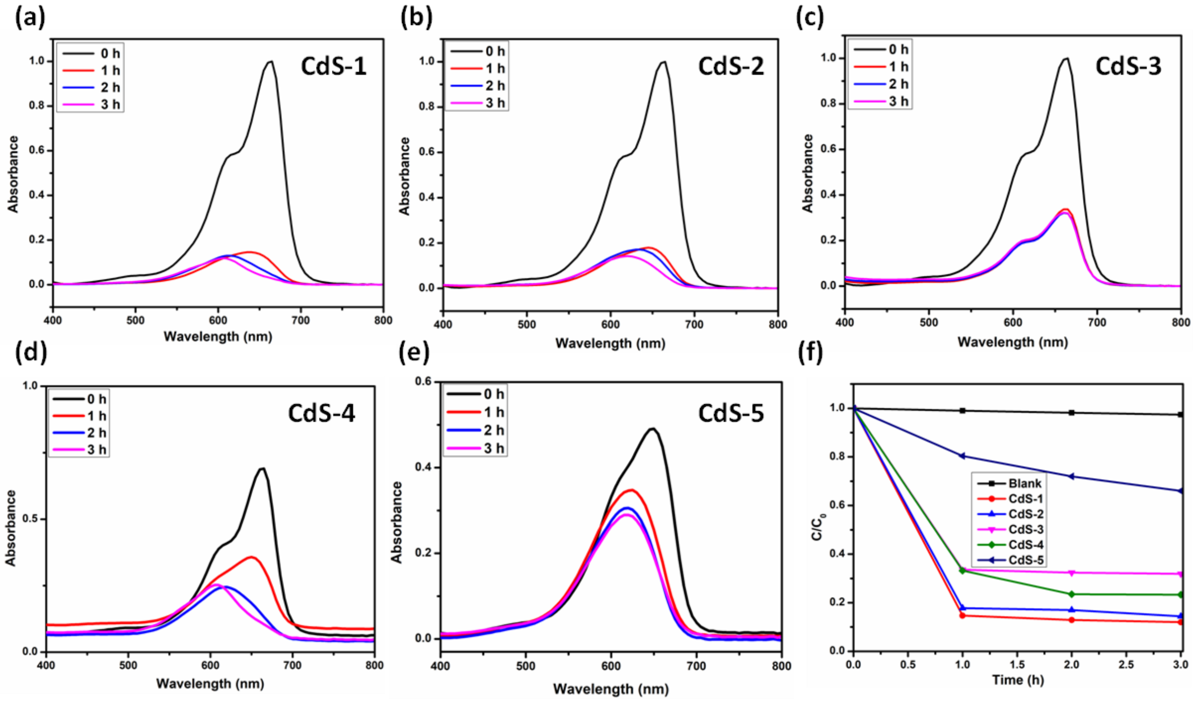

Figure 3.101. (a-e) Photodegradation of methylene blue by **CdS-1** to **CdS-5**, (f) Kinetics of photocatalytic degradation of methylene blue over **CdS-1** to **CdS-5**.

Proposed mechanism for the degradation of methylene blue. With the UV light illumination, e^-/h^+ pairs (equation 1) are generated in the CdS nanostructures. The photoexcited electrons migrate to the surface of the catalyst. Owing to the high crystallinity of the CdS nanostructures, the resistance to the electron migration is relatively slow so as to reduce the recombination of e^-/h^+ pairs. The electrons get accumulated on the surface of CdS which are then scavenged by dissolved oxygen molecules in water to yield highly oxidative species such as the superoxide radical anion

($\cdot O_2^-$) and hydroxyl radical ($\cdot OH$) (equation 3-6), which can mineralize organic substrates effectively (Scheme 3.19). These oxidative species can easily diffuse out of the catalyst to attack the methylene blue dye. The oxidative species are believed to be responsible for decomposing methylene blue which leads to decolouration of dye with time. The proposed initial elementary reactions are listed in equations (1 - 6).[136-138]

$$\mathrm{CdS} + h\nu \longrightarrow h^+ + e^- \quad (1)$$

$$h^+ + H_2O \longrightarrow H^+ + OH^- \quad (2)$$

$$e^- + O_2 \longrightarrow O_2^{\cdot -} \quad (3)$$

$$O_2^{\cdot -} + H^+ \longrightarrow HO_2^{\cdot} \quad (4)$$

$$HO_2^{\cdot} + H^+ + O_2^{\cdot -} \longrightarrow H_2O_2 + O_2 \quad (5)$$

$$H_2O_2 + e^- \longrightarrow \cdot OH + OH^- \quad (6)$$

Scheme 3.19. Reactions involved on the surface of catalyst.

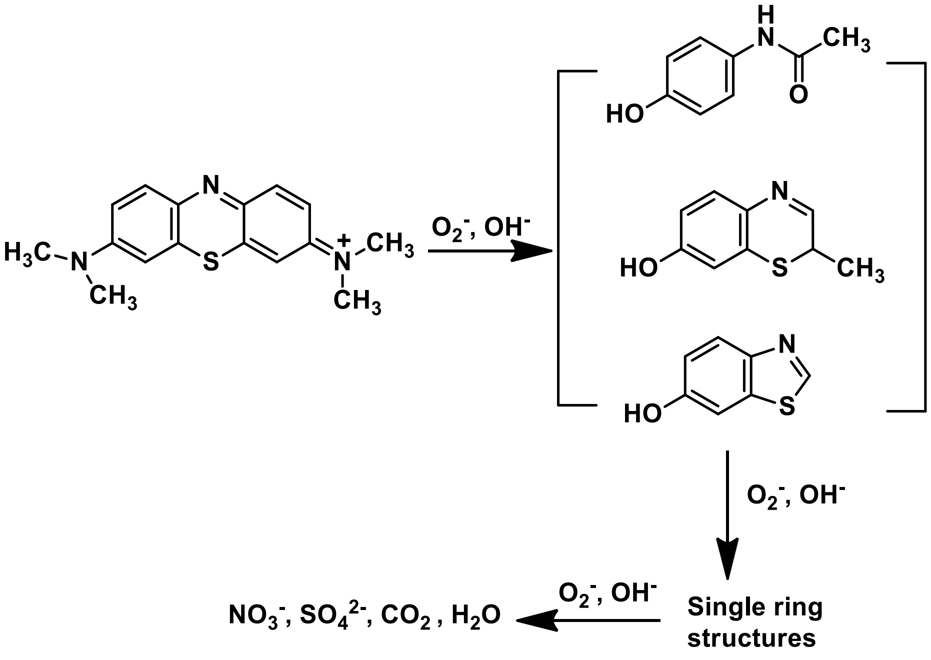

Scheme 3.20. Proposed mechanism for the degradation of methylene blue.

During the course of photocatalysis the absorption edge of methylene blue shows a blue shift to shorter wavelength as shown in Figure 3.89. This is due to the fact that methylene blue molecules get oxidised and converted into smaller molecules with lower degree of π-π conjugation. The λ_{max} of the absorption spectra of these molecules produced during the degradation of methylene blue is shorter than that of methylene blue molecules and further oxidation gives rise to opening of aromatic rings which consequently leads to degradation of methylene blue to CO_2 and H_2O as shown in scheme 3.20.

Solid-state reflectance experiments suggested that the band gap energies of CdS nanostructures follow the order: **CdS-1** = **CdS-2** > **CdS-5** > **CdS-4** > **CdS-3**. Furthermore, the CdS nanostructures **CdS-1** to **CdS-3** showed broad blue emission bands in the range 410-440 nm. Whereas, **CdS-4** showed trap-state emission arising from the surface defect sites at 464 nm and a feature of green emission band was observed for **CdS-5** at 585 nm.

The activity for **CdS-1** to **CdS-4** was found to be more compared to **CdS-5** which implies that an enhancement in the photocatalytic activity was observed when CdS was obtained from 1D coordination polymer than that obtained from $Cd(OAc)_2{\cdot}2H_2O$ as the precursor under similar conditions. It has been observed that the photocatalytic activity of **CdS-1** to **CdS-5** follows the order: **CdS-1** > **CdS-2** > **CdS-4** > **CdS-3 > CdS-5**. The degradation rate of 1.17×10^{-2} min^{-1} for walnut-like multi-hollow CdS microspheres **CdS-1** was found to be faster among other CdS nanostructures **CdS-2** to **CdS-5**.

3.2.2 Effect of concentration

In this study, we have synthesized CdS nanoparticles hydrothermally by changing the concentration of precursors to observe a change in the morphology and optical properties of samples. Inorganic metal coordination polymer $\{[Cd_2(bpma)_2(adc)_2]{\cdot}2H_2O\}_n$ was utilized as a cadmium source and thiourea (sulphur source) was added in different ratios (1:3, 1:5, 1:7, 1:10) to the polymer at 180 ^{o}C for 24 hours to yield nanocrystals with varied particle sizes ranging from 20 to 90 nm. All the CdS samples (**CdS-6** to **CdS-9**) are nanocrystalline in nature with the difference in their average grain sizes.

Synthesis of CdS nanoparticles. CdS nanoparticles were synthesised using 0.034 mmol of $\{[Cd_2(bpma)_2(adc)_2]{\cdot}2H_2O\}_n$ (30 mg) as the Cd(II) source and thiourea as the sulphur source. The precursors were mixed in different ratios (1:3, 1:5, 1:7, 1:10) and water was used as a solvent (Scheme 3.21). The respective mixtures were taken in a Teflon autoclave and 3 mL of water was added. The reaction was carried out hydrothermally at 180 ^{o}C for 24 hours. The yellow precipitates were collected and centrifuged at 5000 rpm for 10 minutes, washed three times with methanol and dried in air at 60 ^{o}C.

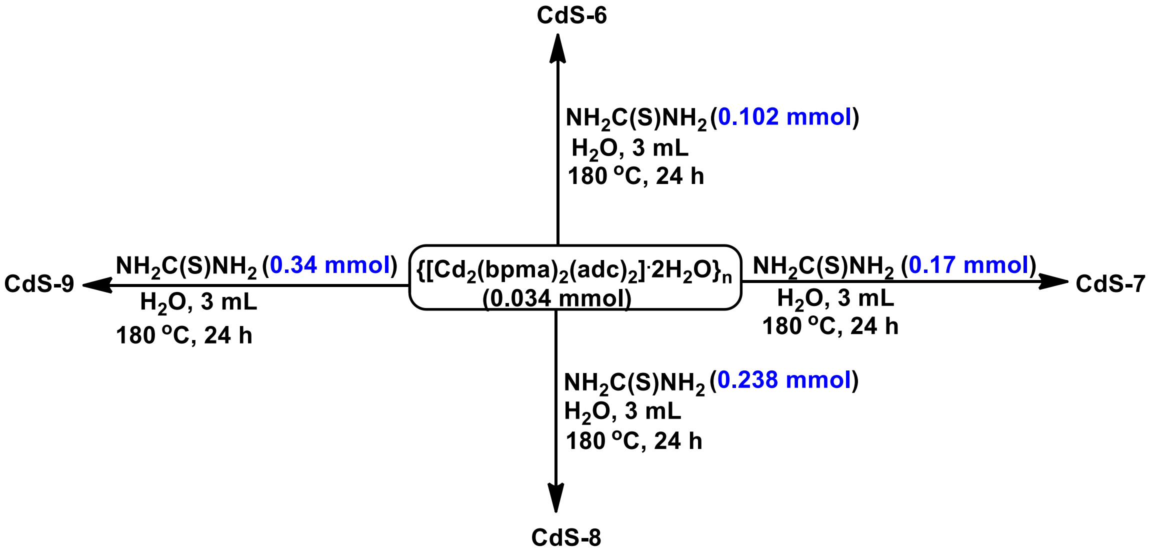

Scheme 3.21. Synthesis of **CdS-6** to **CdS-9**.

Powder X-ray diffraction studies. X-ray diffraction patterns of the as-synthesized CdS nanoparticles are shown in Figure 3.102. All the observed peaks could be clearly indexed to cubic CdS (JCPDS 10-454) and hexagonal phase of CdS (JCPDS 06-314). The characteristic peaks at 2θ = 25.01, 26.52, 28.06, 43.84, 47.87 and 51.93 is attributed to the cubic phase of CdS. Whereas, the less intense peaks at 2θ = 21.93°, 21.91°, 21.96° and 21.94° featured the hexagonal phase of CdS. The CdS nanoparticles prepared hydrothermally exhibited only cubic phase which is metastable and can be transformed into hexagonal phase on further annealing.[139] Though the reflections arising from (111) plane of cubic phase and (002) plane of hexagonal phase overlap at 26.52°, no change has been observed in the relative peak intensity ratio of the cubic phase. These observations clearly indicate that CdS nanoparticles favour no specific crystallographic orientation. Furthermore, the broadening in the peaks appears to be originating from the nanocrystallite sizes of these particles.

The crystallite size of the as-synthesized CdS nanoparticles can be calculated using Debye Scherrer's equation:

$$d\ (nm) = \frac{0.9\,\lambda}{\beta\ \cos\theta}$$

where D is the mean crystallite size, λ is the X-ray wavelength (Cu-kα = 0.154 nm), β is FWHM of the reflection. The calculated grain sizes are given in Table 3.28.

Table 3.28. Crystallite sizes of **CdS-6** to **CdS-9**

Sample	**FWHM**	**Mean crystallite size (nm)**
CdS-6	0.6952	11.55 nm
CdS-7	0.6913	11.54 nm
CdS-8	0.6671	11.95 nm
CdS-9	0.6485	12.37 nm

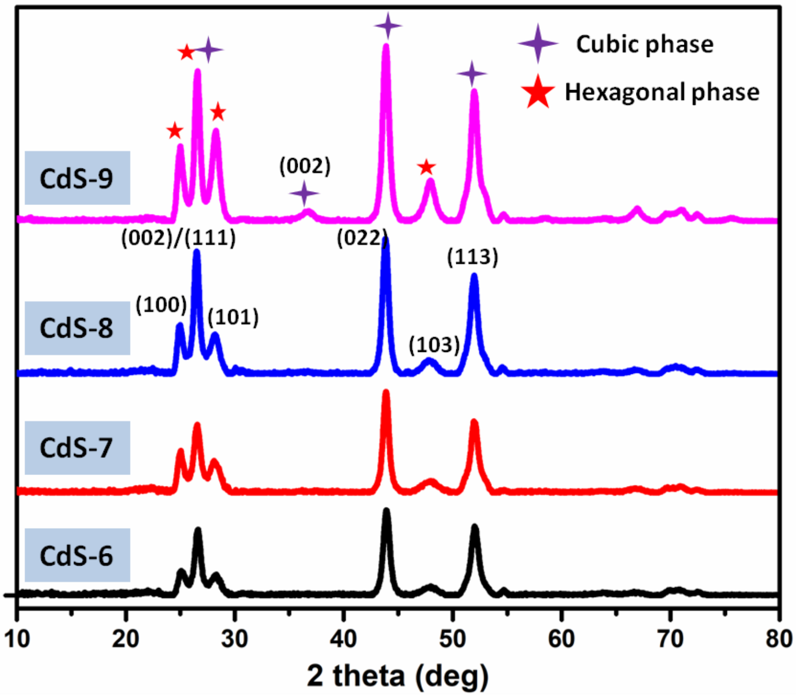

Figure 3.102. PXRD patterns of **CdS-6** to **CdS-9**.

Surface analysis. In order to understand the effect of morphology by changing the precursor concentration to thiourea, the scanning electron microscopy was performed on all the samples. All the samples synthesized are nanocrystalline particles as shown in Figure 3.103 with a little variation in their sizes. A little variation in their sizes has been observed as a result of change in the concentration of thiourea in the samples. The concentration of the precursor have a profound influence on controlling the particle size by affecting the growth rate.[140] In general, the size of the nanocrystals are believed to increase as a function of increased concentration of precursor.

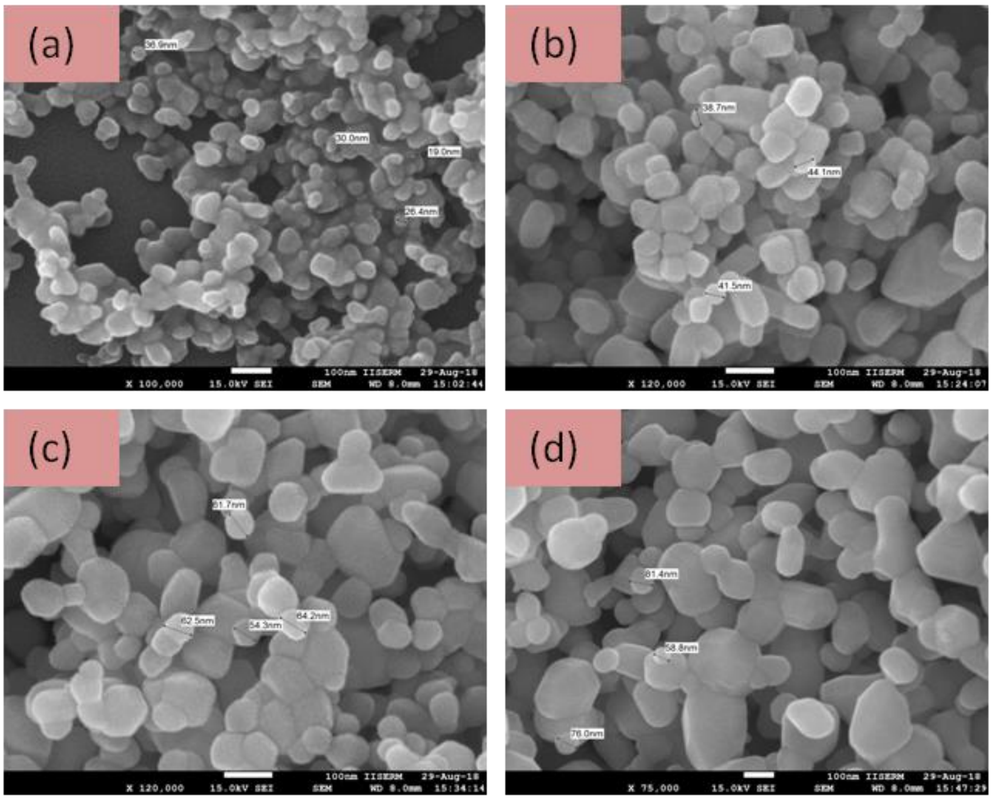

Figure 3.103. CdS samples synthesized using Cd(II) polymer and thiourea in the ratios (a) 1:3, (b) 1:5, (c) 1:7, (d) 1:10.

In the present work, it has been observed that different Cd^{2+}: S^{2-} ratios have influenced the growth rate resulting in yielding crystals with different particle sizes. The Cd^{2+} concentration has been kept constant at 0.034mM whereas the S^{2-} concentration was varied to change the ratios. The particles synthesized with more concentration of thiourea (**CdS-8** with 0.238 mM thiourea and **CdS-9** with 0.34 mM thiourea) were considerably larger than those synthesized with less concentration (**CdS-6** and **CdS-7**). These results are in good agreement with Pattabi et. al[141] which had showed increase in the particle size with the precursor concentration. The average grain size for **CdS-6** was found to be between 20-30 nm (Figure 3.103). On increasing the concentration to 0.17 mmol in **CdS-7**, a relatively larger particle size between 35-50 nm has been obtained. Further with 0.238 mmol concentration of thiourea, the particle size increased to 55-65 nm. However, when the concentration was further increased to 0.34 mM, a very little increase has been observed which is about 5 nm. This slight change could be attributed due to unavailability of surface Cd atoms resulting in no more adsorption of S^{2-} to grow CdS particles. In general, when there is excess concentration of Cd^{2+} ions in the reaction, S atom of thiourea competes with free S^{2-} ions which results in the depletion of free sites on the surface for the reactions of Cd^{2+} and S^{2-} ions yielding smaller particles. Whereas, excess of S^{2-} ions favors the reaction between Cd^{2+} and S^{2-} ions owing to more distribution of S^{2-} ions on the surface resulting in less obstruction in CdS nanoparticle growth. Hence, the particle size can be tuned by changing the concentration of precursors in the reaction.

Optical properties. Figure 3.104 shows the UV-vis absorption spectra of CdS samples synthesized with different concentrations of thiourea (**CdS-6** to **CdS-9**). It has been observed that the absorption peak for **CdS-6** is located at 481 nm. Whereas, when the composition was increased to 1:5 in **CdS-7**, there is a slight shift in the absorption band which is 3 nm (λ_{max} = 484 nm). The similar trend has been observed for **CdS-8** and **CdS-9** whose λ_{max} was found to be 486 and 488 nm, respectively. Thus, it can be concluded that wavelength increases as a function increasing particle sizes. These experimental results showed blue shift in comparison to the band gap value of the bulk CdS (512 nm).[142] This blue shift is observed as a result of reduction in size within nanometre size regime.[143]

The energy band gap of the CdS samples can be determined from the Tauc Plot by plotting $(\alpha h\nu)^2$ vs $h\nu$(eV), where α is the absorption coefficient, ν is the frequency, and h is Planck's constant. The intercept on x-axis gives the direct energy band gap E_g of CdS nanoparticles. The values of band gaps are listed in Table 3.29.

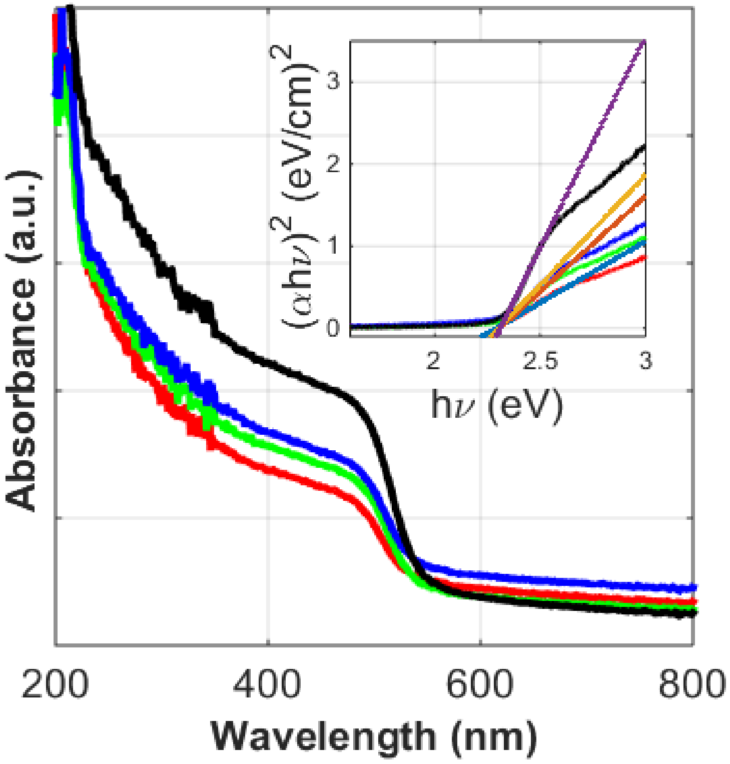

Figure 3.104. Solid state absorption spectra of **CdS-6** to **CdS-9** where (inset) plot of $(\alpha h\nu)^2$ versus $(h\nu)$ where red, green, blue and black colour represents **CdS-6** to **CdS-9**.

Table 3.29. Band gap values of **CdS-6** to **CdS-9**

Sample	Band Gap (E_g) (eV)
CdS-6	2.28
CdS-7	2.27
CdS-8	2.25
CdS-9	2.22

Photoluminescence properties. Photoluminescence spectra have been performed on as-synthesized CdS nanoparticles in order to investigate the luminescent properties. The spectra were recorded at an excitation wavelength of 350 nm. The emission wavelengths were observed at 418, 410, 433 and 428 nm for **CdS-6** to **CdS-9** as an increasing function of their particle sizes (Figure 3.105). These blue emission bands correspond to the band edge luminescence which could be attributed to the recombination of excitons. Whereas, the intensity of green emission band at around 550 nm in these samples were observed to be increasing with increasing particle sizes. This emission band was observed due to the electronic transition from the conduction band to an acceptor level due to interstitial sulphur vacancies as sulphur ions.[14]

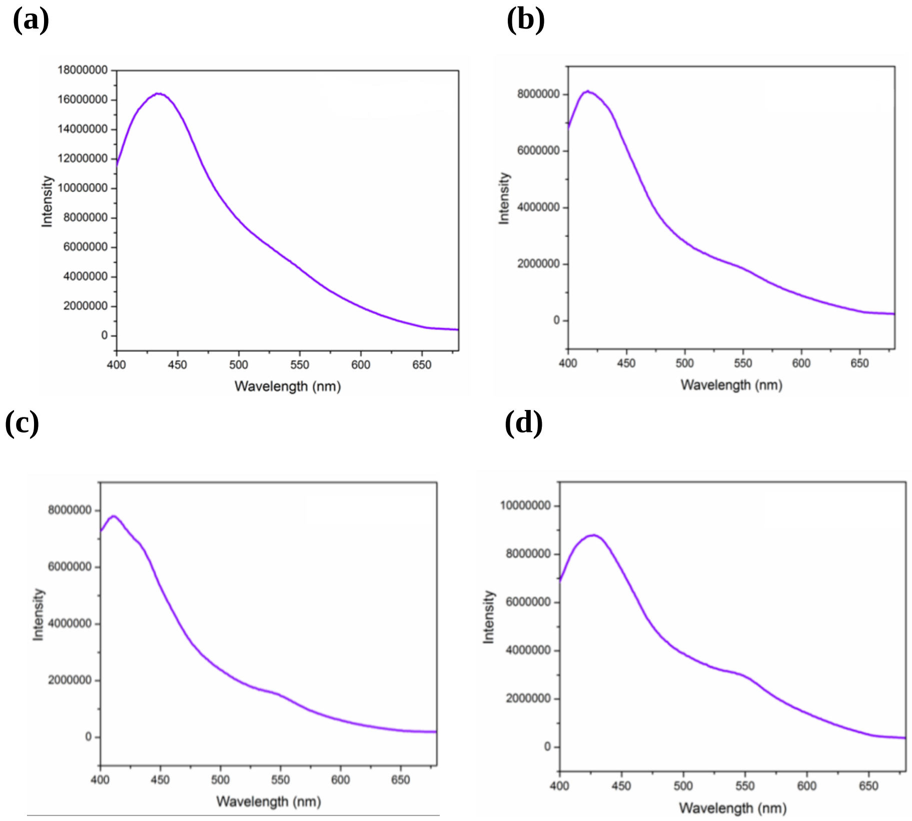

Figure 3.105. Photoluminescence spectra of **CdS-6** to **CdS-9**.

CHAPTER IV

CONCLUSIONS

1. A completely new strategy has been adopted for the synthesis of nanomaterials derived from the coordination polymers without the addition of any surfactant, which can bring impurities to the system. Compared to the traditional use of respective metal salts, such as zinc or cadmium acetate/nitrate, these CPs act as sacrificial templates providing a control over desired morphologies of the nanostructures.

2. Under hydrothermal approach, Zn(II) CPs in the neutral conditions results in giving 3D ZnO flowers and 2D ZnO nanosheets which on further annealing at high temperature results in thermodynamically more stable 1D nanorods. This is the first example where 1D coordination polymers have been utilized for tuning the dimensionality of nanostructures without the addition of any surfactant.

3. The photoluminescence spectra of ZnO nanostructures synthesized at different volumes suggested that increase in volume diminishes the intensity of absorption, i.e., a high concentration of Zn(II) in the reaction mixture plays a major role in enhancing the intensity of absorption.

4. In the basic conditions at pH > 13, $[Zn_2(bpma)_2(adc)_2]_n$ yield ZnO nanorods at three different temperatures 120, 150 and 180 ^{o}C. Since temperature plays a significant role in controlling the overall length and diameter of the rods, it has been observed that increase in temperature resulted in lengthening as well as broadening of the rods. Thus, aspect ratios of the rods can be optimized by varying the hydrothermal temperature.

5. A time dependent synthesis was carried out at 120, 150 and 180 ^{o}C utilizing $[Zn_2(bpma)_2(adc)_2]_n$ in the basic conditions. It was observed that length of the growth time results in increasing the aspect ratios of the nanorods. It is well known that high aspect ratio ZnO nanorods is beneficial for device applications owing to their enhanced optical and electronic properties. Thus, time is an important parameter in influencing and manipulating the aspect ratios of nanorods.

6. The strong emission in the blue region of the visible spectrum results from the defects in ZnO materials which include zinc interstitials and oxygen vacancies. Also, the intensity of emission increased with an increase in the aspect ratios of the nanorods.

7. Since the extended synthesis time resulted in higher aspect ratios of ZnO nanorods which enhances the surface area of these rods. It has been found that relatively large surface area would be beneficial for the adsorption of dyes and enhancing their photocatalytic activity. Thus, the photodegradation of cationic dye (Methylene Blue) and anionic dye (Congo Red) has been carried out with 1D ZnO nanorods synthesized ^{o}C for different growth times at 180 ^{o}C. The maximum photocatalytic activity was achieved with ZnO nanorods obtained with a growth time of 24 hours. The anionic dye Congo Red exhibited the maximum photocatalytic activity for ZnO nanorods in comparison to the cationic dye Methylene Blue.

8. Further annealing of the as-synthesized ZnO nanorods (obtained at 180 ^{o}C) was carried out at 800 ^{o}C for 6 hours. The post synthetic annealing resulted in decrease in the aspect ratios. The decrease in the aspect ratios also leads to a decrease in the defects in the ZnO nanorods. These surface defects could play a very important role in the photocatalytic activity. The annealed samples with less aspect ratios showed less photocatalytic activity against Congo Red dye.

9. The photocatalytic activity of ZnO nanorods against Congo Red dye was tested in different pH solutions ranging from pH = 6 to pH = 12 and it was found that the rate of degradation of dye is maximum at pH = 8. The photocatalytic degradation of the dye was found to be minimum in highly basic conditions.

10. The antibacterial effectiveness of the ZnO nanorods was tested against gram negative *E.Coli*. The bacterial growth was monitored by measuring the optical density (O.D.) at a fixed wavelength of 650 nm. The optical density was measured without and with different ZnO concentrations. The samples prepared with 100 and 150 mg/L concentration of ZnO were found effective in inhibiting the growth of general strain *E.Coli* whereas a limited inhibition was observed with 10 mg/L.

11. When the plate count was used to monitor the bacterial growth. *E.Coli* strains containing different concentrations of ZnO (10, 100 and 150 mg/L), the number of colonies observed were decreased on increasing the concentration from 10 to 150 mg/L. The maximum percentage for bacterial inhibition was found to be 98.41% with ZnO dosage of 150 mg/L.

12. ZnO has also been fabricated at different pH ranging from 9 to 12 and it has been found that after 12 hours full blown flowers were obtained in each case. A detailed

mechanism on the evolution of micro flowers at different pH has been elucidated. The photocatalytic activity against Congo red was found to be maximum with 3D micro flowers fabricated at pH=12 compared to the ones obtained at lower pH.

13. Based on the polarity and boiling point of different solvents, the fabrication of ZnO at 180 ^{o}C in hydrothermal conditions resulted in different morphologies. A difference has also been observed in their emission spectra based on their shapes and sizes.

14. ZnO has also been synthesized by directly calcining the Zn(II) coordination polymers at a temperature of 700 ^{o}C for different retention times (6 h, 12 h, 18 h and 24 h). at 700 ^{o}C, variation in the precursor yield different morphologies (spheres, micro-rods and polyhedrons) of ZnO at different growth times.

15. The photocatalytic activity of ZnO obtained by direct calcination method at different times were tested against methylene blue dye. The maximum photocatalytic activity was obtained for prism shaped ZnO at 500 ^{o}C obtained from $\{[Zn_2(bpta)_2(adc)_2]_n{\cdot}2H_2O\}_n$.

16. ZnO polyhedrons obtained from $\{[Zn_2(bpta)_2(adc)_2]_n{\cdot}2H_2O\}_n$ exhibited the maximum photocatalytic activity followed by nanospheres and micro-rods (fabricated at 700 ^{o}C) in degrading the methylene blue dye. Thus, it can be concluded that variation in precursor as well retention time not only yield different morphologies but a difference in their activity towards the methylene blue dye has also been achieved.

17. The different kinetic models were studied to predict the adsorption kinetics of ZnO samples fabricated via direct calcination at 700 ^{o}C on methylene blue dye (MB). These kinetic models included Elovich’s, Intra-particle diffusion and Pseudo-second order. The adsorption data were fitted in all these models and the respective rate constants and regression values were calculated.

18. Among all the models that were studied to determine the kinetics of the ZnO samples, pseudo second order model fits best with the experimental data in all the cases. From the experimental results, it can be deduced that the degradation of methylene blue follows pseudo second order mechanism.

19. CdS nanostructures were fabricated utilizing $[Cd_2(bpma)_2(adc)_2]_n$ as the source of Cd^{2+} ions and thiourea as the source of sulphide ions in different solvents (methanol, ethanol, t-butanol and water). Two such morphologies, which are rare for any other nanomaterials, namely walnut-shaped multi-hollow hierarchical microspheres in methanol and

honeycomb like porous nanostructures in t-BuOH are discovered for CdS for the first time. Similarly, aggregated hollow nanospheres were synthesized in ethanol. Aggregated nanospheres were obtained in water and aggregated microspheres were seen in methanol using $Cd(OAc)_2.2H_2O$ as the precursor. The as-synthesized structures have been tested for the photodegradation of methylene blue dye. The degradation rate of 1.17×10^{-2} min^{-1} for walnut-like multi-hollow CdS microspheres was found to be faster among other CdS nanostructures.

20. The dominant blue emission was observed for the CdS samples synthesized in different solvents which can be assigned to the recombination of free charge carriers at the surface defect sites of the CdS nanocrystals.

21. The effect of precursor concentration on the particle sizes of CdS has also been investigated. CdS nanoparticles have been synthesized with different ratios of Cd (II) polymer and thiourea. It has been observed that an increasing concentration of thiourea resulted in an increase in their particle sizes which can be directly correlated with their luminescence spectra. It has been demonstrated that an increase in the particle size resulted in an increase in the intensity of green emission in these particles.

REFERENCES:

(1) Filipponi, L.; Sutherland, D. Chapter 4 Fundamental “ Nano - Effects .” In *NANOYOU Teachers Training Kit in Nanotechnologies*; **2010**; 25.

(2) Caminade, A. M.; Turrin, C. O. Dendrimers for Drug Delivery. *J. Mater. Chem. B* **2014**, *2*, 4055–4066.

(3) Yang, Y.; Romano, M.; Feng, G.; Wang, X.; Wu, T.; Holdren, S.; Zachariah, M. R. Growth of Sub-5 Nm Metal Nanoclusters in Polymer Melt Aerosol Droplets. *Langmuir* **2018**, *34*, 585–594.

(4) Raman, N.; Sudharsan, S.; Pothiraj, K. Synthesis and Structural Reactivity of Inorganic-Organic Hybrid Nanocomposites - A Review. *J. Saudi Chem. Soc.* **2012**, *16*, 339–352.

(5) Liu, R.; Duay, J.; Lee, S. B. Heterogeneous Nanostructured Electrode Materials for Electrochemical Energy Storage. *Chem. Commun.* **2011**, *47*, 1384–1404.

(6) Ponnuchamy, K.; Jacob, J. A. Metal Nanoparticles from Marine Seaweeds – a Review. *Nanotechnol. Rev.* **2016**, *5*, 589-600

(7) Amirkhanlou, S.; Ketabchi, M.; Parvin, N. Nanocrystalline/Nanoparticle ZnO Synthesized by High Energy Ball Milling Process. *Mater. Lett.* **2012**, *86*, 122–124.

(8) Manin-Ferlazzo, L.; Couraud, L.; Carcenac, F.; Mejias, M.; Launois, H.; Lebib, A.; Chen, Y.; Vieu, C.; Pépin, A. Electron Beam Lithography: Resolution Limits and Applications. *Appl. Surf. Sci.* **2002**, *164*, 111–117.

(9) Zheng, F.; Lu, H.; Guo, M.; Zhang, M.; Zhen, Q. Hydrothermal Preparation of WO<inf>3</Inf> Nanorod Array and ZnO Nanosheet Array Composite Structures on FTO Substrates with Enhanced Photocatalytic Properties. *J. Mater. Chem. C* **2015**, *3*, 7612–7620.

(10) Tseng, W.-Y.; Lu, J. G.; Fan, Z.; Chang, P.-C.; Wang, D.; Chiou, W.-A.; Hong, J. ZnO Nanowires Synthesized by Vapor Trapping CVD Method. *Chem. Mater.* **2007**, *16*, 5133–5137.

(11) Rao, B. G.; Mukherjee, D.; Reddy, B. M. Novel Approaches for Preparation of Nanoparticles. In *Nanostructures for Novel Therapy: Synthesis, Characterization and Applications*; **2017**; 1–36.

(12) Liu, L.; Chen, X. Titanium Dioxide Nanomaterials: Self-Structural Modifications. *Chem. Rev.* **2014**, *114*, 9890–9918.

(13) Nozik, A. J.; Memming, R. Physical Chemistry of Semiconductor-Liquid Interfaces. *J. Phys. Chem.* **1996**, *100*, 13061–13078.

(14) Wang, Y.; Herron, N. Nanometer-Sized Semiconductor Clusters: Materials Synthesis, Quantum Size Effects, and Photophysical Properties. *Journal of Physical Chemistry*. **1991**, 525–532.

(15) J., Z.; V., C. Toxicology of Nanomaterials Used in Nanomedicine. *Journal of Toxicology and Environmental Health - Part B: Critical Reviews*. **2011**, 593–632.

(16) Cauda, V.; Roppolo, I.; Porro, S.; Chiolerio, A.; Canavese, G.; Gazia, R.; Stassi, S. *Nanostructured ZnO Materials: Synthesis, Properties and Applications*; **2014**.

(17) Herring, C.; Galt, J. K. Elastic and Plastic Properties of Very Small Metal Specimens [32]. *Physical Review*. **1952**, 1060–1061.

(18) Yamada, Y.; Ueno, K.; Fukumura, T.; Yuan, H. T.; Shimotani, H.; Iwasa, Y.; Gu, L.; Tsukimoto, S.; Ikuhara, Y.; Kawasaki, M. Electrically Induced Ferromagnetism at Room Temperature in Cobalt-Doped Titanium Dioxide. *Science (80-.).* **2011**, *332*, 1065–1067.

(19) Kaushik, B. K.; Majumder, M. K. Carbon Nanotube: Properties and Applications. *SpringerBriefs Appl. Sci. Technol.* **2015**, 17–37.

(20) Habisreutinger, S. N.; Schmidt-Mende, L.; Stolarczyk, J. K. Photocatalytic Reduction of CO_2 on TiO_2 and Other Semiconductors. *Angewandte Chemie - International Edition*. **2013**, 7372–7408.

(21) Fujishima, A.; Rao, T. N.; Tryk, D. A. Titanium Dioxide Photocatalysis. *Journal of Photochemistry and Photobiology C: Photochemistry Reviews*. **2000**, 1–21.

(22) Parida, K. M.; Parija, S. Photocatalytic Degradation of Phenol under Solar Radiation Using Microwave Irradiated Zinc Oxide. *Sol. Energy* **2006**, *80*, 1048–1054.

(23) Rehman, S.; Ullah, R.; Butt, A. M.; Gohar, N. D. Strategies of Making TiO_2 and ZnO Visible Light Active. *Journal of Hazardous Materials*. **2009**, 560–569.

(24) Gupta, V. K.; Ali, I.; Saleh, T. A.; Nayak, A.; Agarwal, S. Chemical Treatment Technologies for Waste-Water Recycling - An Overview. *RSC Advances*. **2012**, 6380–6388.

(25) Saravanan, R.; Gracia, F.; Stephen, A. Basic Principles, Mechanism, and Challenges of Photocatalysis; **2017**; 19–40.

(26) Deng, K.; Li, L. CdS Nanoscale Photodetectors. *Adv. Mater.* **2014**, *26*, 2619–2635.

(27) Mathew, X.; Enriquez, J. P.; Romeo, A.; Tiwari, A. N. CdTe/CdS Solar Cells on Flexible Substrates. *Sol. Energy* **2004**, *77*, 831–838.

(28) Zhao, J.; Bardecker, J. A.; Munro, A. M.; Liu, M. S.; Niu, Y.; Ding, I. K.; Luo, J.; Chen, B.; Jen, A. K. Y.; Ginger, D. S. Efficient CdSe/CdS Quantum Dot Light-Emitting Diodes Using a Thermally Polymerized Hole Transport Layer. *Nano Lett.* **2006**, *6*, 463–467.

(29) Vasimalai, N.; John, S. A. Off-on and on-off Chemosensors for Ultratrace Mercury(II) and Copper(II) Using Functionalized Thiazole and Cadmium Sulfide Nanoparticles Fluorophores. *Sensors Actuators, B Chem.* **2014**, *190*, 800–808.

(30) Ma, N.; Yang, J.; Stewart, K. M.; Kelley, S. O. DNA-Passivated CdS Nanocrystals: Luminescence, Bioimaging, and Toxicity Profiles. *Langmuir* **2007**, *23*, 12783–12787.

(31) Khullar, S.; Mandal, S. K. Non-Hydrothermal Synthesis, Structural Characterization and Thermochemistry of Water Soluble and Neutral Coordination Polymers of Zn(II) and Cd(Ii): Precursors for the Submicron-Sized Crystalline ZnO/CdO. *RSC Adv.* **2014**, *4*, 39204–39213.

(32) Prakash, T.; Neri, G.; Bonavita, A.; Ranjith Kumar, E.; Gnanamoorthi, K. Structural, Morphological and Optical Properties of Bi-Doped ZnO Nanoparticles Synthesized by a Microwave Irradiation Method. *J. Mater. Sci. Mater. Electron.* **2015**, *26*, 4913–4921.

(33) Hwang, Y.-H.; Weng, B.; Chang, C.; Kim, H.-K.; Qiu, J.; Shi, Z.; Li, X.; Zhao, L. Synthesis and Characterization of Flower-Like Bundles of ZnO Nanosheets by a Surfactant-Free Hydrothermal Process. *J. Nanomater.* **2014**, *2014*, 1–11.

(34) Segets, D.; Gradl, J.; Taylor, R. K.; Vassilev, V.; Peukert, W. Analysis of Optical

Absorbance Spectra for the Determination of ZnO Nanoparticle Size Distribution, Solubility, and Surface Energy. *ACS Nano* **2009**, *3*, 1703–1710.

(35) Xia, J. B.; Cheah, K. Quantum Confinement Effect in Thin Quantum Wires. *Phys. Rev. B - Condens. Matter Mater. Phys.* **1997**, *55*, 15688–15693.

(36) Janotti, A.; Van De Walle, C. G. Native Point Defects in ZnO. *Phys. Rev. B - Condens. Matter Mater. Phys.* **2007**, *76*, 165202-22

(37) Erhart, P.; Albe, K. Diffusion of Zinc Vacancies and Interstitials in Zinc Oxide. *Appl. Phys. Lett.* **2006**, *88*, 201918.

(38) McCluskey, M. D.; Jokela, S. J. Defects in ZnO. *J. Appl. Phys.* **2009**, *106*, 071101-13

(39) Alex B. F. Martinson; Jeffrey W. Elam; Joseph T. Hupp; Michael J. Pellin. ZnO Nanotube Based Dye-Sensitized\nSolar Cells. *Nano Lett.* **2007**, *7*, 2183–2187.

(40) Nur, O.; Hatamie, A.; Alnoor, H.; Mak, W. C.; Zargar, B.; Sadollahkhani, A.; Willander, M.; Bano, S.; Turner, A. P. F.; Khan, A.; et al. Zinc Oxide Nanostructure-Modified Textile and Its Application to Biosensing, Photocatalysis, and as Antibacterial Material. *Langmuir* **2015**, *31*, 10913–10921.

(41) Wei, A.; Sun, X. W.; Xu, C. X.; Dong, Z. L.; Yu, M. B.; Huang, W. Stable Field Emission from Hydrothermally Grown ZnO Nanotubes. *Appl. Phys. Lett.* **2006**, *88* 213102-3.

(42) Ahmad, R.; Tripathy, N.; Kim, S. H.; Umar, A.; Al-Hajry, A.; Hahn, Y. B. High Performance Cholesterol Sensor Based on ZnO Nanotubes Grown on Si/Ag Electrodes. *Electrochem. commun.* **2014**, *38*, 4–7.

(43) Vayssieres, L.; Keis, K.; Hagfeldt, A.; Lindquist, S. E. Three-Dimensional Array of Highly Oriented Crystalline ZnO Microtubes. *Chem. Mater.* **2001**, *13*, 4395–4398.

(44) Wang, Z.; Qian, X.; Yin, J.; Zhu, Z. Large-Scale Fabrication of Tower-like, Flower-like, and Tube-like ZnO Arrays by a Simple Chemical Solution Route. *Langmuir* **2007**, *20*, 3441–3448.

(45) Redkin, A. N.; Chow, L.; Tiginyanu, I. M.; Chai, G.; Ursaki, V. V.; Emelchenko, G. A.; Lupan, O.; Gruzintsev, A. N. Selective Hydrogen Gas Nanosensor Using

Individual ZnO Nanowire with Fast Response at Room Temperature. *Sensors Actuators B Chem.* **2009**, *144*, 56–66.

(46) Yang, P.; Yan, H.; Mao, S.; Russo, R.; Johnson, J.; Saykally, R.; Morris, N.; Pham, J.; He, R.; Choi, H. J. Controlled Growth of ZnO Nanowires and Their Optical Properties. *Advanced Functional Materials*. **2002**, 323–331.

(47) Li, W.; Sun, Y.; Xu, J. Controllable Hydrothermal Synthesis and Properties of ZnO Hierarchical Micro/Nanostructures. *Nano-Micro Lett.* **2014**, *4*, 98–102.

(48) Gao, Y. J.; Zhang, W. C.; Wu, X. L.; Xia, Y.; Huang, G. S.; Xu, L. L.; Shen, J. C.; Siu, G. G.; Chu, P. K. Hydrothermal Self-Assembling of ZnO Nanorods into Sphere-like Superstructures and Their Optical Characteristics. *Appl. Surf. Sci.* **2008**, *255* (5 PART 1), 1982–1987.

(49) Deng, C. .; Ma, N. .; Aravind, M.; Wang, G. .; Yu, P.; To, C. .; Hung, N. .; Ng, D. H. . Large-Scale Synthesis of Aligned Hexagonal ZnO Nanorods Using Chemical Vapor Deposition. *Mater. Lett.* **2004**, *58*, 2195–2198.

(50) Vlasenko, L. S.; Watkins, G. D. Optical Detection of Electron Paramagnetic Resonance for Intrinsic Defects Produced in ZnO by 2.5-MeV Electron Irradiation in Situ at 4.2 K. *Phys. Rev. B - Condens. Matter Mater. Phys.* **2005**, *72*, 035203-12

(51) Liu, C. Y.; Zhang, B. P.; Binh, N. T.; Wakatsuki, K.; Segawa, Y. Temperature Dependence of Structural and Optical Properties of ZnO Films Grown on Si Substrates by MOCVD. *J. Cryst. Growth* **2006**, *290*, 314–318.

(52) Li, C.; Fang, G.; Fu, Q.; Su, F.; Li, G.; Wu, X.; Zhao, X. Effect of Substrate Temperature on the Growth and Photoluminescence Properties of Vertically Aligned ZnO Nanostructures. *J. Cryst. Growth* **2006**, *292*, 19–25.

(53) Li, F.; Hu, L.; Li, Z.; Huang, X. Influence of Temperature on the Morphology and Luminescence of ZnO Micro and Nanostructures Prepared by CTAB-Assisted Hydrothermal Method. *Journal of Alloys and Compounds*. **2008**, 465, 1-2

(54) Orsini, A.; Falconi, C. Real-Time Monitoring of the Solution Growth of ZnO Nanorods Arrays by Quartz Microbalances and in-Situ Temperature Sensors. *Sci. Rep.* **2014**, *4*, 1-7.

(55) Amin, G.; Zaman, S.; Nur, O.; Willander, M.; Asif, M. H.; Zainelabdin, A.

Influence of PH, Precursor Concentration, Growth Time, and Temperature on the Morphology of ZnO Nanostructures Grown by the Hydrothermal Method. *J. Nanomater.* **2011**, *269692*, 1–9.

(56) Xu, S.; Wang, Z. L. One-Dimensional ZnO Nanostructures: Solution Growth and Functional Properties. *Nano Research*. **2011**, 1013–1098.

(57) Wang, C.; Gao, Y.; Wang, L.; Li, P. Morphology Regulation, Structural, and Photocatalytic Properties of ZnO Hierarchical Microstructures Synthesized by a Simple Hydrothermal Method. *Phys. Status Solidi Appl. Mater. Sci.* **2017**, *214*.

(58) Aditya Sumanth, Y.; Annie Sujatha, R.; Mahalakshmi, S.; Karthika, P. C.; Nithiyanantham, S.; Saravanan, S.; Azagiri, M. Synthesis and Characterization of Nanophase Zinc Oxide Materials. *J. Mater. Sci. Mater. Electron.* **2016**, *27*, 1616–1621.

(59) de Lourdes Ruiz Peralta, M.; García Serrano, J.; Pal, U. Morphology Defined ZnO Nanostructures through Microwave Assisted Chemical Synthesis: Growth Mechanism, Defect Structure, and Emission Behaviours. *Adv. Sci. Lett.* **2012**, *6*, 159–166.

(60) Polsongkram, D.; Chamninok, P.; Pukird, S.; Chow, L.; Lupan, O.; Chai, G.; Khallaf, H.; Park, S.; Schulte, A. Effect of Synthesis Conditions on the Growth of ZnO Nanorods via Hydrothermal Method. *Phys. B Condens. Matter* **2008**, *403*, 3713–3717.

(61) Shabannia, R. Vertically Aligned ZnO Nanorods on Porous Silicon Substrates: Effect of Growth Time. *Prog. Nat. Sci. Mater. Int.* **2015**, *25,* 95–100.

(62) Zhang, W.; Wang, P.; Fei, X.; Xiu, Y.; Jia, G. Growth Mechanism and Morphologies Tuning of ZnO Nanostructures. *Int. J. Electrochem. Sci.* **2015**, *10*, 4688–4695.

(63) Wahab, R.; Ansari, S. G.; Seo, H. K.; Kim, Y. S.; Suh, E. K.; Shin, H. S. Low Temperature Synthesis and Characterization of Rosette-like Nanostructures of ZnO Using Solution Process. *Solid State Sci.* **2009**, *11*, 439–443.

(64) Cho, H. K.; Jeong, J.-R.; Hong, S.-K.; Vo, T. S.; Babu, E. S. Photoelectrochemical Water Splitting Properties of Hydrothermally-Grown ZnO Nanorods with

Controlled Diameters. *Electron. Mater. Lett.* **2015**, *11*, 65–72.

(65) Chandraiahgari, C. R.; De Bellis, G.; Balijepalli, S. K.; Kaciulis, S.; Ballirano, P.; Migliori, A.; Morandi, V.; Caneve, L.; Sarto, F.; Sarto, M. S. Control of the Size and Density of ZnO-Nanorods Grown onto Graphene Nanoplatelets in Aqueous Suspensions. *RSC Adv.* **2016**, *6*, 83217–83225.

(66) Yang, L.; Miklavcic, S. J. Revised Kubelka–Munk Theory III A General Theory of Light Propagation in Scattering and Absorptive Media. *J. Opt. Soc. Am. A* **2005**, *22*, 1866.

(67) Nadjia, L.; Abdelkader, E.; Ahmed, B. Photodegradation Study of Congo Red in Aqueous Solution Using ZnO/ UV-A: Effect of PH And Band Gap of Other Semiconductor Groups. *J. Chem. Eng. Process Technol.* **2012**, *02*, 1–7.

(68) Laouedj, N. ZnO-Assisted Photocatalytic Degradation of Congo Red and Benzopurpurine 4B in Aqueous Solution. *J. Chem. Eng. Process Technol.* **2012**, *02*, 2–10.

(69) Murakami, N.; Katayama, S.; Nakamura, M.; Tsubota, T.; Ohno, T. Dependence of Photocatalytic Activity on Aspect Ratio of Shape-Controlled Rutile Titanium(IV) Oxide Nanorods. *J. Phys. Chem. C* **2011**, *115*, 419–424.

(70) Xue, Y.; Wang, L.; Liu, R.; Zhang, X.; Zhang, B.; Yu, P.; Qin, J. Effect of Aspect Ratio and Surface Defects on the Photocatalytic Activity of ZnO Nanorods. *Sci. Rep.* **2014**, *4,* 1-8

(71) Leelavathi, A.; Madras, G.; Ravishankar, N. Origin of Enhanced Photocatalytic Activity and Photoconduction in High Aspect Ratio ZnO Nanorods. *Phys. Chem. Chem. Phys.* **2013**, *15*, 10795–10802.

(72) Maneerung, T.; Tokura, S.; Rujiravanit, R. Impregnation of Silver Nanoparticles into Bacterial Cellulose for Antimicrobial Wound Dressing. *Carbohydr. Polym.* **2008**, *72*, 43–51.

(73) Nel, A.; Xia, T.; Mädler, L.; Li, N. Toxic Potential of Materials at the Nanolevel. *Science*. **2006**, 622–627.

(74) Jones, N.; Ray, B.; Ranjit, K. T.; Manna, A. C. Antibacterial Activity of ZnO Nanoparticle Suspensions on a Broad Spectrum of Microorganisms. *FEMS*

Microbiol. Lett. **2008**, *279*, 71–76.

(75) Sikora, B.; Fronc, K.; Kaminska, I.; Baranowska-Korczyc, A.; Sobczak, K.; Dłuzewski, P.; Elbaum, D. The Growth Kinetics of Colloidal ZnO Nanoparticles in Alcohols. *J. Sol-Gel Sci. Technol.* **2012**, *61*, 197–205.

(76) Xie, J.; Li, P.; Li, Y.; Wang, Y.; Wei, Y. Solvent-Induced Growth of ZnO Particles at Low Temperature. *Mater. Lett.* **2008**, *62*, 2814–2816.

(77) Kuriakose, S.; Satpati, B.; Mohapatra, S. Effects of Solvent on Structural, Optical and Photocatalytic Properties of ZnO Nanostructures. *Adv. Mater. Lett.* **2015**, *6*, 1104–1110.

(78) Khoza, P. B.; Moloto, M. J.; Sikhwivhilu, L. M. The Effect of Solvents, Acetone, Water, and Ethanol, on the Morphological and Optical Properties of ZnO Nanoparticles Prepared by Microwave. *J. Nanotechnol.* **2012**, *2012*, 1–6.

(79) Gadipelli, S.; Guo, Z. Postsynthesis Annealing of MOF-5 Remarkably Enhances the Framework Structural Stability and CO2 Uptake. *Chem. Mater.* **2014**, *26*, 6333–6338.

(80) Cai, D.; Liu, B.; Wang, D.; Wang, L.; Liu, Y.; Qu, B.; Duan, X.; Li, Q.; Wang, T. Rational Synthesis of Metal-Organic Framework Composites, Hollow Structures and Their Derived Porous Mixed Metal Oxide Hollow Structures. *J. Mater. Chem. A* **2015**, *4*, 183–192.

(81) Deng, X.; Wang, X.; Zhang, S.; Shao, M.; Hou, P.; Xu, X.; Huang, J. Fabrication of ZnO/ZnFe2O4 Hollow Nanocages through Metal Organic Frameworks Route with Enhanced Gas Sensing Properties. *Sensors Actuators B Chem.* **2017**, *251*, 27–33.

(82) Alim, K. A.; Fonoberov, V. A.; Shamsa, M.; Balandin, A. A. Micro-Raman Investigation of Optical Phonons in ZnO Nanocrystals. *J. Appl. Phys.* **2005**, *97*, 1–5.

(83) Kamarulzaman, N.; Kasim, M. F.; Rusdi, R. Band Gap Narrowing and Widening of ZnO Nanostructures and Doped Materials. *Nanoscale Res. Lett.* **2015**, *10*, 346.

(84) Meulenkamp, E. A. Synthesis and Growth of ZnO Nanoparticles. *J. Phys. Chem. B* **2002**, *102*, 5566–5572.

(85) Zainelabdin, A.; Bano, N.; Hussain, I.; Willander, M.; Nur, O.; Sadaf, J. R.; Qadir, M. I.; Zaman, S.; Zainelabdin, A.; Bano, N.; et al. Luminescence from Zinc Oxide Nanostructures and Polymers and Their Hybrid Devices. *Materials (Basel).* **2010**, *3*, 2643–2667.

(86) Weller, H. Quantum Size Colloids: From Size-Dependent Properties of Discrete Particles to Self-Organized Superstructures. *Curr. Opin. Colloid Interface Sci.* **1998**, *3*, 194–199.

(87) Chang, C. H.; Franses, E. I. Adsorption Dynamics of Surfactants at the Air/Water Interface: A Critical Review of Mathematical Models, Data, and Mechanisms. *Colloids and Surfaces A: Physicochemical and Engineering Aspects*. **1995**, pp 1–45.

(88) Farouq, R.; Yousef, N. S. Equilibrium and Kinetics Studies of Adsorption of Copper (II) Ions on Natural Biosorbent. *Int. J. Chem. Eng. Appl.* **2015**, *6*, 319–324.

(89) Ho, Y. S.; McKay, G. Application of Kinetic Models to the Sorption of Copper(II) on to Peat. *Adsorpt. Sci. Technol.* **2003**, *20*, 797–815.

(90) Chien, S. H.; Clayton, W. R. Application of Elovich Equation to the Kinetics of Phosphate Release and Sorption in Soils1. *Soil Sci. Soc. Am. J.* **2010**, *44*, 265.

(91) Wu, F. C.; Tseng, R. L.; Juang, R. S. Initial Behavior of Intraparticle Diffusion Model Used in the Description of Adsorption Kinetics. *Chem. Eng. J.* **2009**, *153*, 1–8.

(92) Sekine, T.; Nakatani, K. Intraparticle Diffusion and Adsorption Isotherm for Sorption in Silica Gel Studied by Single-Microparticle Injection and Microabsorption Methods. *Langmuir* **2002**, *18*, 694–697.

(93) Weber, W. J.; Morris, J. C. Kinetics of Adsorption on Carbon From Solution. *J. Sanit. Eng. Div.* **1963**, *89*, 31–60.

(94) Robati, D. Pseudo-Second-Order Kinetic Equations for Modeling Adsorption Systems for Removal of Lead Ions Using Multi-Walled Carbon Nanotube. *J. Nanostructure Chem.* **2013**, *3*, 55.

(95) Miyake, Y.; Ishida, H.; Tanaka, S.; Kolev, S. D. Theoretical Analysis of the Pseudo-Second Order Kinetic Model of Adsorption. Application to the Adsorption

of Ag(I) to Mesoporous Silica Microspheres Functionalized with Thiol Groups. *Chem. Eng. J.* **2013**, *218*, 350–357.

(96) Wu, F. C.; Tseng, R. L.; Huang, S. C.; Juang, R. S. Characteristics of Pseudo-Second-Order Kinetic Model for Liquid-Phase Adsorption: A Mini-Review. *Chemical Engineering Journal*. 2009,1–9.

(97) Kershaw, S. V.; Jing, L.; Huang, X.; Gao, M.; Rogach, A. L. Materials Aspects of Semiconductor Nanocrystals for Optoelectronic Applications. *Materials Horizons*. **2017**,155–205.

(98) Zhu, L.; Li, C.; Li, Y.; Feng, C.; Li, F.; Zhang, D.; Chen, Z.; Wen, S.; Ruan, S. Visible-Light Photodetector with Enhanced Performance Based on a ZnO@CdS Heterostructure. *J. Mater. Chem. C* **2015**, *3*, 2231–2236.

(99) Pan, C.; Niu, S.; Ding, Y.; Dong, L.; Yu, R.; Liu, Y.; Zhu, G.; Wang, Z. L. Enhanced Cu 2S/CdS Coaxial Nanowire Solar Cells by Piezo-Phototronic Effect. *Nano Lett.* **2012**, *12*, 3302–3307.

(100) Li, G.; Jiang, Y.; Zhang, Y.; Lan, X.; Zhai, T.; Yi, G. C. High-Performance Photodetectors and Enhanced Field-Emission of CdS Nanowire Arrays on CdSe Single-Crystalline Sheets. *J. Mater. Chem. C* **2014**, *2*, 8252–8258.

(101) Cheng, P.; Zhan, X. Versatile Third Components for Efficient and Stable Organic Solar Cells. *Mater. Horizons* **2015**, *2*, 462–485.

(102) Hong, C. W.; Shin, S. W.; Suryawanshi, M. P.; Gang, M. G.; Heo, J.; Kim, J. H. Chemically Deposited CdS Buffer/Kesterite Cu2ZnSnS4 Solar Cells: Relationship between CdS Thickness and Device Performance. *ACS Appl. Mater. Interfaces* **2017**, *9*, 36733–36744.

(103) Zhang, R.; Zhang, B.; Liu, Y.; Sun, S. Preparation of 3D Graphene Networks and a C Dot Grafted Graphene Hybrid by New Methods for Improving the Photovoltaic Performance of CdS/CdSe Quantum Dot Sensitized Solar Cells. *J. Mater. Chem. C* **2016**, *4*, 1633–1644.

(104) Prudnikau, A.; Chuvilin, A.; Artemyev, M. CdSe-CdS Nanoheteroplatelets with Efficient Photoexcitation of Central CdSe Region through Epitaxially Grown CdS Wings. *J. Am. Chem. Soc.* **2013**, *135*, 14476–14479.

(105) Gao, J.; Sun, L.; Li, L.; Yang, X.; Tian, H.; Zhao, J.; Hagfeldt, A. Highly Efficient CdS Quantum Dot-Sensitized Solar Cells Based on a Modified Polysulfide Electrolyte. *J. Am. Chem. Soc.* **2011**, *133*, 8458–8460.

(106) Yuan, K.; Chen, L.; Li, F.; Chen, Y. Nanostructured Hybrid ZnO@CdS Nanowalls Grown in Situ for Inverted Polymer Solar Cells. *J. Mater. Chem. C* **2014**, *2*, 1018–1027.

(107) Mahapatra, N.; Panja, S.; Mandal, A.; Halder, M. A Single Source-Precursor Route for the One-Pot Synthesis of Highly Luminescent CdS Quantum Dots as Ultra-Sensitive and Selective Photoluminescence Sensor for Co2+ and Ni2+ Ions. *J. Mater. Chem. C* **2014**, *2*, 7373–7384.

(108) Bansal, A. K.; Antolini, F.; Zhang, S.; Stroea, L.; Ortolani, L.; Lanzi, M.; Serra, E.; Allard, S.; Scherf, U.; Samuel, I. D. W. Highly Luminescent Colloidal CdS Quantum Dots with Efficient Near-Infrared Electroluminescence in Light-Emitting Diodes. *J. Phys. Chem. C* **2016**, *120*, 1871–1880.

(109) Castelli, A.; Meinardi, F.; Pasini, M.; Galeotti, F.; Pinchetti, V.; Lorenzon, M.; Manna, L.; Moreels, I.; Giovanella, U.; Brovelli, S. High-Efficiency All-Solution-Processed Light-Emitting Diodes Based on Anisotropic Colloidal Heterostructures with Polar Polymer Injecting Layers. *Nano Lett.* **2015**, *15*, 5455–5464.

(110) Zhang, Q.; Wang, C.-F.; Ling, L.-T.; Chen, S. Fluorescent Nanomaterial-Derived White Light-Emitting Diodes: What’s Going On. *J. Mater. Chem. C* **2014**, *2*, 4358–4373.

(111) Han, C.; Wang, F.; Gao, C.; Liu, P.; Ding, Y.; Zhang, S.; Yang, M. Transparent Epoxy-ZnO/CdS Nanocomposites with Tunable UV and Blue Light-Shielding Capabilities. *J. Mater. Chem. C* **2015**, *3*, 5065–5072.

(112) Kwak, J.; Lim, J.; Park, M.; Lee, S.; Char, K.; Lee, C. High-Power Genuine Ultraviolet Light-Emitting Diodes Based on Colloidal Nanocrystal Quantum Dots. *Nano Lett.* **2015**, *15*, 3793–3799.

(113) Saha, A.; Chellappan, K. V.; Narayan, K. S.; Ghatak, J.; Datta, R.; Viswanatha, R. Near-Unity Quantum Yield in Semiconducting Nanostructures: Structural Understanding Leading to Energy Efficient Applications. *J. Phys. Chem. Lett.*

2013, *4*, 3544–3549.

(114) Zheng, C.; Wang, W.; Liu, Y.; Xu, C.; Wang, G.; Liu, Z. Synthesis of CdS Nanoparticles by a Novel and Simple One-Step, Solid-State Reaction in the Presence of a Nonionic Surfactant. *Mater. Lett.* **2003**, *57*, 2755–2760.

(115) Tripathi, R.; Kumar, A. Dielectric Properties of ZnO Nanoparticles Synthesized by Soft Chemical Method. *AIP Conf. Proc.* **2009**, *1147*, 262–268.

(116) Lu, Y.; Li, L.; Ding, Y.; Zhang, F.; Wang, Y.; Yu, W. Hydrothermal Synthesis of Functionalized CdS Nanoparticles and Their Application as Fluorescence Probes in the Determination of Uracil and Thymine. *J. Lumin.* **2012**, *132*, 244–249.

(117) Ayodhya, D.; Venkatesham, M.; Santoshi kumari, A.; Bhagavanth Reddy, G.; Veerabhadram, G. One-Pot Sonochemical Synthesis of CdS Nanoparticles: Photocatalytic and Electrical Properties. *Int. J. Ind. Chem.* **2015**, *6*, 261–271.

(118) Rodríguez-Castañeda, C. A.; Moreno-Romero, P. M.; Martínez-Alonso, C.; Hu, H. Microwave Synthesized Monodisperse CdS Spheres of Different Size and Color for Solar Cell Applications. *J. Nanomater.* **2015**, *2015*.

(119) Xu, W.; Akins, D. L. Reverse Micellar Synthesis of CdS Nanoparticles and Self-Assembly into a Superlattice. *Mater. Lett.* **2004**, *58*, 2623–2626.

(120) Lien, V. T. K.; Ha, C. V.; Ha, L. T.; Dat, N. N. Optical Properties of CdS and CdS/ZnS Quantum Dots Synthesized by Reverse Micelle Method. *J. Phys. Conf. Ser.* **2009**, *187*.

(121) Ding, Y.; Qian, Y.; Zhang, Y.; Fan, Y.; Liao, H.; Li, Y. Solvothermal Elemental Direct Reaction to CdE (E = S, Se, Te) Semiconductor Nanorod. *Inorg. Chem.* **1999**, *38*, 1382–1387.

(122) Yang, J.; Zeng, J. H.; Yu, S. H.; Yang, L.; Zhou, G. E.; Qian, Y. T. Formation Process of CdS Nanorods via Solvothermal Route. *Chem. Mater.* **2000**, *12*, 3259–3263.

(123) Neren Ökte, A.; Yilmaz, Ö. Photodecolorization of Methyl Orange by Yttrium Incorporated TiO2 Supported ZSM-5. *Appl. Catal. B Environ.* **2008**, *85*, 92–102.

(124) Jiang, N.; Xu, Y.; He, N.; Chen, J.; Deng, Y.; Yuan, C.; Han, G.; Dai, L. Synthesis

of Walnut-like Hierarchical Structure with Superhydrophobic and Conductive Properties. *J. Mater. Chem.* **2010**, *20*, 10847–10855.

(125) Tauc, J.; Menth, A. States in the Gap. *J. Non. Cryst. Solids* **1972**, *8–10*, 569–585.

(126) Winter, J. O.; Gomez, N.; Gatzert, S.; Schmidt, C. E.; Korgel, B. A. Variation of Cadmium Sulfide Nanoparticle Size and Photoluminescence Intensity with Altered Aqueous Synthesis Conditions. *Colloids Surfaces A Physicochem. Eng. Asp.* **2005**, *254*, 147–157.

(127) Chestnoy, N.; Harris, T. D.; Hull, R.; Brus, L. E. Luminescence and Photophysics of Cadmium Sulfide Semiconductor Clusters: The Nature of the Emitting Electronic State. *J. Phys. Chem.* **2005**, *90*, 3393–3399.

(128) R. Heath, J. Covalency in Semiconductor Quantum Dots. *Chem. Soc. Rev.* **2005**, *27*, 65.

(129) Wang, W.; Germanenko, I.; El-Shall, M. S. Room-Temperature Synthesis and Characterization of Nanocrystalline Cds, ZnS, and CdxZn1-XS. *Chem. Mater.* **2002**, *14*, 3028–3033.

(130) Dong, C.; Zhong, M.; Huang, T.; Ma, M.; Wortmann, D.; Brajdic, M.; Kelbassa, I. Photodegradation of Methyl Orange under Visible Light by Micro-Nano Hierarchical Cu 2O Structure Fabricated by Hybrid Laser Processing and Chemical Dealloying. *ACS Appl. Mater. Interfaces* **2011**, *3*, 4332–4338.

(131) Sachin B. Kakodkar. Synthesis, Characterisation and Photocatalytic Activity of Cadmium Sulphide Nanoparticles. *Chem. Sci. Trans.* **2016**, *5*, 75–78.

(132) Soltani, N.; Saion, E.; Mahmood Mat Yunus, W.; Navasery, M.; Bahmanrokh, G.; Erfani, M.; Zare, M. R.; Gharibshahi, E. Photocatalytic Degradation of Methylene Blue under Visible Light Using PVP-Capped ZnS and CdS Nanoparticles. *Sol. Energy* **2013**, *97*, 147–154.

(133) Wang, Z.; Yang, X.; Jia, H.; Wang, Y. Preparation of Self-Assembled Hollow Microsphere CdS via Solvothermal Method and Its Optical Properties. *J. Mater. Sci. Mater. Electron.* **2016**, *27*, 9725–9733.

(134) Singh, R.; Pal, B. Woolen Bun Shaped CdS Microspheres Enfolded 1D Nanowires for the Superior Photooxidation of Dyes: A Comparative Case Study. *J. Mol. Catal.*

A Chem. **2015**, *396*, 15–22.

(135) Ganesh, R. S.; Sharma, S. K.; Durgadevi, E.; Navaneethan, M.; Binitha, H. S.; Ponnusamy, S.; Muthamizhchelvan, C.; Hayakawa, Y.; Kim, D. Y. Surfactant Free Synthesis of CdS Nanospheres, Microstructural Analysis, Chemical Bonding, Optical Properties and Photocatalytic Activities. *Superlattices Microstruct.* **2017**, *104*, 247–257.

(136) Raja, P.; Bozzi, A.; Mansilla, H.; Kiwi, J. Evidence for Superoxide-Radical Anion, Singlet Oxygen and OH-Radical Intervention during the Degradation of the Lignin Model Compound (3-Methoxy-4-Hydroxyphenylmethylcarbinol). *J. Photochem. Photobiol. A Chem.* **2005**, *169*, 271–278.

(137) Stylidi, M.; Kondarides, D. I.; Verykios, X. E. Visible Light-Induced Photocatalytic Degradation of Acid Orange 7 in Aqueous TiO2suspensions. *Appl. Catal. B Environ.* **2004**, *47*, 189–201.

(138) Boonstra, A. H.; Mutsaers, C. A. H. A. Relation between the Photoadsorption of Oxygen and the Number of Hydroxyl Groups on a Titanium Dioxide Surface. *J. Phys. Chem.* **1975**, *79*, 1694–1698.

(139) Jing, D.; Guo, L. A Novel Method for the Preparation of a Highly Stable and Active CdS Photocatalyst with a Special Surface Nanostructure. *J. Phys. Chem. B* **2006**, *110*, 11139–11145.

(140) Moloto, N.; Revaprasadu, N.; Musetha, P. L.; Moloto, M. J. The Effect of Precursor Concentration, Temperature and Capping Group on the Morphology of CdS Nanoparticles. *J. Nanosci. Nanotechnol.* **2009**, *9*, 4760–4766.

(141) Nanoparticles, M. A. C. Effect of Precursor Concentration on the Particle Size Of. *J. New Mater. Electrochem. Syst.* **2007**, *47*, 43–47.

(142) Xu, L.; Su, Y.; Cai, D.; Chen, Y.; Feng, Y. Synthesis and Photoluminescence Properties of CdS Nanobelts. *Mater. Lett.* **2006**, *60*, 1420–1424.

(143) Pattabi, M.; Amma, B. S. Synthesis and Stability Studies of Thiophenol Capped CdS Nanoparticles. *Sol. Energy Mater. Sol. Cells* **2006**, *90*, 2377–2383.

(144) Rao, C. N. R.; Kulkarni, G. U.; John Thomas, P.; Edwards, P. P. Size-Dependent Chemistry: Properties of Nanocrystals. *Chem. - A Eur. J.* **2002**, *8*, 28–35.

Vita

The author, Smriti Thakur, was born on October 16, 1991 in Panipat (Haryana) in India. She earned her B.Sc. (Hons.) Chemistry from Ramjas College Delhi, University of Delhi in 2012, and B.Ed. from Kurukshetra University, Kurukshetra (KUK), Haryana in 2013. She joined Indian Institute of Science Education and Research (IISER) Mohali as an Integrated-Ph.D. student in August, 2013 and pursued her M.S.(Chemical Sciences) and started her Ph.D. degree in September, 2015 in Chemistry under the supervision of Professor Sanjay K. Mandal with a fellowship from MHRD, Govt. of India.